

密级: _____



中国科学院大学
University of Chinese Academy of Sciences

博士学位论文

利用低轨卫星加速仪和精密轨道数据估计 热层中性大气密度变化的研究

作者姓名: _____ Andrés Calabia Aibar _____

指导教师: _____ 金双根 (研究员中国科学院上海天文台) _____

学位类别: _____ 理学博士 _____

学科专业: _____ 天体测量与天体力学 _____

研究所: _____ 中国科学院上海天文台 _____

二零一七年五月

**Thermospheric neutral density variations from Low Earth
Orbit accelerometers and precise orbits**

By

Andrés Calabia Aibar

Supervisor:

Prof. Shuanggen Jin

A Dissertation Submitted to

University of Chinese Academy of Sciences

In partial fulfillment of the requirement

For the degree of

Doctor of Philosophy

Shanghai Astronomical Observatory, CAS

May 2017

摘要

热层位于地球大气中间层之上，散逸层之下，受太阳短波辐射处于高度电离状，以及磁层-电离层-热圈（MIT）耦合，其变化和活动过程非常复杂。因此，精确测定热层中性大气密度变化对上层大气研究、精密定轨和无线电传播研究具有重要意义。然而，当前热层中性大气密度经验模型无法准确估计大气密度变化和地预测该层的变化，以及缺乏实测资料，很难准确估计高层大气变化和地理解其耦合机理。如今众多低轨卫星加速度计和精密轨道观测可估计热层中性大气密度，为研究高层大气变化提供了新的观测数据。本论文利用 2003-2016 年 GRACE（重力恢复和气候实验）加速度计和精密轨道数据估计和研究热层中性大气密度变化。其主要研究结果和发现如下：

- 1) 利用 GRACE 精密轨道速度的一阶导数估计了非重力加速度，校准了 GRACE 加速度计。并从 GRACE 精密轨道、时变重立场模型和加速度计测量估计了保守力异常，基于主成分分析（PCA）方法在空间和时间上分析了其异常，发现了其周日内频率有趣结构可能与大气潮汐相关。
- 2) 利用 2003-2016 年重力卫星（GRACE）加速度计和精密轨道数据（POE）分别反演了热层中性大气密度，具有较好的一致性，且好于经验模型 NRLMSISE00。并进一步用新的主成分分析方法分析了热层大气密度变化，以及建立与本地太阳时（LST）、日年和太阳活动通量 P10.7 和地磁指数相关的参数化模型。本地太阳时（LST）参数化模型显示一个有趣的控制中纬度 4 波模式的扰动。该参数化模型能够反映小尺度热层大气密度变化，如赤道质量异常（EMA）和午夜密度最大值（MDM），且可用于改进目前的热层经验模型。
- 3) 在频谱域上进一步分析了主成分分析后的残差，并在辐射潮（P1, K, T2 和 R2）的频率上首次发现了其它的周期性贡献，如 83, 93, 152 和 431 天。其 93 天的周期可能是由卫星近地点漂移引起的，83 天和 152 天周期可能归由于太阳活动造成的。自由核章动频率（431 天）变化可能暗含地球内核与磁层-电离层-热圈（MIT）存在耦合。
- 4) 发现了热层大气密度平均长期变化分布与地球磁场密切相关，且南半球高于北半球。非对称的单元位于极区，南极区增强，北极区减弱，且均位于东极一侧，而在西极

区也具有相应的衰减或增强。且南北极区纬度变化在所有时间段内均为正，主要受太阳辐射的强烈控制。

- 5) 并进一步分析了 2015 年 3 月和 2013 年 3 月地磁暴热层大气密度变化与行为，及其与空间环境和地磁指数关系。结果发现在低纬度区域与磁暴指数 Dst 非常相关，高纬度与综合电场 (Em) 相关。其中 2015 年 3 月磁暴，热层大气密度相比平静状态增加达到 500% 偏差，日平均偏差达到 180%。

本文对全球热层中性密度变化进行了深入的研究与解释，验证了该技术可获得全球热层中性大气密度变化，并获得了经验模型，且残差中新的周期性变化现象暗含着新的科学问题和应用。

关键词：非重力加速度，热层大气密度，精密轨道星历 (POE)，加速度计校准，地球低轨卫星 (LEO)

ABSTRACT

The thermosphere is located above the mesosphere and below the exosphere, and its highly ionized state increases the complexity of its geophysical processes due to the magnetosphere-ionosphere-thermosphere (MIT) coupling. Therefore, accurate measurement of neutral density variations is essential for atmospheric research, Precise Orbit Determination (POD), and radio wave propagation. However, it is difficult to quantify and interpret the upper atmospheric variations due to large uncertainty in the models and lack of measurements from the limited traditional technologies of observation. Nowadays, thermospheric neutral densities estimated from accelerometers and GNSS onboard LEO satellites provide a unique opportunity to study the upper atmosphere with new observational data. In this thesis, thermospheric neutral density variations are inferred and investigated from accelerometers and precise orbits of GRACE (Gravity Recovery and Climate Experiment) for the period 2003-2016. Main results and findings are summarized as follows:

- 1) A new methodology to derive non-gravitational accelerations is presented through the first derivatives of precise-orbit velocities, which can calibrate the GRACE accelerometers. The conservative-force anomalies derived from analytical time-varying gravity models, accurate orbit solutions, and accelerometer measurements along GRACE orbits are analyzed in space and time through a new technique based in the Principal Component Analysis (PCA). The results reveal intriguing structures at the sub-daily frequency probably related to atmospheric tides.
- 2) Thermospheric neutral density variations are estimated from accelerometer measurements and GRACE precise orbits for the period 2003-2016, showing good agreement and a better estimation than the NRLMSISE00 empirical model. Furthermore, thermospheric neutral density variations from GRACE measurements are investigated using the new PCA technique, and the resulting modes have been parameterized in terms of Local Solar Time (LST), day-of-year, and solar P10.7 flux and geomagnetic A_m indices. The LST parameterization shows an interesting fluctuation controlling a middle-latitude 4-wave pattern. This model is suitable to represent small scale variations including, e.g., Equatorial Mass Anomaly (EMA) and Midnight Density Maximum (MDM), and can be used to improve the current thermosphere modeling.

- 3) The residuals from the PCA parameterization are further analyzed in the spectral domain, and additional periodic contributions have been found at the frequencies of the radiational tides (P1, K, T2, and R2). In addition, periodic contributions are found at the periods of 83, 93, 152 and 431 days. The 93-day period could be caused by the satellite's drift of perigee, and the 83 and 152 day periods might be attributed to solar activity. Variations at the free-core nutation frequency (431 day) suggest a possible core-MIT coupling.
- 4) As for the long term variations, the average distribution shows a clear alignment with the geomagnetic field, with higher values in the southern hemisphere than in the northern hemisphere. Two asymmetric cells are located in the polar caps: a southern-enhancement, and a northern-attenuation, both located in their eastern polar sides. In addition, each polar-cell has a corresponding attenuation (enhancement) in the western polar side. The latitudinal variation shows higher values of density in the southern hemisphere during all time-span, and strongly controlled by the solar radiation.
- 5) Thermospheric neutral density variations and behaviors following the March 2013 and March 2015 geomagnetic storms are investigated in relation to space weather and geomagnetic indices, showing good correlation with the *Dst* index and the merging electric field (E_m), for low latitude and high-latitude variations, respectively. In March 2015, density enhancements reached maxima deviations of 500 %, and daily-averaged deviations up to 180 %.

A better understanding of global thermospheric neutral density variations is achieved, which validates the suitability of the technique and the resulting empirical model. The new periodicities and dependences in the residuals promise numerous intriguing questions for future research.

Keywords: Non-gravitational accelerations, Thermospheric density, Precise Orbit Ephemeris (POE), Accelerometer calibration, Low Earth Orbit (LEO) satellites.

I dedicate my dissertation to my beloved family, for our love, encouragement, and sacrifices.

TABLE OF CONTENTS

ABSTRACT..... 3

DEDICATION 5

TABLE OF CONTENTS..... 7

NOMENCLATURE AND ABBREVIATIONS..... 9

LIST OF FIGURES13

LIST OF TABLES23

1. INTRODUCTION25

 1.1. Background25

 1.1.1. *The upper atmosphere processes*25

 1.1.2. *Significance and applications*27

 1.2. Status and progress28

 1.2.1. *Sensing*28

 1.2.2. *Understanding*.....33

 1.2.3. *Modeling*36

 1.3. Problems and motivation.....38

 1.4. Research contents40

2. OBSERVATION AND DATA PROCESSING41

 2.1. The GRACE and GOCE observables.....41

 2.2. Non-gravitational accelerations from POE42

 2.2.1. *Arc-to-chord interpolation threshold*.....42

 2.2.2. *Time-varying gravity model*.....43

 2.2.3. *Transformations between reference systems*54

 2.3. Thermospheric neutral density retrieval.....59

 2.3.1. *Drag-force formula and altitude normalization*59

 2.3.2. *Irradiative accelerations*.....60

 2.3.3. *Drag coefficient vector C*.....65

 2.4. Spatiotemporal PCA of measurements along orbits.....66

3. ACCELEROMETER CALIBRATION AND POD ASSESSMENT71

 3.1. Disturbing sinusoidal signal in GRACE’s and GOCE’s POD71

3.2. Uncertainty of POE-based non-gravitational accelerations	75
3.3. Calibration of GRACE accelerometers	77
3.4. Assessment of conservative force models.....	80
3.5. Summary	86
4. THERMOSPHERIC NEUTRAL DENSITY ESTIMATES FROM GRACE	89
4.1. Neutral density estimates from GRACE accelerometers	89
4.2. Neutral density estimates from POE of GRACE	92
4.3. Filling accelerometer data-gaps with POE-based estimates	93
4.4. Uncertainty analysis of POE-estimated neutral densities.....	95
4.5. Summary	99
5. GLOBAL DISTRIBUTION AND VARIATIONS OF THERMOSPHERIC NEUTRAL DENSITY	101
5.1. Spatiotemporal analysis with PCA.....	101
5.2. Modes and mechanisms.....	103
5.2.1. <i>Parameterization of time-expansion EOF</i>	103
5.2.2. <i>Local Solar Time and annual variations</i>	105
5.2.3. <i>Neutral density variations at the radiational-tides frequency</i>	109
5.2.4. <i>Parameterization and contrast of results</i>	114
5.3. Long-term variations and distribution of thermospheric neutral density	119
5.4. Neutral density variations under geomagnetic storms	121
5.4.1. <i>Space weather and geomagnetic indices</i>	123
5.4.2. <i>The March 2015 geomagnetic storm</i>	125
5.4.3. <i>The March 2013 geomagnetic storm</i>	129
5.5. Summary	134
6. CONCLUSIONS AND PERSPECTIVE.....	137
6.1. Conclusions	137
6.2. Problems and perspective.....	139
APPENDICES	143
REFERENCES.....	161
ACKNOWLEDGMENTS.....	177
CURRICULUM VITAE.....	179

NOMENCLATURE AND ABBREVIATIONS

ADM	Accelerometer Density Model
AIUB	Astronomical Institute of the University of Bern
CACTUS	French acronym meaning ultrasensitive, three-axis, capacitive accelerometric transducer
cgm	Corrected Geomagnetic
CHAMP	Challenging Mini Satellite Payload.
CIR	Co-rotating Interaction Regions
CIRA	Committee on Space Research International Reference Atmosphere
DLR	Deutsches Zentrum Für Luft und Raumfahrt
CME	Coronal Mass Ejection
DORIS	Doppler Orbitography & Radio positioning Integrated by Satellite
DSMC	Direct Simulation Monte Carlo
DS	December Solstice
DTM	Drag Temperature Model
ECCO	Estimating the Circulation and Climate of the Ocean
ECMWF	European Centre for Medium-Range Weather Forecasts
E_m	Solar wind merging electric field
EMA	Equatorial Mass Anomaly
ENU	East-North-Up
EOF	Empirical Orthogonal Function
EOP	Earth Orientation Parameters
ESA	European Space Agency
ETA	Equatorial Thermosphere Anomaly
EUV	Extreme Ultra Violet
FCN	Free-Core Nutation
FWHM	Full Latitudinal Width at Half Maximum
GA/GB	Satellite identifier (GRACE-A/GRACE-B)
GAMDM	Global Average Mass Density Model
GFZ	GeoForschungsZentrum
GIPSY	GPS Inferred Positioning System
GLDAS	Global Land Data Assimilation Systems
GNSS	Global Navigation Systems
GOCE	Gravity Field and Steady-State Ocean Circulation Explorer
GPS	Global Positioning System
GRACE	Gravity Recovery And Climate Experiment
GSM	Geocentric-Solar-Magnetospheric
GSWM	Global-Scale Wave Model
ICRS	International Celestial Reference System
IMF	Interplanetary Magnetic Field
ISDC	Information System and Data Center
ISGI	International Service of Geomagnetic Indices
ITRS	International Terrestrial Reference System
JD	Julian Date
JPL	Jet Propulsion Laboratory
JS	June Solstice
LEO	Low Earth Orbit
LST	Local Solar Time

MDM	Midnight Density Maximum
ME	March Equinox
MESA	Miniature Electrostatic Single-axis Accelerometer
MERRA	Modern Era Retrospective-Analysis for Research and Applications
MIT	Magnetosphere-Ionosphere-Thermosphere
MJD	Modified Julian Date
MLT	Magnetic Local Time
MSIS	Mass Spectrometer and Incoherent Scatter radar
NASA	National Aeronautics and Space Administration
NCEP	National Centers for Environmental Prediction
NRLMSISE00	Naval Research Laboratory Mass Spectrometer and Incoherent Scatter Radar, Version 2000
NRMSD	Normalized RMSD
ODTK	Orbit Determination Tool Kit
ORS	Orbit Reference System
PCA	Principal Component Analysis
POD	Precise Orbit Determination
POE	Precise Orbital Ephemeris
RMSD	Root-Mean-Square Deviation
SBS	Satellite Body System
SD	Standard Deviation
SE	September Equinox
SETA	Satellite Electrostatic Tri-axial Accelerometer
SLR	Satellite Laser Ranging
TAI	International Atomic Time
TDB	Barycentric Dynamical Time
TIME-GCM	Thermosphere-Ionosphere-Electrodynamics General Circulation Model
TLE	Two-Line Element
TOMS	Total Ozone Mapping Spectrometer
TT	Terrestrial Time
TVG	Time-Varying Gravity
UTC	Coordinated Universal Time
UTCSR	University of Texas, Center for Space Research
$[P]$	Rotation matrix for precession
$[N]$	Rotation matrix for nutation
$[S]$	Rotation matrix for sidereal time
$[PM]$	Rotation matrix for polar motion
δ_{jk}	Kronecker's delta
t_i	Instant i of time
Δt	Increment of time
c	Speed of light
U	Gravitational potential
GM	Product of gravitational constant by mass
a_e	Equatorial radius of the Earth
\bar{P}_{lm}	Normalized associated Legendre functions of degree l and order m
\bar{C}_{lm}	Normalized Stokes' coefficient of degree l and order m for cosine
\bar{S}_{lm}	Normalized Stokes' coefficient of degree l and order m for sine

ω_{Earth}	Rotation vector of the Earth
r	Satellite position vector
\dot{r}	Satellite velocity vector
\ddot{r}	Satellite acceleration vector
(φ, λ)	Latitude, longitude
C	Drag coefficient vector
C_D, C_L	Drag and lift coefficients
C_n, C_t	Pressure and shear coefficients
v_r	Relative velocity of the atmosphere with respect to the spacecraft
v_c	Velocity of the co-rotating atmosphere
v_w	Velocity of the horizontal winds

LIST OF FIGURES

Figure 1.1	Terrestrial upper atmosphere processes. Credit: <i>NASA/J. Grobowsky</i>	25
Figure 1.2	Plasma density ecliptic viewed from the north on October 12 th 2016. The Sun is at the center of the plot, the Earth on the right and the two Solar-TERrestrial RELations Observatory (Stereo) spacecrafts on the left. Both CME and CIR can be identified. From http://www.swpc.noaa.gov/products/wsa-enlil-solar-wind-prediction	26
Figure 1.3	Accelerations acting on a satellite. Gravitational accelerations are pictured in blue, and non-gravitational in red.	28
Figure 1.4	Observed, POD-estimated, and modeled non-gravitational accelerations from CHAMP and GRACE for the along-track (top), cross-track (middle) and radial (bottom) direction (first 6 h of 7 November 2003). GEODYN software is used for POD. [<i>Visser et al., 2013, Fig. 5</i>].....	31
Figure 1.5	Measured (accelerometer), and modeled neutral densities from GRACE and CHAMP (first 6 h of 7 November 2003). Estimates correspond to Figure 1.4 accelerometer measurements and model. [<i>Visser et al., 2013, Fig. 6 and 7</i>].	32
Figure 1.6	Measured, modeled and POE-derived neutral densities from GRACE and TerraSAR-X, on September 26-27, 2007. ODTK software is used for POD. [<i>McLaughlin et al., 2013, Fig. 3</i>].....	32
Figure 1.7	Distribution of the dayside thermospheric neutral density (in units of 10^{-12} kg/m ³) under quiet geomagnetic and solar conditions (F10.7 = 150). The black line indicates the dip equator. [<i>Liu et al., 2007</i>].....	33
Figure 1.8	Correlation between CHAMP-derived densities and solar flux level, (a) for the day side and (b) for the night side density. [<i>Müller et al., 2009, Fig.3</i>].....	34
Figure 1.9	Seasonal variation of the density (a) in the day and (b) in the night time sector. The red curves represent the fitted annual harmonics functions. [<i>Müller et al., 2009, Fig.3</i>].....	35
Figure 1.10	Histograms showing the distribution of CHAMP and GRACE-A densities, with their equivalent model densities for MSIS (NRLMSISE-00) and Jacchia (JB-2008) models. The line graphs at both	

	axes show simple two-dimensional histograms of their corresponding data set in black. [Doornbos, 2011, Fig. 5.8]	37
Figure 2.1	Luni-solar tides for GRACE on July 14 th , 2007.	46
Figure 2.2	Earth solid tides for GRACE on July 14 th , 2007.....	49
Figure 2.3	Ocean tides for GRACE on July 14 th , 2007.....	49
Figure 2.4	Earth's solid pole tides for GRACE on July 14 th , 2007.....	51
Figure 2.5	Ocean pole tides for GRACE on July 14 th , 2007.....	52
Figure 2.6	Schwarzschild field for GRACE on July 14 th , 2007.....	52
Figure 2.7	Force-model accelerations (absolute values) for GRACE on July 14 th , 2007.....	54
Figure 2.8	Representation of the star-camera quaternion angles.	56
Figure 2.9	Eclipse computation geometry.....	61
Figure 2.10	Induced direct solar radiation acceleration for GRACE-A in the SBS on April 1 st 2005.	63
Figure 2.11	Induced (a) terrestrial infrared radiation acceleration and (b) Earth albedo acceleration for GRACE-A in the SBS on April 1 st 2005.	64
Figure 2.12	Grid clipping of interpolated measurements (ascending-orbits).....	67
Figure 2.13	The matrix $F =$ instant of time x given location. [Bjornsson and Venegas, 1997]	68
Figure 3.1	Accelerations of GRACE on July 15 th , 2006. POE-based non-gravitational accelerations are in cyan and accelerometer measurements in black. Dotted blue line represents the POE-based non-gravitational accelerations corrected from systematic errors. [Calabia and Jin, 2016a, Fig.1]	71
Figure 3.2	Residuals from Figure 3.1, after removing the systematic error on axis Y_{SBS} and smoothing the solution on axis Y_{SBS} . The periodic behavior of varying amplitude of Y_{SBS} can also be seen in Bezděk [2010, Figure 7] . Results for both satellites are similar. Plots are not equally scaled. [Calabia et al., 2015, Fig.1]	72

Figure 3.3	In dashed line for GRACE-A and solid line for GRACE-B, fitted parameters of the sinusoidal function f_H , which removes the systematic error on Y_{SBS} axes. Parameters of function f_L are not plotted because are similar, but with amplitude of $\sim 0.65\mu\text{m/s}^2$. Here, $f_i = a \cdot \sin(bx + c)$, for $i = H, L$ and $x = (x' - \text{mean}(x')) / \text{std}(x')$ is the normalization by mean and standard deviation of $x' = \text{JD}(\text{UTC}) - 2.455\text{E}6$. [<i>Calabia et al., 2015, Fig.2</i>].73	73
Figure 3.4	Accelerations of GOCE on February 15 th , 2011. POE-based non-gravitational accelerations are in cyan line and accelerometer measurements in black line. Dotted blue line represents the smoothed POE-based non-gravitational accelerations. [<i>Calabia and Jin, 2016a, Fig.2</i>].74	74
Figure 3.5	Non-gravitational accelerations (three superior panels) and thermospheric mass densities normalized to 475km (bottom) along GRACE's orbital path. 14 February 2011 on the left and 13 April 2012 on the right. Calibrated accelerometer measurements are in black, and the estimations from GPS POE are represented in green. In the bottom panel, the NRLMSISE00 model estimations are shown in blue thick line. [<i>Calabia and Jin, 2017, Fig.1</i>].76	76
Figure 3.6	From top to bottom, correlation for each of the three axes in the SBS, and SD (including fitted trend) of daily POE non-gravitational accelerations with respect to the accelerometer measurements. [<i>Calabia and Jin, 2017, Fig.4</i>].77	77
Figure 3.7	Differences of GRACE's accelerometer biases with respect to <i>Bettadpur [2009]</i> : results from <i>Bruinsma et al. [2007]</i> are shown in cyan, from <i>Bezděk [2010]</i> in magenta, and this study in blue color. Fitted polynomial functions (Table 3.2) are in black color. Plots are not equally scaled. [<i>Calabia et al., 2015, Fig. 4</i>].79	79
Figure 3.8	Anomaly at 19:40 h February 15 th , 2011. Zoom for X_{SBS} and Z_{SBS} from Figure 3.1.81	81
Figure 3.9	Interpolation of GRACE's differences along orbits between accelerometer and POE-based accelerations in the Z_{SBS} axis from 16 th to 19 th of January 2006. Julian Date (JD) is represented on top of figure. Dotted line represents the satellite trajectory at 50s interval. [<i>Calabia and Jin, 2016a, Fig. 3</i>].82	82
Figure 3.10	Mean value of the differences (2006 to 2009) between the POE-based non-gravitational accelerations and the accelerometer measurements of GRACE for the Z_{SBS} axis. [<i>Calabia and Jin, 2016a, Fig. 4</i>].82	82

Figure 3.11	First (top) and second (bottom) PCA components for the variability of the differences between the POE-based non-gravitational accelerations and the accelerometer measurements (GRACE Z_{SBS} axis, descending orbits, 2006 to 2009). Respectively, 31 % and 22 % of the variability explained. Maps are time-variable in latitude (31,37sec per southward degree) and longitude (3.99min per westward degree). Time-expansion PCA coefficients only shown for half year of 2006. [<i>Calabia and Jin, 2016a, Fig. 5</i>].	83
Figure 3.12	Same as Figure 3.11 but for the third (top) and fourth (bottom) PCA components. [<i>Calabia and Jin, 2016a, Fig. 6</i>].	84
Figure 3.13	Long-term variations of the differences between the POE-based non-gravitational accelerations and the accelerometer measurements (GRACE Z_{SBS} axis, 2006 to 2009, descending orbits PCA5 for (a) and combined solution for (b), (c) and (d)). Right panel in (a) includes the evolution of β' angle values. [<i>Calabia and Jin, 2016a, Fig. 7</i>].	85
Figure 4.1	Statistical comparisons with respect the estimates of <i>Sutton [2011]</i> in black, and with respect the NRLMSISE-00 empirical model in green. From top to bottom, (a) background density, (b) correlation coefficients, (c) relative error, and (d) relative SD. [<i>Calabia and Jin, 2016b, Fig. 1</i>].	89
Figure 4.2	Median average (a) and SD (b) of relative differences between the MSIS and the GRACE density estimates, i.e. $(MSIS - GRACE)/GRACE$. Dip isoclinic lines are plotted in dash-dot gray format. Values are dimensionless. [<i>Calabia and Jin, 2016b, Fig. 2</i>].	90
Figure 4.3	First fourth PCA components of the relative differences between accelerometer-based densities and the NRLMSISE00 model, i.e. $(NRLMSISE00 - GRACE)/GRACE$. The explained variability amounts to 65.5 %, 9 %, 6 %, and 2 %, respectively from (a) to (d). Dip isoclinic lines are plotted in dash-dot format. Values are dimensionless.	91
Figure 4.4	Thermospheric mass densities along GRACE's orbital path (normalized to 475km) on (a) February 14 th 2011 and (b) April 13 th 2012. Accelerometer-based densities are plotted in black color, the NRLMSISE00 model estimations are shown in dashed line, and the estimations from GRACE GPS-POD are represented in thick gray line.	93
Figure 4.5	Days without accelerometer records. GRACE-A in gray and GRACE-B in black.	94

-
- Figure 4.6** Non-gravitational accelerations (X-Y-Z satellite body frame) inferred from the GPS-POD of GRACE-A on 11 November 2011. During this month, accelerometer measurements are unavailable due to instrument power-off. Similar results for GRACE-B.94
- Figure 4.7** Thermospheric neutral densities for GRACE’s orbital path on (a) 23 April 2012 Accelerometer measurements were power-off. The NRLMSISE00 model is plotted in dashed line, and the results from GRACE GPS-POD are shown in thick gray line.94
- Figure 4.8** Daily averages of thermospheric neutral densities inferred from GRACE’s descending orbits. Accelerometer-based estimates are in black color and POE-based estimates in gray color.94
- Figure 4.9** Correlation, RMSD, NRMSD, and differences of POE (blue) and MSISE (green) with respect to accelerometer estimates (top to bottom, 5-day mean averages). Mean background density in the bottom panel. [*Calabria and Jin, 2017, Fig. 5*].95
- Figure 4.10** Mean average (top) and SD (bottom) of relative errors based on the differences between the POE-based and the accelerometer-based thermospheric mass densities, i.e. $(\text{POE-ACC})/\text{ACC}$, inferred from GRACE measurements during 2011-2016. Dip isoclinic lines are plotted in dash-dot format. [*Calabria and Jin, 2017, Fig. 6*].96
- Figure 4.11** Global daily averaged densities and differences of relative errors between POE-based and accelerometer-based densities (2011-2016), i.e. $(\text{POE-ACC})/\text{ACC}$. Ascending orbits in top panels and descending orbits in bottom panels. Accelerometer-based densities in black and GRACE POE-based estimates in green. Days when accelerometer measurements were off are plotted in the bottom time-line. [*Calabria and Jin, 2017, Fig. 7*].97
- Figure 4.12** Four main PCA components for the differences between POE-based and accelerometer densities (2011 to 2016). Values are dimensionless. From top to bottom, each component explains the 11 %, 8 %, 5 % and 4 % of the total variability. The global averaged densities from Figure 4.11 are below the first PCA. Ascending orbits in green and descending orbits in red. Dip isoclinic lines are in gray dash-dot format. [*Calabria and Jin, 2017, Fig. 8*].98
- Figure 5.1** Main PCA components of thermospheric neutral mass density variability from GRACE measurements (475 km altitude). From top to bottom, each component individually explains the 90.3 %, 3.5 %, 2.9 %, 0.1, and 0.1 %

	of the total variance. Dip isoclinic lines are plotted in dash-dot gray format to show the alignments. Values are dimensionless. [<i>Calabia and Jin, 2016b, Fig. 3</i>].	102
Figure 5.2	Fitting of the first PCA time-expansion coefficient (Figure 5.1a) in terms of P10.7 and Am indices. Parameterization is given in Table K.1 (Appendix K). Corresponding spatial pattern is shown in Figure 5.1a, and given in Table K.3 (Appendix K). Y-axis values are dimensionless. [<i>Calabia and Jin, 2016b, Fig. 4</i>].	103
Figure 5.3	Fitting of time-expansion EOF, as seen from periodic variations of the S1 constituent (represented in LST). Data normalized to P10.7=110 common flux. Parameterizations are given in Table K.2 (Appendix K), including the modulation in amplitude. Corresponding spatial patterns are shown in Figure 5.1 and given in Table K.3 (Appendix K). Y-axis values are dimensionless. [<i>Calabia and Jin, 2016b, Fig. 5</i>].	106
Figure 5.4	Fitting of PCA time-expansion coefficients, as seen from periodic annual variations. Data normalized to P10.7=110 common flux. Parameterizations are given in Table K.2 (Appendix K), including the modulation in amplitude. Corresponding spatial patterns are shown in Figure 5.1 and given in Table K.3 (Appendix K). Y-axis values are dimensionless. [<i>Calabia and Jin, 2016b, Fig. 6</i>].	108
Figure 5.5	Periodograms of main PCA time-expansion coefficients in magenta. In black solid line the periodograms of the residuals from removing solar, magnetospheric, annual (A), and LST (S) variations (data reduced to P10.7=110). Gray dash-dotted line represents the 95 % confidence bounds. The significant periodicities are marked with vertical lines. [<i>Calabia and Jin, 2016b, Fig. 7</i>].	111
Figure 5.6	Fitting of time-expansion EOF, as seen from periodic 171-day variations (P1 wave). Data normalized to P10.7=110 common flux. Parameterizations are given in Table K.2 (Appendix K), including the modulation in amplitude. Corresponding spatial patterns are shown in Figure 5.1 and given in Table K.3 (Appendix K). Y-axis values are dimensionless. [<i>Calabia and Jin, 2016b, Fig. 8</i>].	112
Figure 5.7	Fitting of time-expansion EOF, as seen from periodic 2731-day variations (K wave). Data normalized to P10.7=110 sfu. Parameterizations are given in Table K.2 (Appendix K), including the modulation in amplitude. Corresponding spatial patterns are shown in Figure 5.1 and given in	

	Table K.3 (Appendix K). Y-axis values are dimensionless. [<i>Calabria and Jin, 2016b, Fig. 9</i>].	113
Figure 5.8	Fitting of time-expansion EOF, as seen from periodic 283-day variations (R2 wave). Data normalized to P10.7=110 sfu. Parameterizations are given in Table K.2 (Appendix K), including the modulation in amplitude. Corresponding spatial patterns are shown in Figure 5.1 and given in Table K.3 (Appendix K). Y-axis values are dimensionless. [<i>Calabria and Jin, 2016b, Fig. 10</i>].	114
Figure 5.9	Fitting of time-expansion EOF, as seen from periodic 112-day variations (T2 wave). Data normalized to P10.7=110 sfu. Parameterizations are given in Table K.2 (Appendix K), including the modulation in amplitude. Corresponding spatial patterns are shown in Figure 5.1 and given in Table K.3 (Appendix K). Y-axis values are dimensionless. [<i>Calabria and Jin, 2016b, Fig. 11</i>].	114
Figure 5.10	Main PCA coefficients (black) and corresponding parameterizations (green), in function of P10.7, LST, and annual variations. Descending orbits on the left panels and ascending orbits in the right panels. Dimensionless values. [<i>Calabria and Jin, 2017, Fig. 9</i>].	115
Figure 5.11	Global averaged relative residuals (i.e., residual/density) for (a) ascending orbits and (b) descending orbits, for the parameterized PCA and for the MSIS empirical model. [<i>Calabria and Jin, 2016b, Fig. 14</i>].	116
Figure 5.12	Thermospheric density variations at 475 km altitude, in function of LST and latitude (fixed at Greenwich meridian), and for different season and solar-flux conditions. (a) P10.7=80 sfu and (b) P10.7=120 sfu. From top to bottom, it plots at ME, JS, SE and DS. In each scenario (8 cases), from left to right, averaged accelerometer and MSIS -based densities along GRACE orbits (raster plots), and direct calculations (contour plots) from the parameterization and from MSIS. Each bar-graph corresponds to the occurrences between ± 15 sfu and ± 3 h LST with respect to each scenario (for raster plots only). The direct calculations using the models have been computed with the representative parameters of each scenario. [<i>Calabria and Jin, 2016b, Fig.12</i>].	117
Figure 5.13	Thermospheric density variations at 475 km altitude, in function of <i>doy</i> and latitude (fixed at Greenwich meridian), and for different LST and solar-flux conditions. (a) P10.7=80 sfu and (b) P10.7=120 sfu. From top to bottom, plots at 5, 11, 17, and 23 h LST, In each scenario (8 cases), from left to right, averaged accelerometer and MSIS -based densities	

- along GRACE orbits (raster plots), and direct calculations (contour plots) from the parameterization and from MSIS. Each bar-graph corresponds to the occurrences between ± 15 sfu and ± 3 h LST with respect to each scenario (for raster plots only). The direct calculations using the models have been computed with the representative parameters of each scenario. [*Calabia and Jin, 2016b, Fig. 13*].....118
- Figure 5.14** Global distribution of the averaged thermospheric neutral mass density from 12-year of GRACE accelerometer-based estimates normalized at 475 km altitude (LT and annual variations have been removed). Dip isoclinic lines are plotted in dash-dot gray format to show the alignments. [*Calabia and Jin, 2016c, Fig. 1*].....119
- Figure 5.15** Differences between each polar quadrant of 81-day averages of thermospheric densities. [*Calabia and Jin, 2016c, Fig. 2*].....120
- Figure 5.16** The 81-day averages of planetary thermospheric neutral densities are scaled in the left side, together with the differences between polar caps. The values inferred from GRACE accelerometer are plotted in gray line, the fitting in terms of solar F10.7 index (f1) is plotted in dashed black line, and the fitting in terms of the combined solution of F10.7 and A_m indices (f2) is plotted in solid black line. The geomagnetic A_m index (dotted line) is scaled in the right side. [*Calabia and Jin, 2016c, Fig. 3*].....121
- Figure 5.17** Correlation coefficients versus delay-times for space weather and geomagnetic indices with respect to density variations during 2011-2016 (free from annual and LST variations). Values for (left) northern, (middle) equatorial, and (right) southern regions. [*Calabia and Jin, 2017, Fig. 10*].....123
- Figure 5.18** Densities inferred from GRACE for the G4-level (severe) geomagnetic storm of March 2015 (Top panel). Note that annual and LST variations have not been removed from density estimates. Dip isoclinic lines are plotted in dash-dot gray format to show the alignments. Bottom panels show the merging electric field (E_m), and geomagnetic A_m and Dst indices. [*Calabia and Jin, 2016d, Fig. 2*].....126
- Figure 5.19** Daily maxima deviation per latitude with respect to the monthly median (in %), for the G4-level (severe) geomagnetic storm of March 2015. The dashed line denotes the solar F10.7 index and the solid line the geomagnetic A_p index, both scaled on the right.....127
- Figure 5.20** Daily mean deviation per latitude with respect to the monthly median (in %), for the G4-level (severe) geomagnetic storm of March 2015. The

- dashed line denotes the solar F10.7 index and the solid line the geomagnetic Ap index, both scaled on the right.....127
- Figure 5.21** In green color neutral densities inferred from GRACE accelerometers normalized to 475 km on 17-18 March, 2015. Note that annual and LST variations have not been removed from density estimates. In blue color the NRLMSISE-00 neutral densities calculated along the satellite orbit at the same times as the accelerometer measurements. [*Calabia and Jin, 2016d, Fig. 3*].....128
- Figure 5.22** Mean values per orbit of neutral densities for GRACE normalized to 475 km on March, 2015. In blue color accelerometer measurements, in red color the NRLMSISE-00 neutral densities calculated along the satellite orbit at the same times as the accelerometer measurements. Parameterized densities $f_1(E_m, F10.7)$ and $f_2(A_p, F10.7)$ are plotted in magenta and green colors, respectively. [*Calabia and Jin, 2016d, Fig. 4*].129
- Figure 5.23** Top panel shows profiles at equator (dEq) and poles (dN , dS) of thermospheric neutral density inferred from GRACE POE (free from LST and annual variations). Space weather and geomagnetic indices are plotted in the below panels (see Section 5.4.1 for description of each index). Magnitudes have been re-scaled as indicated in the legends.....130
- Figure 5.24** Thermospheric neutral density variations inferred from GRACE POE (free from LST and annual variations) and its profiles at equator (dEq) and poles (dN , dS), plotted together with E_m , AE , Ap , An , and, As indices, for the moderate G2-level geomagnetic storm of 16-17 March 2013 (from right to left and from bottom to top: 12^h 36^m 16/March/2013 to 11^h 35^m 18/March/2013). GRACE's angle β during this period is 173° (Sun to ascending leg). Accelerometer-based densities are not available due to instrument power-off during this month. Dip isoclinic lines are plotted in dash-dot gray format to show the alignments. [*Calabia and Jin, 2017, Fig. 11*].....132
- Figure 5.25** Thermospheric neutral density variations inferred from GRACE POE (free from LST and annual variations) and its profiles at equator (dEq) and poles (dN , dS), plotted together with E_m , AE , Ap , An , and As indices, for the minor G1-level geomagnetic storm of 28-29 March 2013 (from right to left and from bottom to top: 11^h 42^m 28/March/2013 to 10^h 41^m 30/March/2013). GRACE's angle β during this period is 186° (Sun to ascending leg). Accelerometer-based densities are not available due to instrument power-off during this month. Dip isoclinic lines are plotted in

	dash-dot gray format to show the alignments. [<i>Calabia and Jin, 2017, Fig. 12</i>].	133
Figure 6.1	Density (color scale) and wind (arrows) data from both GOCE and CHAMP accelerometers, on April 5, 2010. Densities normalized to 300 km altitude. The background wind field is from the HWM07 model. From [<i>Doornbos et al. [2014a, Fig. 5.1]</i>].	142

LIST OF TABLES

Table 2.1	Arc-to-chord approximation error in GRACE.....	43
Table 2.2	Low-degree coefficients of the conventional geopotential model.....	45
Table 2.3	Coefficients of the IERS 2010 mean pole model.....	45
Table 2.4	Nominal values of solid Earth tide external potential Love numbers	47
Table 2.5	Force models with maximum amplitudes and mean values for GRACE on July 14 th , 2007. [<i>Calabia and Jin, 2016a, Table 1</i>].	54
Table 3.1	Disturbing signal in POD. [<i>Calabia and Jin, 2016a, Table 2</i>].	75
Table 3.2	Parameters for bias calibration of GRACE accelerometers. [<i>Calabia et al., 2015</i>].	80
Table 3.3	Variance and amplitudes of mean and PCAs shown in Figures 3.10 to 3.13a. [<i>Calabia and Jin, 2016a, Table 3</i>].	86
Table 5.1	GRACE's alias periods for the main radiation-waves.....	110
Table 5.2	Maximum values and respective delay-times for space weather and geomagnetic indices with respect to density variations during 2011-2016 (free from annual and LST variations). Values are given for northern, equatorial, and southern regions. [<i>Calabia and Jin, 2017, Table 1</i>]......	124
Table K.1	Coefficients for solar and magnetospheric variations used in Section 5.2.1.	157
Table K.2	Coefficients for periodic variations used in Section 5.2, including % correlation coefficients for each parameterization (93-day period might not be used for modelling).	158
Table K.3	Spherical harmonics parameterization of PCA spatial patterns, including % contribution to the total variance (Section 5.1, Figure 5.1).	159

1. INTRODUCTION

1.1. Background

1.1.1. *The upper atmosphere processes*

Terrestrial upper atmosphere processes exhibit substantial complexity (Figure 1.1) due to ion-neutral coupling (e.g., *Forbes and Roble [1990]*) and highly variable forcing from the Sun. Above an altitude of ~160 Km, the density of the upper atmosphere is too low for molecular interaction, and the dynamics are mainly driven by the diurnal and annual cycles of heating resulting from absorption of solar Extreme Ultra Violet (EUV). Variations in solar EUV flux variations produce the expansion and contraction of the thermosphere, and the consequent changes of neutral density at a given altitude.

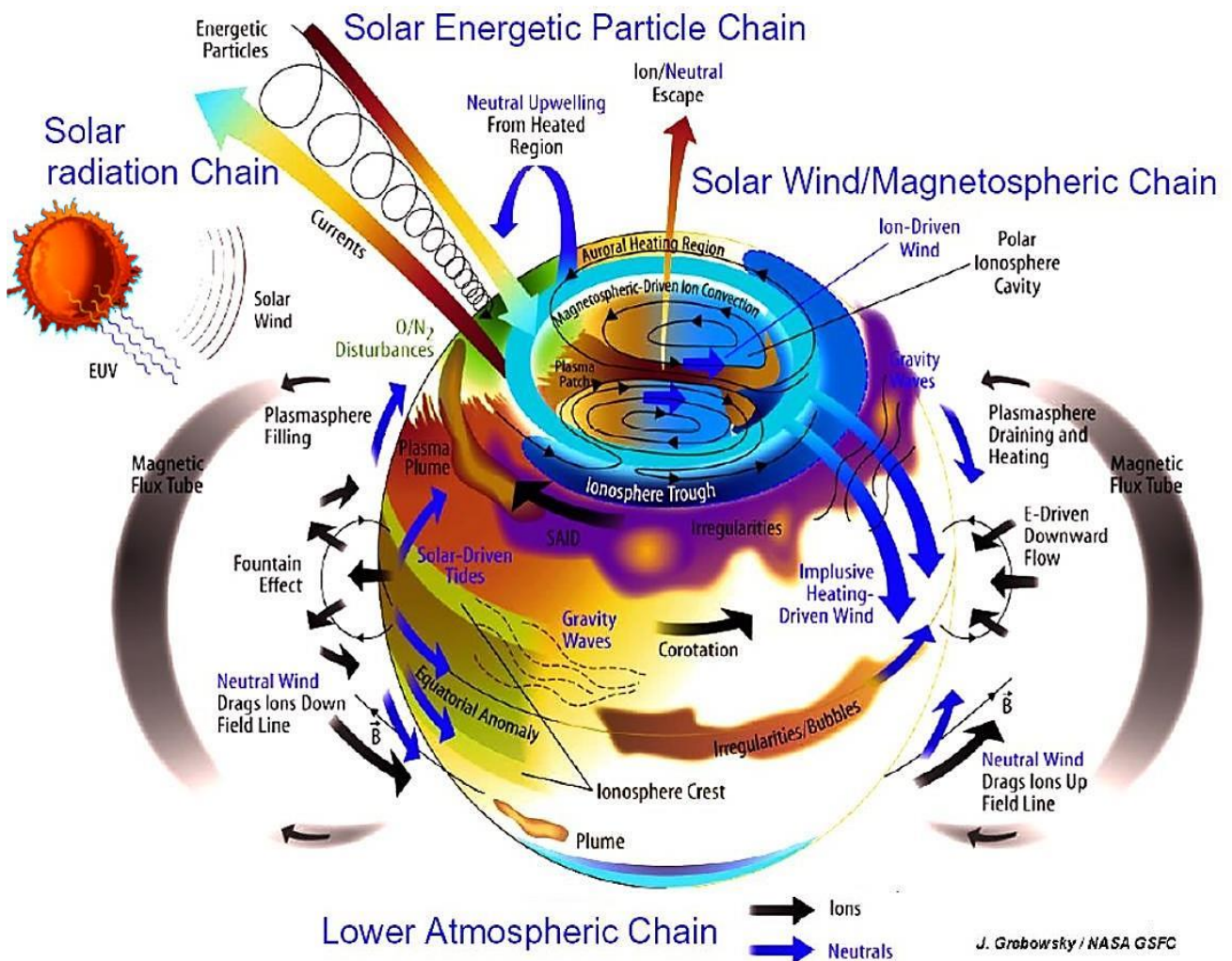


Figure 1.1 Terrestrial upper atmosphere processes. Credit: *NASA/J. Grobowsky*

In addition, the solar wind plasma, combined with a favorable alignment of the Interplanetary Magnetic Field (IMF), produces thermospheric Joule heating and auroral particle precipitation at high-latitudes. Solar flares are ejections of clouds of electrons, ions, and atoms through the corona of the Sun into space, which with the increasing of X-ray and EUV irradiance, can cause immediate energy-absorption, ionization, and dissociation of molecules in the upper atmosphere. Generally, solar flares and geomagnetic storms produce more localized and abrupt short-term neutral density changes in comparison with those given by diurnal and annual variations of solar EUV heating. The rotational variation of the Sun (~27day) produce secular appearances of bright regions (identified as solar plages), which are usually associated with sunspots. Different sunspots in the solar corona provide different speeds and densities of solar wind, which usually form a spiral with outward fast-moving and slow-moving streams (see Figure 1.2). Fast moving streams tend to overtake slower streams, forming turbulent Co-rotating Interaction Regions (CIR). In addition, recurrent geomagnetic forcing related to CIRs can produce density variations with a periodicity at sub-harmonics of the solar rotation period (~9day, ~7day, ~5 day).

A Coronal mass ejection (CME) is a fast-moving burst of plasma caused by release of magnetic energy at the corona of the Sun. Analogous to the CIRs effects, CMEs can produce rapid thermospheric Joule heating and particle precipitation along the Earth's magnetic field lines. Figure 1.2 shows the difference between a CME and a CIR, for the solar storm of October 12th 2016. The effects of CMEs and CIRs in the thermosphere usually conduct high latitude phenomena, mainly are located at the auroral zone, through ionization, dissociation, and excitation of neutral constituents. Shortly afterwards, the whole thermosphere can respond with southward traveling gravity waves from the auroral zone, and with a global expansion of the whole atmosphere for several hours up to several days.

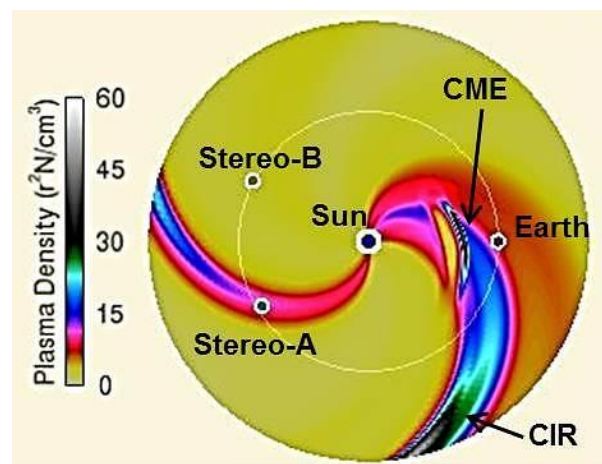


Figure 1.2 Plasma density ecliptic viewed from the north on October 12th 2016. The Sun is at the center of the plot, the Earth on the right and the two Solar-Terrestrial Relations Observatory (Stereo) spacecrafts on the left. Both CME and CIR can be identified. From <http://www.swpc.noaa.gov/products/wsa-enlil-solar-wind-prediction>.

1.1.2. *Significance and applications*

The magnetosphere-ionosphere-thermosphere (MIT) system is highly variable in time and space, and its geophysical processes are still not well understood. Consequences of the MIT's environmental conditions on human activity emphasize the necessity to better understand the MIT coupling and dynamics, and their potentially negative effects on orbiting and ground-based technologies. For instance, it is well known the practical importance of the ionosphere in radio propagation (e.g., [Li and Liu \[2004\]](#); [Jin et al. \[2006\]](#); [Jin and Park \[2007\]](#); [Jin et al. \[2008\]](#)), or the damaging effects of geomagnetic storms and solar flares on orbiting and ground-based technologies (e.g., [Lechtenberg et al. \[2013\]](#); [Gummow \[2002\]](#); [Molinski \[1996\]](#); [Kappenman \[1996\]](#)). Among these effects, the most important influence is the orbital perturbation and decay of Low Earth Orbit (LEO) satellites due to elevated aerodynamic drag associated with increases in neutral density, which results from the upper atmosphere expansion in response to increased solar activity.

Currently, half of the world's active satellites operate in LEO, ranging from altitudes of 160 Km up to 2000 Km. Unfortunately, atmospheric drag in LEO is the major cause of orbital decay and perturbations, limiting the lifetime of the satellite missions. The accurate prediction of precise orbital ephemeris (POE) in Precise Orbit Determination (POD) is the result of an integrated knowledge of atmospheric density and space weather, where the force models provide the inputs for a mission lifetime [[Owens et al., 2000](#)]. In the POD process, the position and velocity of an orbiting object is statistically estimated by a set of equations of motion and a set of discrete observations [[Tapley et al., 2004](#)]. Currently, the most precise techniques for orbital tracking include satellite-to-satellite Global Navigation Systems (GNSS), Satellite Laser Ranging (SLR), and Doppler Orbitography & Radio positioning Integrated by Satellite (DORIS). The three main techniques currently used in POD include the dynamic, the kinematic, and the reduced-dynamic approaches [[Wu et al., 1991](#)]. The dynamical method in POD estimates an object position and velocity at a single epoch, for which the resulting model trajectory best fits the tracking observables. In fact, the measurements determine the state of the satellite (position and velocity) at some initial epoch, and the solution is mapped forward in time using the dynamical models. In the kinematic approach, the state of the satellite is determined sequentially at each observational measurement and without dependence on the dynamical models. In the reduced-dynamic approach, the parameters to solve for the dynamic models are fixed when a solution is

obtained, and with additional accelerations estimated from the observational measurements. The combination of high-precision GNSS observables with the dynamical models (e.g., time-variable gravity-field, non-gravitational force-models) can counterbalance both the disadvantages of the GNSS measurement noises and the uncertainties in the models. The main external forces include gravitational forces, atmospheric drag, and irradiative pressures (Figure 1.3).

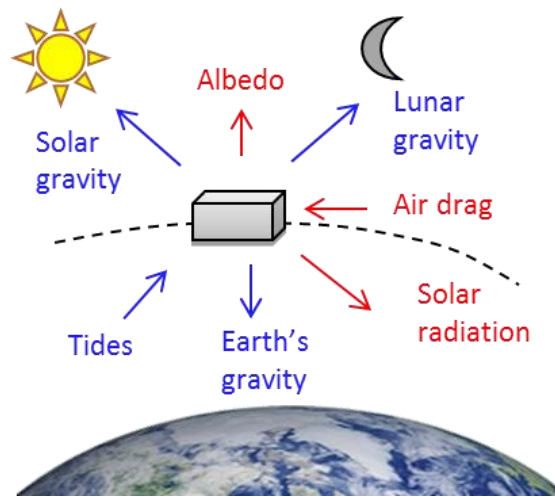


Figure 1.3 Accelerations acting on a satellite. Gravitational accelerations are pictured in blue, and non-gravitational in red.

1.2. Status and progress

1.2.1. *Sensing*

Besides pressure gauge (e.g., [Rice et al. \[1973\]](#)) and neutral mass spectrometry (e.g., [Hedin \[1983\]](#); [Chakrabarti et al. \[1990\]](#)), the analysis of satellite orbital decay through the Gauss's form of Lagrange's planetary equations (perturbation equations) has been the basis to derive thermospheric mass densities since 1958 [[Priester et al., 1967](#)]. By determining the time derivatives of the energy and the angular momentum of an orbiting object over time [[Burns, 1976](#)], the equations of [King-Hele \[1987\]](#) showed that the primary effect of drag acceleration is to monotonically reduce the orbital semi-major axis. Thus, by only measuring discrete changes in the magnitude of the semi-major axis, the corresponding density averages along the trajectory of a LEO object can be derived with temporal resolution from hours to days [[Emmert et al., 2004](#); [Picone et al., 2005](#); [Zadunaisky, 2003](#)]. Mathematical and data processing description related to this technique can be found in [Doornbos \[2011\]](#), including examples derived from the Two-Line Element (TLE) format. Note that TLE is a 69-character compact-format of orbital information of a very large number of space objects, which has been designed and is distributed by the United States Strategic Command (USSTRATCOM).

Nowadays, the retrieval of thermospheric neutral densities and cross-track winds is currently providing an unprecedented detail and accuracy when accelerometer-derived aerodynamic accelerations are employed (e.g., [Bruinsma et al. \[2004\]](#); [Doornbos \[2011\]](#); [Visser et al. \[2013\]](#)). The technique is based on removing accurate radiation pressure models from non-gravitational accelerations, which are measured by precise accelerometers. Afterwards, density and wind estimates can be computed using the drag-force formula.

First accelerometers onboard satellites were flown in 1968 (for thermospheric-modelling purposes), e.g., MESA (Miniature Electrostatic Single-axis Accelerometer), SETA (Satellite Electrostatic Triaxial Accelerometer), and CACTUS (French acronym meaning ultrasensitive, three-axis, capacitive accelerometric transducer). Unfortunately, the sparse spatiotemporal distribution of their measurements limited the resulting scientific research, products, and models, but, recently, the Challenging Mini-satellite Payload (CHAMP), GRACE, and GOCE (Gravity Field and Steady-State Ocean Circulation Explorer) missions have provided continuous and accurate accelerometer measurements for the periods 2000-2010, 2002-2015, and 2009-2013, respectively. In addition, the accelerometers onboard each of the three Swarm satellites are currently taking non-gravitational measurements since November 2013.

First derivations of thermospheric winds can be found in [Marcos and Forbes \[1985\]](#), where the authors analyzed tri-axial accelerometer measurements from SETA. [Sutton et al. \[2007\]](#) described two different approaches for density and wind derivation, and an improved iterative algorithm was developed in [Doornbos et al. \[2010\]](#). Recent publications on thermospheric wind variations can be found in, e.g., [Doornbos et al. \[2014a\]](#), and [Lieberman et al. \[2013\]](#). In principle, wind determination can be also performed for the radial direction, but accurate instrument calibration and radiation pressure and lift force-models are required.

Unfortunately, not all the LEO satellites carry accelerometers, and carrying ones produce data loss and measurement failure, due to possible files corruption, instrument malfunction, or battery performance. It is therefore that in the recent years, several studies have investigated how to estimate non-gravitational accelerations and neutral densities through GPS POD of LEO. First attempts were made in [IJssel et al. \[2004\]](#) and [IJssel and Visser \[2005\]](#), where the authors estimated the non-gravitational accelerations from CHAMP accelerometers by omitting the non-gravitational force models in a highly-reduced dynamic POD process. In their scheme, the GEODYN software (Bayesian weighted batch least-squares estimator) was

employed for all POD computations, employing a piecewise linear function at 10-15 min resolution. Recent results using this technique [Visser *et al.*, 2013] are shown in Figure 1.4, where the non-gravitational accelerations from GRACE and CHAMP are estimated for the first 6 h of November 7th 2003. In this Figure, both predicted by models and accelerometer measurements are also plotted for comparison with the POD-based estimates (the corresponding wind and density estimates are plotted in Figure 1.5). Moreover, several publications have shown the suitability of this method for other missions, including the results from Swarm [Siemes *et al.*, 2016] or GOCE [Ijssel, 2014; Doornbos *et al.*, 2014b].

In the POD process, atmospheric densities can also be obtained as a correction to an atmospheric model. For instance, McLaughlin *et al.* [2013] used a set of POEs in a sequential orbit determination scheme to estimate thermospheric neutral densities from GRACE, CHAMP, and TerraSAR-X. Using the Orbit Determination Tool Kit (ODTK), the authors input POE in a sequential processing, filtering, and smoothing scheme to obtain the time variable densities and ballistic coefficients. The ODTK software package uses the technique developed by Wright [2003] for density and ballistic coefficient estimation. In McLaughlin *et al.* [2013], comparisons with CHAMP and GRACE accelerometer measurements showed that their POE-based densities were more accurate than the densities estimated from commonly used empirical models. Figure 1.6 shows the measured, modeled and POE-derived neutral densities from GRACE, and TerraSAR-X, on 26-27 September, 2007. This is a clear example where non-gravitational accelerations are derived from GNSS measurements when accelerometers are not available (e.g., TerraSAR-X).

By applying all best available force models in multiple LEO, Kuang *et al.* [2014] computed non-gravitational accelerations and inferred thermospheric mass densities by estimating the stochastic accelerations that compensate for the dynamic model errors in a reduced-dynamic POD. Daily solutions were generated using orbit arcs of 30 h, with stochastic accelerations estimated from GPS ionosphere-free carrier phase and carrier-smoothed pseudo-range measurements. Contrasting with the technique of Ijssel *et al.* [2004], both accuracy and resolution were improved because estimating accelerations to compensate for the model errors (smaller estimations) allows stronger stochastic constraints in the reduced-dynamic filtering. Through the error analysis of several LEO satellites, the authors identified useful data from CHAMP, GRACE-A/B, TerraSAR-X, and SAC-C, with useful density estimates up to altitude of 715 km, and at 5 min interval.

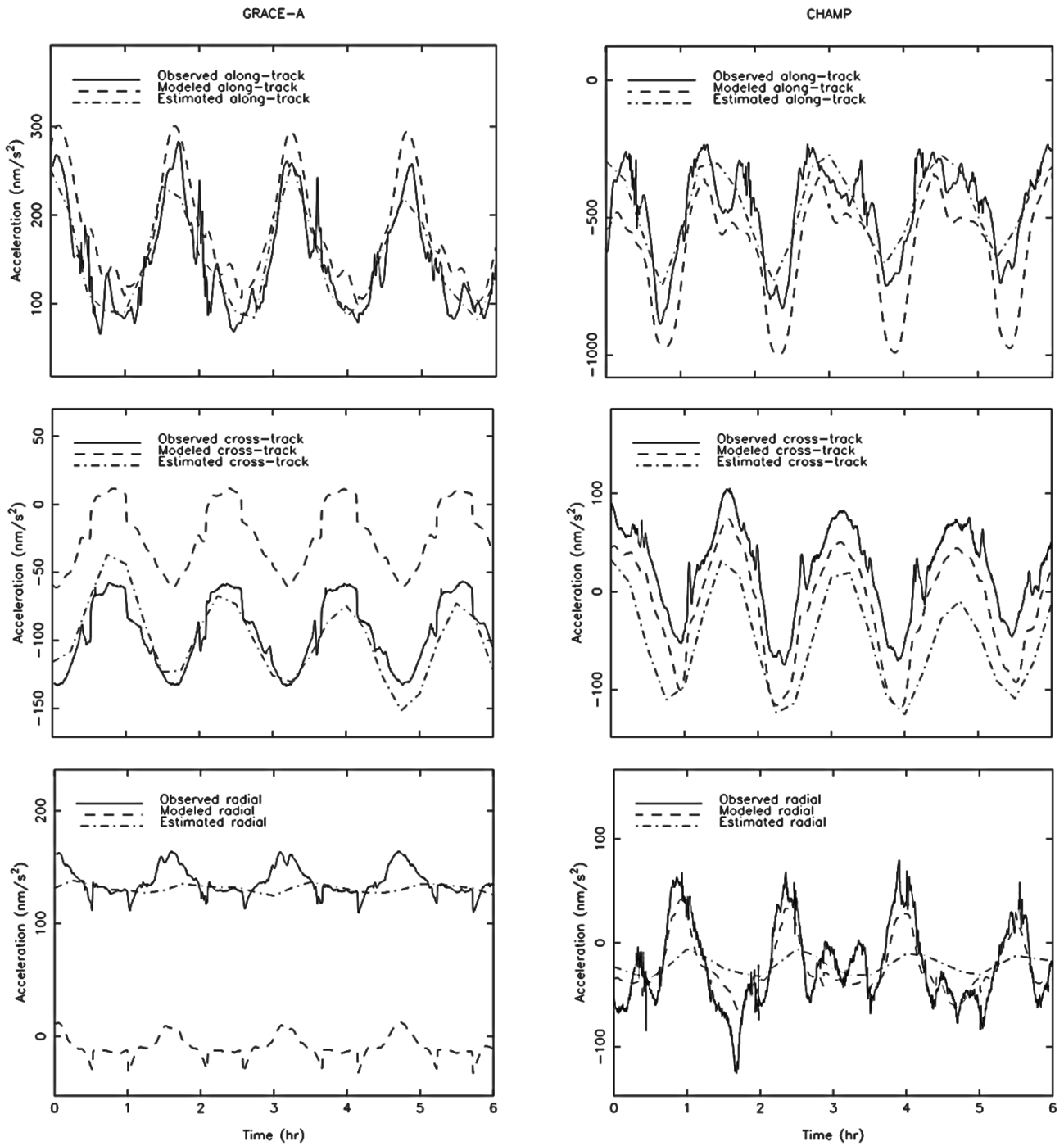


Figure 1.4 Observed, POD-estimated, and modeled non-gravitational accelerations from CHAMP and GRACE for the along-track (top), cross-track (middle) and radial (bottom) direction (first 6 h of 7 November 2003). GEODYN software is used for POD. [Visser *et al.*, 2013, Fig. 5].

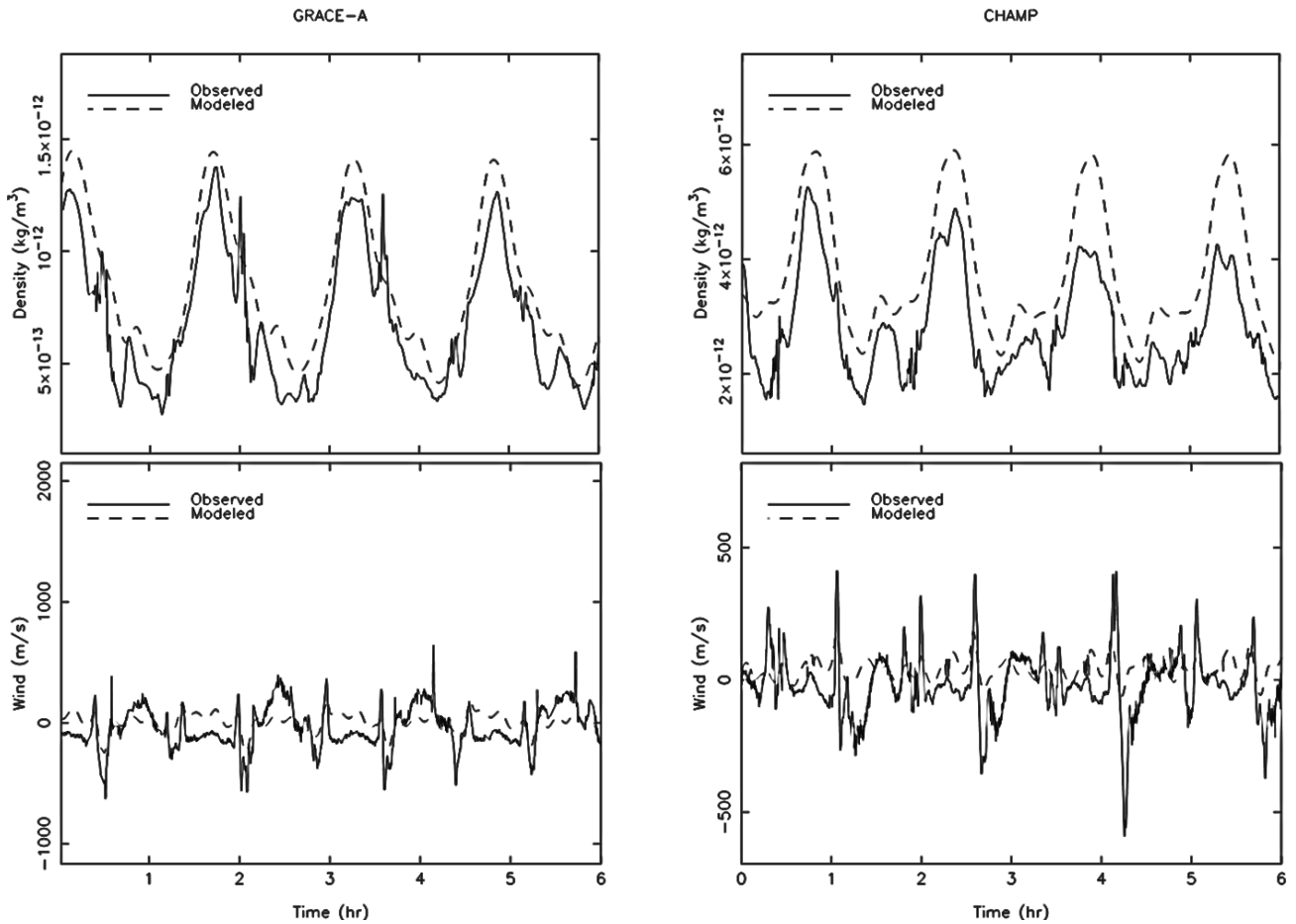


Figure 1.5 Measured (accelerometer), and modeled neutral densities from GRACE and CHAMP (first 6 h of 7 November 2003). Estimates correspond to Figure 1.4 accelerometer measurements and model. [Visser *et al.*, 2013, Fig. 6 and 7].

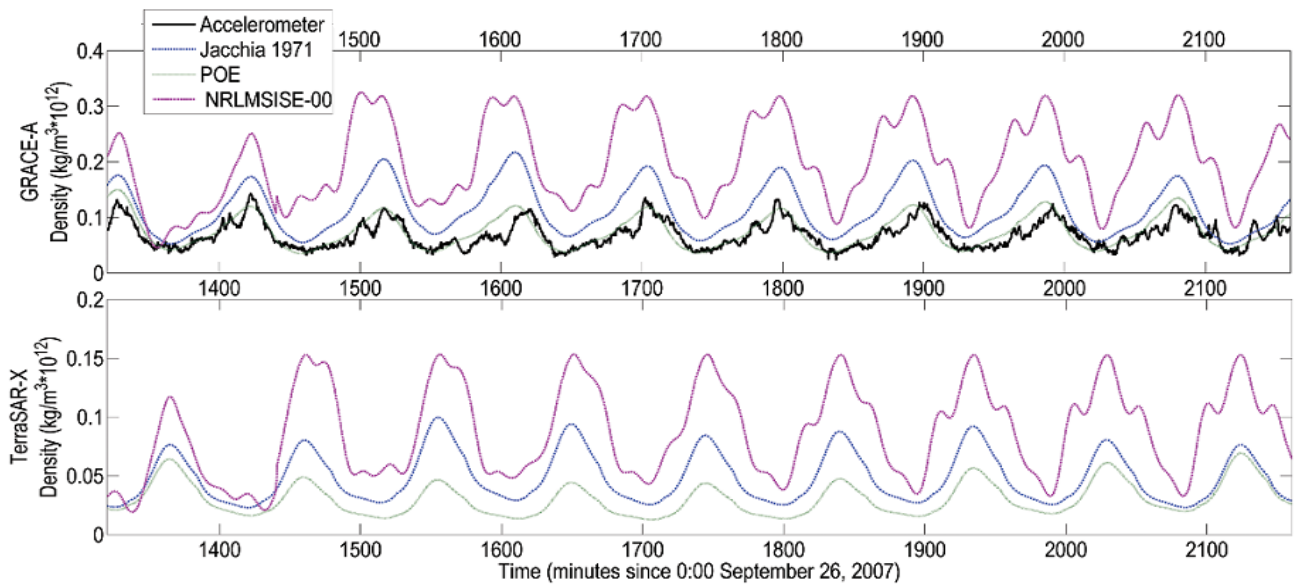


Figure 1.6 Measured, modeled and POE-derived neutral densities from GRACE and TerraSAR-X, on September 26-27, 2007. ODTK software is used for POD. [McLaughlin *et al.*, 2013, Fig. 3].

1.2.2. *Understanding*

During the last decade, the technical advance in thermospheric neutral density retrieval has enlarged the research efforts on understanding the processes in the thermosphere. The higher spatial and temporal resolution provided by LEO accelerometers has revealed numerous intriguing features in the global distribution of thermospheric density [Emmert, 2015a]. For instance, Liu *et al.* [2005] derived a global distribution of the thermospheric total mass density from one-year (2002) of CHAMP accelerometer measurements. Several structures were shown to be related to the equatorial ionization anomaly and to the midnight temperature maximum. However, only a general characterization in Local Solar Time (LST) coordinates was provided, and no temporal variations were analyzed due to limited data. Then, the concept of Equatorial thermospheric Mass-density Anomaly (EMA) was introduced by Liu *et al.* [2007], where the variations with season, geomagnetic activity and solar flux levels were investigated using 4 years of CHAMP measurements (2002-2005). The EMA was defined as a minimum on the dayside, clearly aligned to the geomagnetic equator, and with two maxima at $\pm 20^\circ$ geomagnetic latitude. In their work, only the geographical distribution of the day-side mass density was depicted, and no variations at high-latitude (above 60°) were studied (Figure 1.7).

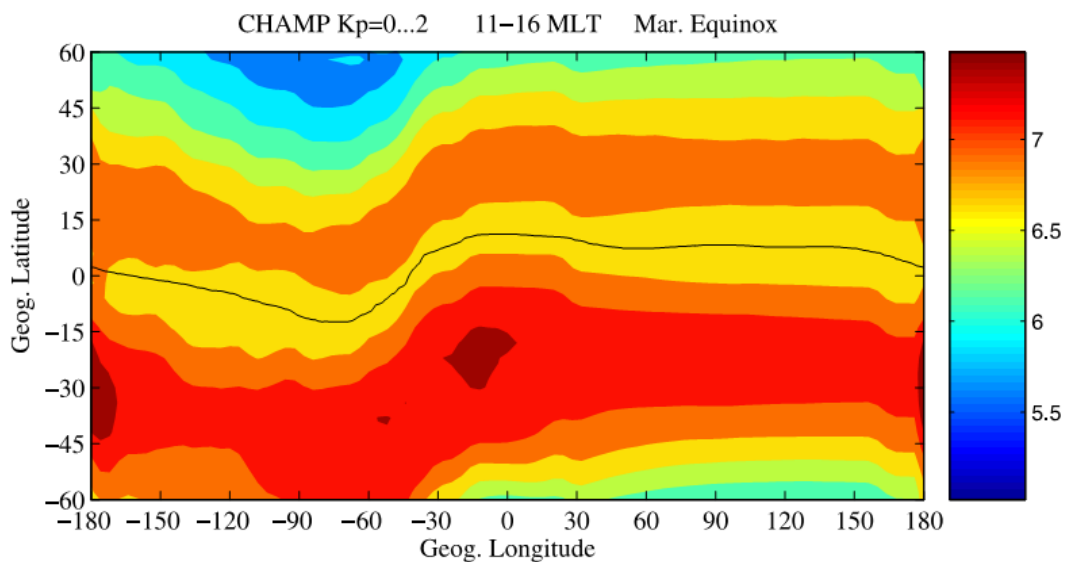


Figure 1.7 Distribution of the dayside thermospheric neutral density (in units of 10^{-12} kg/m^3) under quiet geomagnetic and solar conditions ($F_{10.7} = 150$). The black line indicates the dip equator. [Liu *et al.*, 2007].

Lei et al. [2012b] showed that the Equatorial Thermosphere Anomaly (ETA) can be attributed to energy transfer from thermal plasma to the neutrals through collisions, due to their temperature differences. Recently, an anomalous behavior of the equatorial anomaly has been investigated in the night-side mass density distribution (e.g., *Ma et al. [2010]*; *Akmaev et al. [2010]*; *Ruan et al. [2014, 2015]*), i.e., the Midnight Density Maximum (MDM). It seems that the MDM has a maximum, instead of minimum around the equator, and lower values instead higher values, at middle latitudes.

More complete studies on changes with geophysical conditions have been presented, e.g., in *Müller et al. [2009]*, *Guo et al. [2007]*, and *Lathuillère et al. [2008]*. For instance, *Guo et al. [2007]* performed an extensive study on the relation between solar-irradiance indices and thermospheric mass densities during the period 2002-2004. However, 3 year of data was not enough to characterize long-term variations. A shorter period was investigated in *Lathuillère et al. [2008]*, where the density response to magnetic activity was analyzed depending on the prevailing background. *Müller et al. [2009]* studied the solar and magnetospheric forcing of the low latitude thermospheric mass density as observed by CHAMP accelerometers, and provided a detailed study on the day-to-night mass density ratio (Figure 1.8) and the seasonal variations (Figure 1.9). Unfortunately, their day-to-night study was insufficient to properly describe local time variations, but the seasonal dependence was better characterized than that of previous studies, e.g., *Bowman et al. [2008a]*; *Guo et al. [2008]*. The improvement was achieved by removing the local time, solar flux and magnetic activity effects before the analysis. The study provided the linear fits for the solar and magnetospheric forcing of the low latitude mass density, but only during the period 2002-2005.

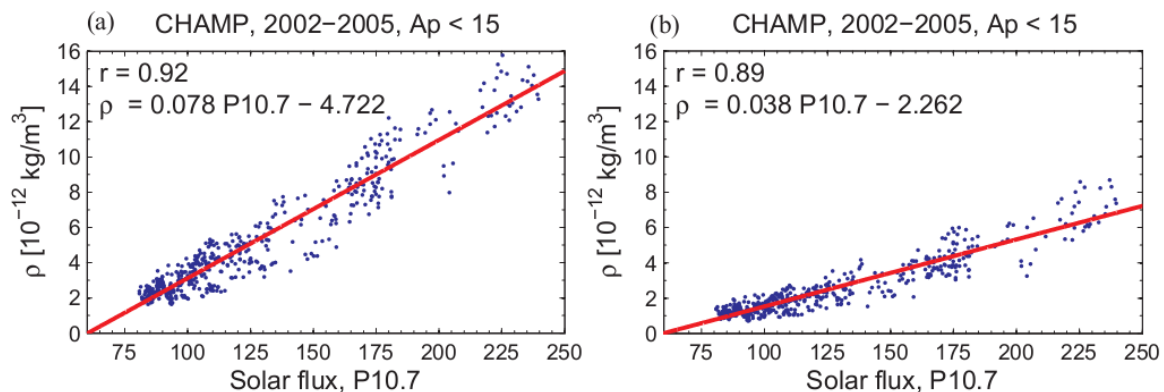


Figure 1.8 Correlation between CHAMP-derived densities and solar flux level, (a) for the day side and (b) for the night side density. [*Müller et al., 2009, Fig.3*].

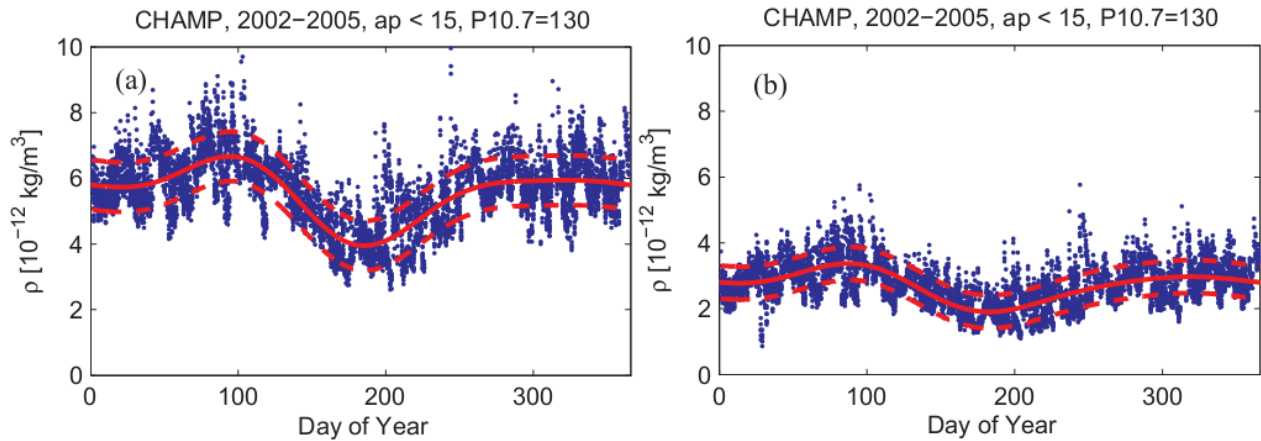


Figure 1.9 Seasonal variation of the density (a) in the day and (b) in the night time sector. The red curves represent the fitted annual harmonics functions. [Müller *et al.*, 2009, Fig.3].

In recent years, several other studies have investigated the seasonal variation of thermospheric neutrals using different and innovative techniques. For instance, *Guo et al.* [2008] deduced the seasonal variations from CHAMP accelerometer measurements (2002-2005) using daily averages compared to the JB2006 model [Bowman *et al.*, 2008b], in which the seasonal dependence was deactivated. Unfortunately, their results showed strong dependence on the performance of the empirical model JB2006. Moreover, several studies have detected that the amplitude of seasonal variations increases with solar activity [e.g., Emmert and Picone [2010]; Matsuo and Forbes [2010]], and a further study of on the latitudinal dependence of seasonal variations has been performed in *Lei et al.* [2012a]. Concerning longitudinal variations of thermospheric neutral density, *Xu et al.* [2013] revealed from CHAMP and GRACE accelerometers a hemispherically asymmetric distribution, positive always near the magnetic poles and with strong seasonal variations.

In addition, considerable improvements have been achieved during the last decade on the subject of thermosphere response to geomagnetic storms. For instance, *Liu and Lühr* [2005] and *Sutton et al.* [2005] investigated the severe geomagnetic storm of November 2003 from CHAMP accelerometer measurements. Later, *Bruinsma et al.* [2006] included the accelerometer measurements from GRACE to study the same storm. Their results showed density increments up to 800 %, a negligible time delay at high latitudes, and about a 4 h delay at the equator. Then, *Sutton et al.* [2009] studied the thermospheric response to variations produced by the July 2004 geomagnetic storm from CHAMP accelerometer measurements. The resulting thermospheric time response showed to be significantly shorter

than those used by the empirical models. *Liu et al. [2010, 2011]* modeled the dependence of neutral density on the solar wind merging electric field (E_m) from CHAMP and GRACE accelerometers. Their results showed that CIRs produce, in general, larger variations than the storms driven by CMEs. Recently, *Chen et al. [2014]* have studied the effects of CIR and CME induced geomagnetic activity on thermospheric density. Their results demonstrate that the larger effect of CIR storms over CME storms is caused by their relatively long duration.

1.2.3. *Modeling*

First empirical density models were based on orbital decay of satellites and started in the 1960s with those given by *Harris and Priester [1962]* and *Jacchia [1964]*. Along time, the Jacchia models have been improved with the use of new algorithms and proxies (e.g., *Bowman et al. [2008b, 2008c]*). First series of DTM (Drag Temperature Model) were based on observations of satellite drag and neutral atmospheric temperatures [*Barlier et al., 1978*]. Currently, DTM incorporates accelerometer, mass spectrometer, incoherent scatter radar and optical airglow measurements [*Bruinsma, 2015*]. The MSIS (Mass Spectrometer and Incoherent Scatter radar) series of models were originally based on mass spectrometer and incoherent scatter radar observations [*Hedin et al., 1977*]. While the mathematical formulations of MSIS and DTM use the exponential Bates profile [*Bates, 1959*], the Jacchia series use the arctangent function to represent an asymptotic behavior for the upper thermosphere. Nowadays, MSIS is the standard for international space research, and the current release (NRLMSISE-00) has been updated with satellite drag data and solar UV occultation [*Picone et al., 2002*]. The temperature and density parameters of MSIS depend on solar flux and geomagnetic indices, modulated by longitude, latitude and LST. Figure 1.10 pictures the histograms of GRACE and CHAMP data versus MSIS and Jacchia models. In this figure, the best match is pictured by the Jacchia model, showing a data cloud-better positioned along the diagonal.

Additional thermospheric models have been developed with the finality to accurately represent the climatological thermospheric density variations, e.g., the Accelerometer Density Model (ADM) of *Marcos et al. [1983]*, the Global Average Mass Density Model (GAMDM2.1) of *Emmert [2015b]*, the CHAMP-based model of *Liu et al. [2013]*, or the parameterized principal component analysis (PCA) of GRACE density estimates in *Calabria and Jin [2016b]*.

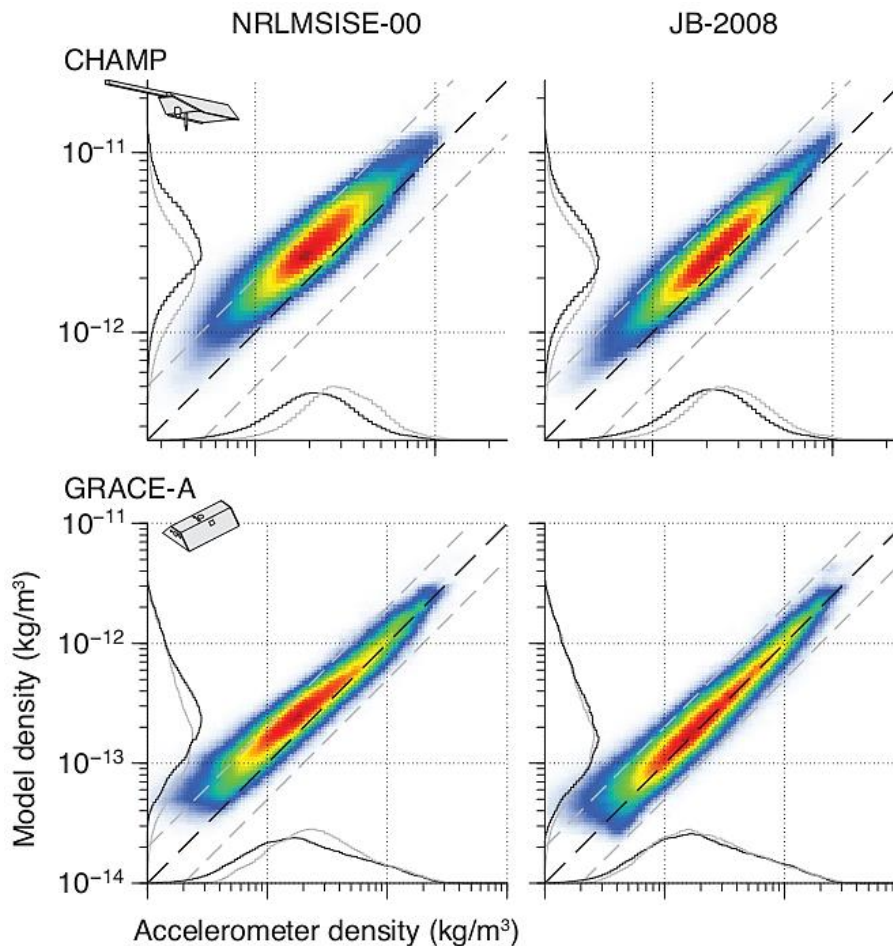


Figure 1.10 Histograms showing the distribution of CHAMP and GRACE-A densities, with their equivalent model densities for MSIS (NRLMSISE-00) and Jacchia (JB-2008) models. The line graphs at both axes show simple two-dimensional histograms of their corresponding data set in black. [Doornbos, 2011, Fig. 5.8].

In the same line as the MSIS model, the HWM07 horizontal wind model [Drob *et al.*, 2008] is a statistical representation from the ground to the exosphere, based on gradient winds from CIRA-86 (Committee on Space Research International Reference Atmosphere) plus rocket soundings, incoherent scatter radar, medium-frequency radar, and meteor radar data. Their predecessors were the HWM93, HWM90, and HWM87 [Hedin *et al.*, 1996]. The HWM07 model can represent both quiet and disturbed geomagnetic conditions, and the parameterization of solar activity is planned to be included in future versions. A recent update (HWM14) provides an improved time-dependent, observationally based, global empirical specification of the upper atmospheric general circulation patterns and migrating tides [Drob *et al.*, 2015].

Compared to the above thermospheric empirical models, MIT physical models require more expert knowledge and, therefore, are more suitable for scientific investigations than for routine applications, as for example orbit determination. Detailed descriptions for the available upper atmosphere models are given in the review of [Emmert \[2015a\]](#) and [Akmaev \[2011\]](#). For instance, the Thermosphere-Ionosphere-Electrodynamics General Circulation Model (TIME-GCM) [[Richmond et al., 1992](#); [Qian et al., 2014](#)] solve three-dimensional fluid equations for the mutual diffusion of N₂, O₂, and O, and includes a coupled ionosphere. The reactions in the TIME-GCM involve ion species and energy budget, as well as self-consistent generation of middle and low latitude electric fields by neutral winds. [Kim et al. \[2012\]](#) incorporated NRLMSISE-00 partial pressures of He into TIE-GCM, contributing to variations in mass density, specific heat, viscosity, and thermal conductivity. [Hagan et al. \[2001\]](#) attempted to extend the Global-Scale Wave Model (GSWM) with migrating solar tides, using the TIME-GCM to calculate the neutral gas heating that dominates the forces from solar activities. The main idea was to confirm whether the model fitted the seasonal characteristics and the solar cycle variability. Diurnal temperature amplitude did vary with solar activity, while there was no corresponding wind caused by solar cycle variability. The new GSWM showed a good consistency with the TIME-GCM results. Moreover, [Häusler et al. \[2014\]](#) proposed a new boundary scheme in TIME-GCM based on NASA MERRA (Modern Era Retrospective-Analysis for Research and Applications) temperature, which self-consistently could explain the day-to-day tidal and planetary wave variability. The model showed a more variable and complicated pattern especially of the neutral temperature. The non-migrating tide in the lower boundary scheme TIME-GCM/MERRA was larger than that in TIME-GCM/GSWM, causing stronger vertical atmospheric transport. The authors pointed that stronger vertical transport lead to a smaller density due to the compositional mixing effect dominated by the atomic oxygen.

1.3. Problems and motivation

From previous sections, it is clear that accurate thermospheric neutral density models are essential for the upper-atmosphere research and applications, but the current geophysical models are unable to predict the variability as accurately and efficiently required. The upper atmospheric expansion describes an increase in the temperature and density of Earth's upper atmosphere, producing atmospheric drag on LEO spacecraft. Increased drag decelerates satellites, moving their orbit closer to Earth, decreasing the lifespan of space assets, and

making satellite tracking difficult. In addition, the exponential increase of space objects (including the recent collision of the commercial Iridium satellite) has recently highlighted the importance of debris tracking, and the prediction of potential collisions with orbiting satellites has recently become an essential task. During the last decades, numerous studies have been addressed to different aspects of thermospheric density variations because the scientific community still needs more complete studies to characterize and predict the thermospheric neutral density variability in an accurate and efficient manner. Understanding and modeling the MIT system and its relationship to atmospheric drag is essential to maintain safe and effective operations of space-based assets, and the research on this topic will improve accurate satellite tracking, collision avoidance, object custody, and reentry prediction. This dissertation investigates thermospheric neutral density variations inferred from GRACE accelerometers for the period 2003-2016. The results will contribute for a better understanding of all involved parameters and the interconnections between the functional dependences in the upper atmosphere.

In addition, since the use of POD least-squares estimators to derive density measurements can become a complex task, this study introduces a new technique to derive non-gravitational accelerations from numerical differentiation of POE, which can also be used for accelerometer calibration. Space accelerometers measure the force needed to keep a proof of mass accurately at the spacecraft's center of mass, where the gravity is exactly compensated by the centrifugal force. However, accelerometers on-board satellites are based on the electrostatic principle, and suffer from dc biasing voltage fluctuations which must be calibrated after the measurement. This new method for accelerometer calibration does not require a POD scheme, and serves as a reliable reference with unbiased solution. In addition, the current Time-Varying Gravity (TVG) modelling still fails in an accurate and real-time functional (pre-processing independency) analytical models reliable for satellite gravimetry or altimetry, and the differences between accelerometer measurements and the numerical differentiation of POE in the radial axis can be employed for the assessment of conservative force models. Finally, since thermospheric neutral densities can be derived from the drag force, an additional challenge in this dissertation is whether POE-based non-gravitational accelerations can be used to replace accelerometer measurements.

In this scheme, since the orbital precession represents a major limitation in the spatiotemporal statistical analysis of satellite measurements, this work proposes a new

methodology based on the PCA or also called Empirical Orthogonal Function (EOF) analysis, where the eigenvalue solution of the covariance matrix of static grids is obtained by interpolation of consecutive orbital arcs. This new method will be applied in three case-studies thoroughly this dissertation:

- In the first case, for the conservative-force anomalies derived from analytical TVG models, accurate orbit solutions, and accelerometer measurements.
- In the second case, for the differences between accelerometer-based densities and the NRLMSISE00 estimates for the period 2003-2015.
- In the last and most important case, for thermospheric neutral density distribution and variations from 13 years (2003-2015) of GRACE measurements.

1.4. Research contents

The structure of this document is presented as follows. Chapter 2 introduces the observational data and models, as well as the data processing and methods used. In Chapter 3, the accuracy of the new observables (POE-based non-gravitational accelerations) is analyzed and a better calibration of the GRACE accelerometers is presented. In addition, a new method to analyze the accuracy of the current conservative-force models with the use of the PCA is introduced with the analysis of 4 years of differences between POE-based non-gravitational accelerations and accelerometer measurements (2006-2009). Moreover, Chapter 4 analyzes the accuracy of both accelerometer and POE-based density estimates, and demonstrates the capability to employ POE-based densities when accelerometer measurements are not available. Furthermore in Chapter 5, an extensive study on thermospheric neutral density distribution and variations is given from 13 years of GRACE measurements (2003-2015). Besides the principal modes and mechanisms of thermospheric density variations, Chapter 5 includes a study on long-term variations, and keeps record of two studies on thermospheric neutral density variations induced by geomagnetic storms, one for the severe G4-level geomagnetic storm of March 2015 from accelerometer measurements, and the other for the moderate G2-level geomagnetic storm of March 2013 from POE-based estimates. Finally in Chapter 6, conclusions and future perspectives are given.

2. OBSERVATION AND DATA PROCESSING

2.1. The GRACE and GOCE observables

GRACE is a joint mission between the *National Aeronautics and Space Administration* (NASA) in the United States and the *Deutsches Zentrum Für Luft und Raumfahrt* (DLR) in Germany, which is widely employed in geodesy and climate change applications (e.g., *Jin et al. [2011, 2013]*). GRACE's Level 1B format record files can be downloaded from the Information System and Data Center (ISDC) *GeoForschungsZentrum* (GFZ) website (<http://isdc-old.gfz-potsdam.de/>) in binary big-endian byte-ordering format [*Case et al., 2002*]. GOCE is the first dedicated gravity field mission of the Living Planet Program of the European Space Agency (ESA), and their Level 1B format record files are downloaded from the ESA GOCE Virtual Archive (<http://eo-virtual-archive1.esa.int/Index.html>) in txt format [*SERCO/DATAMAT, 2006*].

The twin satellites of the GRACE mission are equipped with three-axis capacitive Super-STAR accelerometers to measure the non-gravitational forces acting on the satellites. The precision of the X_{SBS} and Z_{SBS} axes is specified to be 0.1nm/s^2 and 1nm/s^2 for the Y_{SBS} axes. Note in SBS (Satellite Body System), the X_{SBS} axis is the long axis of symmetry of the satellite, pointing in the direction of the microwave horn, the Y_{SBS} axis is the vertical axis of symmetry, and the Z_{SBS} axis completes the right-handed coordinate system. Accelerometer measurements at a second interval are included in the ACC_1B files. The star camera mounted on GRACE satellites provides the precise attitude references to determine the satellite's absolute orientation with respect to the International Celestial Reference System (ICRS). Star camera measurements are given at a 5 s time-sampling interval as a set of quaternion in the SCA_1B GRACE's files. GRACE's precise position and velocity, at 5 s interval and including formal error, have been computed in a reduced-dynamic POD by the GPS Inferred Positioning System (GIPSY) software of JPL. Precise position and velocity solutions are included in the GNV_1B files. Thruster activation times and satellite mass records are included in TRH_1B and MASS_1B files, respectively.

The GOCE mission carry as primary science instrument a gradiometer, consisting of three pairs of accelerometers on orthogonal axes. For two out of three axes, the precision is specified to be 10^{-3}nm/s^2 and an order of magnitude lower for the 3rd axis. The so-called GOCE's Common-Mode (CM) accelerations provide a very good observation of non-gravitational forces acting on the satellite. Calibrated accelerometer measurements at a

second interval are included in the EGG_NOM_1b files. GOCE's gradiometer inertial attitude quaternion records at a second interval are included in the EGG_NOM_1b files. Official GOCE's precise position and velocity have been computed in a reduced-dynamic POD by the BERNESE software at the Astronomical Institute of the University of Bern (AIUB). Precise position and velocity solutions are included in the SST_PSO_2 files.

2.2. Non-gravitational accelerations from POE

2.2.1. *Arc-to-chord interpolation threshold*

As usually, precise accelerations are not part of the available POD products, and several approaches have been tested to assess the accuracy of interpolated and numerically differentiated POE. In order to minimize the error of interpolation, low-degree polynomials are not sufficient, high-degree polynomials introduce undesired oscillations, and the Fast Fourier Transform (FFT) approach is not considered due to presence of data gaps and outliers [Weigelt and Sneeuw, 2005]. As it has been demonstrated in previous studies (e.g., Reubelt et al. [2006]), the best alternative is a piece-wise interpolation such as splines or Hermite polynomials.

In this study, different algorithms have been tested by interpolating odd from even original precise velocity states. The error committed has been evaluated by simple differences between interpolated and original data (10 s sampling), and the 8-data point piece-wise Lagrange interpolation [Henning, 2014] has provided a white noise error of standard deviation of ~10nm/s. Similar results have been obtained when testing the piece-wise cubic Hermite interpolation method. The second derivatives provided as an output in the algorithms of interpolation did not provide enough accuracy, and the numerical differentiation of precise velocities has been finally chosen. Furthermore, when calculating total accelerations by a simple differentiation of velocities, the first approximations to numerical derivatives have been found to produce large bias [Bezdek, 2010]. In this study, total accelerations have been calculated by simple differentiation of velocities for a several sampling interval (Δt). The results are given in Table 2.1, and show that the bias is proportional to Δt . Therefore, we can deduce that the bias is caused by the three-point formula. arc-to-chord approximation. The three-point formula written in the form of two-velocity states is given by:

$$\ddot{\mathbf{r}}_{t_0} = \lim_{\Delta t \rightarrow 0} \dot{\mathbf{r}}''_{t_0} = \lim_{\Delta t \rightarrow 0} \frac{\dot{\mathbf{r}}'_{t_1} - \dot{\mathbf{r}}'_{t_{(-1)}}}{\Delta t} = \lim_{\Delta t \rightarrow 0} \frac{\mathbf{r}_{t_2} - 2\mathbf{r}_{t_0} + \mathbf{r}_{t_{(-2)}}}{(\Delta t)^2} \quad (2.1)$$

where simple and double quotation mark denotes simple or double approximation, respectively, and $t_{(i+1)} - t_i = \Delta t$. Equation (2.1) is itself the definition of the instantaneous acceleration and implies that the velocity at a given state only can be calculated accurately only if the error associated to the non-linear path is taken into account (a simple difference between two positions). Similarly, it can be deduced that the error associated to a non-linear change in velocity is clearly present when computing accurate accelerations from pairs of consecutive velocity states. Following to this, a precise numerical approximation can be achieved by minimizing the increment of time up to a desired accuracy.

In this scheme, precise orbit velocities have been interpolated and differentiated by an increment of time (Δt) which minimizes the error committed at a given threshold. The accuracy threshold has been implemented by comparing accelerations calculated from different Δt , achieving an optimal error for a value of 0.05 s (bias-error smaller than 1nm/s^2 in the arc-to-chord approximation). Bigger

Table 2.1 Arc-to-chord approximation error in GRACE

Δt (s)	Error (nm/s^2)
0.05	1
0.1	3
0.2	12
0.5	50
1	120
2	1500

sampling intervals have shown larger biases (Table 2.1). A feasible MATLAB computation for each coordinate-axis is given in Appendix A. Centripetal accelerations from angular velocities and radius of three-point-fitted circles were also tested and provided unbiased results, but delivered several large discrepancies probably caused by the nature of the non-circular orbit configuration.

2.2.2. *Time-Varying Gravity model*

Besides the static mean gravity field (e.g., [Pavlis et al. \[2012\]](#); [Goiginger et al. \[2011\]](#); [Förste et al. \[2011\]](#)), the TVG is a major interest within the fields of satellite gravimetry or mass redistributions in the Earth's system. During the last decade, several TVG series have been computed from GRACE [[Luthcke et al., 2006](#); [Lemoine et al., 2007](#); [Bruinsma et al., 2010](#); [Bettadpur, 2012](#); [Watkins and Yuan, 2012](#); [Dahle et al., 2013](#)] and many studies have studied alternative approaches to obtain real-time TVG models (e.g., [Fletcher \[2007\]](#); [Cheng et al. \[2011\]](#); [Zelensky et al. \[2012\]](#); [Cerri et al. \[2013\]](#)). Among these studies, the TVG

forward modeling or so-called “de-aliasing products” (e.g., [Fletcher \[2007\]](#)) provide time-series of conservative forces which are computed from geophysical models (e.g., National Centers for Environmental Prediction, NCEP; European Centre for Medium-Range Weather Forecasts, ECMWF; Estimating the Circulation and Climate of the Ocean, ECCO; Global Land Data Assimilation Systems, GLDAS), including atmosphere, hydrology and wind-forcing changes in ocean mass. However, the availability and latency of these geophysical models is a serious problem, and several approximating analytical models are developed for the modeling of regular variations and trends (e.g., [Biancale and Bode \[2006\]](#)).

In this study, non-gravitational accelerations at each state are obtained by removing the standard TVG model from the precise orbit accelerations (computed in the previous section). The conventional gravity model based on the EGM2008 [[Petit and Luzum, 2010](#)], describes with Stokes’ coefficients the static part of the gravitational field and the underlying background for the secular variations of its \bar{C}_{20} , \bar{C}_{21} , \bar{S}_{21} , \bar{C}_{30} and \bar{C}_{40} coefficients. In addition, when computing the gravitational forces acting on the user’s satellite, other time-varying effects must be also taken into account. These include the third body tide caused by the Moon and Sun [[Montenbruck and Gill, 2013](#)], the solid Earth tides [[Petit and Luzum, 2010](#)], the ocean tides (e.g., [Rieser et al. \[2012\]](#)), the solid Earth pole tide [[Petit and Luzum, 2010](#)], the ocean pole tide [[Desai, 2002](#)], and the relativistic terms [[Petit and Luzum, 2010](#)].

The geopotential field V in geocentric coordinates (r, φ, λ) is expanded in spherical harmonics with up to degree N as:

$$V(r, \varphi, \lambda) = \frac{GM_{Earth}}{r} \sum_{n=0}^N \left(\frac{a_e}{r} \right)^n \sum_{m=0}^n \left[\bar{C}_{nm} \cos(m\lambda) + \bar{S}_{nm} \sin(m\lambda) \right] \bar{P}_{nm}(\sin \varphi) \quad (2.2)$$

where GM_{Earth} and a_e EGM2008 values ($398600.4415 \text{ km}^3/\text{s}^2$ and 6378136.3 m respectively) should be used as scaling parameters with its gravitational potential coefficients. In order to use the conventional static gravitational field properly and projected it in time, the secular low degree \bar{C}_{20} (zero-tide), \bar{C}_{30} and \bar{C}_{40} rates have been accounted for:

$$\bar{C}_{n0}(t) = \bar{C}_{n0}(t_0) + \frac{d\bar{C}_{n0}}{dt}(t - t_0) \quad (2.3)$$

were t_0 is the epoch J2000.0, and the values of $\bar{C}_{n0}(t_0)$ and rates of $d\bar{C}_{n0}(t_0)/dt$ are given in Table 2.2.

Table 2.2 Low-degree coefficients of the conventional geopotential model

Coefficient	Value at 2000.0	Rate (yr ⁻¹)
\bar{C}_{20} (zero tide)	$-0.48416948 \cdot 10^{-3}$	$11.6 \cdot 10^{-12}$
\bar{C}_{30}	$0.9571612 \cdot 10^{-6}$	$4.9 \cdot 10^{-12}$
\bar{C}_{40}	$0.5399659 \cdot 10^{-6}$	$4.7 \cdot 10^{-12}$

In order to provide a mean figure axis coincident with the mean pole and consistent with the Terrestrial Reference Frame, the values for the coefficients \bar{C}_{21} and \bar{S}_{21} are:

$$\begin{aligned}\bar{C}_{21}(t) &= \sqrt{3} \bar{x}_p(t) \bar{C}_{20} - \bar{x}_p(t) \bar{C}_{22} + \bar{y}_p(t) \bar{S}_{22} \\ \bar{S}_{21}(t) &= -\sqrt{3} \bar{y}_p(t) \bar{C}_{20} - \bar{y}_p(t) \bar{C}_{22} - \bar{x}_p(t) \bar{S}_{22}\end{aligned}\quad (2.4)$$

Recent values of \bar{C}_{20} , \bar{C}_{22} and \bar{S}_{22} are adequate for a 10^{-14} accuracy, e.g., the values of the present conventional model ($-0.48416948 \cdot 10^{-3}$, $2.4393836 \cdot 10^{-6}$, and $-1.4002737 \cdot 10^{-6}$ respectively). The variables \bar{x}_p and \bar{y}_p (in radian) represent the IERS conventional mean pole:

$$\begin{aligned}\bar{x}_p(t) &= \sum_{i=0}^3 (t-t_0)^i \bar{x}_p^i \\ \bar{y}_p(t) &= \sum_{i=0}^3 (t-t_0)^i \bar{y}_p^i\end{aligned}\quad (2.5)$$

where t_0 is the year 2000.0 and the coefficients \bar{x}_p^i and \bar{y}_p^i (mas·yr⁻ⁱ) are given in Table 2.3.

Table 2.3 Coefficients of the IERS 2010 mean pole model

Degree i	Before 2010.0		After 2010.0	
	\bar{x}_p^i	\bar{y}_p^i	\bar{x}_p^i	\bar{y}_p^i
0	55.974	346.346	23.513	358.891
1	1.8243	1.7896	7.6141	-0.6287
2	0.18413	-0.10729	0.0	0.0
3	0.007024	-0.000908	0.0	0.0

The gravitational acceleration of a third body [Montenbruck and Gill, 2013] can be described as a difference between the accelerations of the satellite and the Earth caused by a third body B:

$$\Delta \ddot{\mathbf{r}}_{\text{sat}} = GM_{\text{B}} \left(\frac{\mathbf{r}_{\text{B}} - \mathbf{r}_{\text{sat}}}{|\mathbf{r}_{\text{B}} - \mathbf{r}_{\text{sat}}|^3} - \frac{\mathbf{r}_{\text{B}}}{|\mathbf{r}_{\text{B}}|^3} \right) \quad (2.6)$$

where \mathbf{r}_{sat} and \mathbf{r}_{B} are the geocentric coordinates of the satellite and of a third body of mass M_{B} .

Since accelerations on near-Earth satellites from other planets actions are relatively small ($< 0.1 \text{ nm/s}^2$), only lunisolar accelerations are calculated. Moon and Sun coordinates have been interpolated from the solar and planetary ephemerides (DE-421) provided by the *Jet Propulsion Laboratory* (JPL) in the form of Chebyshev approximations. The evaluation of these polynomials yields Cartesian coordinates in the ICRS for the Earth-Moon barycenter $\mathbf{b}_{\text{Earth,Moon}}$ and the Sun \mathbf{b}_{Sun} with respect to the barycenter of the solar system, while Moon positions \mathbf{r}_{Moon} are given with respect to the center of the Earth. The geocentric position of the Sun can be computed as:

$$\mathbf{r}_{\text{Sun}} = \mathbf{b}_{\text{Sun}} - \mathbf{b}_{\text{Earth,Moon}} + \frac{\mathbf{r}_{\text{Moon}}}{1 + \mu^*} \quad (2.7)$$

where μ^* denotes the ratio of the Earth's and the Moon's masses.

The Luni-solar tides for GRACE on July 14th, 2007 are shown in Figure 2.1.

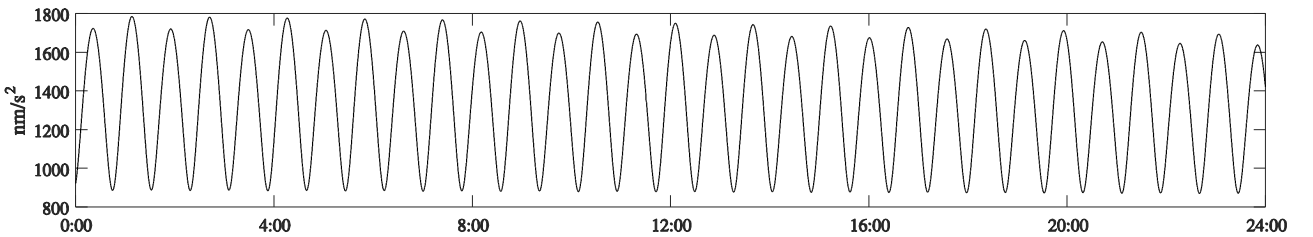


Figure 2.1 Luni-solar tides for GRACE on July 14th, 2007.

Since the changes induced by the Earth's solid tides [Petit and Luzum, 2010] due to its rotation under effects of ellipticity and Coriolis force, can be described in terms of the Love numbers, variations in the low-degree Stokes' coefficients can be easily computed. Dependent and independent frequency corrections are calculated using lunar and solar

ephemerides, Doodson's fundamental arguments, the nominal values of the Earth's solid tide external potential Love numbers, and the in-phase and out-of-phase amplitudes of the corrections for frequency-dependent Love values. First, changes induced by the tide generating potential in the normalized geopotential coefficients for both $n=2$ and $n=3$, for all m , are given by the frequency-independent corrections in the form:

$$\Delta\bar{C}_{nm} - i\Delta\bar{S}_{nm} = \frac{k_{nm}}{2n+1} \sum_{B=Sun, Moon} \frac{GM_B}{GM_{Earth}} \left(\frac{a_e}{r_B} \right)^{n+1} \bar{P}_{nm}(\sin\varphi_B) e^{-im\lambda_B} \quad (2.8)$$

and

$$\Delta\bar{C}_{4m} - i\Delta\bar{S}_{4m} = \frac{k_{2m}^{(+)}}{5} \sum_{B=Sun, Moon} \frac{GM_B}{GM_{Earth}} \left(\frac{a_e}{r_B} \right)^3 \bar{P}_{2m}(\sin\varphi_B) e^{-im\lambda_B} \quad \forall m = \{0, 1, 2\} \quad (2.9)$$

where

k_{nm} is the nominal Love number for degree n and order m ,

r_B is the distance from geocenter to Moon or Sun,

φ_B is the body-fixed geocentric latitude of Moon or Sun,

λ_B is the body-fixed east longitude (from Greenwich) of Moon or Sun.

Note that anelasticity of the mantle causes k_{nm} and $k_{nm}^{(+)}$ to acquire small imaginary parts (Table 2.4).

Table 2.4 Nominal values of solid Earth tide external potential Love numbers

		Elastic Earth		Anelastic Earth		
n	m	k_{nm}	$k_{nm}^{(+)}$	$\text{Re}(k_{nm})$	$\text{Im}(k_{nm})$	$k_{nm}^{(+)}$
2	0	0.29525	-0.00087	0.30190	-0.00000	-0.00089
2	1	0.29470	-0.00079	0.29830	-0.00144	-0.00080
2	2	0.29801	-0.00057	0.30102	-0.00130	-0.00057
3	0	0.093	...			
3	1	0.093	...			
3	2	0.093	...			
3	3	0.094	...			

To calculate r_B , φ_B and λ_B , geocentric Moon and Sun Cartesian coordinates must be rotated from the ICRS to the International Terrestrial Reference System (ITRS) and transformed to the spherical coordinates as usually (see next section). Frequency dependent

corrections are computed as the sum of contributions from a number of tidal constituents belonging to the respective bands:

$$\begin{aligned}
 \Delta\bar{C}_{20} - i\Delta\bar{S}_{20} &= \sum_b A_b^{ip} \cos(\bar{n}_b \cdot \bar{\beta}) - A_b^{op} \sin(\bar{n}_b \cdot \bar{\beta}) \\
 \Delta\bar{C}_{21} - i\Delta\bar{S}_{21} &= \sum_a A_a^{ip} \sin(\bar{n}_a \cdot \bar{\beta}) + A_a^{op} \cos(\bar{n}_a \cdot \bar{\beta}) - i \sum_a A_a^{ip} \cos(\bar{n}_a \cdot \bar{\beta}) - A_a^{op} \sin(\bar{n}_a \cdot \bar{\beta}) \\
 \Delta\bar{C}_{22} - i\Delta\bar{S}_{22} &= \sum_c A_c \cos(\bar{n}_c \cdot \bar{\beta}) - i \sum_c -A_c \sin(\bar{n}_c \cdot \bar{\beta})
 \end{aligned} \tag{2.10}$$

where

$\bar{\beta}$ is the six-vector of Doodson's fundamental Lunisolar arguments (τ, s, h, p, N', p_s);

\bar{n}_j is the six-vector of multipliers of the fundamental Lunisolar arguments ($j=a, b, c$);

A_j is the In-phase (ip) and out-of-phase (op) amplitudes ($j=a, b, c$);

$j=a, b, c$ correspond to the parameters from Tables 6.5a, 6.5b and 6.5c given in [Petit and Luzum, 2010].

Doodson's variables are related to Delaunay's by:

$$\begin{aligned}
 \tau &= \gamma - s \\
 s &= F + \Omega \\
 h &= s - D \\
 p &= s - l \\
 N' &= -\Omega \\
 p_s &= s - D - l'
 \end{aligned} \tag{2.11}$$

and Delaunay's fundamental Lunisolar arguments can be computed as:

$$\begin{aligned}
 \gamma &= (67310.54841 + (876600 \times 3600 + 8640184.812866)t + 0.093104t^2 - 6.2 \times 10^{-6}t^3)15 + 648000 \\
 l &= -0.00024470t^4 + 0.051635t^3 + 31.8792t^2 + 1717915923.2178t + 485868.249036 \\
 l' &= -0.00001149t^4 - 0.000136t^3 - 0.5532t^2 + 129596581.0481t + 1287104.79305 \\
 F &= 0.00000417t^4 - 0.001037t^3 - 12.7512t^2 + 1739527262.8478t + 335779.526232 \\
 D &= -0.00003169t^4 + 0.006593t^3 - 6.3706t^2 + 1602961601.2090t + 1072260.70369 \\
 \Omega &= -0.00005939t^4 + 0.007702t^3 + 7.4722t^2 - 6962890.2665t + 450160.398036
 \end{aligned} \tag{2.12}$$

where t is measured in Julian centuries of Barycentric Dynamical Time (TDB).

In Equation (2.12), the Terrestrial Time (TT) can be used, in practice, instead the TDB (assuming a difference in the CIP location smaller than 0.01 μs):

$$t = (JD_{TT} - 2451545)/36525$$

$$JD_{TT} = JD_{UTC} + TAI - UTC + 32.184 \quad (2.13)$$

The Earth solid tides for GRACE on July 14th, 2007 are shown in Figure 2.2.

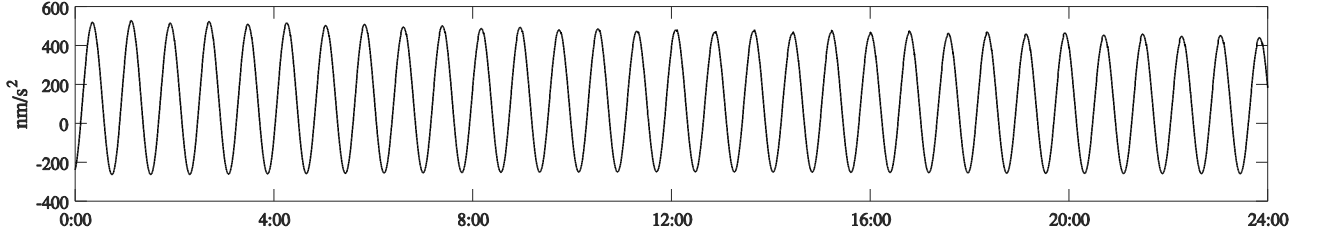


Figure 2.2 Earth solid tides for GRACE on July 14th, 2007.

Accounting for the dynamical effects of ocean tides, the periodic variations in the normalized Stokes' coefficients are calculated based on the most recent ocean tide model EOT11a [Rieser et al., 2012]. The potential coefficients for the mass redistribution effect of ocean tides are available in the form of $cnmCos$, $snmCos$ and $cnmSin$, $snmSin$ (including the loading potential and the Doodson-Warburg phase corrections) up to maximum degree and order 120 for each tide s , and obtained for Doodson's arguments $\bar{\beta}$ by:

$$\begin{aligned} \Delta \bar{c}_{nm,s} &= cnmCos \cos(\bar{n}_s \cdot \bar{\beta}) + cnmSin \sin(\bar{n}_s \cdot \bar{\beta}) \\ \Delta \bar{s}_{nm,s} &= snmCos \cos(\bar{n}_s \cdot \bar{\beta}) + snmSin \sin(\bar{n}_s \cdot \bar{\beta}) \end{aligned} \quad (2.14)$$

Rieser et al. [2012] also provided the influences of additional minor tide constituents that are not included in the tide model EOT11a and should not be neglected in LEO. This function evaluates the contribution of altogether 256 tides. Ocean tides for GRACE on July 14th, 2007 are shown in Figure 2.3.

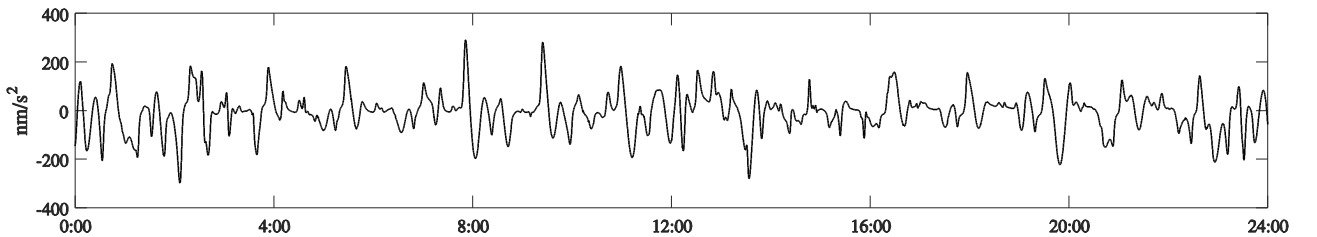


Figure 2.3 Ocean tides for GRACE on July 14th, 2007.

Changes in the geopotential value due to the centrifugal effect of pole motion, known as the Earth's solid pole tides [Petit and Luzum, 2010], can be readily computed in function of the wobble variables and calculated under sub-daily polar motion variations as:

$$\begin{aligned}\Delta\bar{C}_{21} &= -1.333 \cdot 10^{-9} (m_1 + 0.0115 m_2) \\ \Delta\bar{S}_{21} &= -1.333 \cdot 10^{-9} (m_2 - 0.0115 m_1)\end{aligned}\quad (2.15)$$

where m_1 and m_2 in seconds of arc are obtained from the difference between the polar motion and the IERS conventional mean pole (above defined) as:

$$\begin{aligned}m_1 &= x_p - \bar{x}_p \\ m_2 &= -(y_p - \bar{y}_p)\end{aligned}\quad (2.16)$$

The standard pole coordinates of the parameters x_p and y_p are from the IERS (<http://hpiers.obspm.fr/iers/eop/eopc04/>) with additional components to account for the effect of ocean tides $(\Delta x_p, \Delta y_p)_{\text{ocean}}$ and forced terms $(\Delta x_p, \Delta y_p)_{\text{libration}}$ with periods of less than two days in space. These sub-daily variations are not part of the polar motion values published by the IERS and are therefore to be added after interpolation. Feasible computation is available in Section 2.2.3:

$$\begin{aligned}\Delta x_p &= \sum_o \left[x_o^{\cos} \cos(\bar{n}_o \cdot \bar{F}) + x_o^{\sin} \sin(\bar{n}_o \cdot \bar{F}) \right] + \sum_l \left[x_l^{\cos} \cos(\bar{n}_l \cdot \bar{F}) + x_l^{\sin} \sin(\bar{n}_l \cdot \bar{F}) \right] \\ \Delta y_p &= \sum_o \left[y_o^{\cos} \cos(\bar{n}_o \cdot \bar{F}) + y_o^{\sin} \sin(\bar{n}_o \cdot \bar{F}) \right] + \sum_l \left[y_l^{\cos} \cos(\bar{n}_l \cdot \bar{F}) + y_l^{\sin} \sin(\bar{n}_l \cdot \bar{F}) \right]\end{aligned}\quad (2.17)$$

where

\bar{F} is the six-vector of Delaunay's fundamental arguments $(\gamma, l, l', F, D, \Omega)$;

\bar{n}_j is the six-vector of multipliers of the fundamental arguments ($j=o, l$);

x_j^{\cos}, x_j^{\sin} are the amplitudes in x_p for cosinus and sinus respectively ($j=o, l$);

y_j^{\cos}, y_j^{\sin} are the amplitudes in y_p for cosinus and sinus respectively ($j=o, l$);

$j=o, l$ makes reference to oceanic 'o' and libration 'l' parameters, respectively.

Oceanic parameters are retrieved from Tables 8.2a and 8.2b and libration parameters ($n=2$) from Table 5.1a of *Petit and Luzum [2010]*. Earth's solid pole tides for GRACE on July 14th, 2007 are shown in Figure 2.4.

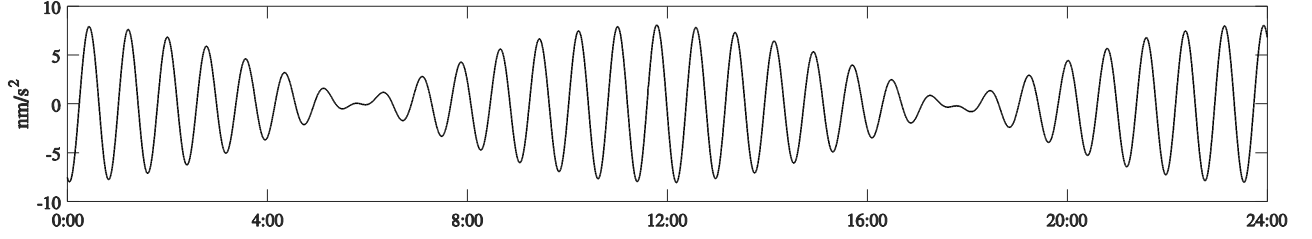


Figure 2.4 Earth's solid pole tides for GRACE on July 14th, 2007.

The ocean pole tide, generated by the centrifugal effect of pole motion on the oceans, is calculated as a function of sub-daily wobble variables from the coefficients (\bar{A}_{nm} and \bar{B}_{nm}) of the self-consistent equilibrium model [*Desai, 2002*]. These perturbations to the normalized geopotential coefficients are given by:

$$\begin{bmatrix} \Delta \bar{C}_{nm} \\ \Delta \bar{S}_{nm} \end{bmatrix} = R_n \left\{ \begin{bmatrix} \bar{A}_{nm}^R \\ \bar{B}_{nm}^R \end{bmatrix} (m_1 \gamma_2^R + m_2 \gamma_2^I) + \begin{bmatrix} \bar{A}_{nm}^I \\ \bar{B}_{nm}^I \end{bmatrix} (m_2 \gamma_2^R + m_1 \gamma_2^I) \right\} \quad (2.18)$$

where

$$R_n = \frac{\omega_{Earth}^2 a_e^2}{GM_{Earth}} \frac{4\pi G \rho_w}{g_e} \left(\frac{1 + k'_n}{2n + 1} \right) \quad (2.19)$$

and

$$\omega_{Earth} = 7.292115 \cdot 10^{-5} \text{ rad}^{-1};$$

$$\rho_w = 1025 \text{ kg/m}^3;$$

$$G = 6.67428 \cdot 10^{-11} \text{ m}^3/(\text{kg} \cdot \text{s}^2);$$

$$g_e = 9.7803278 \text{ m/s}^2;$$

$$k'_2 = -0.3075, k'_3 = -0.195, k'_4 = -0.132, k'_5 = -0.1032, k'_6 = -0.0892;$$

$$\gamma_2^R = 0.6870 \text{ and } \gamma_2^I = 0.0036.$$

Ocean pole tides for GRACE on July 14th, 2007 are shown in Figure 2.5.

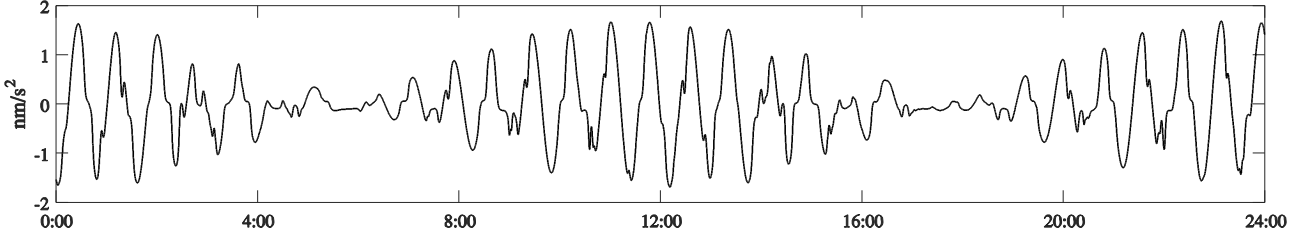


Figure 2.5 Ocean pole tides for GRACE on July 14th, 2007.

Only the main relativistic effects (described by the Schwarzschild field of the Earth itself $\sim 16.5 \text{ nm/s}^2$), are calculated, since the effects of the Lense-Thirring precession (frame-dragging) and the geodesic (de Sitter) precession are two orders of magnitude smaller at a near-Earth satellite orbit [Petit and Luzum \[2010\]](#):

$$\Delta \ddot{\mathbf{r}}_{sat} = \frac{GM_{Earth}}{c^2 r_{sat}^3} \left\{ \left[4 \frac{GM_{Earth}}{r_{sat}} - (\dot{\mathbf{r}}_{sat} \cdot \dot{\mathbf{r}}_{sat}) \right] \cdot \mathbf{r}_{sat} + 4 (\mathbf{r}_{sat} \cdot \dot{\mathbf{r}}_{sat}) \cdot \dot{\mathbf{r}}_{sat} \right\} \quad (2.20)$$

The relativistic Schwarzschild field for GRACE on July 14th, 2007 is shown in Figure 2.6.

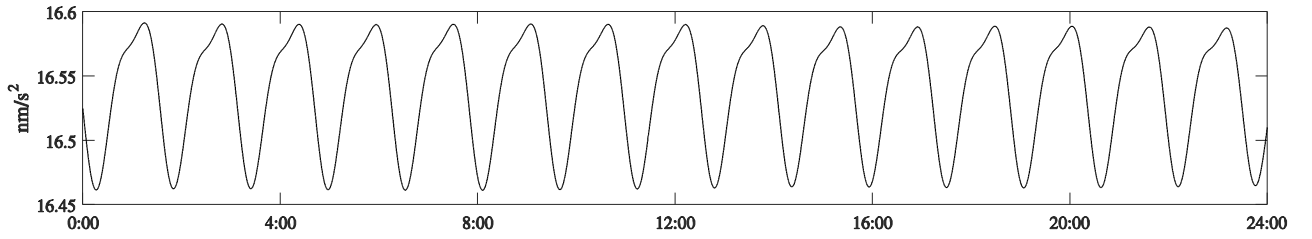


Figure 2.6 Schwarzschild field for GRACE on July 14th, 2007.

Time-varying Stokes' coefficients up to a degree and order 120 have been computed under an increment of time small enough to desensitize from discontinuities (~ 400 s), and the gravity for every satellite position calculated by using the first derivative of the gravitational potential in Cartesian coordinates. With the substitution of $\bar{P}_{nm} = \bar{P}_{nm}(\sin \varphi)$ and $\bar{P}'_{nm} = \partial \bar{P}_{nm}(\sin \varphi) / \partial \varphi$, the first derivative of the gravitational potential of the Earth in spherical coordinates is calculated as:

$$\begin{aligned} \frac{dU}{dr} &= \frac{-GM_{Earth}}{r^2} \sum_{n=0}^{n_{max}} (n+1) \left(\frac{a_e}{r} \right)^n \sum_{m=0}^n \bar{P}_{nm} (\bar{C}_{nm} \cos m\lambda + \bar{S}_{nm} \sin m\lambda) \\ \frac{dU}{d\varphi} &= \frac{GM_{Earth}}{r} \sum_{n=0}^{n_{max}} \left(\frac{a_e}{r} \right)^n \sum_{m=0}^n \bar{P}'_{nm} (\bar{C}_{nm} \cos m\lambda + \bar{S}_{nm} \sin m\lambda) \\ \frac{dU}{d\lambda} &= \frac{GM_{Earth}}{r} \sum_{n=0}^{n_{max}} \left(\frac{a_e}{r} \right)^n \sum_{m=0}^n m \bar{P}_{nm} (\bar{S}_{nm} \cos m\lambda - \bar{C}_{nm} \sin m\lambda) \end{aligned} \quad (2.21)$$

and the gravity:

$$\begin{aligned}
 \ddot{x} &= \frac{\partial U}{\partial x} = \frac{\partial U}{\partial r} \frac{\partial r}{\partial x} + \frac{\partial U}{\partial \varphi} \frac{\partial \varphi}{\partial x} + \frac{\partial U}{\partial \lambda} \frac{\partial \lambda}{\partial x} \\
 \ddot{y} &= \frac{\partial U}{\partial y} = \frac{\partial U}{\partial r} \frac{\partial r}{\partial y} + \frac{\partial U}{\partial \varphi} \frac{\partial \varphi}{\partial y} + \frac{\partial U}{\partial \lambda} \frac{\partial \lambda}{\partial y} \\
 \ddot{z} &= \frac{\partial U}{\partial z} = \frac{\partial U}{\partial r} \frac{\partial r}{\partial z} + \frac{\partial U}{\partial \varphi} \frac{\partial \varphi}{\partial z}
 \end{aligned} \tag{2.22}$$

where the partial derivatives are

$$\begin{aligned}
 \partial r / \partial x &= \cos \varphi \cos \lambda \\
 \partial r / \partial y &= \cos \varphi \sin \lambda \\
 \partial r / \partial z &= \sin \varphi \\
 \partial \theta / \partial x &= \sin \varphi \cos \lambda / r \\
 \partial \theta / \partial y &= \sin \varphi \sin \lambda / r \\
 \partial \theta / \partial z &= -\cos \lambda / r \\
 \partial \lambda / \partial x &= -\sin \lambda / (r \cos \varphi) \\
 \partial \lambda / \partial y &= \cos \lambda / (r \cos \varphi)
 \end{aligned} \tag{2.23}$$

The derivative of the normalized associated Legendre function can be computed as:

$$\bar{P}'_{nm} = k_{n,m} \bar{P}_{n,m+1} - m \tan \varphi \bar{P}_{n,m} \tag{2.24}$$

where the scale factor is

$$k_{nm} = (1 - \delta_{nm}) \left[(1 - \delta_{m0}) \sqrt{(n+m+1)(n-m)} + \delta_{m0} \sqrt{(n+1)(n/2)} \right] \tag{2.25}$$

Maximum amplitudes and mean values of all conservative-force models for GRACE on July 14th, 2007 are shown in Table 2.5 and plotted in Figure 2.7.

Table 2.5 Force models with maximum amplitudes and mean values for GRACE on July 14th, 2007. [*Calabia and Jin, 2016a, Table 1*].

Models	Details	Mean (m/s ²)	Max. Amp. (m/s ²)
Earth gravity	EGM2008 with low degree rates. Degree 120.	8.5	6e-2
Third bodies	Moon and Sun from JPL DE421.	1.3e-6	1e-6
Earth tides	Due to Moon and Sun, Wahr terms.	1e-7	8e-7
Ocean tides	EOT11a (256 tides). Degree 120.	0	6e-7
Solid Earth pole tide	IERS 2010 using sub-daily wobble variables	0	2e-8
Ocean pole tide	<i>Desai [2002]</i> with sub-daily wobble variables. Deg. 120	0	4e-9
Relativity	Schwarzschild correction.	1.65 e-8	2e-10

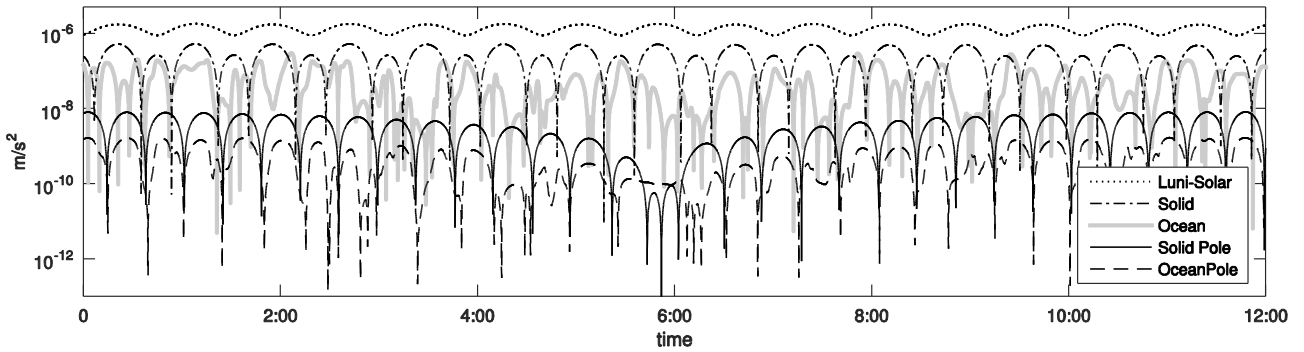


Figure 2.7 Force-model accelerations (absolute values) for GRACE on July 14th, 2007.

A feasible computation in MATLAB can be done as follows: a first function *tides()* computes the gravity *gtidt* in ITRS at 400 s resolution from the EGM2008, including the frequency-independent and dependent solid tides, the rates for C low-degree, the C_{20} permanent tide, the oceanic tide, the pole solid tide, and the pole ocean tide. This function is given in Appendix B. A continuation, *gtidt* must be rotated to the ICRS (Section 2.2.3) as it were position, to obtain *gtidc*. Then, *gtidc* can be removed from the time-state accelerations A_c (Section 2.2.1) and rotated to the SBS, to finally be removed from the lunisolar tides and the relativistic effects (Appendix C).

2.2.3. *Transformations between reference systems*

In order to compare POE-based non-gravitational accelerations and accelerometer measurements, several transformations between reference-systems are required (i.e., POD solutions are usually given in the ITRS and accelerometer measurements in the SBS).

Lunisolar direct tides are calculated in the ICRS and the other involved forces in the ITRS as Stokes' coefficients. The computation must be done under an increment of time small enough to desensitize from temporal variations (~400 s). Gravitational accelerations must be rotated to the ICRS as they were positions, because the Stokes' coefficients have already included the contribution of the Earth's rotation. Moreover, the attitude of the satellites is based on celestial body observations, so the rotation to the SBS implies to pass through the ICRS. First, the gravitational accelerations must be subtracted from the POE-based accelerations to obtain the non-gravitational accelerations. Then, computed non-gravitational accelerations can be rotated to the SBS, and finally the differences to accelerometer measurements can be evaluated by means of simple difference of median averages, or by Least Squares adjustment.

For the followings, the basic rotations in the tri-axial reference system are defined as:

$$\begin{aligned}
 \mathbf{R}_1(\psi_x) &= \begin{bmatrix} 1 & 0 & 0 \\ 0 & \cos \psi_x & \sin \psi_x \\ 0 & -\sin \psi_x & \cos \psi_x \end{bmatrix} \\
 \mathbf{R}_2(\psi_y) &= \begin{bmatrix} \cos \psi_y & 0 & -\sin \psi_y \\ 0 & 1 & 0 \\ \sin \psi_y & 0 & \cos \psi_y \end{bmatrix} \\
 \mathbf{R}_3(\psi_z) &= \begin{bmatrix} \cos \psi_z & \sin \psi_z & 0 \\ -\sin \psi_z & \cos \psi_z & 0 \\ 0 & 0 & 1 \end{bmatrix} \tag{2.26}
 \end{aligned}$$

The rotation ICRS to SBS is derived from the star-camera quaternion (Figure 2.8):

$$\mathbf{r}_{\text{SBS}} = [\mathbf{R}_{\text{ib}}] \mathbf{r}_{\text{ICRS}} = \begin{bmatrix} q_0^2 + q_1^2 - q_2^2 - q_3^2 & 2(q_1q_2 + q_0q_3) & 2(q_1q_3 - q_0q_2) \\ 2(q_1q_2 - q_0q_3) & q_0^2 - q_1^2 + q_2^2 - q_3^2 & 2(q_2q_3 + q_0q_1) \\ 2(q_1q_3 + q_0q_2) & 2(q_2q_3 - q_0q_1) & q_0^2 - q_1^2 - q_2^2 + q_3^2 \end{bmatrix} \mathbf{r}_{\text{ICRS}} \tag{2.27}$$

where

$$\begin{aligned}
 q_0 &= \cos(\psi / 2) \\
 q_1 &= \sin(\psi / 2) \cos \alpha \\
 q_2 &= \sin(\psi / 2) \cos \beta \\
 q_3 &= \sin(\psi / 2) \cos \gamma
 \end{aligned} \tag{2.28}$$

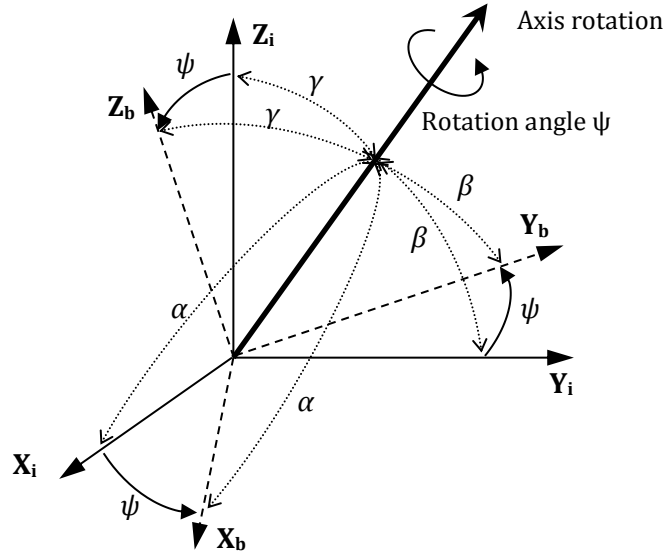


Figure 2.8 Representation of the star-camera quaternion angles.

The transition from ITRS to ICRS is realized through a sequence of rotations that account for precession [P], nutation [N] and Earth rotation [S], including polar motion [PM] [*Petit and Luzum, 2010*]:

$$\mathbf{r}_{\text{ICRS}} = [P][N][S][PM]\mathbf{r}_{\text{ITRS}}$$

$$\dot{\mathbf{r}}_{\text{ICRS}} = [P][N][S]\{[PM]\dot{\mathbf{r}}_{\text{ITRS}} + \boldsymbol{\omega}_{\text{Earth}} \cdot [PM]\mathbf{r}_{\text{ITRS}}\}$$

$$\ddot{\mathbf{r}}_{\text{ICRS}} = [P][N][S]\{[PM]\ddot{\mathbf{r}}_{\text{ITRS}} + \boldsymbol{\omega}_{\text{Earth}} \cdot (\boldsymbol{\omega}_{\text{Earth}} \cdot [PM]\ddot{\mathbf{r}}_{\text{ITRS}}) + 2\boldsymbol{\omega}_{\text{Earth}} \cdot [PM]\dot{\mathbf{r}}_{\text{ITRS}}\} \quad (2.29)$$

where the nominal mean Earth's angular velocity corrected from the variable Length Of Day (LOD) is:

$$\boldsymbol{\omega}_{\text{Earth}} = 7.29211514670698 \cdot 10^{-5} [1 - (LOD + \Delta LOD) / 86400]$$

Similarly to polar motion, additional components should be added to the values from the IERS for $UT1$ and LOD , to account for the sub-daily effects of ocean tides:

$$\Delta UT1 = \sum_o O_{UT1}^{\cos} \cos(\bar{n}_o \cdot \bar{F}) + O_{UT1}^{\sin} \sin(\bar{n}_o \cdot \bar{F})$$

$$\Delta LOD = \sum_o O_{LOD}^{\cos} \cos(\bar{n}_o \cdot \bar{F}) + O_{LOD}^{\sin} \sin(\bar{n}_o \cdot \bar{F}) \quad (2.30)$$

where the effects of libration have been neglected due to its small size, and

\bar{F} is the six-vector of Delaunay's fundamental arguments ($\gamma, l, l', F, D, \Omega$);

\bar{n}_o is the six-vector of multipliers of the fundamental arguments;

$O_{UT1}^{cos}, O_{UT1}^{sin}$ are the oceanic amplitudes in *UT1* for cosinus and sinus respectively;

$O_{LOD}^{cos}, O_{LOD}^{sin}$ are the oceanic amplitudes in *LOD* for cosinus and sinus respectively.

which oceanic parameters are retrieved from Tables 8.3a and 8.3b of [Petit and Luzum, 2010].

Then, the Earth rotation matrix $[S]$ has the form $[S]=R_3(-ERA)$, where

$$ERA= 2\pi (0.7790572732640+1.00273781191135448 JD_{UT});$$

$$JD_{UT} = JD_{UT1} - 2451545;$$

$$UT1= UTC + (UT1-UTC) + \Delta UT1; \quad (2.31)$$

Polar motion consists of two quasi-periodic components and a gradual drift. The two main periodic parts are the *Chandler wobble* and the seasonal motions. The longer term variation is less well understood (motions in the Earth's core and mantle, water mass redistribution, and the isostatic rebound). The rotation matrix for polar motion is given by $[PM]=R_3(-s') \cdot R_2(x_p+\Delta x_p) \cdot R_1(y_p+\Delta y_p)$, where $s' = (-47 \cdot 10^{-6} t)\pi / (3600 \cdot 180)$. The standard pole coordinates x_p and y_p are those from IERS, and the additional sub-daily variations of pole coordinates (Δx_p and Δy_p) and the parameter t (\sim Julian centuries of TT) have been formulated in Section 2.2.2.

A combined transformation $[Q]$ for precession $[P]$ and nutation $[N]$ is defined in terms of co-declination d , right ascension E , and the instantaneous right ascension of the instantaneous pole (parameter s) as:

$$[Q]=[P] \cdot [N]=R_3(-E) \cdot R_2(-d) \cdot R_3(E) \cdot R_3(-s) \quad (2.32)$$

For convenience, the coordinates are redefined as:

$$\begin{bmatrix} X \\ Y \\ Z \end{bmatrix} = \begin{bmatrix} \sin d \cos E \\ \sin d \sin E \\ \cos d \end{bmatrix} \quad (2.33)$$

and the matrix $[Q]$ becomes:

$$Q = \begin{bmatrix} 1 - aX^2 & -aXY & X \\ -aXY & 1 - aY^2 & Y \\ -X & -Y & 1 - a(X^2 + Y^2) \end{bmatrix} \mathbf{R}_3(s) \quad (2.34)$$

where $a = 0.5 + (X^2 + Y^2)/8$

The IAU 2006/2000A developments for the parameters X , Y and s are:

$$\begin{aligned} X &= 10^{-6} \left\{ \begin{aligned} &-16617'' + 2004191898'' t - 429782.9'' t^2 - 198618.34'' t^3 + 7.578'' t^4 + 5.9285'' t^5 \\ &+ \sum_{j=0}^4 \sum_i \left[(a_j^{\sin})_i t^j \sin(\bar{A} \cdot \bar{n}) + (a_j^{\cos})_i t^j \cos(\bar{A} \cdot \bar{n}) \right] \end{aligned} \right\} \\ Y &= 10^{-6} \left\{ \begin{aligned} &-6951'' - 25896'' t - 22407274.7'' t^2 + 1900.59'' t^3 + 1112.526'' t^4 + 0.1358'' t^5 \\ &+ \sum_{j=0}^4 \sum_i \left[(b_j^{\sin})_i t^j \sin(\bar{A} \cdot \bar{n}) + (b_j^{\cos})_i t^j \cos(\bar{A} \cdot \bar{n}) \right] \end{aligned} \right\} \\ s &= -\frac{XY}{2} + 10^{-6} \left\{ \begin{aligned} &94.0'' + 3808.65'' t - 122.68'' t^2 - 72574.11'' t^3 + 27.98'' t^4 + 15.62'' t^5 \\ &+ \sum_{j=0}^4 \sum_i \left[(c_j^{\sin})_i t^j \sin(\bar{A} \cdot \bar{n}) + (c_j^{\cos})_i t^j \cos(\bar{A} \cdot \bar{n}) \right] \end{aligned} \right\} \end{aligned} \quad (2.35)$$

where

\bar{n} is the 14-vector of multipliers of the fundamental arguments of the nutation theory;

\bar{A} is the 14-vector of fundamental arguments of the nutation theory, of which lunisolar ones (l , l' , F , D and Ω) have been defined in the previous section, and the planetary ones (in radian) are:

$$\begin{aligned} L_{Me} &= 4.402608842 + 2608.7903141574t; \\ L_{Ve} &= 3.176146697 + 1021.3285546211t; \\ L_E &= 1.753470314 + 628.3075849991t; \\ L_{Ma} &= 6.203480913 + 334.06124267t; \\ L_J &= 0.599546497 + 52.9690962641t; \\ L_{Sa} &= 0.874016757 + 21.329910496t; \\ L_U &= 5.481293872 + 7.4781598567t; \\ L_{Ne} &= 5.311886287 + 3.8133035638t; \\ p_A &= 0.02438175t + 0.00000538691t^2. \end{aligned} \quad (2.36)$$

The parameter t (~Julian centuries of TT) has been defined in the previous section. Amplitudes $(a_j^{sin})_i, (a_j^{cos})_i, (b_j^{sin})_i, (b_j^{cos})_i, (c_j^{sin})_i, (c_j^{cos})_i$ and the multipliers of the fundamental arguments are available at the IERS Conventions 2010 website (<ftp://tai.bipm.org/iers/conv2010/chapter5/>).

After parameters X and Y are calculated, the IERS celestial pole offsets ΔX and ΔY can be added. These are provided by the IERS' EOP. Feasible algorithms for the ICRS-ITRS rotation can be found in [Vallado \[2013\]](#), and the sub-daily EOP parameters are given in Appendix D.

Summarizing all the process, the precise orbit positions and velocities must be rotated to the ICRS using the computed sub-daily EOP. Then, the POE-based accelerations must be computed on the ICRS, and the direct tides calculated from the Sun and Moon ICRS coordinates. Sun and Moon coordinates must be also rotated to the ITRS to compute the frequency-independent solid tides. Then, gravitational accelerations must be rotated to the ICRS (as they were positions), and finally the differences to POE-based accelerations rotated to the SBS.

2.3. Thermospheric neutral density retrieval

2.3.1. Drag-force formula and altitude normalization

Non-gravitational forces acting on a LEO satellite's surface include atmospheric drag (F_D), irradiative accelerations and thruster firings. Whilst thruster firings can be easily removed by computing the activation records, irradiative accelerations comprise a more elaborated modeling (Section 2.3.2). Then, thermospheric mass densities can be inferred using the drag-force formula:

$$F_D = \frac{1}{2} C A \rho v_r^2 \quad (2.37)$$

where C is the drag coefficient vector (Section 2.3.3), A is the cross-sectional area perpendicular to v_r , ρ is the atmospheric mass density, and v_r is the relative velocity of the atmosphere with respect to the spacecraft, which includes the co-rotating atmosphere v_c and the horizontal winds v_w [[Doornbos, 2011](#)]:

$$v_r = -\dot{r}_{sat} + v_c + v_w \quad (2.38)$$

Horizontal winds velocities \mathbf{v}_w can be computed from the HWM07 [Drob *et al.*, 2008] and, since these are given in the East-North-Up (ENU) local frame, these must be transformed to the terrestrial frame (ITRS). The velocity of the co-rotating atmosphere \mathbf{v}_c is computed as the vector product between the Earth angular rotation and the satellite's position vector. Then, using the formula given in Bruinsma [2004], the neutral density can be retrieved accounting each satellite plate i as follows:

$$\rho = \frac{-2\mathbf{F}_D}{\sum_{i=1}^{n_p} [A_i C_{Di} (\mathbf{v}_r \hat{\mathbf{n}}_i) \mathbf{v}_r + A_i C_{Li} (\mathbf{v}_r \times \hat{\mathbf{n}}_i) \times \mathbf{v}_r]} \quad (2.39)$$

where, C_{Di} and C_{Li} are the drag and lift coefficients for each plate i , n_p is the number of plates, A_i is the surface area of each plate i , and $\hat{\mathbf{n}}_i$ is the unit plate normal.

Several approaches and simplifications for density estimation can be found in Doornbos [2011], including the projection of the aerodynamic acceleration on the relative velocity (drag), and the projection of drag on the inertial velocity. These approximations allow assuming that the drag acceleration vector is coplanar with the orbital plane, and therefore apply the in-plane perturbation equations from celestial mechanics.

After computing the neutral density at each orbital position, the derived mass density can be normalized to a common height [Rentz, 2008], with the help of an atmospheric model (e.g., NRMSISE00):

$$\rho(475km) = \rho_{obs}(h) \frac{\rho_{model}(475km)}{\rho_{model}(h)} \quad (2.40)$$

2.3.2. Irradiative accelerations

The amount of incoming radiation from the Sun and Earth causes irradiative accelerations on the user's satellite plates. Basically, the main sources of this kind of accelerations are the direct solar radiation pressure, the reflected solar radiation pressure, and the terrestrial infrared radiation. While the terrestrial infrared radiation (long-wave radiation) is almost independent from illumination conditions, the other two solar radiations (short-wave radiations) must account for a planetary eclipse ratio sh [Montenbruck and Gill, 2013]. Figure 2.9 depicts the eclipse geometry for an accurate computation (given in Appendix E). In the ITRS, the coordinates of the Sun (Sun) and the spacecraft (*sat*), with respect to the occulting body B (for each case; B= Moon, Earth) are:

$$\begin{aligned} \mathbf{s}_B^{sat} &= \mathbf{r}_{sat} - \mathbf{r}_B \\ \mathbf{s}_B^{Sun} &= \mathbf{r}_{Sun} - \mathbf{r}_B \end{aligned} \quad (2.41)$$

Note that for Earth $\mathbf{r}_{Earth}=0$. Then, the fundamental plane (plane perpendicular to the shadow axis and passes through the satellite) intersects the shadow axis at a distance:

$$s_0 = (-\mathbf{s}_B^{sat} \cdot \mathbf{s}_B^{Sun}) / s_B^{Sun} \quad (2.42)$$

and the penumbra and umbra angles are:

$$\begin{aligned} \sin f_1 &= (R_{Sun} + R_B) / s_B^{Sun} \\ \sin f_2 &= (R_{Sun} - R_B) / s_B^{Sun} \end{aligned} \quad (2.43)$$

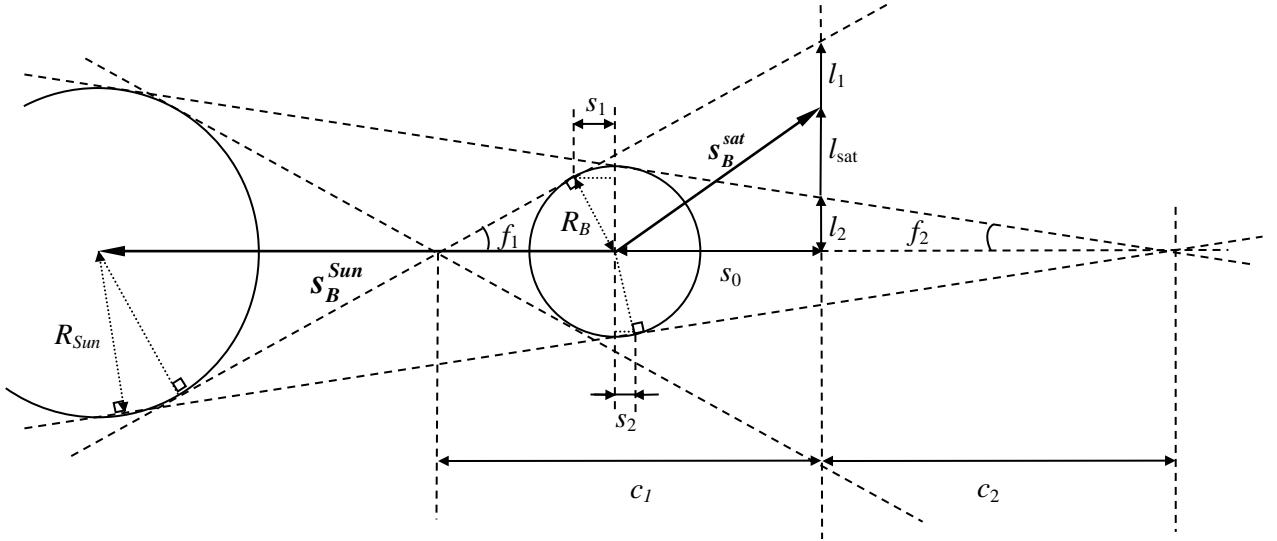


Fig. 2.8 Eclipse computation geometry

Following to this approach, the distances needed to compute the shadow algorithm are:

$$\begin{aligned} s_1 &= -R_B \sin f_1 \\ s_2 &= R_B \sin f_2 \\ c_1 &= s_0 + (R_B / \sin f_1) \\ c_2 &= s_0 - (R_B / \sin f_2) \\ l_1 &= c_1 \tan f_1 \\ l_2 &= c_2 \tan f_2 \\ l_{sat} &= \sqrt{s_B^{sat2} - s_0^2} \end{aligned} \quad (2.44)$$

Then, if l_{sat} is major than l_2 and minor than l_1 , and s_0 is major than s_1 , the spacecraft is in penumbra. Otherwise, if s_0 is major than s_2 , and l_{sat} is minor than l_2 , the spacecraft is umbra ($sh=0$). For other cases, the spacecraft is in sunlight ($sh=1$). When the spacecraft is in penumbra, a fractional area of the solar disc that is blocked by the occulting body can be applied to the incoming solar flux ($sh=f_g$). Using the circumflex mark as for denoting unit vectors, the closest point to the Earth on the Sun-satellite vector s_{Sun}^{sat} is:

$$\mathbf{r}_p = \mathbf{r}_{sat} - \left(\hat{s}_{Sun}^{sat} \cdot \mathbf{r}_{sat} \right) \hat{s}_{Sun}^{sat} \quad (2.45)$$

and the apparent radius of the solar disc projected on a plane through this point, perpendicular to the satellite-Sun vector is:

$$R'_{Sun} = \frac{\left\| \left(\hat{s}_{Sun}^{sat} \cdot \mathbf{r}_{sat} \right) \hat{s}_{Sun}^{sat} \right\|}{s_{Sun}^{sat}} R_{Sun}$$

$$\eta = \frac{r_p - R_{Earth}}{R'_{Sun}} \delta_{sh, penumbra}$$

$$f_g = 1 - \frac{1}{\pi} \arccos(\eta) + \frac{\eta}{\pi} \sqrt{1 - \eta^2} \quad (2.46)$$

From Stefan-Boltzmann law and satellite measurements, the normalized (1AU) solar flux on the Earth's atmosphere is well known as 1366 W/m^2 . This magnitude must be corrected from the yearly period of the Earth's orbit eccentricity (actual satellite-Sun distance, s_{sun}^{sat}) to obtain the corrected solar radiation by applying the inverse square law:

$$E_{sr} = sh \cdot 1366 \left(1AU / s_{sun}^{sat} \right)^2 \quad (2.47)$$

On the plates of the user's satellite, one part of this incoming radiation is absorbed, and the other is reflected diffusely and specularly. The following equation can be used to determine the entire resultant force on the satellite due to solar radiation [Wertz, 1991; Luthcke et al., 1997]:

$$\mathbf{a}_{sr} = \sum_{i=1}^{n_p} - \frac{E_{sr} A_i \hat{\mathbf{n}}_i \hat{s}_{sun}^{sat}}{m c} \left[2 \left(\frac{c_{rd,i}}{3} + c_{rs,i} \hat{\mathbf{n}}_i \hat{s}_{sun}^{sat} \right) \hat{\mathbf{n}}_i + (1 - c_{rs,i}) \hat{s}_{sun}^{sat} \right] \quad (2.48)$$

where, n_p is the number of plates, A_i is the plate area, c is the speed of light, $c_{rd,i}$ is the coefficient of diffusive reflectivity, $c_{rs,i}$ is the coefficient of specular reflectivity, m is the

satellite mass, and $\hat{\mathbf{n}}_i$ is the unit plate normal. Since the satellite's panel properties (e.g., for GRACE these from [Bettadpur \[2007\]](#)) provide the coefficients of reflectivity for both, the visible (VIS) and the infrared (IR) part of the electromagnetic spectrum, these can be combined by weighting in function of the amount of solar flux given for each spectral window (43 % for VIS and 53 % for IR). A feasible computation for the solar radiation is given in Appendix F. Figure 2.10 shows the resulting solar radiation acceleration for GRACE in the SBS on April 1st 2005.

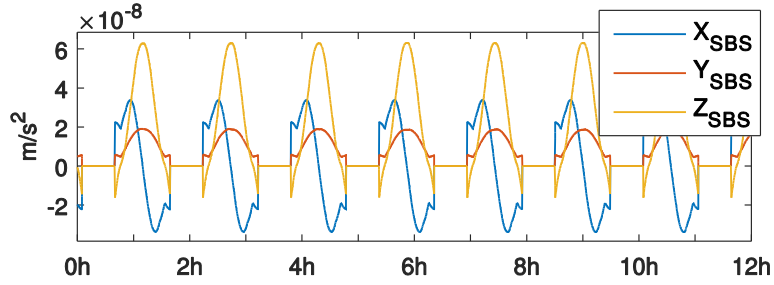


Figure 2.10 Induced direct solar radiation acceleration for GRACE-A in the SBS on April 1st 2005.

In a similar way, the Earth albedo can be formulated as

$$\mathbf{a}_{ea} = \sum_{i=1}^{n_p} \sum_{j=1}^{grid} - \frac{E_{ea,j} A_i \hat{\mathbf{n}}_i \hat{\mathbf{s}}_j^{sat}}{mc} \left[2 \left(\frac{c_{rd,i}}{3} + c_{rs,i} \hat{\mathbf{n}}_i \hat{\mathbf{s}}_j^{sat} \right) \hat{\mathbf{n}}_i + (1 - c_{rs,i}) \hat{\mathbf{s}}_j^{sat} \right] \quad (2.49)$$

where, the parameter $E_{ea,j} = E_{ea}^R + E_{ea}^{IR}$ is decomposed in short-wave E_{ea}^R and long-wave E_{ea}^{IR} radiation. The short-wave radiation results from the reflected solar radiation, and the long-wave radiation can be modeled for Earth, as that of a black body with a surface temperature of 288°K. Since the reflected radiant flux is a fraction of the incoming flux, this can be computed from the reflectivity index σ . The Earth's reflectivity index σ has been measured for several years in the Total Ozone Mapping Spectrometer (TOMS) project. TOMS provides grids of 1° in latitude by 1.25° in longitude of daily measurement for the duration of the mission. In this study, monthly averages from 2003 to 2005 have been derived to account for the annual variation. The following task is to derive the short-wave radiation $E_{ea,j}^R$ reflected from each cell j of TOMS as follows:

$$E_{ea,j}^R = f_j v_j E_{sr} \frac{A_j (\hat{\mathbf{n}}_j \hat{\mathbf{s}}_j^{sun}) (\hat{\mathbf{n}}_j \hat{\mathbf{s}}_j^{sat}) \sigma_j}{\pi |\hat{\mathbf{s}}_j^{sat}|^2} \quad (2.50)$$

where, f_j and v_j are the field of view of the satellite and the sunlight function, E_{sr} is the incident irradiance, A_j is the area of each cell, and the reflection angle on each cell is defined by the direction of the satellite \hat{s}_j^{sat} , the Sun \hat{s}_j^{Sun} and the cell normal-vector \hat{n}_j . A feasible algorithm can be found in [Bhanderi \[2005\]](#). Concerning the long-wave radiation, the spectrum is mainly infrared (IR) and its exitance is about 239 W/m^2 [[Taylor, 2005](#); [Liebmann et al., 1996](#)]. Earth's IR radiation is variable with latitude and season, and its fraction value has been modeled by [Knocke and Ries \[1987\]](#):

$$e_{IR} = e_0 + e_1 P_1 \sin \varphi + e_2 P_2 \sin \varphi$$

$$e_1 = k_0 + k_1 \cos[\omega(JD - t_0)] + k_2 \sin[\omega(JD - t_0)] \quad (2.51)$$

where, t_0 is the epoch (Dec. 22,1981), ω is the Earth orbit pulsation ($2\pi/365.5$), φ is the equatorial geocentric latitude, JD is the Julian Date, P_n is the Legendre polynomial of degree n , and $e_0=0.68$; $e_2= -0.18$; $k_0=0$; $k_1= -0.07$ and $k_2=0$. Then, the IR irradiance $E_{ea, j}^{IR}$ from each visible cell of the Earth's surface reads as follows:

$$E_{ea, j}^{IR} = f_j 239 \left(\frac{1\text{AU}}{s_{Sun}^j} \right)^2 e_{IR, j} \frac{A_j \hat{n}_j \hat{s}_j^{sat}}{\pi |\hat{s}_j^{sat}|^2} \quad (2.52)$$

A feasible computation for the Earth albedo is given in Appendix G. Figure 2.11 show the resulting terrestrial infrared radiation acceleration and Earth albedo acceleration for GRACE on April 1st 2005.

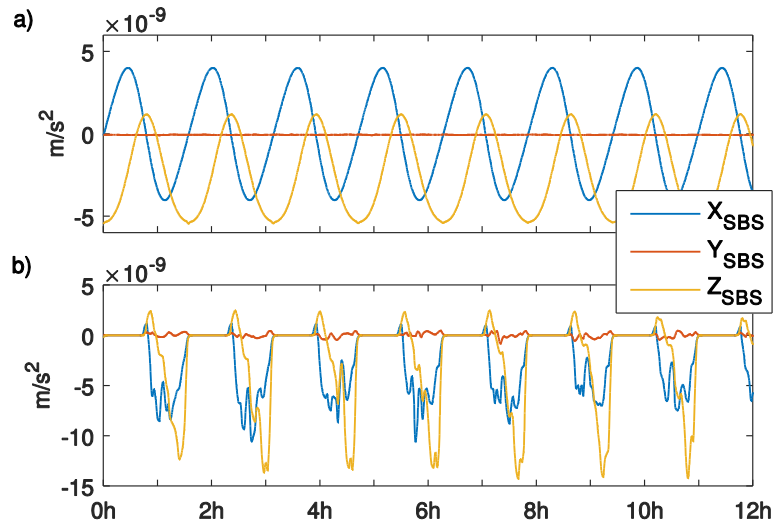


Figure 2.11 Induced (a) terrestrial infrared radiation acceleration and (b) Earth albedo acceleration for GRACE-A in the SBS on April 1st 2005.

2.3.3. Drag coefficient vector C

The dimensionless drag coefficient C is required to represent the interaction between the satellite and the flow. The drag coefficient vector C can be decomposed in drag C_D and lift C_L or pressure C_n (normal to surface) and shear C_t (tangential to surface), depending on the reference frame used:

$$C = -(C_D \cdot \hat{u}_D + C_L \cdot \hat{u}_L) = -(C_n \cdot \hat{n} + C_t \cdot \hat{t}) \quad (2.53)$$

Most of LEO satellites flow in the regime of high vacuum (flow can be considered to be individual particles moving in straight lines), and several analytical methods have been developed to represent the free molecular flow (e.g., [Schamberg \[1959\]](#); [Sentman \[1961\]](#)). Simplified assumptions to Schamberg's formulas, where the drag coefficient vector C is decomposed in drag C_D and lift C_L for each plate i are given by [Cook \[1965\]](#):

$$C_{Li} = \frac{4}{3} \sqrt{1 + \alpha_i \left(\frac{T_{w,i}}{T_a} - 1 \right)} \sin \theta_i$$

$$C_{Di} = 2 + \frac{4}{3} \sqrt{1 + \alpha_i \left(\frac{T_{w,i}}{T_a} - 1 \right)} \cos \theta_i \quad (2.54)$$

where, T_a is the temperature of the atmosphere (e.g. from NRLMSISE-00), $T_{w,i}$ is the temperature of the plate ($\sim 300^\circ\text{K}$ for GRACE), θ_i is the angle of incident gas flow with respect to the plate, and α_i is the high-speed substrate material accommodation coefficient [[Goodman, 1964](#)]:

$$\alpha_i = \frac{3.6 \mu_i}{(1 + \mu_i)^2} \quad (2.55)$$

The molecular mass ratio μ can be obtained from the mean molecular density of the atmosphere, divided by the molecular density of each plate. For the GRACE satellites, the surfaces are Kapton (382 g/mol), solar array glass (144 g/mol), and Teflon (100 g/mol). The mean molecular density (g/mol) of the atmosphere is obtained from the sum of the NRLMSISE-00 partial number-densities (m^{-3}), multiplied by their atomic mass (He=4.002, O=15.999, N2=28.134, O2=31.998, Ar=39.948, H=1.007, N=14.0067, Oa=16.999, all in g/mol), and divided by the total volume.

Unfortunately, free molecular closed-form solutions cannot accurately account for multiple reflections, but new computational methods are being developed to compute physical drag coefficients (e.g., [Mehta et al. \[2013\]](#)). These method can include, e.g., Direct Simulation Monte Carlo (DSMC) simulations or test particle modeling. For instance, physical drag coefficients computed using different gas-surface interaction models are compared in [Mehta et al. \[2014\]](#). [Metha et al. \[2013\]](#) provided the parameterizations of pressure C_n and shear C_t coefficients for the GRACE mission as follows:

$$\begin{aligned} C_n &= a \alpha_{eff}^b + c \\ C_t &= a \cdot \exp(b \cdot T \cdot n_{He}) + c \cdot \exp(d \cdot T \cdot n_{He}) \end{aligned} \quad (2.56)$$

where the effective energy accommodation coefficient α_{eff} can be calculated as:

$$\alpha_{eff} = \frac{\alpha_i + K \cdot n_o \cdot T}{1 + K \cdot n_o \cdot T} \quad (2.57)$$

where $K=7.50E-17$ is the Langmuir isotherm parameter [[Pilinski, 2011](#)], n_o is the mole fraction of atomic oxygen (NRLMSISE-00), T is the exospheric temperature in Kelvin (NRLMSISE-00), and α_i is the high-speed substrate material accommodation coefficient mentioned above. The remaining parameters are the product ($^{\circ}K/m^3$) of exospheric temperature T by the mole fraction of Helium n_{He} (NRLMSISE-00), and the coefficients given in [Metha et al. \[2013\]](#), which must be interpolated for each pitch Φ and sideslip β angle. A feasible computation for these pressure and shear drag-coefficients is given in Appendix H.

2.4. Spatiotemporal PCA of measurements along orbits

In order to derive a complete grid of densities, the orbital trajectory for the 2003-2016 time-series has been divided in ascending and descending orbits. For the development in longitude, the values have been biased 360° after a grid is completed. Then, the interpolation and clipping of each grid has been conducted (Figure 2.12). Different algorithms were compared and the linear interpolation showed the bests results. In this scheme, the period and the equatorial shift of the orbit both respectively produce a latitudinal and a longitudinal variation, through which each grid is influenced. For the GRACE mission, the orbital period corresponds to 94.10 min, and the equatorial orbit shift to 23.6° . This means that grids and

PCA components both vary 3.99 min per westward degree, and 31.37 s per latitudinal degree. The latitudinal component is northwards or southwards depending on using ascending or descending orbits, and should take into account when employed together as input in a statistical analysis. Following to this approach, the variability of each grid is synthesized in two temporal dimensions: the latitudinal variation, defined by the half orbital period (3.99 min per westward degree), and the longitudinal variation, defined by the equatorial orbit shift (31.37 s per latitudinal degree). A feasible computation is given in Appendix I.

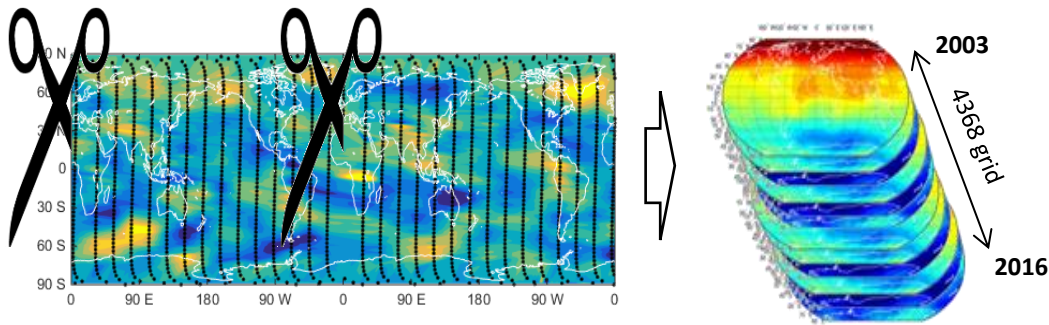


Figure 2.12 Grid clipping of interpolated measurements (ascending-orbits).

Finally, the spatial patterns of variability, their time variation and the measure of their importance are conducted via the PCA. The aim of the EOF technique is to determine a new set of variables that capture most of the observed variance from the data through a linear combination of the original variables based on Eigen Decomposition. Instead of attempting to estimate principal components with a sequential nonlinear regression analysis of one-dimensional measurements along satellite tracks [Matsuo *et al.*, 2002; Matsuo and Forbes, 2010; Lei *et al.*, 2012a], this study examines in detail the covariance matrix of a grid time series, via conventional PCA. With the finality of separating space-time variability, previous studies have treated the data variability over the course of orbital time to be stationary (~ 90 min for GRACE). In this study, this variability is regarded as non-stationary, and the analysis can provide information about the variations in the latitudinal dimension. As for the PCA modes, previous authors have mapped the data to a time-invariant orthogonal basis at every orbit time, where the orthogonal basis is composed by 7 orders of spherical harmonics. Therefore, it might be induced that the resolution of their PCA modes is restricted by the maximum order of the orthogonal basis. In this methodology, taking into account the time processing and the physical memory required for the PCA calculation in a standard desktop computer, an optimal resolution of 3° (120x60) is achieved.

Detailed analyses for the use of the PCA technique and the selection of retained modes for static grids can be found in *Preisendorfer [1998]* and *Wilks [1995]*, and a readily computable algorithm in *Bjornsson and Venegas [1997]*. The method requires the use of a two-dimensional matrix F where each row represents a given instant of time, and each column a time series for a given location (Figure 2.13).

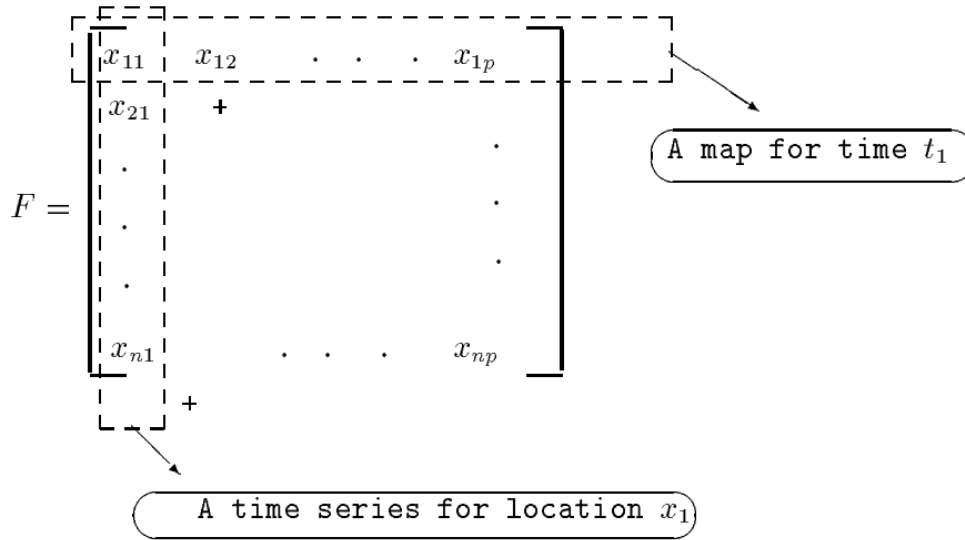


Figure 2.13 The matrix $F =$ instant of time \times given location. [*Bjornsson and Venegas, 1997*].

Following to this approach, each grid has been expanded into one-dimensional array (120x60=7200), and a matrix of 7200x4762 values has been created from the 4762 grids to be analyzed (grids from 2003 to 2016). Note that each grid corresponds to 23 h 56 min, so it results into 2x17 grids extra in the period 2003-2016. In addition, ascending and descending orbits have been concatenated to obtain a singular solution, so the final matrix becomes 7200x9524.

The covariance matrix $R=F^t F$ has been computed for the eigenvalue problem $RC=CA\Lambda$ [*Bjornsson and Venegas, 1997*], where Λ is a diagonal matrix containing the eigenvalues λ_i of R , and each c_i column of C are the eigenvectors of R corresponding to the eigenvalues λ_i . Each of these eigenvectors can be regarded as a map, and its contribution to the total variability is given by its corresponding eigenvalue. To see how each eigenvector evolves in time, the time-expansion PCA coefficients are calculated as the projections of the initial matrix on each eigenvector. Usually, the analysis is presented as dimensionless maps that are often normalized so that the highest value is ± 1 . To be adjusted, each spatial pattern is multiplied by the standard deviation of the corresponding temporal component. Therefore,

each spatial pattern is considered as an anomaly map with the same units as the original data, and each mode of variability is reconstructed by multiplying the spatial patterns with their corresponding temporal components (time-expansion PCA coefficients). Thus, by summing over only the main set of eigenvectors, noise can be greatly reduced and only physically significant signal remains in the compressed data set. For the purpose of this research, sub-daily variations are not investigated, and since all derived grid are equally affected by longitudinal and latitudinal variations, the resulting PCA components will follow the same pattern.

3. ACCELEROMETER CALIBRATION AND POD ASSESSMENT

This chapter provides a comprehensive study on differences between POE-based non-gravitational accelerations (Section 2.2.2) and accelerometer measurements. First section provides a brief report of the behavior of a disturbing sinusoidal signal found in the POD solution of GRACE and GOCE; the uncertainty of GRACE's POE-based non-gravitational accelerations is analyzed in the second section; the calibration of GRACE accelerometers, and an assessment of conservative force models and POE are presented in the two last sections.

3.1. Disturbing sinusoidal signal in GRACE's and GOCE's POD

After subtracting the standard time-varying gravity model from POE-based accelerations (Chapter 2), cross-track axes of both GRACE satellites seem to be affected by a periodic error of unknown source. The results for GRACE-A on July 15th, 2006 are shown in Figure 3.1, and the residuals in Figure 3.2.

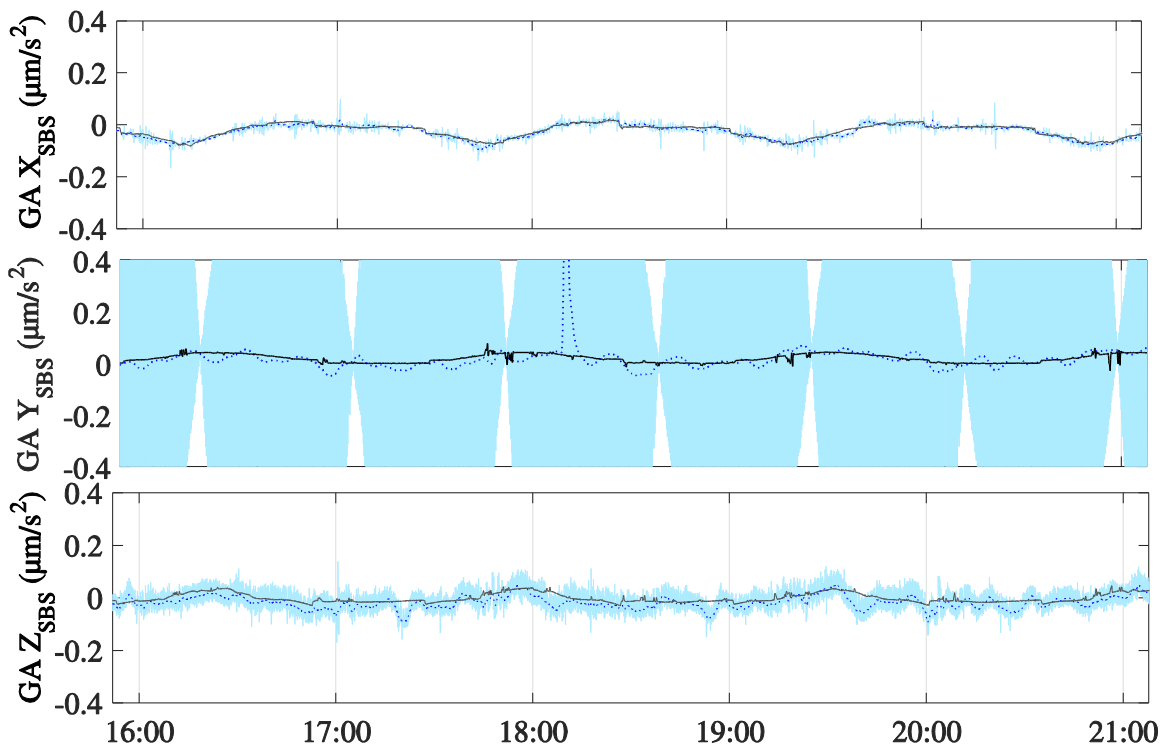


Figure 3.1 Accelerations of GRACE on July 15th, 2006. POE-based non-gravitational accelerations are in cyan and accelerometer measurements in black. Dotted blue line represents the smoothed POE-based non-gravitational accelerations corrected from systematic errors. [Calabia and Jin, 2016a, Fig.1].

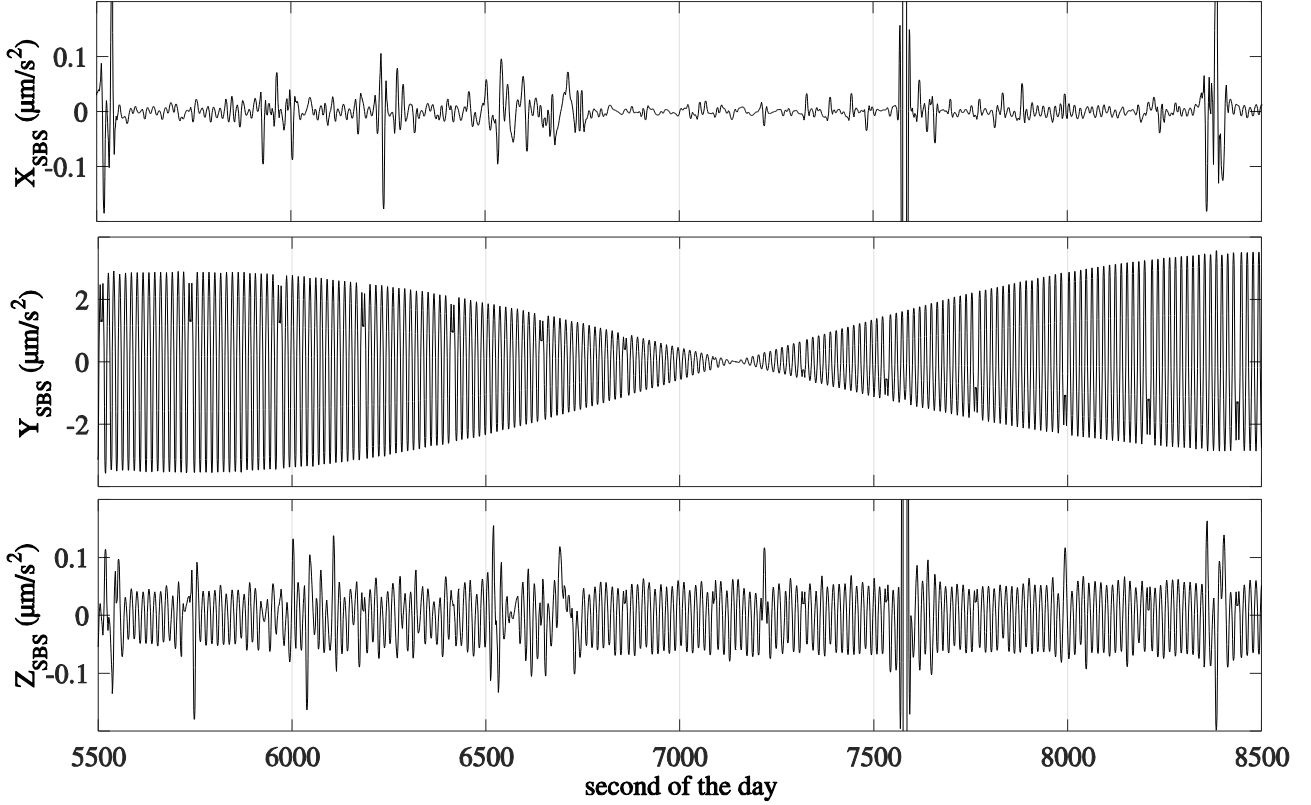


Figure 3.2 Residuals from Figure 3.1, after removing the systematic error on axis Y_{SBS} and smoothing the solution on axis Y_{SBS} . The periodic behavior of varying amplitude of Y_{SBS} can also be seen in [Bezděk \[2010, Figure 7\]](#). Results for both satellites are similar. Plots are not equally scaled. [[Calabia et al., 2015, Fig.1](#)].

With the finality of extracting the underlying information contained in the Y_{SBS} axis, the disturbing signal has been modeled and successfully subtracted by applying the sinusoidal robust fitting. The periodic behavior of its varying amplitude suggested the fitting of sinusoidal functions based on the robust least-squares regression analysis. The linear fitting M-estimator method Tukey's biweight (also known as bisquare) has been applied to avoid outliers. The idea is to recover the underlying signal by subtracting a sinusoidal function fitted on the envelope of the modulated amplitude. In the process, a first function regularizes the envelope of the modulated amplitude of which shape is approximated by an elaborated smoothing computed over the 5 s sampling solution. Then, a second function (the envelope of modulated amplitude) is approximated by subtracting smoothed POE-based non-gravitational accelerations from non-smoothed accelerations. The modulating envelope is approximated by absolute values multiplied by a ± 1 binary term, which is dependent on the positive or negative values of the first function.

Two daily functions $f_i = a \cdot \sin(bx + c)$, for $i = H, L$, have been fitted to the approximated results. Figure 3.3 shows the temporal behavior of the fitted parameters. In order to apply the corrections, the first function (f_L) is directly subtracted from the POE-based non-gravitational accelerations and converted into binary (± 1) function for the next step. Absolute values of the resulting data can be then multiplied by this binary function, while the second function (f_H) is removed. Since only sinusoidal functions are removed, the mean values of the resulting solution remains unchanged, and consequently the corresponding calibration parameters (Section 3.2).

Recovered amplitudes, phases and frequencies of this purely sinusoidal disturbing signal can be used in future studies as a constraints in the POD. Note that the frequency, amplitude and phase coincide with the magnitude of the orbital semi-major axis, inclination and inflexion points of eccentricity satellite orbit, respectively. The evolution of GRACE mean orbits can be found at the *University of Texas, Center for Space Research (UTCSR)* website (<http://www.csr.utexas.edu/grace/>).

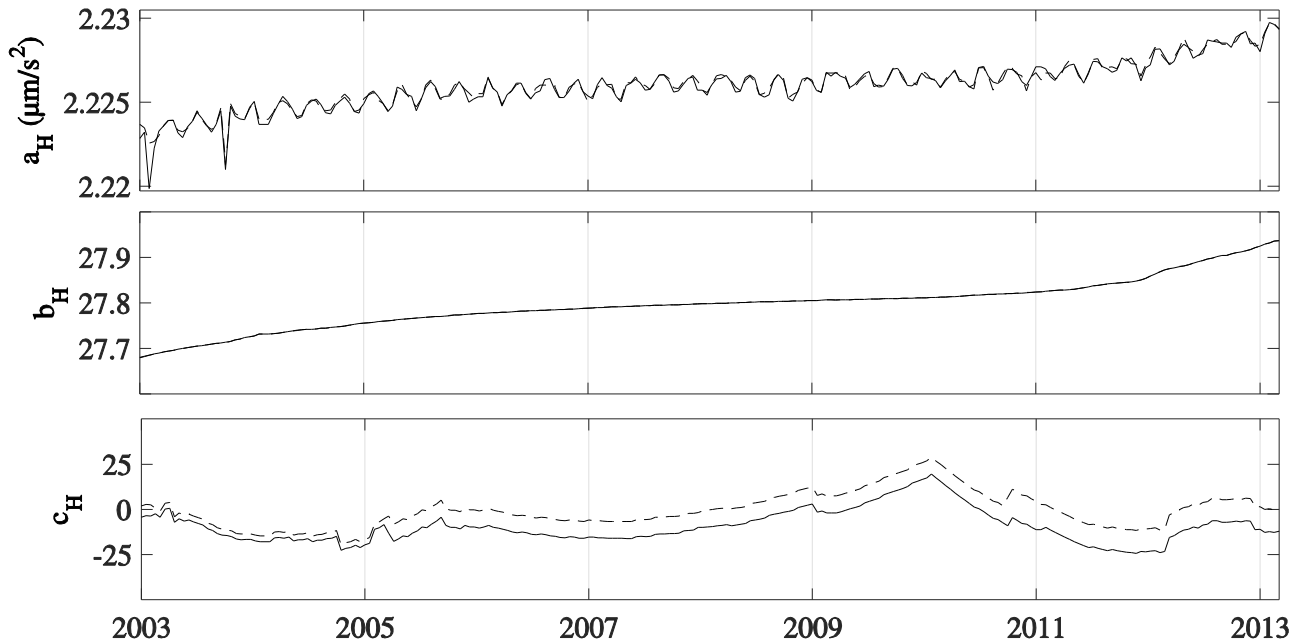


Figure 3.3 In dashed line for GRACE-A and solid line for GRACE-B, fitted parameters of the sinusoidal function f_H , which removes the systematic error on Y_{SBS} axes. Parameters of function f_L are not plotted because are similar, but with amplitude of $\sim 0.65 \mu\text{m/s}^2$. Here, $f_i = a \cdot \sin(bx + c)$, for $i = H, L$ and $x = (x' - \text{mean}(x')) / \text{std}(x')$ is the normalization by mean and standard deviation of $x' = \text{JD}(\text{UTC}) - 2.455\text{E}6$. [Calabia et al., 2015, Fig.2].

The following question is whether the systematic error found in the Y_{SBS} axis could be inherent to the generalized POD scheme, or could be related to only the GRACE mission. In order to answer this question, a similar analysis is performed for the GOCE mission. After subtracting the conservative force-model from GOCE's POE-based accelerations, a 1.5-hour periodic error of $1.5 \mu\text{m/s}^2$ amplitude maxima is present in all three axes. Figure 3.4 shows GOCE's POE-based non-gravitational accelerations with respect to calibrated accelerometer measurements. Although the GRACE's POD disturbing signal is bigger in magnitude, the results from GOCE are worse. Unfortunately, modeling or smoothing the GOCE's disturbing signal allocated little improvements, and no viable algorithm was able to recover any clear underlying information from the GOCE's POE-based non-gravitational accelerations. Maximum amplitudes of the disturbing signal for GRACE and GOCE are shown in Table 3.1. The fact that GOCE and GRACE missions have provided similar disturbing signal confirms the existence of a systematic error inherent to the generalized POD scheme (i.e., algorithms, propagator, etc.).

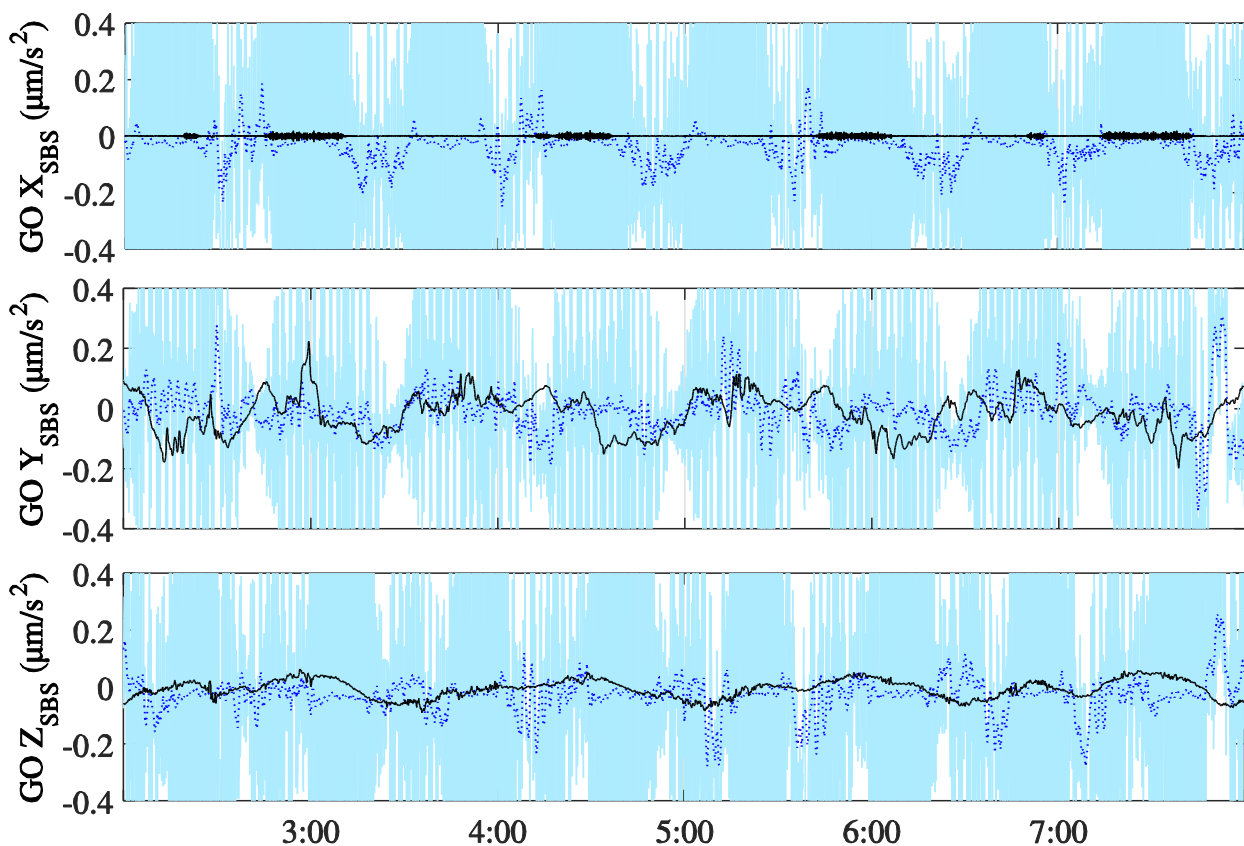


Figure 3.4 Accelerations of GOCE on February 15th, 2011. POE-based non-gravitational accelerations are in cyan line and accelerometer measurements in black line. Dotted blue line represents the smoothed POE-based non-gravitational accelerations. [Calabia and Jin, 2016a, Fig.2].

Table 3.1. Disturbing signal in POD. [*Calabia and Jin, 2016a, Table 2*].

Source	Details	Max. Amplitude (m/s ²)
GRACE POD	Systematic error in Z body-frame axes	5e-8
GRACE POD	Systematic error in Y body-frame axes	6e-6
GOCE POD	Systematic error in each of the body-frame axis	1.5e-6

3.2. Uncertainty of POE-based non-gravitational accelerations

The assessment of accuracy of GRACE's POE-based non-gravitational accelerations can be performed by using accurate accelerometer measurements as a reference. For instance, two different drag-conditions are pictured in Figure 3.5, showing accelerometer measurements in the SBS together with the POE-based non-gravitational accelerations on February 14th 2011, and April 13th 2012. Note that in the SBS, the X-axis is the long axis of symmetry of the satellite, pointing in the direction of the microwave horn, the Y-axis is the vertical axis of symmetry, and the Z-axis completes the right-handed coordinate system. In this figure, it can be seen that non-gravitational accelerations in April 2012 have larger amplitudes than those in February 2011. Though, the differences between accelerometer measurements and POE-estimates show no dependence on the background density.

Middle panels of Figure 3.5, the Y_{SBS} and Z_{SBS} components show relatively strong short-term deviations with respect to accelerometer measurements (note that Y_{SBS} and Z_{SBS} panels are not equally scaled with respect to X_{SBS} panels). For the Y-axis, deviations are mostly related to errors in the horizontal-wind model and those included by the POD process (e.g., sinusoidal disturbing signal found in previous section). For the Z-axis, the short-term variations can be mostly attributed to errors in the gravitational and irradiative force-models. A further study on these short-term deviations for the Z-axis can be found in Section 3.4. Bottom of Figure 3.5 shows the corresponding densities inferred from accelerometer measurements and from POE estimates, together with the NRLMSISE00 empirical model. Note that inferred densities are mostly dependent on the along-track direction. In the bottom panels of Figure 3.5, the POE-based mass densities show good agreement with the accelerometer-based densities, and are more similar in amplitude and shape than the NRLMSISE00 empirical model. A more complete uncertainty analysis for this new generated density dataset is provided in next chapter.

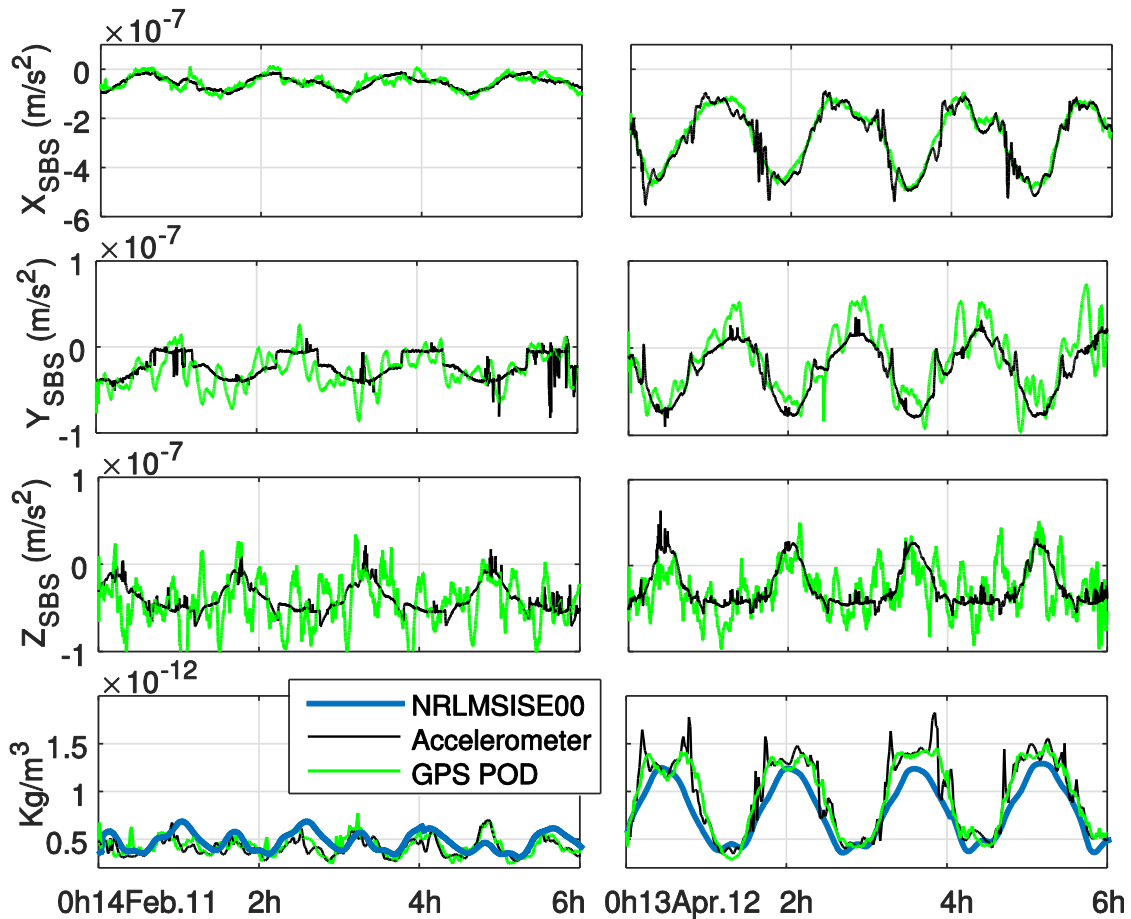


Figure 3.5 Non-gravitational accelerations (three superior panels) and thermospheric mass densities normalized to 475km (bottom) along GRACE’s orbital path, February 14th 2011 on the left panels and April 13th 2012 on the right panels. Calibrated accelerometer measurements are in black, and the estimations from GPS POE are represented in green. In the bottom panel, the NRLMSISE00 model estimations are shown in blue thick line. [Calabria and Jin, 2017, Fig.1].

Figure 3.6 shows Pearson's linear correlation coefficients and the standard deviations (SD) for each SBS-axis of daily GPS POE non-gravitational accelerations with respect to accelerometer measurements. The correlation coefficients for the X_{SBS} , Y_{SBS} , and Z_{SBS} axes have mean values of 97 %, 58 %, and 36 % respectively. A clear periodicity of 165 day suggests dependence on the LST, increasing the correlation when the satellite’s orbit plane is aligned with the Earth-Sun line (i.e., the day-night variation increases the correlation). The bottom panel in Figure 3.6 shows that the SD of the differences between accelerometer measurements and GPS POE-estimates increases its value from 20-30 nm/s^2 in 2011 to 40-50 nm/s^2 in 2015. This phenomenon might be caused by the orbital decay.

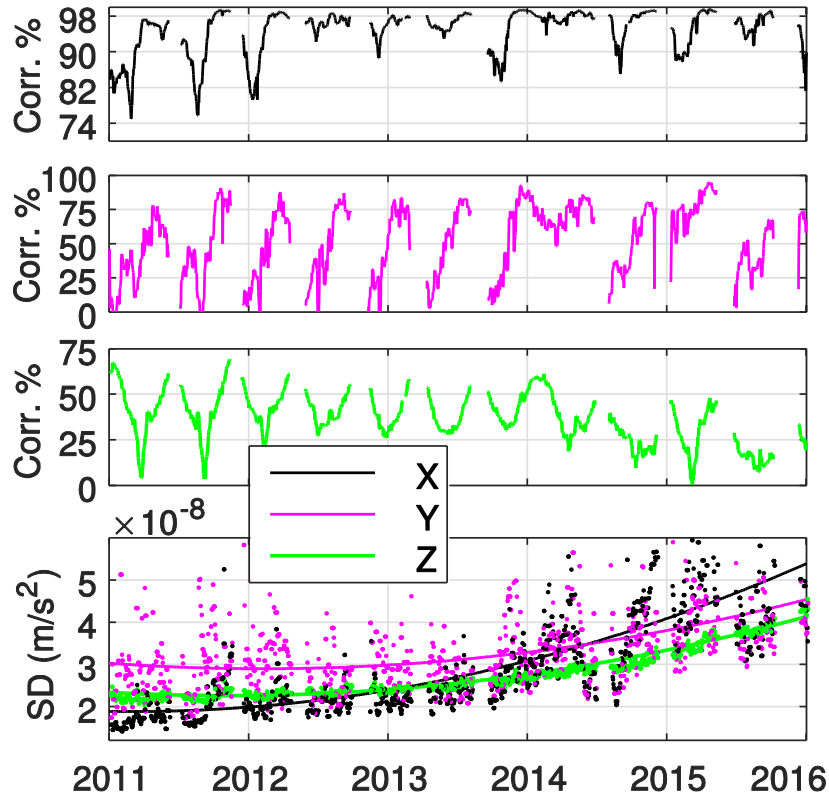


Figure 3.6 From top to bottom, correlation for each of the three axes in the SBS, and SD (including fitted trend) of daily POE non-gravitational accelerations (with respect to accelerometer measurements). [Calabia and Jin, 2017, Fig.4].

3.3. Calibration of GRACE accelerometers

The principle of a satellite accelerometer is based on measuring the force needed to keep a proof of mass accurately at the spacecraft's center of mass, where the gravity is exactly compensated by the centrifugal force. Plus and minus drive voltages are applied to electrodes with respect to opposite sides of the proof mass, whose electrical potential is maintained at a *dc* biasing voltage. Unfortunately, this *dc* level is the source of bias and bias fluctuations of the most electrostatic space accelerometers.

Since accelerations can be derived from a numerical differentiation along precise orbits, the acceleration approach for accelerometer calibration aims on comparing the standard accelerations with the accelerometer readouts added to the time-varying gravity model. In this section, 10-year (2003 to 2013) of biases between GRACE's POE-based non-gravitational accelerations and accelerometer outputs are calculated by simple differences from daily-median-averaged values. Scale parameters are assumed to be equal to unit. Polynomial fit of the resulting biases are summarized in Table 3.2, and graphically

represented in Figure 3.7, with respect to the solution of *Bettadpur [2009]*. Calibration parameters from *Bruinsma et al. [2007]* and *Bezděk [2010]* are also included in Figure 3.7 for comparison. For these last parameters, a pre-processing was needed to synchronize dates, remove outlines and interpolate data gaps.

In Figure 3.7, the biases in the X_{SBS} axes are in agreement with *Bruinsma et al. [2007]*, while the solutions are smoother than those of *Bezděk [2010]*. On the other hand, Y_{SBS} and Z_{SBS} biases better follow the solutions of *Bezděk [2010]*. For the biases in the Z_{SBS} axes, since the nature of circular orbits implies a constant behavior of the arc-to-chord error, the real magnitude (bigger) of radial accelerations seems to cause a constant bias (~ 20 nm) to the solutions of *Bezděk [2010]* and *Bettadpur [2009]*. In general terms, the results show that calibration parameters of *Bruinsma et al. [2007]* and *Bezděk [2010]* are worse for the Y_{SBS} and X_{SBS} axes, respectively. The difference with respect to the solutions of *Bruinsma et al. [2007]* for Z_{SBS} axes shows a clear systematic error in the solution.

In Figure 3.7, it is interesting to see that since electrostatic accelerometers are sensible to temperature changes, the correlation between Y_{SBS} biases and the β' angle (angle between the Earth-Sun line and the orbit plane) is clearly recognized. Note here that the β' angle is defined such that it is zero when the Sun is within the orbit plane and, consequently, the perturbation of Y_{SBS} biases is minimized. The opposite situation happens maximum β' angle, in which the solar radiation has the same direction as the Y_{SBS} axes, and maximizes its bias perturbation. These variations are disregarded in the polynomial fitting given in Table 3.2, being this solution a more close approximation to values of β' angle zero than the real β' angle value. The evolution of β' angle values can be seen at the UTCSR website.

Biases can be differenced in four separate data spans, as shown in Table 3.2. For X_{SBS} and Y_{SBS} axes of both GRACE satellites, the changes of bias are clearly defined when satellite positions were swapped on December of 2005, and from possible maneuvers at the end of mission on July 2010 and April 2011. As seen in both GRACE-A and GRACE-B satellites, the Z_{SBS} axes were not affected from swapping positions, but instead there is a change at common dates on January in 2004 and 2011. During the middle-end mission, Z_{SBS} biases jumped on December 2009 for GRACE-A and April 2010 for GRACE-B. All these approximate dates are seen in MJD format in Table 3.2.

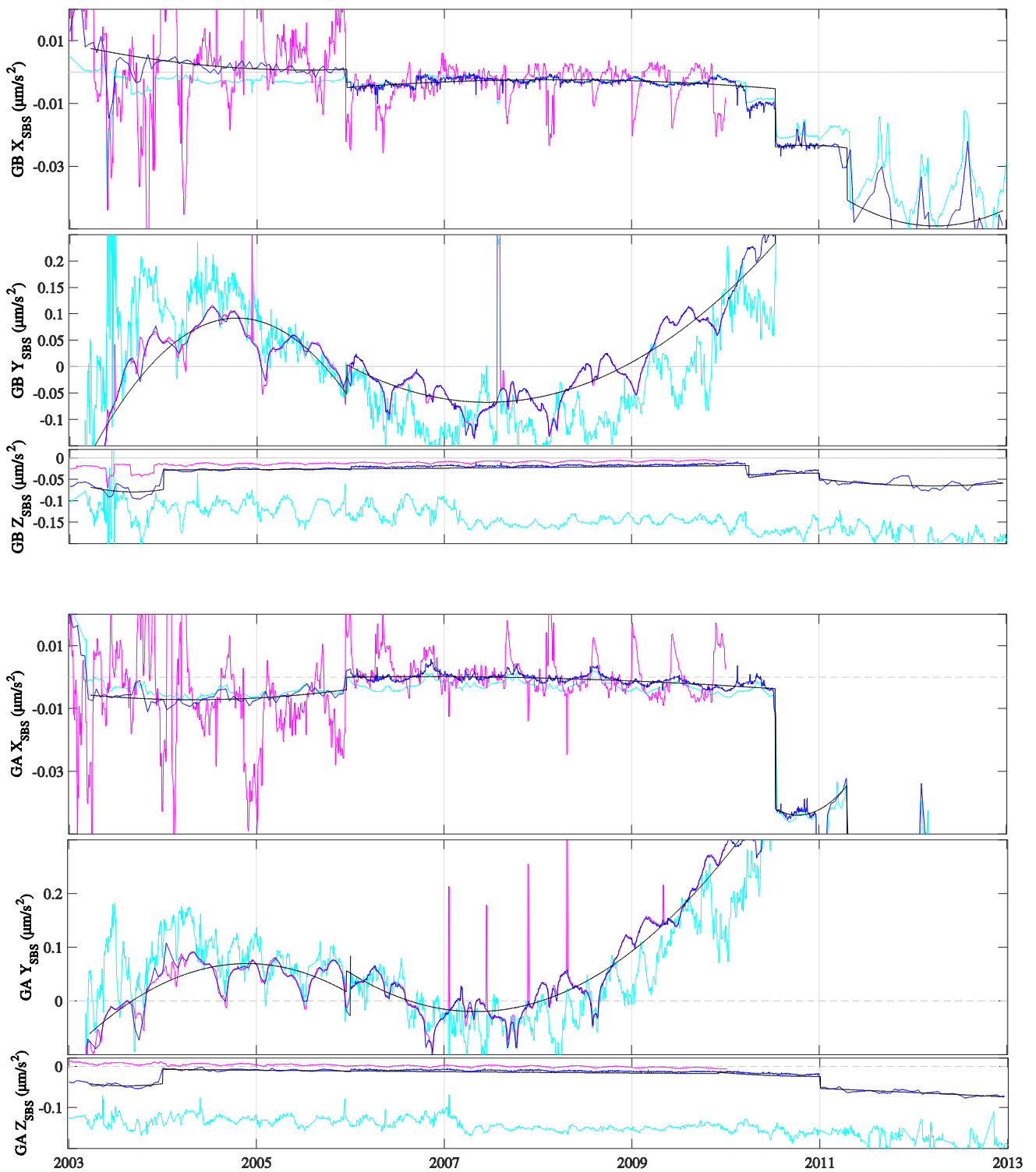


Figure 3.7 Differences of GRACE's accelerometer biases with respect to *Bettadpur [2009]*: results from *Bruinsma et al. [2007]* are shown in cyan, from *Bezdek [2010]* in magenta, and this study in blue color. Fitted polynomial functions (Table 3.2) are in black color. Plots are not equally scaled. [*Calabia et al., 2015, Fig. 4*].

Table 3.2 Parameters for bias calibration of GRACE accelerometers. [Calabia et al., 2015].

Axis		Time span in MJD(UTC)			
		52720-53720	53720-55390	55390-55670	55670-56276
X _{SBS} GA	a	1.8661E-10	7.6744E-11	2.6610E-09	-2.1745E-09
	b	3.7589E-09	-1.2267E-09	3.4110E-09	2.0266E-08
	c	-1.2067E-06	-1.2572E-06	-1.2949E-06	-1.3772E-06
X _{SBS} GB	a	1.3180E-10	-3.6244E-12	-3.1007E-10	7.3652E-10
	b	3.1492E-09	-1.5015E-09	-1.0071E-09	-7.1242E-09
	c	-5.9029E-07	-6.3587E-07	-6.5277E-07	-6.6374E-07
Y _{SBS} GA	a	-7.3899E-09	-8.6972E-10	-3.6298E-08	2.1178E-08
	b	-2.3187E-07	4.1156E-09	-6.5976E-08	-2.1715E-07
	c	2.7577E-05	2.9751E-05	3.0619E-05	3.2154E-05
Y _{SBS} GB	a	-1.2166E-08	-1.9175E-09	2.4402E-08	2.7737E-08
	b	-3.9671E-07	2.0905E-08	4.5169E-08	-2.3808E-07
	c	7.4314E-06	1.1700E-05	1.2362E-05	1.3520E-05
Axis		Time span in MJD(UTC)			
		52720-53005	53005-55166	55166-55562	55562-56276
Z _{SBS} GA	a	2.5641E-09	4.1747E-11	6.9776E-10	-7.2715E-12
	b	1.3726E-07	7.7995E-10	1.1175E-09	-1.3730E-09
	c	1.2378E-06	-5.6749E-07	-5.7292E-07	-6.0213E-07
Axis		Time span in MJD(UTC)			
		52720-53005	53005-55287	55287-55562	55562-56276
Z _{SBS} GB	a	3.9394E-09	-5.8487E-11	-1.9218E-09	7.5564E-10
	b	2.1614E-07	3.0758E-09	1.3300E-09	-4.9383E-09
	c	2.0507E-06	-7.3738E-07	-7.5710E-07	-7.7023E-07

$$\text{Equation: } bias = ax^2 + bx + c, \text{ where } x = (\text{MJD}(UTC) - 55555)/100.$$

3.4. Assessment of conservative force models

For most of LEO missions, the accuracy of the force-models used as input in the dynamic and the reduced-dynamic POD is not comparable to that required in satellite gravimetry or altimetry, and the TVG usually is simplified into the static gravity field model. For the other missions, however, current modelling still fails in an accurate and real-time functional (pre-processing independency) TVG analytical model. During the last decades, many studies have examined the ocean-tide models errors by differencing hydrodynamic models (e.g. tide gauges and acoustic tomography) or by running Monte Carlo analyses with inverse models (e.g., Ray et al. [2001]; Knudsen & Andersen [2002]). Other studies have also investigated the sensitivity to different TVG models by evaluating absolute values of root-mean-square fits of observations on satellite orbital arcs (e.g., Couhert et al. [2015]; Melachroinos et al. [2014]; Rudenko et al. [2014]; Zelensky et al. [2014]; Lemoine et al. [2010]). Despite SLR,

DORIS, or altimeter measurements have proven to be of practical benefit in the previous studies, little attention has been paid to the differences to accelerometer measurements.

This section analyzes and assesses the conservative-force anomalies derived from analytical TVG models, accurate orbit solutions, and accelerometer measurements. On the one hand, accurate accelerometers measure the force needed to keep a proof mass exactly at the spacecraft's center of mass, where the gravity is exactly compensated by the centrifugal force. On the other hand, modeled time-varying forces of gravitational origin are subtracted from precise orbit accelerations to obtain POE-based non-gravitational accelerations. Thus, the differences between the measured and the POE-based non-gravitational accelerations can provide an assessment about the error committed in the POD scheme.

Aside the good agreement between GRACE's accelerometer measurements and GPS POE-estimates seen in previous sections, interesting local discrepancies can be identified. For instance, Figure 3.8 (zoom for X_{SBS} and Z_{SBS} axes from Figure 3.1) shows a clear anomaly of $\sim 0.1 \mu\text{m/s}^2$ in the Z_{SBS} axis at 19:40 h February 15th, 2011. In the X_{SBS} axis, the model first overestimates the accelerometer measurements at 19:35 h, and then underestimates the measured acceleration at 19:45 h. Note that the overestimation of the model in the Z_{SBS} axis reaches a maximum value when the satellite is the vertical of the anomaly (19:45 h), and consequently the differences in the X_{SBS} axis is zero. These discrepancies are attributed to variations not included in the model such as local tides, post-glacial rebound or hydrological cycles. In the following paragraphs, the local discrepancies between accelerometer measurements and GPS POE-estimates of GRACE are investigated in space and time. The results will assess the future modeling of forces acting on LEO satellites.

Due to the difficulty in retrieving GOCE's POE-based non-gravitational accelerations, the analysis is only performed for GRACE. Since the differences between accelerometer and the POD solution are mainly reflected in the radial direction, only the differences in the Z_{SBS} axis are analyzed.

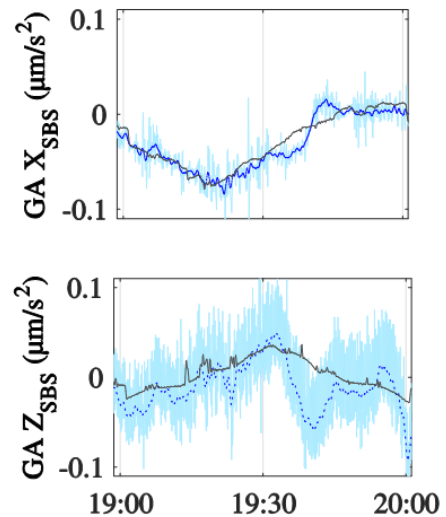


Figure 3.8 An anomaly at 19:40 h February 15th, 2011. Zoom for X_{SBS} and Z_{SBS} from Figure 3.1.

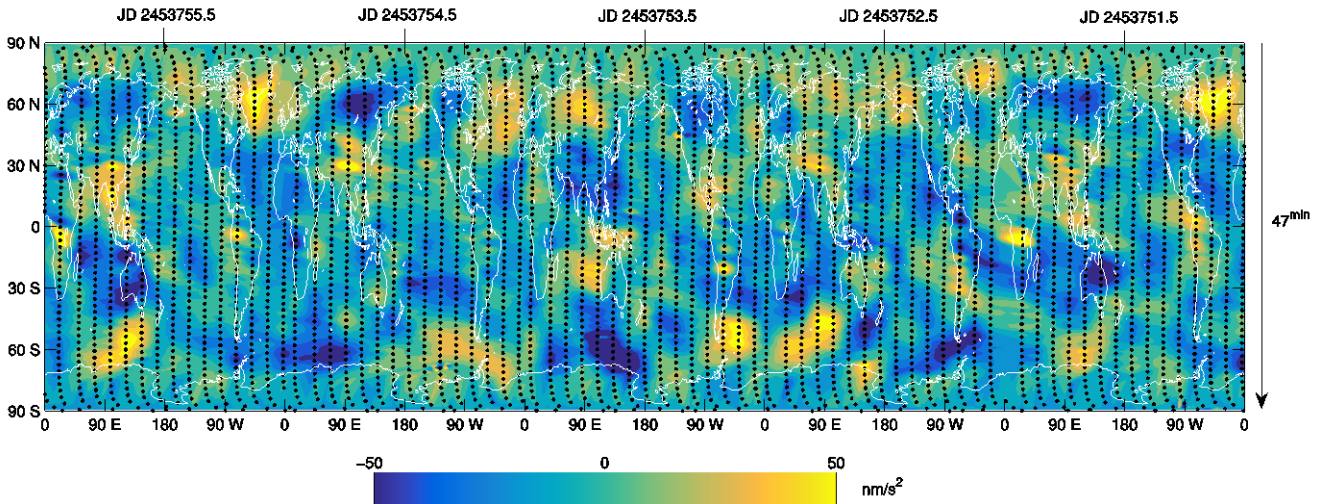


Figure 3.9 Interpolation of GRACE’s differences along orbits between accelerometer and POE-based accelerations in the Z_{SBS} axis from January 16th to 19th 2006. Julian Date (JD) is represented on top of figure. Dotted line represents the satellite trajectory at 50 s interval. [Calabia and Jin, 2016a, Fig. 3].

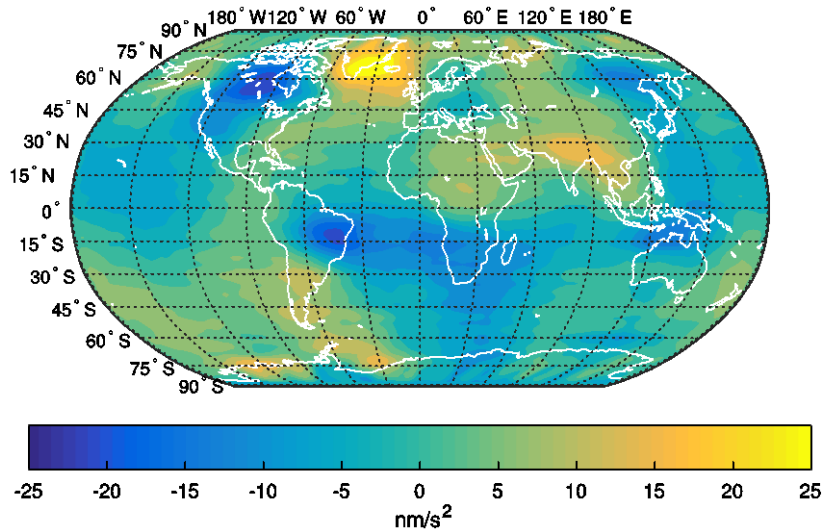


Figure 3.10 Mean value of the differences (2006 to 2009) between the POE-based non-gravitational accelerations and the accelerometer measurements of GRACE for the Z_{SBS} axis. [Calabia and Jin, 2016a, Fig. 4].

In Figure 3.9, a short time-series of interpolated differences between the conservative force-model and the accelerometer measurements in the Z_{SBS} axis is shown as example. In this figure, GRACE’s descending orbits from January 16th to 19th 2006 are plotted in dotted line. The time variation is defined from right to left as the equatorial orbit shift precesses westwards, and from North to South (74 min) as only descending orbits are represented. Figure 3.9 clearly shows that all anomalies are correlated between continuous orbits. With

amplitudes maxima of 50 nm/s^2 (negative at Canada and Brazil and positive at Greenland) the mean-value map of 4-year (2006-2009) of measurements is pictured in Figure 3.10.

Furthermore, the PCA is implemented for the spatiotemporal data analysis of consecutive grids of differences as detailed in previous chapter. The resulting two first pair of PCA components shows amplitudes maxima of 80 nm/s^2 and 50 nm/s^2 (Figures 3.11 and 3.12). The four leading eigenvectors together account for 74 % of the total variance and, individually, explain 31 %, 22 %, 11 % and 9 % of the variance. Maximum amplitudes and percentage of the explained variances are shown in Table 8. Unfortunately, their corresponding time-expansion PCA coefficients allocate too low resolution to define periodicities. LST variations seem to be related to variations caused by reduction of mass produced by the expansion of atmospheric layers under solar heating. The use of an atmospheric tide model, as for example, *Biancale and Bode [2006]*, is strongly recommended for future research.

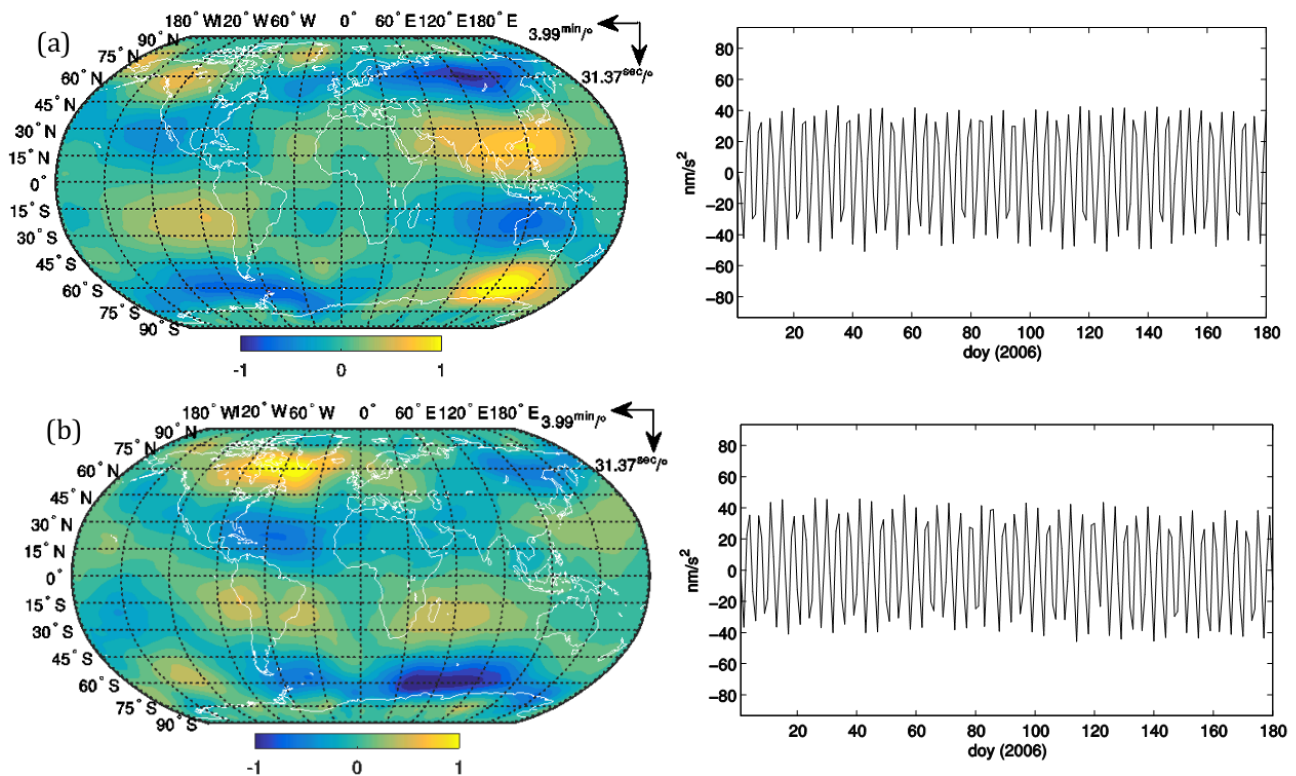


Figure 3.11 First (top) and second (bottom) PCA components for the variability of the differences between the POE-based non-gravitational accelerations and the accelerometer measurements (GRACE Z_{SBS} axis, descending orbits, 2006 to 2009). Respectively, 31 % and 22 % of the variability explained. Maps are time-variable in latitude ($31,37 \text{ sec}$ per southward degree) and longitude ($3,99 \text{ min}$ per westward degree). Time-expansion PCA coefficients only shows half year of 2006 (similar results for the other years). [*Calabia and Jin, 2016a, Fig. 5*].

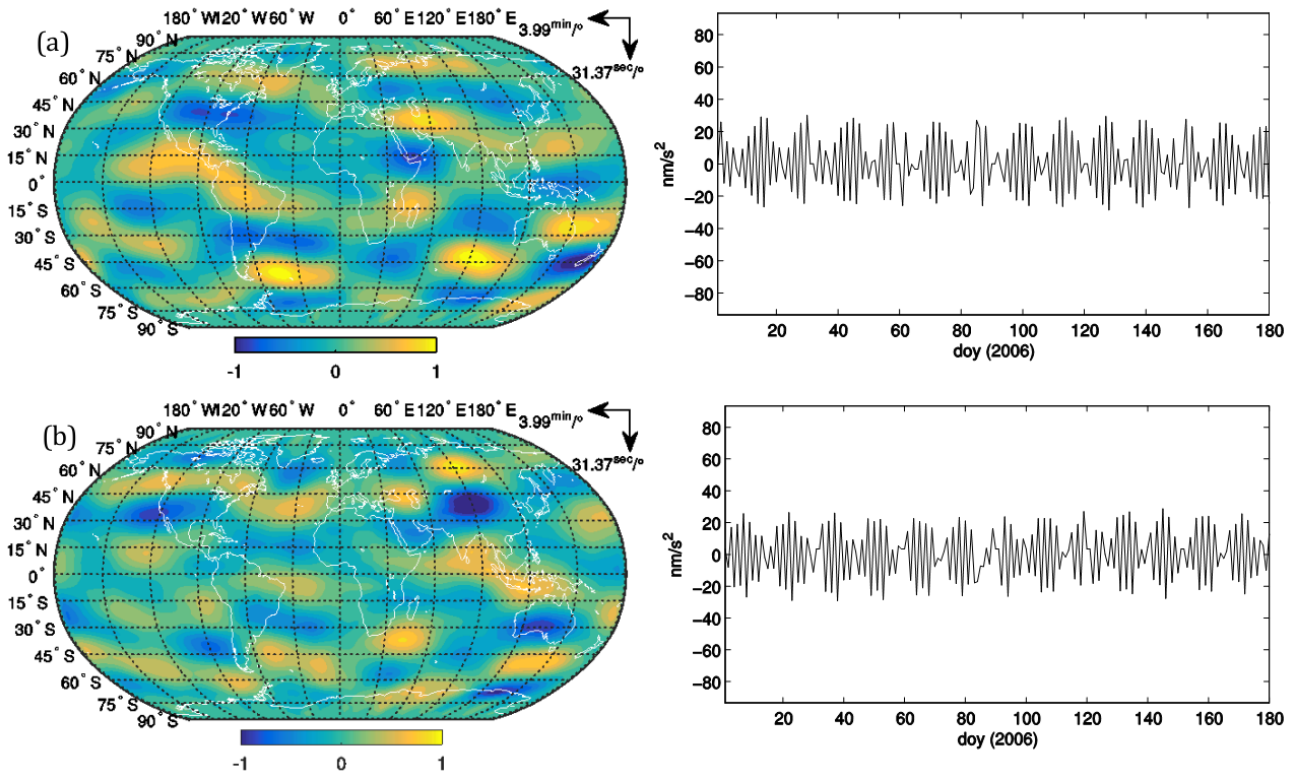


Figure 3.12 Same as Figure 3.11 but for the third (top) and fourth (bottom) PCA components. [Calabia and Jin, 2016a, Fig. 6].

Concerning the long-term anomalies, the fifth PCA component (Figure 3.13a) reveals a clear latitudinal variation of 15 nm/s^2 amplitude maxima. This mode is strongly correlated to the eclipse times. Note that the amplitude follows the orbital β' angle variation (angle between the Earth–Sun line and the orbit plane). The evolution of β' angle values can be seen at the right panel of Figure 3.13a, where 0° corresponds to alternative midnight and noon times. In this panel, it is clearly seen that descending orbits on February, 2006, e.g., the satellite at noon is affected by a positive force of 10 nm/s^2 in the southern hemisphere, and negative in the northern hemisphere. On the contrary, at midnight (e.g. on June, 2006), the satellite is affected by a negative force of 5 nm/s^2 in the southern hemisphere, and positive in the northern hemisphere. Similar results are given from ascending orbits data. In the following panels (Figures 3.13b to 3.13d), the PCA components are obtained from a monthly-average combination of ascending and descending orbits. The technique of monthly-average combination aims to cancel the binary behavior of the first 4 modes shown in Figures 3.11 and 3.12. Figure 3.13b shows a trend of $3 \text{ nm/s}^2\text{yr}$ in the Indian Ocean, which might be related to internal geophysical processes. The remaining components (Figure 3.13c and 3.13d) might be attributed to geodynamical and hydrological processes, as for example,

tectonic processes of California, Japan and Indonesia. The use of a bigger sampling interval and the use of ascending and descending data for the analysis of variations in shorter time-scales is suggested future research.

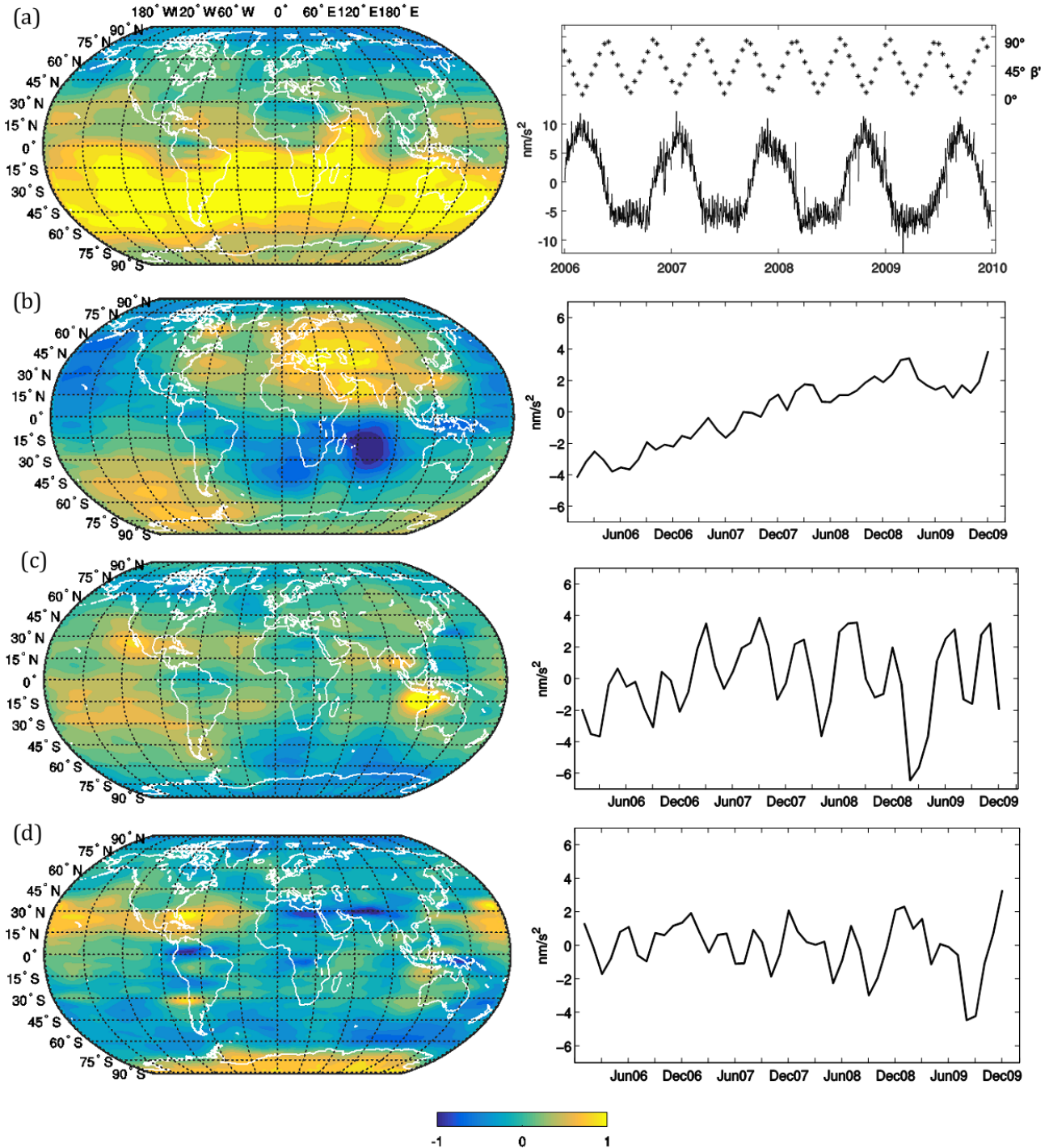


Figure 3.13 Long-term variations of the differences between the POE-based non-gravitational accelerations and the accelerometer measurements (GRACE Z_{SBS} axis, 2006 to 2009, descending orbits PCA5 for (a) and combined solution for (b), (c) and (d)). Right panel in (a) includes the evolution of β' angle values. [Calabia and Jin, 2016a, Fig. 7].

Table 3.3 Variance and amplitudes of mean and PCAs shown in Figures 3.10 to 3.13a.[*Calabia and Jin, 2016a, Table 3*].

Component	% variance explained	Max. Ampl. (m/s ²)
Mean	-	5e-8
PCA1	31 %	8e-8
PCA2	22 %	8e-8
PCA3	11 %	5e-8
PCA4	9 %	5e-8
PCA5	5 %	1.5e-8

3.5. Summary

In this chapter, the first derivatives of precise-orbit velocities of GRACE and GOCE missions have been computed through the a-priori arc-to-chord threshold plus the subtraction of the time-varying gravity model [*Calabia and Jin, 2015*]. The main results are then summarized:

- A new methodology is proposed to derive non-gravitational accelerations. The method does not require a POD scheme, and serves as a reliable reference with unbiased solution for accelerometer calibration. Calibration parameters for GRACE accelerometers have been modelled with lineal functions through least squares robust fitting and are presented in Table 3.2.
- After subtracting the modelled time-varying gravity forces from the POE-based accelerations, cross-track axes of both GRACE satellites have shown to be affected by a periodic error of unknown source. For the GOCE mission, the periodic error is present in all three axes and with similar amplitudes and frequencies. Therefore, it is to assume these systematic errors are inherent to the generalized POD scheme, and not caused by errors related to a specific mission. With the purpose of extracting the underlying information from the resulting POE-based non-gravitational accelerations, the systematic error of GRACE is modelled and subtracted successfully. Unfortunately, no viable algorithm has been able to recover any clear underlying information in GOCE's POE-based non-gravitational accelerations.

- The differences between accelerometer measurements and POE-estimates for the GRACE mission shows a Pearson's correlation of 97 %, 58 %, and 36 % for the X_{SBS} , Y_{SBS} , and Z_{SBS} axes respectively, with SD mean values from 20-30 nm/s^2 in 2011 up to 40-50 nm/s^2 in 2015, probably related to the orbital decay.
- In addition, the conservative-force anomalies derived from analytical TVG models, accurate orbit solutions, and accelerometer measurements can be analyzed in space and time through the PCA technique. The results shown in this chapter reveal intriguing structures at the sub-daily frequency. The use of an atmospheric tide model, as for example, *Biancale and Bode [2006]*, is strongly recommended for future research. Long-term anomalies show a clear latitudinal variation of 15 nm/s^2 amplitude maxima correlated to the eclipse times, and further residuals seem to be related to geodynamical and hydrological processes.

4. THERMOSPHERIC NEUTRAL DENSITY ESTIMATES FROM GRACE

4.1. Neutral density estimates from GRACE accelerometers

In order to assess the uncertainty of the new generated accelerometer-based neutral density dataset, this section aims to provide a brief statistical comparison with respect to Sutton's density derivation [Sutton, 2011], as well as to neutral densities estimated with the NRLMSISE-00 empirical model. The estimates from NRLMSISE-00 have been calculated along the satellite orbit at the same times as the accelerometer measurements. The estimates of Sutton [2011] are the solution of Sentman [1961] drag-coefficient formulas, which include the thermal drag effect (phenomenon that increases the coefficient of drag for long satellites). Density estimations derived from Sutton [2011] have been downloaded from the University of Colorado at Boulder website (<http://sisko.colorado.edu/sutton/data/ver2.2/>), and have been normalized to 475 km using the NRLMSISE-00 model following the indications of Rentz and Lühr [2008], which are based in Equation (2.40).

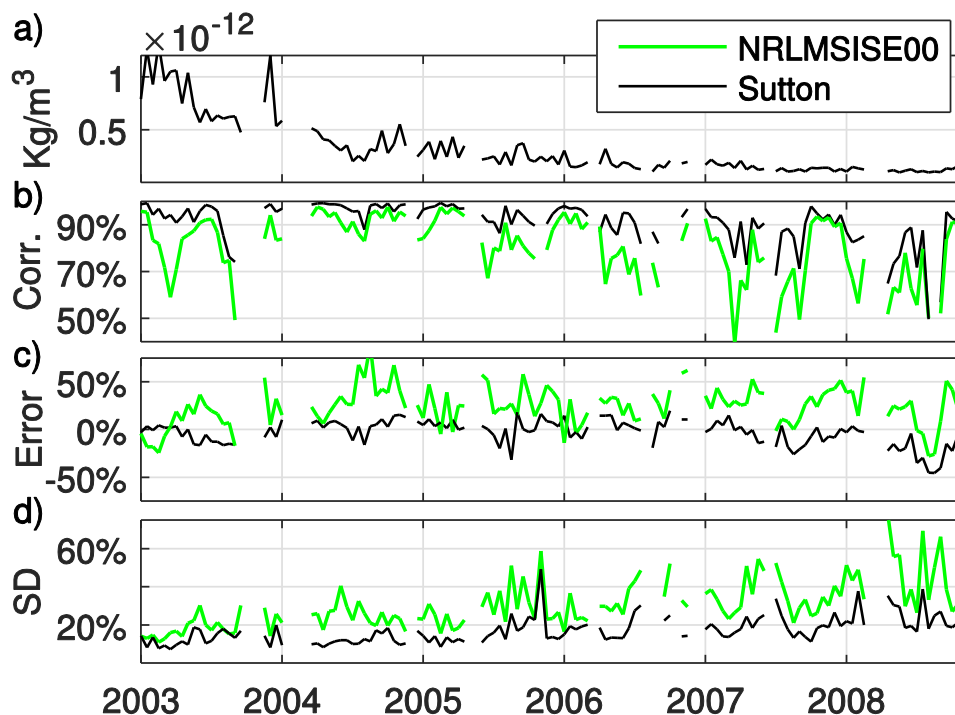


Figure 4.1 Statistical comparisons of neutral density estimates with respect to the derivations of Sutton [2011], in black, and with respect the NRLMSISE-00 empirical model, in green. From top to bottom, (a) background density, (b) correlation coefficients, (c) relative error, and (d) relative SD. [Calabia and Jin, 2016b, Fig. 1].

Statistical comparisons of the new density estimates are presented in Figure 4.1, showing correlation coefficients, relative error (with respect to the background density), and relative SD every 15 day from 2003 to 2009. Note that these statistics are strongly dependent on the satellite's LST as well as solar-flux conditions, i.e., satellite positions at around 6 / 18 h LST, as well as low values in the background density, will influence negatively in the relative statistics. Figure 4.1b shows that densities of Sutton [2011] have 10 % better correlation to the new estimates than the estimates computed with the NRLMSISE-00 model. The mean value of correlation for Sutton's estimates is 94 %, and for the NRLMSISE-00 model 84 %. On Figure 4.1c, while the mean difference with respect to estimates of Sutton [2011] is centered at zero, the NRLMSISE-00 estimates are positively deviated in 25 % (relative to the background density).

Concerning the relative SD with respect to the background density, Figure 4.1d shows that the differences to the estimates of Sutton has a mean value of 16 %, while the differences to the NRLMSISE-00 has a mean value of 27 %.

Plotted in geographical coordinates, Figure 4.2 shows the relative differences between the new GRACE measurements and the NRLMSISE-00 model during the period 2003-2016. In Figure 4.2a, the median average of relative differences (i.e. $(\text{NRLMSISE00-GRACE})/\text{GRACE}$) shows a mean global overestimation of 0.15. The overestimation is less pronounced at the northern polar

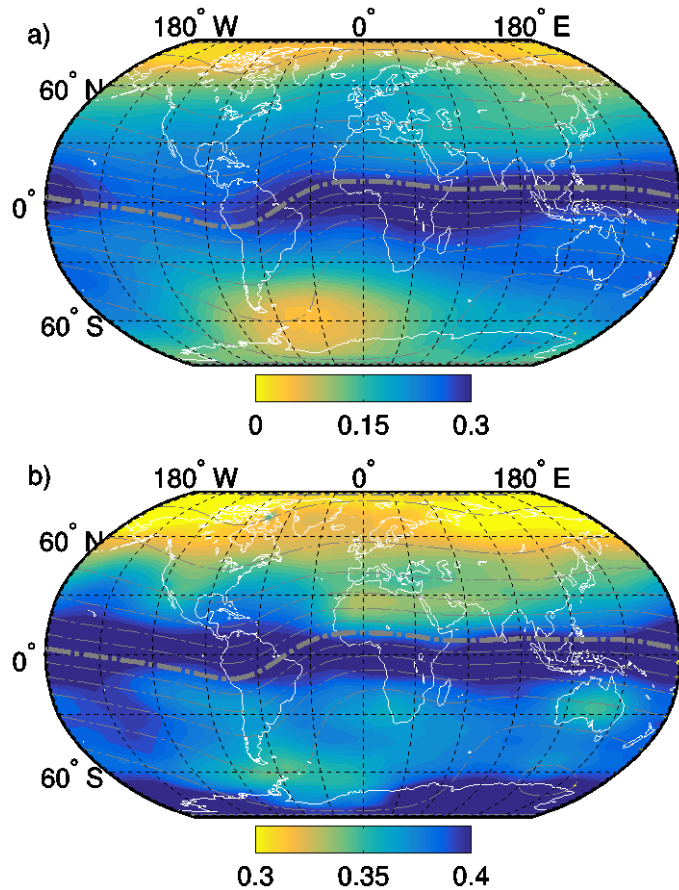


Figure 4.2 Median average (a) and SD (b) of relative differences between the MSIS and the GRACE density estimates, i.e. $(\text{MSIS} - \text{GRACE})/\text{GRACE}$. Dip isoclinic lines are plotted in dash-dot gray format. Values are dimensionless. [Calabia and Jin, 2016b, Fig. 2].

cap and at the Cape Horn region, but more prominent at the equator with a value of about 0.3. The SD of relative differences is presented in Figure 4.2b, with a mean value of 0.3. Marked peaks (~ 0.4) are pictured at the southern polar region and along the equator, and lower values (~ 0.3) are pictured at the northern polar region.

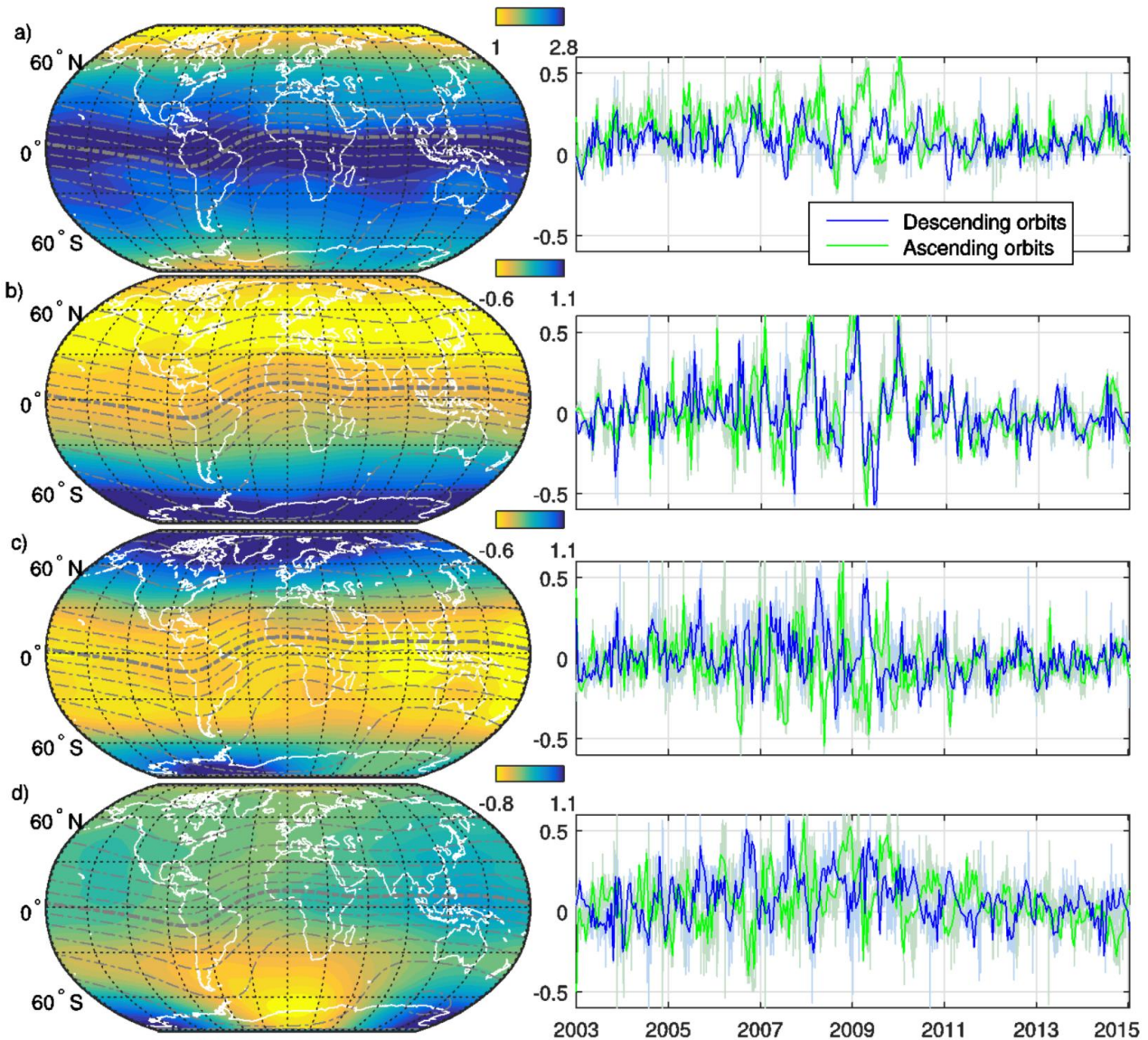


Figure 4.3 First fourth PCA components of the relative differences between accelerometer-based densities and the NRLMSISE00 model, i.e. $(\text{NRLMSISE00} - \text{GRACE}) / \text{GRACE}$. The explained variability amounts to 65.5 %, 9 %, 6 %, and 2 %, respectively from (a) to (d). Dip isoclinic lines are plotted in dash-dot format. Values are dimensionless.

Figure 4.3 shows the PCA of the relative differences between accelerometer-based densities and the NRLMSISE00 model during the period 2003-2015, i.e. $(\text{NRLMSISE00} - \text{GRACE}) / \text{GRACE}$. The four leading eigenvectors together account for 82 % of the total

variance and, individually, explain 65.5 %, 9 %, 6 %, and 2 % of the total variability. The high percentage for the first component (Figure 4.3a) indicates marked patterns of variability, with a mean relative overestimation of about 0.3 at the equator, and about 0.15 at high latitudes (note that a queried value on the map must be multiplied by its corresponding value on the time-expansion series). During the period of low solar activity (2006 to 2010), Figures 4.3a, 4.3c, and 4.3d clearly show a periodic opposite variation between ascending and descending orbits. The period of these variations is recognized as the GRACE's precession rate (~322 day). Figure 4.3c represents a latitudinal variation in the curvature of the global density distribution, and Figure 4.3d pictures a southern-cusp pattern. The clear alignment with the southern dip-pole suggests a miss-modeled contribution from the coupled MIT system, but a further study to relate space weather, geomagnetic indices and thermospheric densities is required. On the other side, having an identical phase for both ascending and descending orbits, the second time-expansion PCA component (Figure 4.3b) is recognized as an annual variation, with maxima amplitude (~0.5) during low solar activity (2006 to 2010).

4.2. Neutral density estimates from POE of GRACE

In the recent years, several studies have shown that non-gravitational accelerations, and derived neutral densities, can be estimated through POD (e.g., [Siemes et al. \[2016\]](#); [Ijssel \[2014\]](#); [Doornbos et al. \[2014b\]](#); [Visser et al. \[2013\]](#); [McLaughlin et al. \[2013\]](#); [Kuang et al. \[2014\]](#); [Ijssel and Visser \[2005\]](#)). However, the use of POD least-squares estimators to derive non-gravitational accelerations and density estimates can become a complex task, and numerical differentiation of POE could simplify the process. This dissertation proves that non-gravitational accelerations can be derived from numerical differentiation of POE, and these used to derive thermospheric neutral density estimates.

In this work, thermospheric mass densities along GRACE's orbital paths are estimated for the period 2011-2016 through numerical differentiation of POE. Figure 4.4 shows a clear example for two different drag-conditions, February 14th 2011 and April 13th 2012. As commented in Section 3.2, densities in April 2012 have larger amplitudes than in February 2011, but the differences between accelerometer measurements and POE-estimates seem not to be dependent on the background density. Note in both cases that the NRLMSISE00 model is unable to accurately represent storm-time density variations.

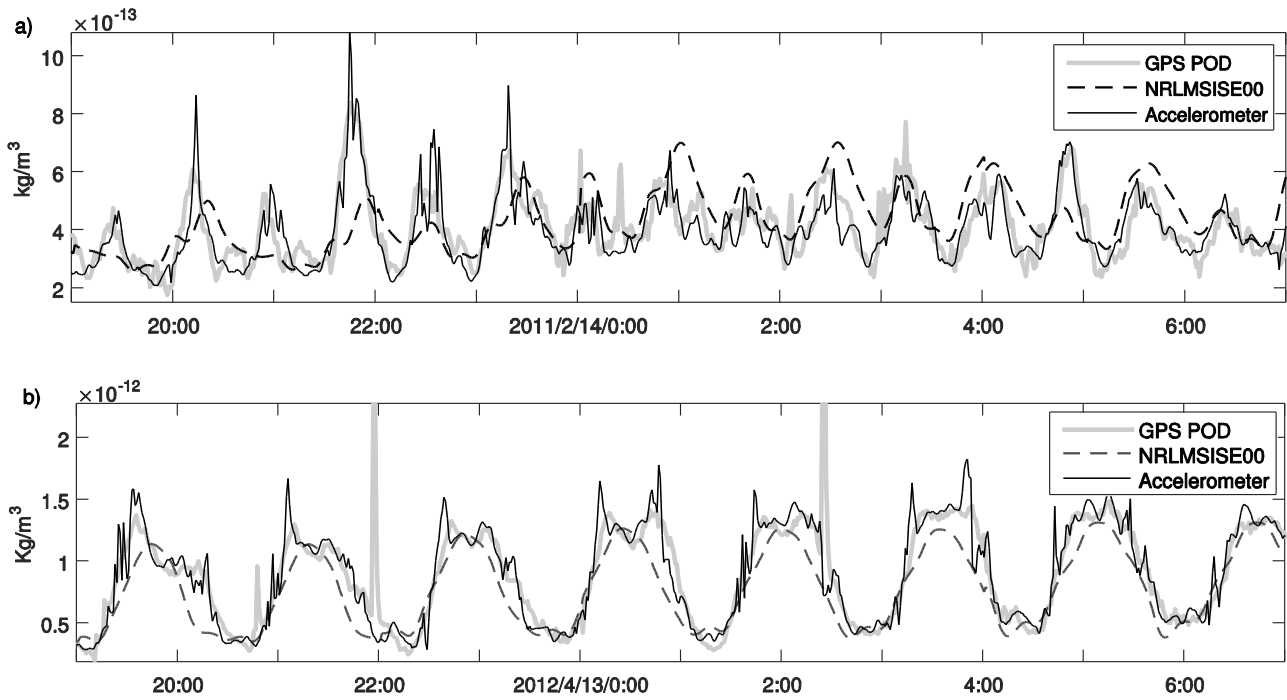


Figure 4.4 Thermospheric mass densities along GRACE's orbital path (normalized to 475km) on (a) February 14th 2011 and (b) April 13th 2012. Accelerometer-based densities are plotted in black color, the NRLMSISE00 model estimations are shown in dashed line, and the estimations from GRACE GPS-POD are represented in thick gray line.

4.3. Filling accelerometer data-gaps with POE-based estimates

After 9 year of continuous operability, the battery performance of the GRACE mission forced to turn off the accelerometers during intermittent periods of approximately one month. Figure 4.5 shows the periods without accelerometer measurements in a timeline from 2011 to 2015. In order to fill the data-gaps, thermospheric mass densities inferred from numerical differentiation of POE can be used to provide the missing data. For example, Figure 4.6 shows the non-gravitational accelerations (X-Y-Z satellite body frame) inferred from the GPS-POD of GRACE A on November 11th 2011. During this month, accelerometer measurements were unavailable for both for GRACE A and B satellites. Figure 4.7 shows the resulting POE-based thermospheric mass density estimates together with the NRLMSISE00 empirical model. In Figure 4.8, the daily averages of thermospheric densities are plotted for both accelerometer and POD -based techniques. Note that the accelerometer data gaps shown in the timeline of Figure 4.5 are clearly recognized and covered by the new POE-based neutral densities.

4. Thermospheric neutral density estimates from GRACE

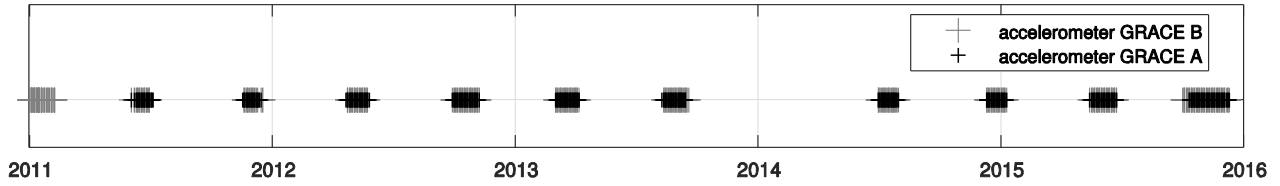


Figure 4.5 Days without accelerometer records. GRACE-A in gray and GRACE-B in black.

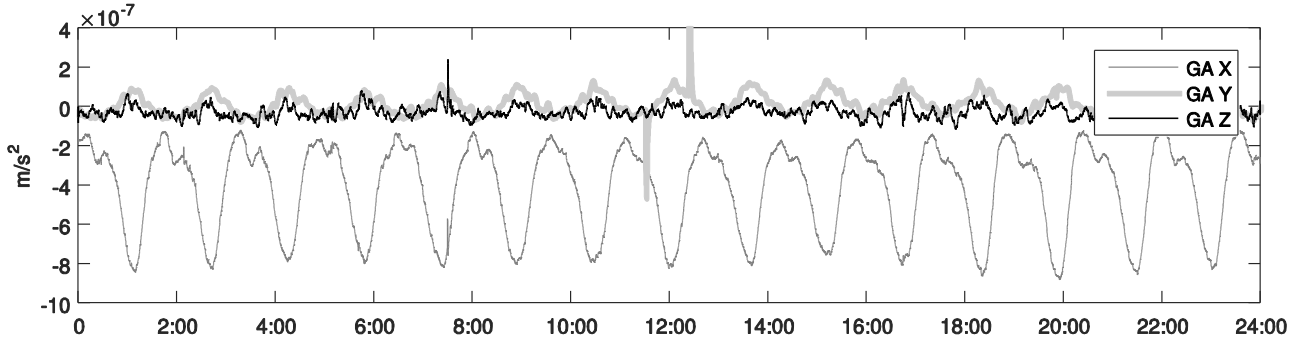


Figure 4.6 Non-gravitational accelerations (X-Y-Z satellite body frame) inferred from the GPS-POD of GRACE-A on November 11th 2011. During this month, accelerometer measurements are unavailable due to instrument power-off. Similar results for GRACE-B.

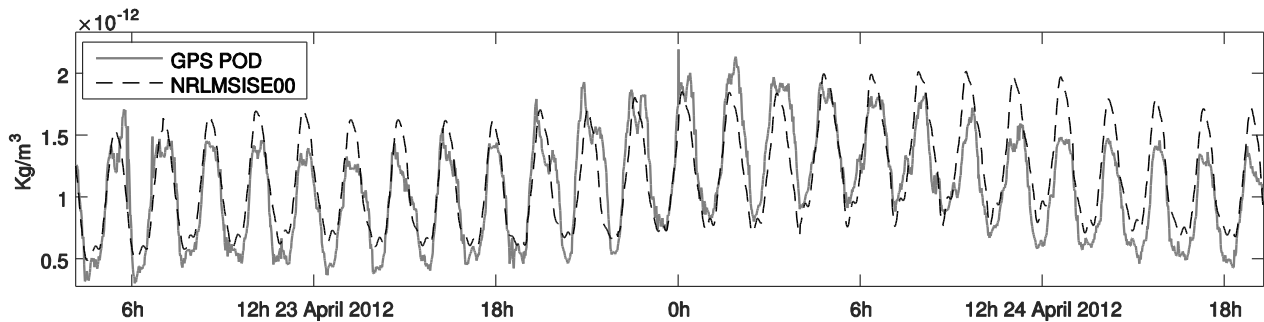


Figure 4.7 Thermospheric neutral densities for GRACE's orbital path on (a) April 23rd 2012. Accelerometer measurements were power-off. The NRLMSISE00 model is plotted in dashed line, and the results from GRACE GPS-POD are shown in thick solid line.

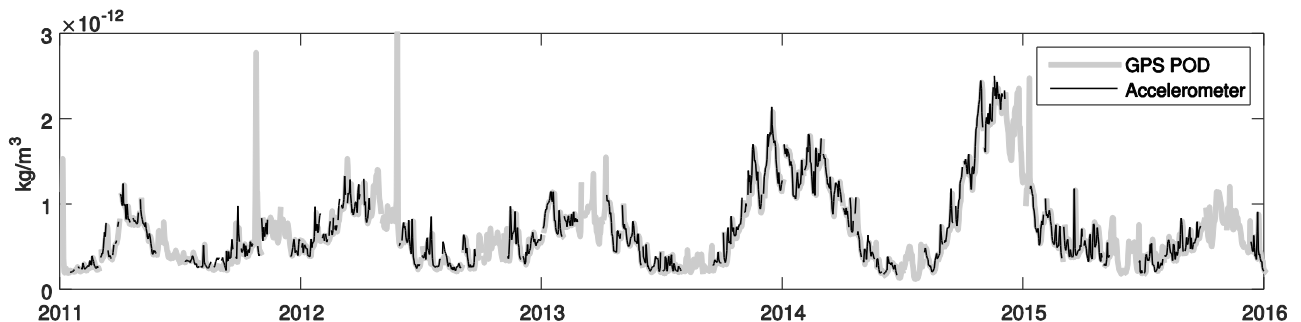


Figure 4.8 Daily averages of thermospheric neutral densities inferred from GRACE's descending orbits. Accelerometer-based estimates are in black color and POE-based estimates in gray color.

4.4. Uncertainty analysis of POE-estimated neutral densities

The analysis presented in this section aims to provide the assessment in space and time for the accuracy of POE-based mass density estimates, as well as for the NRLMSISE00 empirical model, using the accurate accelerometer measurements as a reference. Comparisons for the POE-based and the NRLMSISE00 estimates (2011-2016) with respect to the accelerometer-based densities are shown in Figure 4.9. From top to bottom, Figure 4.9 shows the correlation coefficients, the differences in terms of root-mean-square deviation (RMSD), the normalized RMSD (NRMSD) and direct differences, and the density values along the GRACE's orbital path (time series of 5-day averaged values). In Figure 4.9 (top), with a mean correlation coefficient of 96 %, the GPS POD densities show 3 % better correlation than the NRLMSISE00 estimates. A clear periodicity of 165 day suggests dependence on the LST, increasing the correlation when the satellite's orbit plane is aligned with the Earth-Sun line (i.e., the day-night variation increases the correlation). In next panel, the RMSD shows a decreasing trend of $4 \cdot 10^{-14} \text{ kg/m}^3$ from 2011 to 2016. In Figure 4.9, the corresponding normalized RMSD (NRMSD) pictures a trend from 12 % to 5 %, following the magnitude of the background density. Lower variations are seen during high-density periods and higher variations during low-density periods (see bottom panel). On the other side, the differences of NRLMSISE00 to accelerometer densities (Figure 4.9, 3rd panel) show a mean overestimation of 15 % \pm 18 % with respect to background density.

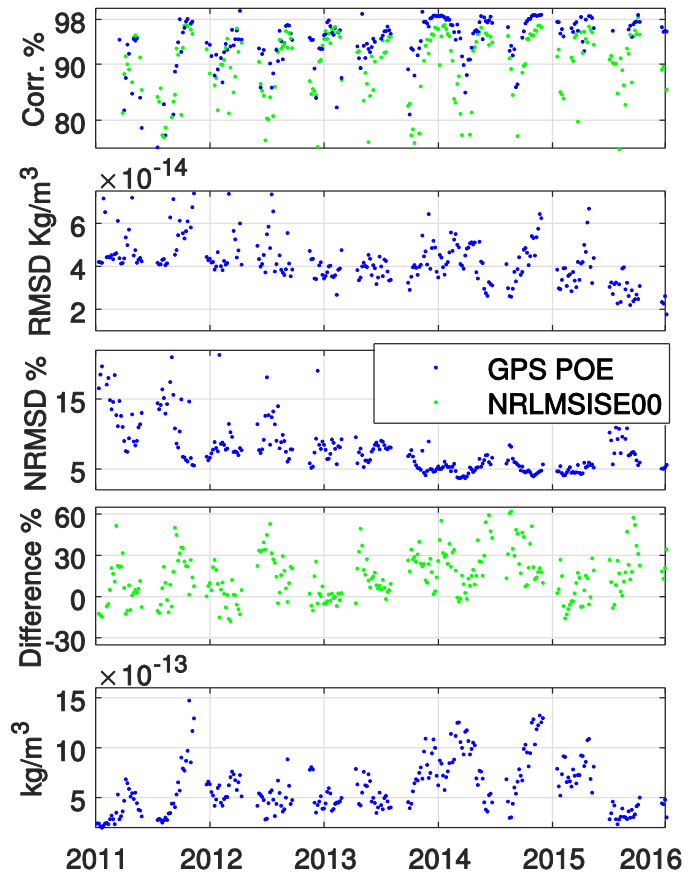


Figure 4.9 Correlation, RMSD, NRMSD, and differences of POE (blue) and MSISE (green) with respect to accelerometer estimates (top to bottom, 5-day mean averages). Mean background density in the bottom panel. [Calabia and Jin, 2017, Fig. 5].

Figure 4.10 shows the mean averages (top) and the SD (bottom), in geographical coordinates, of the relative differences between the POE-based and the ACC-based densities (i.e., $(\text{POE}-\text{ACC})/\text{ACC}$) during the period 2011-2016. The map of mean averages (Figure 4.10, top) shows a mean overestimation by 7 % at the equator and the poles, with marked anomalies near the magnetic cusps, and clear alignments with the dip isoclinic lines. The middle latitude is underestimated by 5 %, following the dip isoclinic lines. The SD map (Figure 4.10, bottom) shows a mean value of 15 %, with lower values at the equator (7 %) and especially higher at the southern pole (up to 30 %). A possible role of orbit errors due to geomagnetic activity might produce these marked alignments with geomagnetic equator and poles.

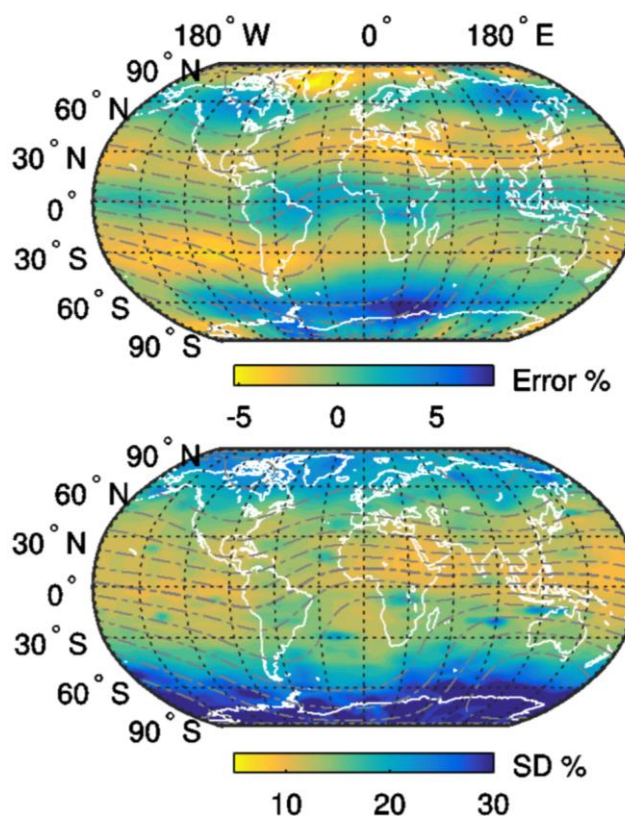


Figure 4.10 Mean average (top) and SD (bottom) of relative errors based on the differences between the POE-based and the accelerometer-based thermospheric mass densities, i.e. $(\text{POE}-\text{ACC})/\text{ACC}$, inferred from GRACE measurements during 2011-2016. Dip isoclinic lines are plotted in dash-dot format. [Calabia and Jin, 2017, Fig. 6].

In Figure 4.11, the global averaged densities along descending and ascending orbits are plotted for both accelerometer and POE based techniques. The days when accelerometers were powered off are pictured in the bottom time line. The corresponding discontinuities in the accelerometer-based densities can be seen in all the panels of Figure 4.11. Taking accelerometer measurements as accurate reference, the relative errors for the POE-based estimates are shown for both ascending and descending orbits. As expected, the maxima amplitude of the differences reaches up to 10 %, mostly during low density periods. During low-density periods, the differences stay mostly below 5 % of the background density.

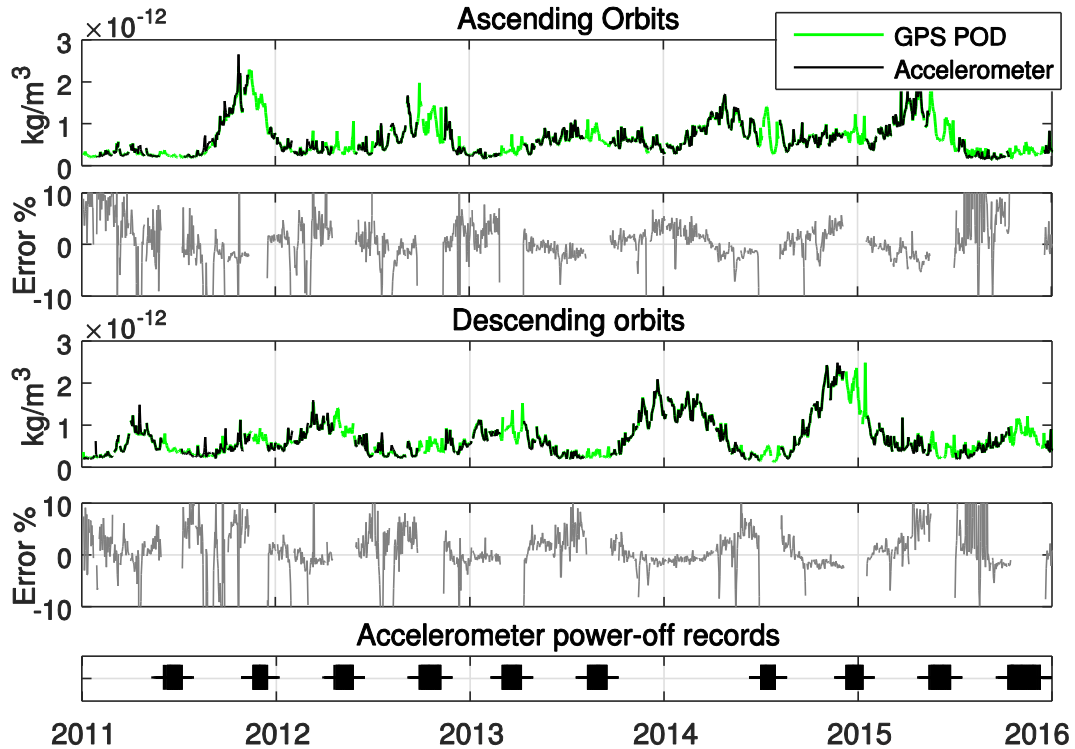


Figure 4.11 Global daily averaged densities and differences of relative errors between POE-based and accelerometer-based densities (2011-2016), i.e. $(POE-ACC)/ACC$. Ascending orbits in top panels and descending orbits in bottom panels. Accelerometer-based densities in black and GRACE POE-based estimates in green. Days when accelerometer measurements were off are plotted in the bottom time-line. [Calabia and Jin, 2017, Fig. 7].

Finally, a comprehensive PCA is employed to accurately study the differences between the POE-based and the accelerometer-based thermospheric mass densities for the period 2011-2016. The four leading eigenvectors together account for 28 % of the total variance and, individually, explain 11 %, 8 %, 5 % and 4 % of the total variability. The small percentages of both, each pattern and the sum of them indicate that the variability is considerably noisy. The first spatial PCA component (Figure 4.12, top) shows a clear alignment with the dip isoclinic lines, showing the possible role of orbit errors related to geomagnetic activity. The corresponding time-expansion coefficient is correlated at 60 % with the background mean density (panel below PCA1). The second PCA component seems to define a mid-latitude underestimation, and an overestimation at the equator and polar region, and with a northern cusp-related anomaly. It can be seen for this component a clear opposite behavior between ascending and descending orbits. Their corresponding time-expansion coefficients are centered at $5 \cdot 10^{-14}$, being negative for ascending orbits and positive for descending orbits. The third and fourth PCA components seem to be defined as a time series of southern-cusp

variations. Both PCA3 and PCA4 show correlation all along the period 2011-2016. An anomaly from unknown provenance is detected in January-March 2014 for the PCA3. This anomaly is also present for the parameterizations of LST and annual variations (Figure 4.12), and suggests a possible relation with the solar polar field reversal, which occurred during this time.

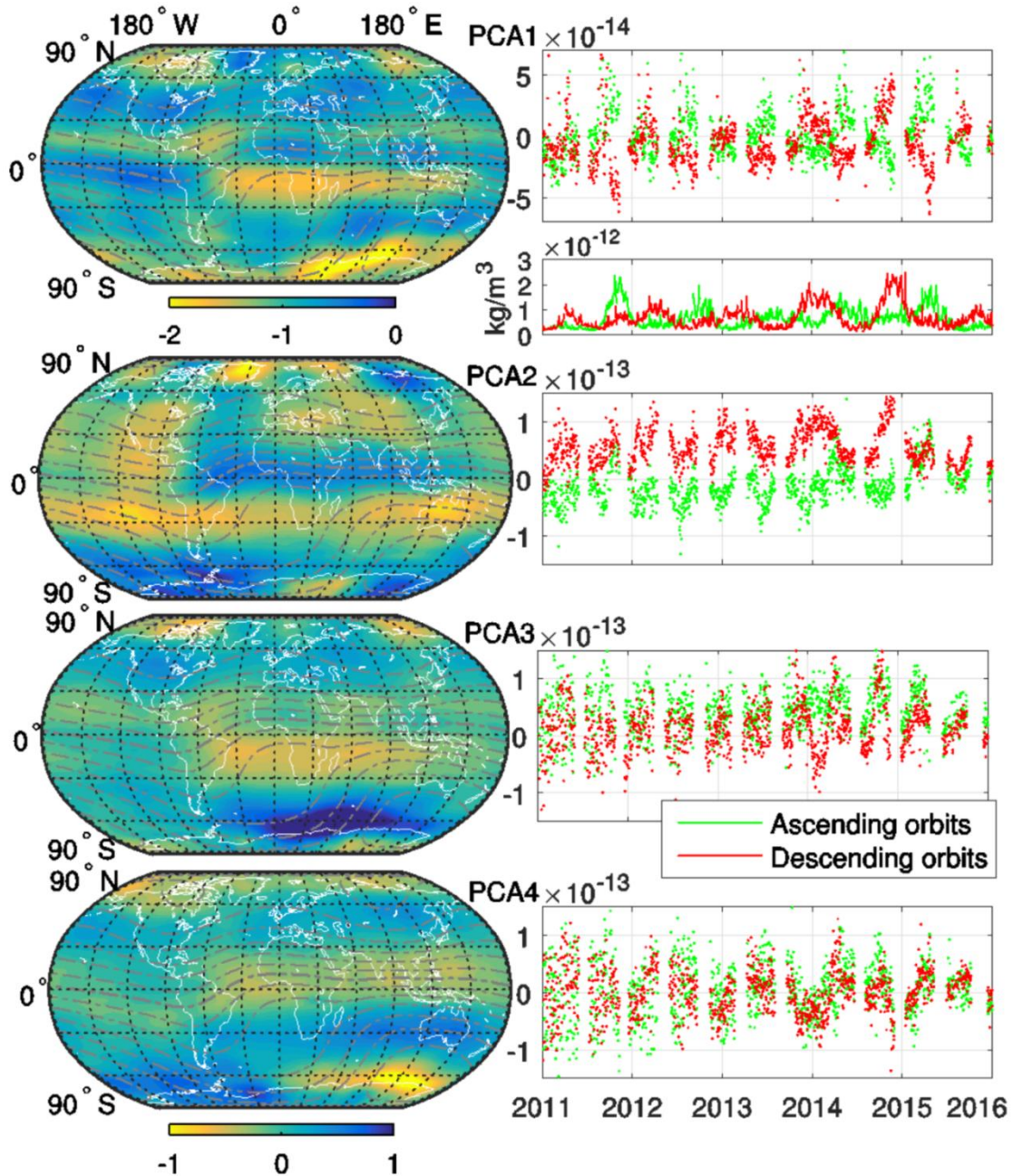


Figure 4.12 Four main PCA components for the differences between POE-based and accelerometer densities (2011 to 2016). Values are dimensionless. From top to bottom, each component explains the 11 %, 8 %, 5 % and 4 % of the total variability. The global averaged densities from Figure 4.11 are below the first PCA. Ascending orbits in green and descending orbits in red. Dip isoclinic lines are in gray dash-dot format. [Calabia and Jin, 2017, Fig. 8].

4.5. Summary

Following the indications in Chapter 2, thermospheric neutral mass densities along GRACE orbit have been estimated from accelerometer measurements and from the first derivatives of GRACE precise-orbit velocities. In this chapter, the accuracy of these new estimates has been assessed by comparison to the estimates of *Sutton* [2011] and comparison to the NRLMSISE-00 empirical model estimates. The main results are summarized as follows:

- GRACE's accelerometer-based neutral density estimates from this study correlate with Sutton's estimates at 94 %, and at 84 % with NRLMSISE00. The mean difference with respect to estimates of *Sutton* [2011] is centered at zero, while the NRLMSISE00 estimates are positively deviated in 25 %. Concerning the relative SD with respect to the background density, the differences to the estimates of Sutton have a mean value of 16 %, while the differences to NRLMSISE-00 have a mean value of 27 %. The uncertainty analysis using the PCA, for the relative differences between accelerometer-based densities and the NRLMSISE00 model during the period 2003-2015, i.e. $(\text{NRLMSISE00} - \text{GRACE}) / \text{GRACE}$, shows big percentages for the first component. The first four leading eigenvectors together account for 82 % of the total variance and, individually, explain 65.5 %, 9 %, 6 %, and 2 % of the total variability. The high percentage indicates marked patterns of variability between the NRLMSISE-00 model and the GRACE estimates. The first component shows a mean relative overestimation of about 0.3 at the equator, and about 0.15 at high latitudes.
- GRACE's POE-based neutral density estimates from this study show good agreement with accelerometer-based densities and a better estimation than the NRLMSISE00 empirical model. The relative differences with respect to the accurate accelerometer measurements have a mean value below 5 % (with respect the background density), and a mean correlation coefficient of 96 %. The RMSD from 2011 to 2016 shows a decreasing trend of $4 \cdot 10^{-14} \text{ kg/m}^3$, and the corresponding NRMSD pictures a trend from 12 % to 5 %. The POE-based density estimates show 3 % better correlation with respect accelerometer measurements than the NRLMSISE00 estimates. The differences of NRLMSISE00 to accelerometer density estimates show a mean overestimation of 15 % \pm 18 % with respect to the background density. The uncertainty analysis with PCA, for the differences between POE and accelerometer densities, shows small percentages for the fourth first

main patterns (11 %, 8 %, 5 % and 4 %), and the sum of them (28 %) indicates a variability considerably noisy.

5. GLOBAL DISTRIBUTION AND VARIATIONS OF THERMOSPHERIC NEUTRAL DENSITY

Besides the principal modes and mechanisms of thermospheric density variations from 13 years of GRACE measurements, this chapter conducts a study on long-term variations and responses to two geomagnetic storms, one from accelerometer measurements for the severe G4-level storm of March 2015, and the other from POE-based estimates for the moderate G2-level storm of March 2013.

5.1. Spatiotemporal analysis with PCA

The spatial patterns of 13 year (2003-2015) of neutral density variability, their time variation, and the measure of their importance have been extracted via the PCA. The first eight main eigenvectors together account for 98.6 % of the total variance, and individually explain the 90.3 %, 3.5 %, 2.9 %, 1.2 %, 0.3 %, and the 0.1 % for each of the last three ones. The fourth, fifth and sixth EOFs have been recognized as the gradient of density variations driven by energetic geomagnetic contributions, and therefore excluded from the analysis because no clear periodicities to investigate were detected. Figure 5.1 shows the five main EOFs of thermospheric density variability in geographic coordinates. The first component (Figure 5.1a) shows higher values in the southern hemisphere, a trough that follows the geomagnetic equator, and two peaks located at the cusps. Maxima values are located at the southern cusp and minima at the northern cusp. Previous studies using PCA techniques [*Matsuo and Forbes, 2010; Lei et al., 2012a*] provided no clear descriptions for these features. In comparison with *Liu et al. [2005, 2007, 2009]*, Figure 5.1a shows an improved characterization of the EMA. Since the EOF separates in a different component the variations due to the movement of the subsolar point, the EMA structure as well as its fluctuations in time can be better analyzed. For instance, Figure 5.1a shows more pronounced and symmetric crests where the geomagnetic equator is close to the geographical equator (i.e., 90° to 180° W), while in the other side (i.e., 0° to 180° E), the northern crest becomes less prominent. Figures 5.1b and 5.1c show a clear dependence to latitudinal variations following the sub-solar-point, plus changes in latitudinal curvature due to LST variations. Figures 5.1d and 5.1e show more detailed variations in latitude, and a clear 4-peak longitudinal-pattern, which has previously reported *Liu et al. [2009]*.

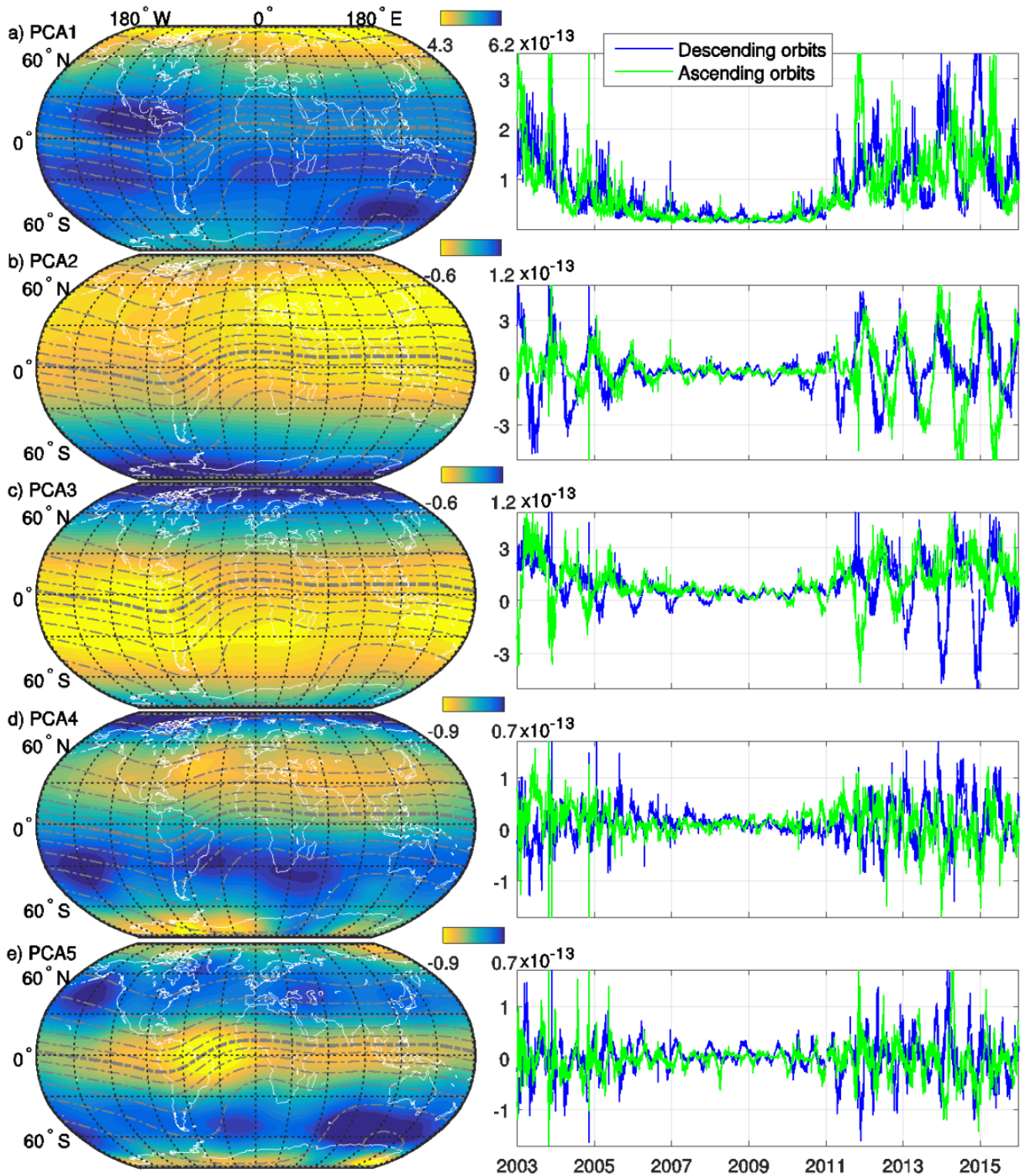


Figure 5.1 Main PCA components of thermospheric neutral mass density variability from GRACE measurements (475 km altitude). From top to bottom, each component individually explains the 90.3 %, 3.5 %, 2.9 %, 0.1, and 0.1 % of the total variance. Dip isoclinic lines are plotted in dash-dot gray format to show the alignments. Values are dimensionless. [Calabria and Jin, 2016b, Fig. 3].

5.2. Modes and mechanisms

5.2.1. *Parameterization of time-expansion EOF*

Since the main contribution on thermospheric density variations is known to be driven by the solar and magnetospheric forcing, the main time-expansion coefficient (PCA1, Figure 5.1a) has been simultaneously modeled in a 2-dimensional degree-2 polynomial fitting (Figure 5.2). Instead the lineal response given by previous studies (e.g., Müller *et al.* [2009]; Ruan *et al.* [2014], Figure 2), Figure 5.2 depicts a clear quadratic response. The fitting is based on applying a robust least-squares regression analysis, where the robust linear fitting M-estimator method Tukey's biweight (also known as bisquare) is employed to avoid possible outliers. The resulting polynomial fit uses the coefficients given in Table K.1 (Appendix K) in the following form:

$$F(Am, P107) = p00 + p10 \cdot Am + p01 \cdot P107 + p20 \cdot Am^2 + p11 \cdot Am \cdot P107 + p02 \cdot P107^2 \quad (5.1)$$

where Am is the k-derived geomagnetic index (http://isgi.unistra.fr/data_download.php), and $P107$ is the composite index $P10.7=0.5 (F10.7+(F10.7_{81 \text{ days}}))$ from the previous day, which is derived from the $F10.7$ solar radio flux at 10.7cm (<http://omniweb.gsfc.nasa.gov>). Note that previous authors have shown that the $P10.7$ (previous day) and the Am indices better correlate with the thermospheric density variations (e.g., Muller *et al.* [2009]; Guo *et al.* [2007]).

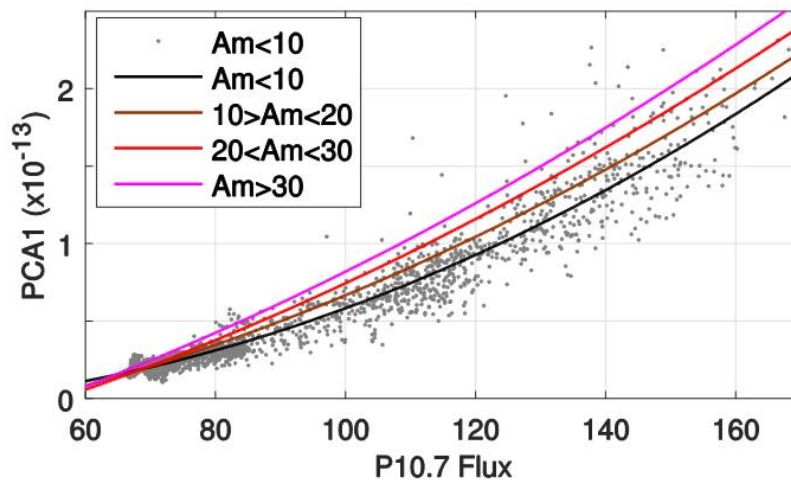


Figure 5.2 Fitting of the first PCA time-expansion coefficient (Figure 5.1a) in terms of P10.7 and Am indices. Observables with $Am > 10$ are not plotted. Parameterization is given in Table K.1 (Appendix K). Corresponding spatial pattern is shown in Figure 5.1a, and given in Table K.3 (Appendix K). Y-axis values are dimensionless. [Calabia and Jin, 2016b, Fig. 4].

After removing solar and magnetospheric contributions from the first time-expansion PCA coefficient, the residuals have shown variations at LST and at annual periods, which are strongly modulated in amplitude by the solar flux. Then, these variations have been extracted from the first time-expansion PCA coefficient, and have been parameterized in terms of LST and *doy* (day-of-year) with sinusoidal functions modulated by the P10.7 index. Note from now that each time-expansion EOF is represented by the sum of all the corresponding parameterized functions.

In order to reduce the number of variables in the fitting process, an iterative two-step process has been conducted as follows: first, data normalization to common flux has been implemented following the indications in *Müller et al. [2009]*; then, the sinusoidal fitting based in Fourier functions has been conducted; finally, a polynomial fitting modulates the flux-dependent amplitude of the functions computed in the previous step. Note that in all cases the bisquare least-squares fitting is employed. The resulting functions for the main secular variations are shown in Figures 5.3, 5.4, and 5.6 to 5.9. For these variations, the coefficients given in Table K.2 (Appendix K) stand to be used in the following form:

$$G(\chi, P107) = 10^{-15} \cdot 10^a \cdot P107^b \cdot \left(a0 + \sum_{i=1}^n [an \cdot \cos(n \cdot \chi) + bn \cdot \sin(n \cdot \chi)] \right) \quad (5.2)$$

were a , b , $a0$, an , and bn are the constant and amplitudes, and χ takes different values for each periodic case: for the annual variations, χ is $doy \cdot 2\pi/365$; for the LST (S1) and other radiational variations (i.e., K, P, R, T), χ is the argument defined by the vector product between the six-vector of Doodson's fundamental arguments (equation 2.11) and their corresponding six-vector of multipliers [*Petit and Luzum, 2010*]; for the other periodic cases (e.g., 93-day), χ is the product between the corresponding angular frequency ($=2\pi/\text{period}$) and the days since J2000.0 (days since 51544.5 in modified Julian date format). Note that Doodson's fundamental arguments are computed at the times when the satellite crosses the Greenwich meridian.

Fitted parameters and correlation coefficients between the time-expansion PCA series and the parameterized ones are given in Table K.2 (Appendix K). The parameterizations achieve 96 %, 92 %, 91 %, 75 %, and 75 % correlation with respect to the 1 to 5 PCA components, respectively.

5.2.2. Local Solar Time and annual variations

This section aims to identify and discuss the main LST and annual variations of thermospheric neutral density estimates from GRACE, and compare the main PCA parameterizations with Figures 5.12 and 5.13. Figure 5.12 shows the thermospheric neutral density variations derived from GRACE accelerometers and MSIS, in function of LST and latitude (fixed at Greenwich meridian), for the scenarios of March Equinox (ME), June Solstice (JS), September Equinox (SE) and December Solstice (DS), and for solar-flux conditions of $P_{10.7}=80$ and $P_{10.7}=120$ s.f.u. (8 scenarios in total). In each scenario, accelerometer and MSIS -based densities along GRACE orbits (raster plots), and the direct calculations from the parameterization and from the MSIS (contour plots) are plotted from left to right. Values of density along GRACE orbit have been averaged in between ± 15 s.f.u. and ± 30 day, and the corresponding occurrences are summarized in a bar-graph on the left side. Due to the disperse nature of the resulting map of averages, the raster format is employed for a better representation (pair of plots on the left side). On the right side (pair of contour-plots in each scenario), the models are directly computed using the *doy*, flux, and LST parameters corresponding to each scenario (i.e., no averaged solution). Figure 5.13 shows a similar analysis to Figure 5.12, but in function of *doy* and latitude, for scenarios at 5, 11, 17, and 23 h LST. In this figure, the averaged densities (raster plots) are restricted in between ± 15 s.f.u. and in between ± 3 h LST.

Figure 5.3 shows the LST variations for each time-expansion PCA component. For the first component (Figure 5.3a), the results given by previous authors (e.g., [Liu et al. \[2005\]](#); [Matsuo and Forbes \[2010\]](#); [Lei et al. \[2012a\]](#)) are in agreement with the equatorial diurnal maximum at 14:30 h LST and the minimum at 4 h LST. From Figures 5.12 and 5.13, the highest values of density ($\sim 15 \cdot 10^{-13}$ kg/m³) are pictured at ~ 14 h LST in DS and ME, and the lowest values ($< 0.5 \cdot 10^{-13}$ kg/m³) at ~ 4 h LST in JS. It can be seen that the combination of PCA1 with the LST variations of PCA2 and PCA3 (Figures 5.3b and 5.3c) produces a fluctuation in the latitudinal curvature of the global density distribution. A maximum value for the positive curvature is located at 15 h LST. From that point, the curvature is reduced to a minimum at midnight. The minimum remains stable until 6 h LST, and then arises to maxima at 15 h LST. Note that a positive curvature is here defined as a low-latitude increment with a high-latitude reduction (and the reciprocal negative).

The results from PCA4 and PCA5 show an interesting response to LST variations. The component PCA4 (Figures 5.1d) shows a hemispherically asymmetrical modulation with opposite behavior in the poles. The moderated LST contributions of PC4 (Figure 5.3d) show higher values in the northern hemisphere and during the whole day, but are cancelled at 11 h LST (note the opposite values at the poles). Additional periodic residuals in PC4 are investigated in the following sections.

PCA5 (Figure 5.1e) shows a density enhancement at mid-latitude, and a reduction at equator and cusps (as well as the negative reciprocal). In Figure 5.3e, LST variations of PCA5 show two maxima as follows. First maximum occurs at 12 h LST, and decreases to a minimum at 17 h LST. Interestingly, the inflection-point is zero, and coincides with the LST maxima peaks of PCA1, PCA2, and PCA3 at 14:30 h LST. Note that PCA5 increases (decreases) middle-latitude densities previous (after) to reach the PCA1 diurnal maximum at 14:30 h LST. It seems that the LST contribution of PCA5

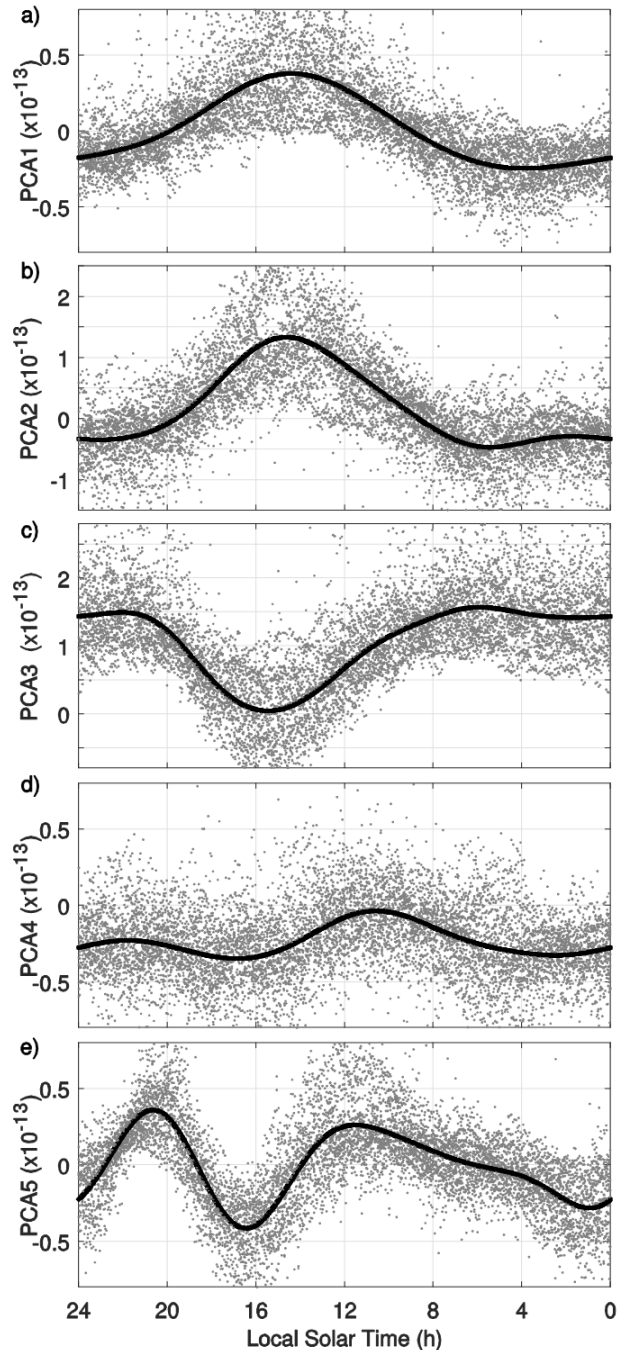


Figure 5.3 Fitting of time-expansion EOF, as seen from periodic variations of the S1 constituent (represented in LST). Data normalized to P10.7=110 common flux. Parameterizations are given in Table K.2 (Appendix K), including the modulation in amplitude. Corresponding spatial patterns are shown in Figure 5.1 and given in Table K.3 (Appendix K). Y-axis values are dimensionless. [Calabia and Jin, 2016b, Fig. 5].

behaves as a dumped response to the solar forcing, which might modulate the dissipation of density to (from) middle latitudes. Afterwards, the LST variations of PCA5 increase from the minimum at 17 h LST up to a second maximum at 21 h LST, and later decrease to a secondary minimum at 1 h LST. Note as well a null-valued inflection-point at 23 h LST, which interestingly coincides with the secondary density maximum peak at the night-side equator of *Liu et al. [2005]*.

As for the seasonal variations, the combination of the annual parameterizations of PCA2 and PCA3 (Figure 5.4b and 5.4c, respectively) represent the main latitudinal fluctuation following the sub-solar point. This variation is clearly present in Figure 5.12 and 5.13. The separation of the annual wave into two different modes (PCA2 and PCA3) is due to the PCA, which provides a combined solution of LST and annual variations (i.e., PCA2 and PCA3 represent both the variation in the latitudinal curvature and the latitudinal variation following the sub-solar-point). Having a similar shape for both PCA2 and PCA3 annual variations (Figure 5.4b and 5.4c), two maxima are depicted in June, and only one in December. The two maxima around June are separated by a relative minimum at the JS point (171 doy). The first maximum at early May (122 doy) shows a bigger amplitude than the secondary at end of July (213 doy). The peak in December is located 10 day before to the DS point (344 doy). The two peaks around June are clearly present in most of panels of Figure 5.13. At equinox periods, the annual variation seems to have two asymmetrical decelerated intervals (i.e., periods where the velocity of change is slowed down) as it passes from solstice to solstice. The annual asymmetry of these decelerated intervals is shown to appear one month previously to the ME point, and half month ahead from the SE point. These two decelerated intervals are also recognized in Figure 5.13, scenarios 11 h and 17 h LST.

Furthermore, note that the annual variation of PCA1 at Figure 5.4a has been previously reported and investigated by numerous authors (e.g., *Lei et al. [2012a]*; *Emmert and Picone [2010]*; *Müller et al. [2009]*; *Guo et al. [2008]*; *Bowman et al. [2008a]*; *Liu et al. [2007]*). In agreement with these previous studies, the PCA1 annual variation shows to increase with solar and magnetospheric activity, and during equinox seasons, with higher values in December than in June (Figure 5.1a). No clear asymmetry is depicted between March and September. The maxima peaks in equinox show to be 10-day delayed from ME (90 doy) and about one month from SE (300 doy). Minima at solstice show a delay of 20 day from the JS point (191 doy), and about one month from the DS point (15 doy).

The equatorial anomaly is a very interesting and important feature of the thermosphere, which is recently being investigated by several researchers. Previous studies have shown a minimum on the dayside, clearly aligned to the geomagnetic equator, and with two maxima at $\pm 20^\circ$ geomagnetic latitude (e.g., [Liu et al. \[2007\]](#); [Ma et al. \[2010\]](#)). This feature is pictured by the PCA1 (Figures 5.1a and 5.4a), and also in Figure 5.12, scenarios of ME and SE at ~ 14 h LST. The corresponding time expansion coefficient is mainly dependent on solar flux (e.g., P10.7) and magnetospheric forcing (e.g., A_m index), and modulated by the LST variation (Figures 5.2 and 5.3a). On the night side, several authors (e.g., [Ma et al. \[2010\]](#); [Ruan et al. \[2014\]](#)) have pictured a maximum aligned to the geographic equator,

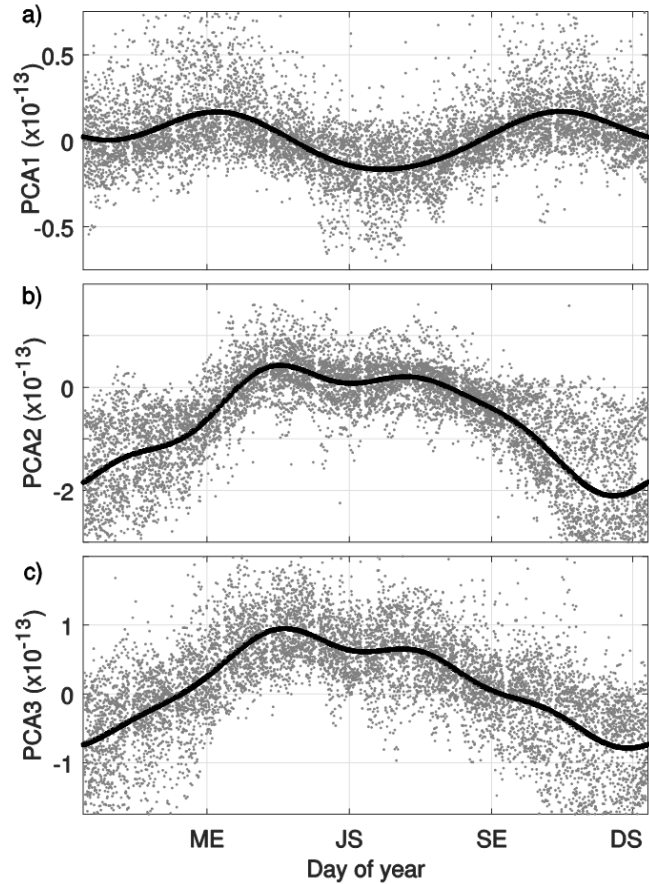


Figure 5.4 Fitting of PCA time-expansion coefficients, as seen from periodic annual variations. Data normalized to P10.7=110 common flux. Parameterizations are given in Table K.2 (Appendix K), including the modulation in amplitude. Corresponding spatial patterns are shown in Figure 5.1 and given in Table K.3 (Appendix K). Y-axis values are dimensionless. [[Calabia and Jin, 2016b, Fig. 6](#)].

with two minima at $\pm 40^\circ$ geographic latitude. This feature is pictured by the PCA5 (Figures 5.1e and 5.3e) and also in Figure 5.12 (scenario DS at ~ 4 h LST). The LST parameterization of PCA5 (Figures 5.3e) shows a null-valued inflection-point at 14:30 h LST, which seems represent the change of concavity in response to the solar forcing of diurnal maximum (Figure 5.3a, 14.30 h LST). This singularity might to be related to changes on the latitudinal dissipation of density. A second maximum is pictured at 21 h LST, and a second minimum at 1 h LST (Figure 5.3e). As a result, the PCA5 contributions at midnight (negative at mid-latitude and positive at equator, Figure 5.1e) show reduced enhancements with the

increasing of PCA1, during high solar activity (Figure 5.2). Reciprocally, midnight PCA5 show stronger negative contributions during solar minimum. These features are in agreement with the above mentioned studies on EMA and MDM.

Concerning the seasonal variations of EMA, Figure 5.4a shows maxima values during equinoxes and minima during solstices, being the minima in June stronger than in December. In reference to Figures 5.12 and 5.13, the EMA is clearly pictured on ME and SE at ~ 14 h LST. This seasonal asymmetry has been previously reported in the low-latitude studies of *Liu et al.* [2007, Figure 4] and *Müller et al.* [2009, Figure 8], and in the PCA's of *Matsuo and Forbes* [2010, Figure 2, left panel] and *Lei et al.* [2012a, Figure 2]. Furthermore, under weak solar and magnetospheric forcing (Figure 5.2) the EMA is reduced by the negative values of the night-time (Figure 5.3a) and the JS minima (Figure 5.4a). This feature is clearly present in Figure 5.12, being the EMA stronger in DS than in JS. On the night side, midnight mid-latitude PCA5 enhancements (Figure 5.1e) are stronger due to the reduction of PCA1 during solstice periods (Figure 5.3a). Reciprocally, the increasing of PCA1 at equinox reduces the midnight mid-latitude enhancements of PCA5. These features are in agreement with *Ma et al.* [2010], where the authors showed a MDM stronger during solstices. In reference to Figures 5.12 and 5.13, the MDM is pictured as two minima at $\pm 45^\circ$ on DS and JS at 4 h LST.

In general, the MSIS empirical model agrees well with LST, season and solar-flux variations derived from the GRACE accelerometers. However, clear differences are detected when comparing in detail. For instance, a clear overestimation of density is pictured in all scenarios, and nor EMA nor two peaks around June can be recognized in the MSIS. In addition, a delay of about 1-2 h LST (Figure 5.12) and an advance of about 1-2 month (Figure 5.13) are pictured when comparing the parameterizations with the MSIS model.

5.2.3. Neutral density variations at the radiational-tides frequency

In this section, after subtracting modeled solar, magnetospheric, annual, and LST variations, the residuals are analyzed in the spectral domain. Figure 5.5 shows the power spectral density estimate (from 75 to 500 day/cycle) for the residuals of each PCA time-expansion coefficient. The long-wave periods are not represented due to the limited time-series (13-year). In order to confirm that no significant oscillations are derived from the process of removing solar, magnetospheric, annual, and LST variations, the periodogram of each original

time-expansion coefficient is plotted together with their corresponding residuals. In addition, the 95 %-confidence bounds are included to locate the significant peaks (i.e., when the value exceeds the upper confidence bound for surrounding power spectral density estimates). In Figure 5.5, the significant peaks are highlighted with vertical lines:

- ✓ strong signatures at the period of 83 day can be seen in the PCA4 and PCA5;
- ✓ the period of 93 day is clearly noticed in PCA1, PCA2 and PCA3;
- ✓ the presence of 112 day period (T) is clear in PCA4;
- ✓ strong signatures of 152-day period can be seen in PCA1 and PCA4;
- ✓ the presence of 171 day period (P) is clear in all the PCA components;
- ✓ the period of 290 day (R) is clear in the PCA4;
- ✓ a 431-day periodicity can be seen in PCA1;
- ✓ additional periodicities are found at 1700 (K+) and 2719 day (K).

In order to explain the peaks of periodicities in a scientific manner, a possible geophysical explanation can be given by the constituents of the theory of tides. In *Munk and Cartwright [1966, Figure 8]*, the authors introduced the concept of "radiational tides" to associate their residuals with the tidal phenomena derived from solar heating. Therefore, since the driving force of radiational variations in the thermosphere should contain the same spectral structure as the main radiation-tides, it seems to be meaningful to look into the thermospheric neutral mass density time series for peaks at frequencies, which are marked in the tidal spectrum by the most energetic radiational constituents (Table 5.1).

Table 5.1. GRACE's alias periods for the main radiation-waves

Darwin symbol	Period (day)	Alias period (day) for GRACE
P1	1.0027454	171.13
S1 (LST)	1.0000000	322.00
K1	0.9972696	2719.68
K+	0.9971964	3399.74
T2	0.5006854	111.74
R2	0.4993165	287.89

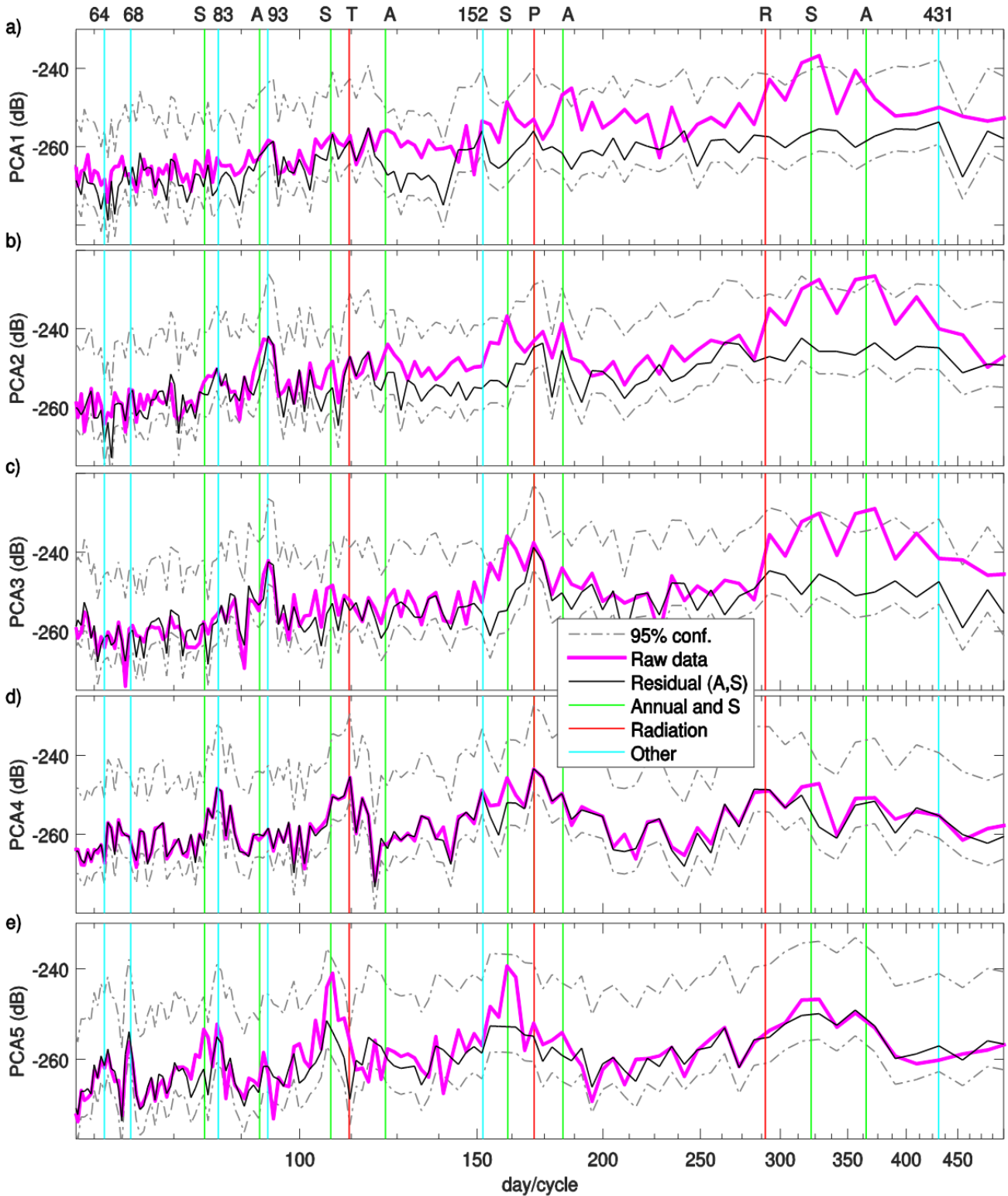


Figure 5.5 Periodograms of main PCA time-expansion coefficients in magenta. In black solid line the periodograms of the residuals from removing solar, magnetospheric, annual (A), and LST (S) variations (data reduced to P10.7=110). Gray dash-dotted line represents the 95 % confidence bounds. The significant periodicities are marked with vertical lines. [Calabria and Jin, 2016b, Fig. 7].

From the perspective of the GRACE satellites (with subscript *sat*), the wave frequencies associated to each radiational constituent vary depending on the satellite's equatorial orbit shift, i.e., GRACE's precession rate $\sigma_{sat}^{Sun} = -1/322(\text{cycle/day})$. From the perspective of a ground-based station (subscript *Earth*), the Earth's self-rotation frequency with respect to the Sun is $\sigma_{Earth}^{Sun} = 1(\text{cycle/day})$ and with respect to, e.g., the P1 radiational constituent, is $\sigma_{Earth}^{P1} = \sigma_{Earth}^{Sun} - 1/365.2434$, so $1/\sigma_{Earth}^{P1} = 1.002745$, or 24.06589 h, which is confirmed as the Solar diurnal P1 period [Petit and Luzum, 2010].

Since the phase speed of the radiational constituent (e.g., in the P1 case $C^{P1} = 1/365.2434$) is constant for each sinusoidal mode [Forbes et al. 2013], by subtracting the equations derived from both perspectives $ref = \{sat, Earth\}$, i.e., $\sigma_{ref}^{P1} = \sigma_{ref}^{Sun} - C^{P1}$, it is possible to isolate the satellite's associated wave frequencies.

The periods for the radiational constituents are extracted from Petit and Luzum [2010] and listed in Table 5.1, together with the corresponding alias period for GRACE. The following equation is presented as example to calculate the wave frequency associated to the P1 radiational constituent. In the case of GRACE, the precession rate has a negative value, reflecting the opposite precession of the satellite

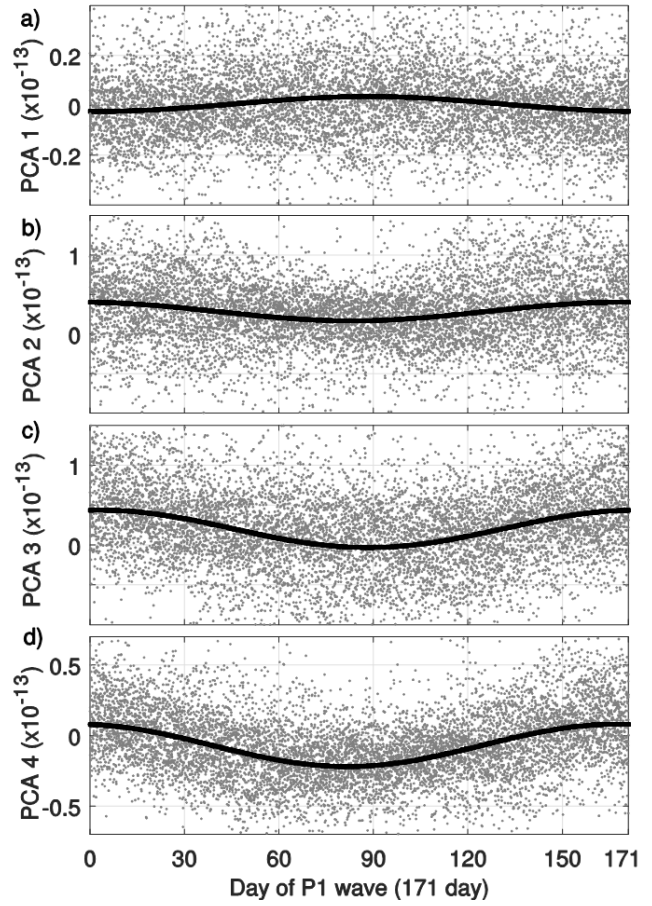


Figure 5.6 Fitting of time-expansion EOF, as seen from periodic 171-day variations (P1 wave). Data normalized to P10.7=110 common flux. Parameterizations are given in Table K.2 (Appendix K), including the modulation in amplitude. Corresponding spatial patterns are shown in Figure 5.1 and given in Table K.3 (Appendix K). Y-axis values are dimensionless. [Calabia and Jin, 2016b, Fig. 8].

than that given by the Earth, both with respect to the Sun.

$$\sigma_{sat}^{P1} = \sigma_{sat}^{Sun} + \sigma_{Earth}^{P1} - \sigma_{Earth}^{Sun} = -0.005843 = -\frac{1}{171.1306} \quad (5.3)$$

The hypothesis here proposed is based on driving forces of radiational origin, which should contain the same spectral signature as the main radiation-tides. In [Munk and Cartwright \[1966, Figure 8\]](#), the most energetic radiation was depicted by the T, P, R, S and K constituents. From the perspective of GRACE, the wave periods associated to these radiational constituents are 112, 171, 288, 322, and 2720 day, respectively (shown in Table 5.1). Validating the hypothesis here suggested with GRACE measurements, besides the 322-day period (S), which has been already removed by LST variations in previous section, the others periodicities (112, 171, 288, and 2720 day) are clearly present in the residuals (Figure 5.5).

The fitted sinusoidal functions for the P1, K, R2 and T2 variations are plotted in Figures 5.6 to 5.9, respectively. Note that the number next to each period (e.g., R2) indicates diurnal (1) or semidiurnal (2) specie. Concerning the period of 93 day, this contribution could be originated by the GRACE's drift of perigee (having the same period). Note that unlike for the radiational periods, the NRLMSISE-00 empirical model did not include any periodicity at 93 day. It seems that scaling the densities at 475 km does not completely remove all the variations caused by orbiting at different altitudes.

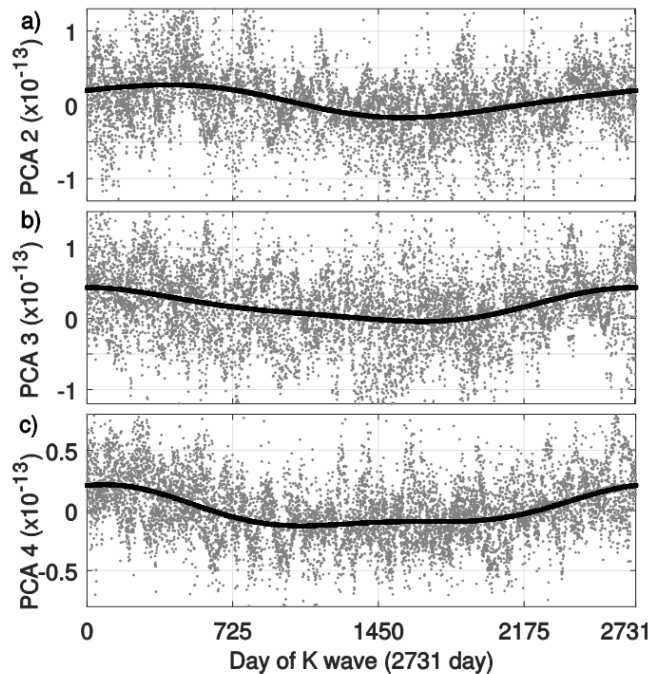


Figure 5.7 Fitting of time-expansion EOF, as seen from periodic 2731-day variations (K wave). Data normalized to $P_{10.7}=110$ sfu. Parameterizations are given in Table K.2 (Appendix K), including the modulation in amplitude. Corresponding spatial patterns are shown in Figure 5.1 and given in Table K.3 (Appendix K). Y-axis values are dimensionless. [[Calabia and Jin, 2016b, Fig. 9](#)].

The period of 431 day could be related with the free-core nutation (FCN) theory [Petit and Luzum, 2010]. The core-mantle electromagnetic dynamo (interaction of the mantle and the fluid, ellipsoidal core as it rotates) might produce changes in the magnetic field and induce variations through the MIT coupling (the collisions between the ionospheric plasma and the neutrals fluctuate in accordance to the 431-day induced magnetic field). Concerning the 83 and 152 day periods, several studies have reported similar periodicities in solar activity (e.g., Cane *et al* [1998]; Joshi and Joshi [2005]), which could be the precursors of thermospheric density variations at these periods.

5.2.4. Parameterizations and contrast of results

Parameterizations for the time-expansion EOF are given in Tables K.1 and K.2 (in Appendix K) and must be used with equations given in Section 5.2.1. The corresponding EOF spatial patterns are given in the form of Stokes coefficients in Table K.3

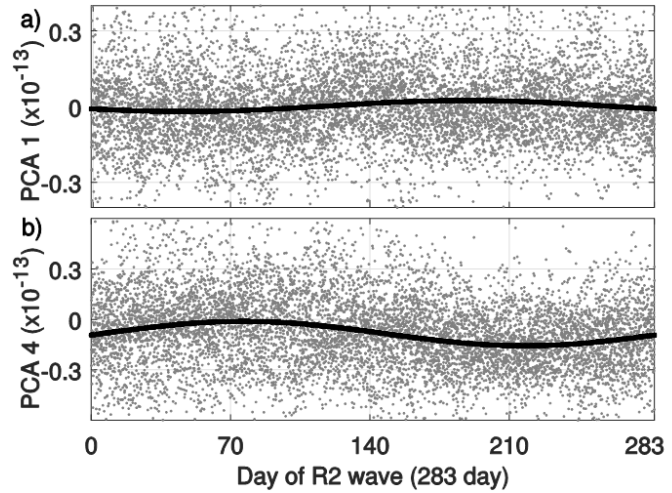


Figure 5.8 Fitting of time-expansion EOF, as seen from periodic 283-day variations (R2 wave). Data normalized to P10.7=110 sfu. Parameterizations are given in Table K.2 (Appendix K), including the modulation in amplitude. Corresponding spatial patterns are shown in Figure 5.1 and given in Table K.3 (Appendix K). Y-axis values are dimensionless. [Calabia and Jin, 2016b, Fig. 10].

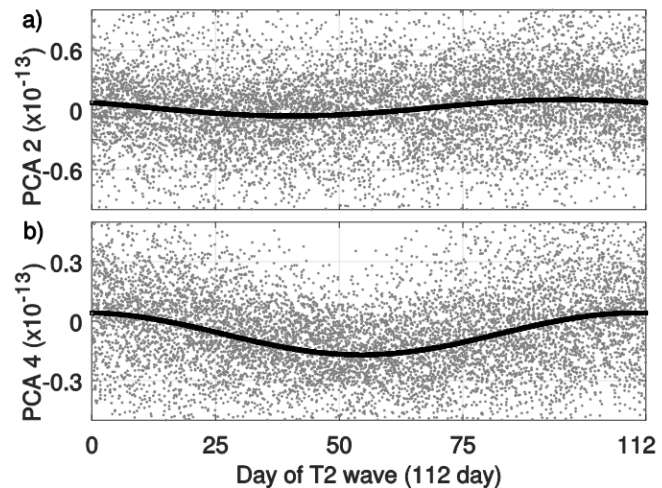


Figure 5.9 Fitting of time-expansion EOF, as seen from periodic 112-day variations (T2 wave). Data normalized to P10.7=110 sfu. Parameterizations are given in Table K.2 (Appendix K), including the modulation in amplitude. Corresponding spatial patterns are shown in Figure 5.1 and given in Table K.3 (Appendix K). Y-axis values are dimensionless. [Calabia and Jin, 2016b, Fig. 11].

(Appendix K). A feasible MATLAB computation to obtain the grids of the spatial patterns is given in Appendix I.

Figure 5.10 shows the main time-expansion EOF and the parameterizations in terms of P10.7, LST, and annual variations, for 13 year (2003-2015) of accelerometer-based densities. The four leading PCA components together account for 99.8 % of the total variance and, individually, explain 92 %, 3.5 %, 3 %, and 1.3 % of the total variability. The high percentage for the first PCA component is due to the main dependence on the EUV radiation, and the high percentage for the sum of four leading PCA components indicates low noise with few marked patterns of variability. The correlation coefficients for the parameterized time series are respectively 96 %, 93 %, 90 %, and 83 %, being more than acceptable for the purpose of this study.

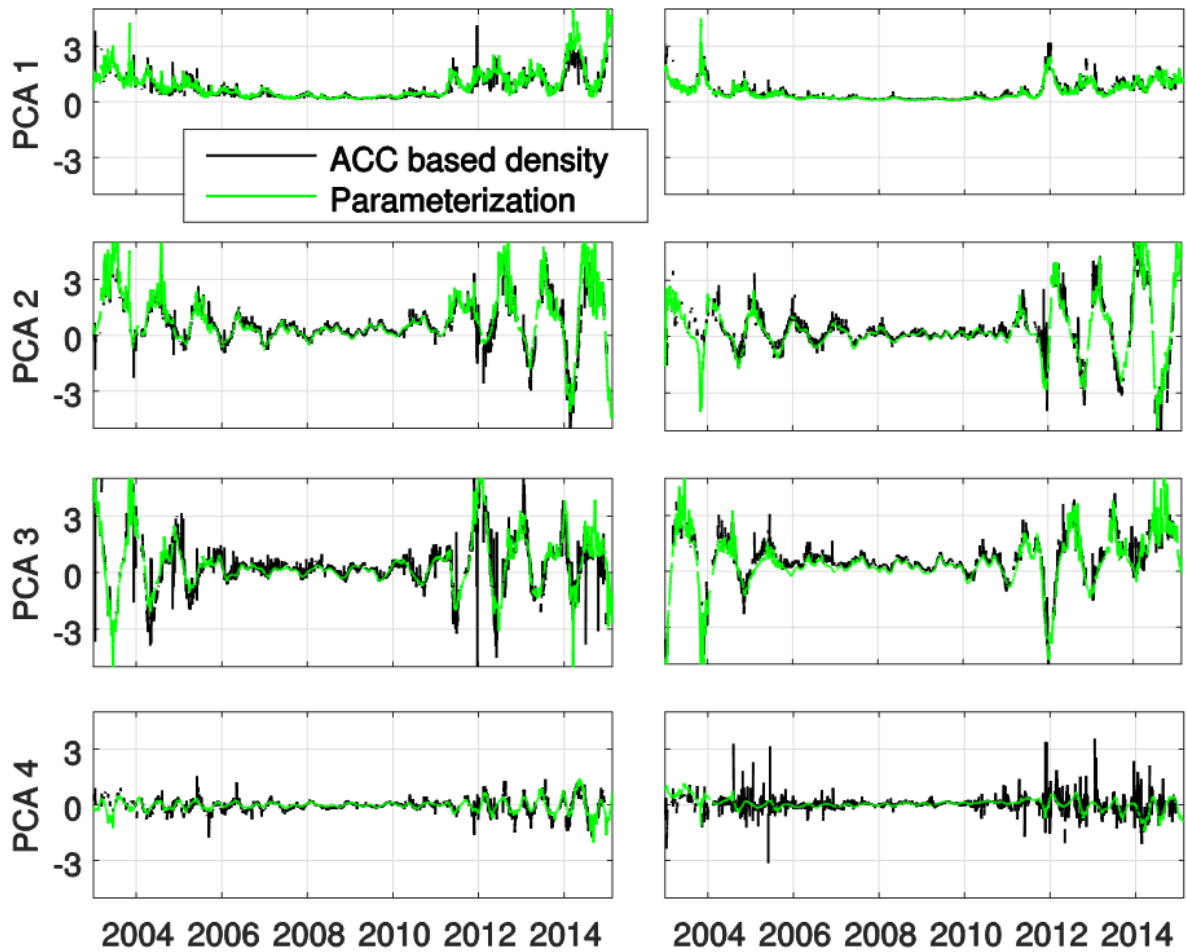


Figure 5.10 Main PCA coefficients (black) and corresponding parameterizations (green), in function of P10.7, LST, and annual variations. Descending orbits on the left panels and ascending orbits in the right panels. Dimensionless values. [Calabia and Jin, 2017, Fig. 9].

The global averaged relative residuals (i.e. residual/density) with respect accelerometer estimates for both the MSIS model and the PCA parameterizations are shown in Figure 5.11. Both models seem to follow a similar pattern of variations. The relative residuals for the PCA parameterizations are ~60 % smaller than those of NRLMSISE-00, and show absolute values below the ~20 % error.

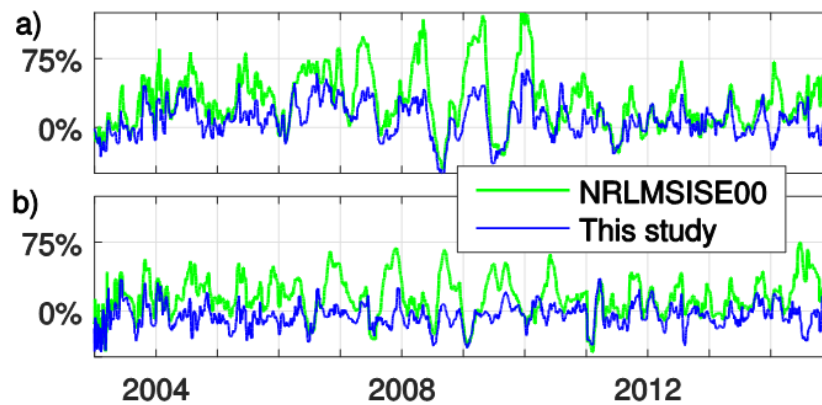


Figure 5.11 Global averaged relative residuals (i.e., residual/density) with respect accelerometer estimates for (a) ascending orbits and (b) descending orbits, for the parameterized PCA and for the MSIS empirical model. [Calabia and Jin, 2016b, Fig. 14].

Figures 5.12 and 5.13 have been already introduced in Section 5.2.2 as follows: “Figure 5.12 shows the thermospheric density variations derived from GRACE accelerometers and MSIS, in function of LST and latitude (fixed at Greenwich meridian), for the scenarios of March equinox (ME), June solstice (JS), September equinox (SE) and December solstice (DS), and for solar-flux conditions of $P_{10.7}=80$ and 120 s.f.u. (8 scenarios in total). In each scenario, accelerometer-based and MSIS-based densities along GRACE orbits (raster plots), and the direct calculations from the parameterization and from the MSIS (contour plots) are plotted from left to right. In each scenario, the values of density along GRACE orbit have been averaged in between ± 15 s.f.u. and ± 30 day, and the corresponding occurrences are summarized in the bar-graph on the left. Due to the disperse nature of the resulting averages, the raster format is employed for a better representation (pair of plots on the left). On the right side (pair of contour-plots in each scenario), the models are directly computed (i.e., no averaged solution) with doy, flux, and LST inputs corresponding to each scenario. Figure 5.13 shows a similar analysis to Figure 5.12, but in function of doy and latitude for scenarios at 5, 11, 17, and 23 h LST. In this figure, the averaged densities (raster plots) are restricted in between ± 15 s.f.u. and ± 3 h LST.”

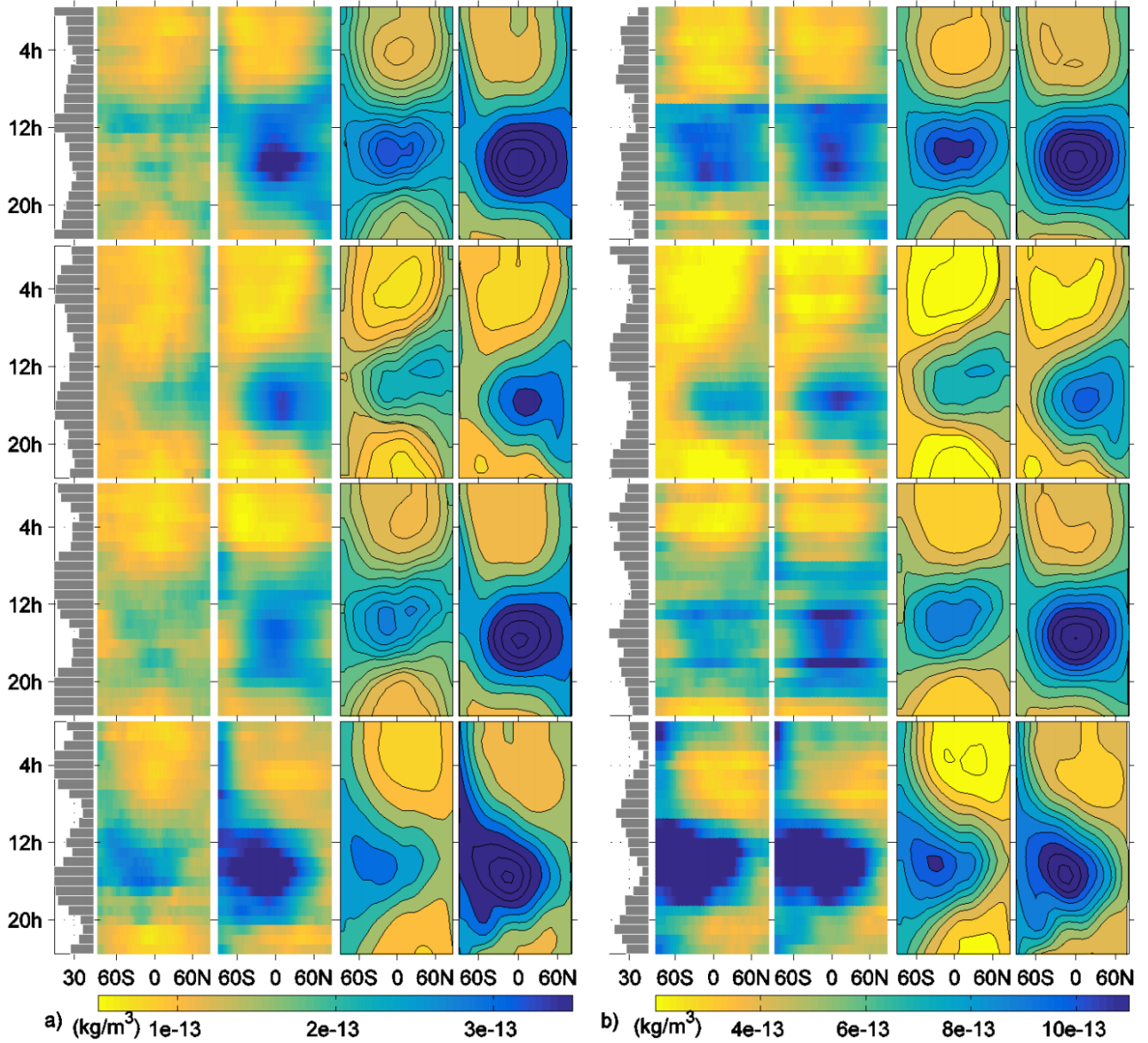


Figure 5.12 Thermospheric density variations at 475 km altitude, in function of LST and latitude (fixed at Greenwich meridian), and for different season and solar-flux conditions. (a) $P_{10.7}=80$ s.f.u. and (b) $P_{10.7}=120$ s.f.u.. From top to bottom, it plots at ME, JS, SE and DS. In each scenario (8 cases), from left to right, averaged accelerometer and MSIS -based densities along GRACE orbits (raster plots), and direct calculations (contour plots) from the parameterization and from MSIS. Each bar-graph corresponds to the occurrences between ± 15 s.f.u. and ± 3 h LST with respect to each scenario (for raster plots only). The direct calculations using the models have been computed with the representative parameters of each scenario. [Calabia and Jin, 2016b, Fig. 12].

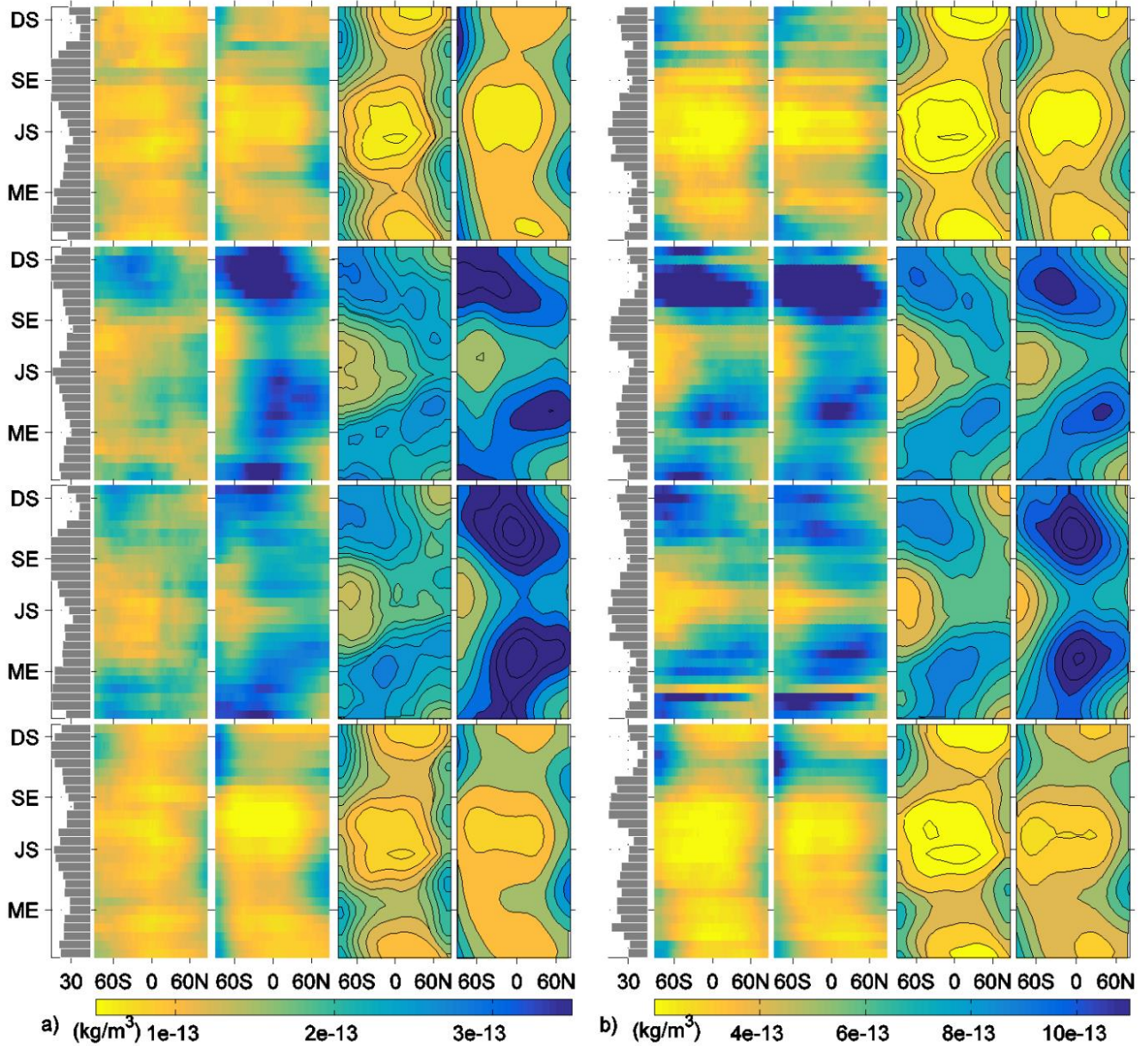


Figure 5.13 Thermospheric density variations at 475 km altitude, in function of *doj* and latitude (fixed at Greenwich meridian), and for different LST and solar-flux conditions. (a) $P_{10.7}=80$ s.f.u. and (b) $P_{10.7}=120$ s.f.u.. From top to bottom, plots at 5, 11, 17, and 23 h LST. In each scenario (8 cases), from left to right, averaged accelerometer and MSIS -based densities along GRACE orbits (raster plots), and direct calculations (contour plots) from the parameterization and from MSIS. Each bar-graph corresponds to the occurrences between ± 15 s.f.u. and ± 3 h LST with respect to each scenario (for raster plots only). The direct calculations using the models have been computed with the representative parameters of each scenario. [Calabia and Jin, 2016b, Fig. 13].

5.3. Long-term trend variations and distribution of thermospheric neutral density

This section investigates long-term trend and global distribution of thermospheric neutral densities derived from GRACE accelerometer measurements. In order to remove LST and annual variations, parameterizations provided in Section 5.2 have been subtracted from the time-series of accelerometer estimates. Figure 5.14 shows the resulting global distribution of the averaged thermospheric neutral mass density (free from LT and annual variations) derived from 12-year of GRACE measurements.

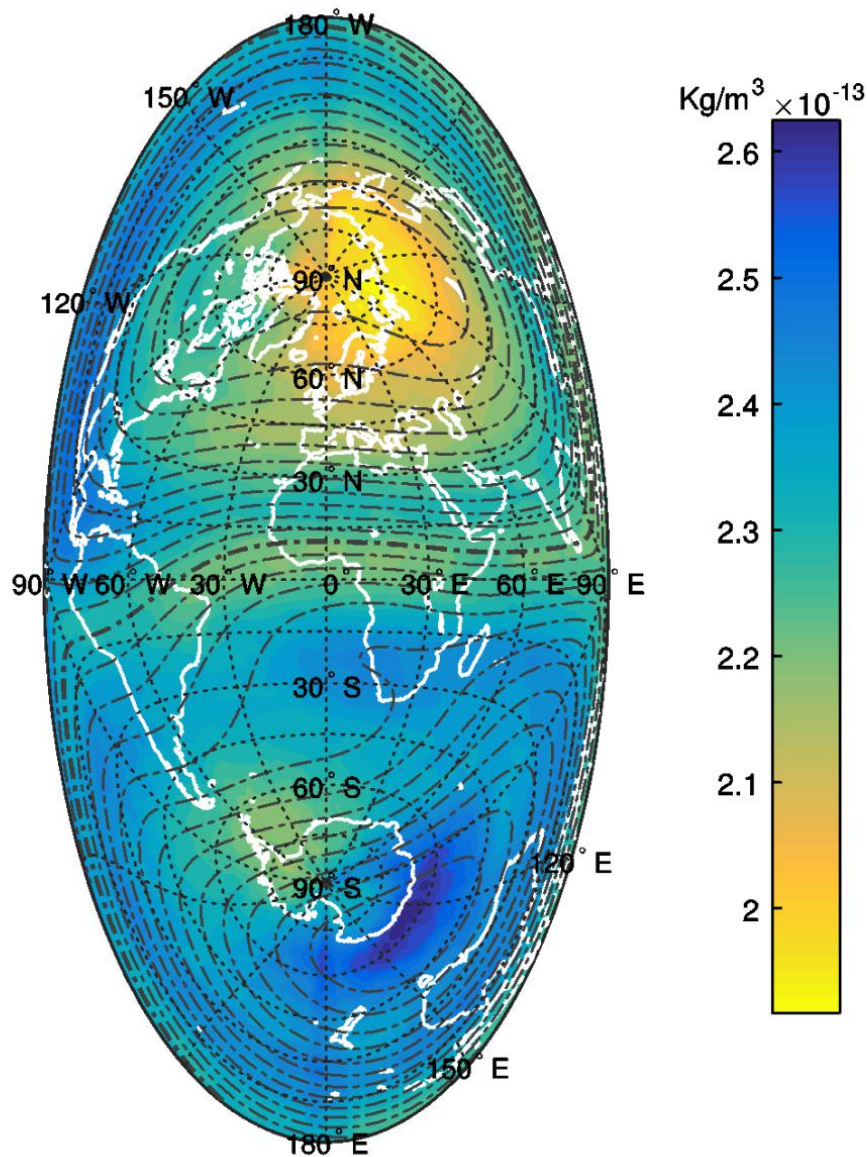


Figure 5.14 Global distribution of the averaged thermospheric neutral mass density from 12-year of GRACE accelerometer-based estimates normalized at 475 km altitude (LT and annual variations have been removed). Dip isoclinic lines are plotted in dash-dot gray format to show the alignments. [Calabia and Jin, 2016c, Fig. 1].

Main features of the global distribution of averaged thermospheric neutral mass densities (Figure 5.14) show higher values in the southern hemisphere, lower values in the northern hemisphere, and a trough that follows the magnetic equator. Two hemispherical asymmetric cells can be recognized in the polar caps. The southern-enhancement is centered in the geomagnetic dip-pole (60S, 120E), showing a relative attenuation centered in the western polar side (75S, 60W). Asymmetrically, the northern-attenuation is located in eastern polar side (75N, 90E), and its corresponding asymmetric relative enhancement in the western polar side (60N, 90W).

Figure 5.15 shows the density differences between the four semi-hemispheric quadrants. The differences in latitude show proportionality between both longitudinal sides (SW-NW \propto SE-NE) as well as the differences in longitude between both latitudinal sides (SW-SE \propto NW-NE). Noticeable differences can be seen during high solar activity (solar F10.7 index is plotted in Figure 5.16, f1), more pronounced in latitude (S-N) than in longitude (W-E).

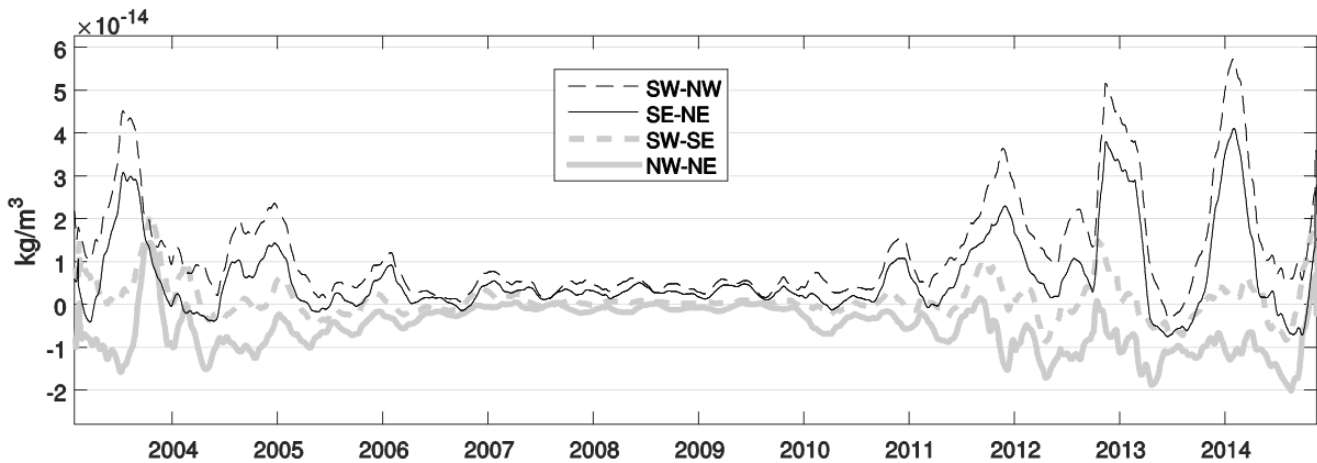


Figure 5.15 Differences between each polar quadrant of 81-day averages of thermospheric densities. [Calabia and Jin, 2016c, Fig. 2].

Hemispheric differences along the time series are plotted in Figure 5.16, together with the 81-day average solution of global densities (free from LST and annual variations), and the parameterization in terms of solar radiation and geomagnetic indices. The latitudinal variation shows higher values of density in the southern hemisphere during all time-span, and strongly controlled by the solar radiation. Maximum values for the 81-day average of South-North differences reach up to $2e-13$ Kg/m³ (e.g., June, 2003; January, 2014). The 81-day average solution of global densities best correlates with the combined solution of F10.7 and A_m

indices (f_2). If only using the solar F10.7 index (f_1) instead, the mean magnitude is underestimated during the year 2003 in $\sim 1.5 \text{ kg/m}^3$.

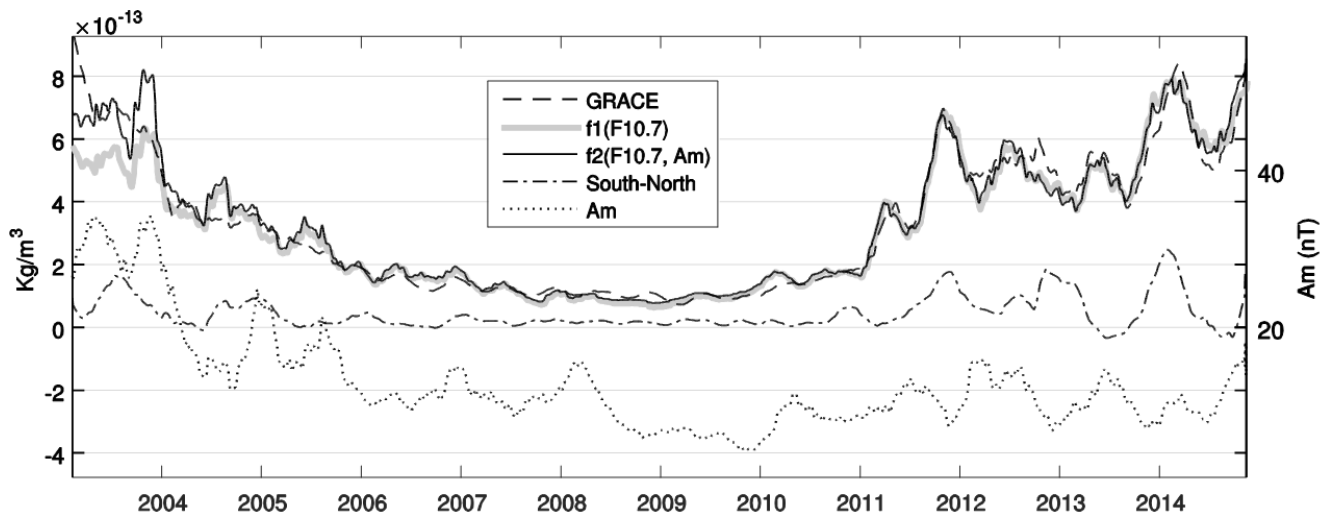


Figure 5.16 The 81-day averages of planetary thermospheric neutral densities are scaled in the left side, together with the differences between polar caps. The values inferred from GRACE accelerometer are plotted in gray line, the fitting in terms of solar F10.7 index (f_1) is plotted in dashed black line, and the fitting in terms of the combined solution of F10.7 and Am indices (f_2) is plotted in solid black line. The geomagnetic Am index (dotted line) is scaled in the right side. [Calabia and Jin, 2016c, Fig. 3].

5.4. Neutral density variations under geomagnetic storms

Thermospheric neutral density distribution during storm-time is of great importance for LEO POD and for the understanding of the MIT coupling. However, these variations are still not well understood and many studies are focusing their research efforts for a better knowledge and modeling of this geophysical phenomenon.

Liu et al. [2005] firstly showed two structured arc-shaped enhancements of $\sim 2000 \text{ km}$ diameter in the aurora regions. The enhancements were located between 75° S and 80° S from 11 h to 18 h MLT, and between 71° S and 74° S at post-midnight. Under perturbed conditions, an expansion toward lower latitudes showed neutral density enhancements in the pre-midnight sector between 50° N and 72° N and between 60° S and 75° S .

Rentz and Lühr [2008] investigated the climatology of the cusp-related thermospheric mass density anomaly, as derived from CHAMP's accelerometer measurements. Their study showed stronger cusp anomalies in the northern hemisphere by a factor of 1.35. The

combined effect of annual JS minimum with a decreasing insolation showed a hemispheric asymmetry with very weak anomalies in the southern cusp. The northern anomaly was located in ME and DS at 74° N cgm and in JS and SE at 72° N cgm. The full latitudinal width at half maximum (FWHM) centered at 12 h MLT rated from 15.9° in JS to 12.3°-14° in the other seasons. The southern anomaly showed to be smaller by 10 %, and shifted to morning hours when compared to the northern anomaly. The Southern latitude was located from 68° S to 76° S, with a FWHM value of 17° to 13°. With one hour delayed and not detectable for values below 1 mV/m, the increase in density anomaly showed to be proportional to the square of the merging electric field (E_m).

Kwak et al. [2009; 2011] showed strong dependence of the southern high-latitude thermospheric densities on the orientation of the IMF. For positive B_y and B_z values, the density variations were respectively opposite to those for negative B_y and B_z . The densities for negative B_z showed a general enhancements over the southern summer hemisphere, and more significant in the cusp region, but with a small decrease at 6 h and 19 h MLT. For negative B_y in the southern summer hemisphere, enhanced values were shown at 12 h and 1 h MLT, and reduced values at 10 h and 19 h MLT. In the southern hemisphere at ME, negative (positive) B_y and B_z values increased (decreased) the high-latitude southern thermospheric densities. On the other hand, in the southern hemisphere at SE, negative (positive) B_y values and positive (negative) B_z values did not show significant changes.

Based on the variations of the ratio between ascending and descending orbits, *Muller et al. [2009]* showed a slightly better parameterization of neutral density δ employing the A_m index instead the A_p index ($\delta(\text{day})=0.012*A_m+0.035$ and $\delta(\text{night})=0.012*A_m-0.045$), with a 3h-delay for the day side, and a 4h-delay for the night-side.

In the following sections, two geomagnetic storms are investigated from accelerometer measurements of the GRACE mission. The first case-study focuses on the severe G4-level storm of March 2015 through neutral density estimates inferred from accurate accelerometer measurements. The second case-study focuses on the moderate G2-level storm of March 2013. For the last case, the GRACE accelerometer measurements were unavailable due to instrument power-off. Fortunately, the POE-based neutral mass density estimates are employed to characterize the anomalous thermospheric neutral density variations during the storm.

5.4.1. *Space weather and geomagnetic indices*

This section investigates the available space weather and geomagnetic indices with the finality to better represent neutral density variations during geomagnetic storm circumstances. First of all, parameterized annual and LST variations of GRACE's thermospheric neutral densities (Section 5.2) have been removed from GRACE's 2011-2016 time-series. Afterwards, three density profiles (North, South, and Equator) have been extracted and correlated for a different time delays to the available space weather and geomagnetic indices. Figure 5.17 shows the correlation coefficients for space weather and geomagnetic indices with respect density variations free from LST and annual dependence.

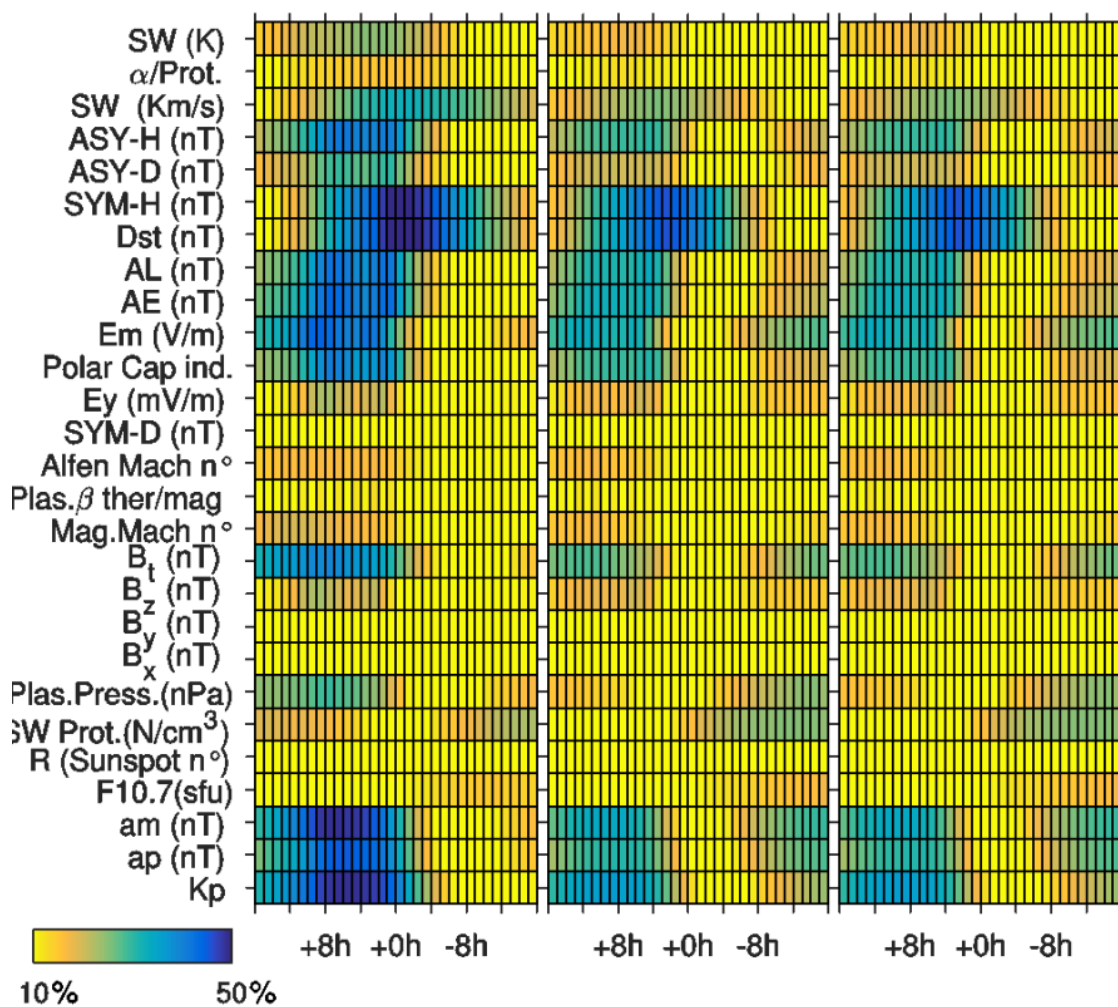


Figure 5.17 Correlation coefficients versus delay-times for space weather and geomagnetic indices with respect to density variations during 2011-2016 (free from annual and LST variations). Values for (left) northern, (middle) equatorial, and (right) southern regions. [Calabia and Jin, 2017, Fig. 10].

Table. 5.2 Maximum values and respective delay-times for space weather and geomagnetic indices with respect to density variations during 2011-2016 (free from annual and LST variations). Values are given for northern, equatorial, and southern regions. [Calabia and Jin, 2017, Table 1].

	North		Equator		South	
	max (%)	delay (h)	max (%)	delay (h)	max (%)	delay (h)
<i>Kp</i>	49	6	36	9	40	3
<i>Ap</i> (nT)	45	6	31	7	36	3
<i>Am</i> (nT)	49	7	34	9	41	4
<i>Bz</i> (nT)	23	9	20	7	22	3
<i>Bt</i> (nT)	40	8	29	12	30	8
<i>Ey</i> (mV/m)	24	8	20	6	24	2
<i>PC</i> ind.	41	8	31	5	37	1
<i>Em</i> (V/m)	45	9	33	13	38	3
<i>AE</i> ind.(nT)	44	8	34	5	41	1
<i>AL</i> ind. (nT)	42	8	33	5	40	1
<i>Dst</i> (nT)	52	0	46	3	43	0
<i>SYM-H</i> (nT)	51	0	46	3	43	0
<i>ASY-D</i> (nT)	30	1	21	5	27	1
<i>ASY-H</i> (nT)	41	6	30	5	36	1
<i>SW</i> Vel.(Km/s)	33	0	26	4	29	0
<i>SW</i> Temp.(K)	25	4	18	8	23	2

Space weather and geomagnetic indices have been downloaded from the Low Resolution OMNI (LRO) data set of NASA (<http://omniweb.gsfc.nasa.gov/form/dx1.html>), and from the International Service of Geomagnetic Indices (ISGI) website (http://isgi.unistra.fr/data_download.php). The merging electric field (E_m) has been computed following the indications in Liu *et al.* [2010]: $E_m = v_{sw} B_T \sin^2(\theta/2)$, where v_{sw} is the solar wind speed, $B_T = \sqrt{B_y^2 + B_z^2}$ is the transverse component of IMF in Geocentric-Solar-Magnetospheric (GSM) coordinates, and θ is the IMF clock angle defined by $\tan(\theta) = |B_y| / B_z$ ($0 \leq \theta \leq \pi$).

Correlation coefficients have been calculated for hourly delay-times ranging from ± 16 h for the northern (dN), southern (dS), and equatorial regions (dEq). Density profiles for each region correspond to an averaged neutral density of a 30° band in latitude. Maximum correlations and their respective delay-times for some selected indices are given in table 5.2. Best correlations are found when employing the k-derived planetary indices (Kp , Ap , Am), the

interplanetary total magnetic field B_T , the Polar Cap index horizontal component disturbances PC , the E_m , the auroral index horizontal component disturbances (AE , AL), the equatorial index horizontal component disturbances Dst , the longitudinally asymmetric and symmetric horizontal component disturbances ($SYM-H$, $ASY-D$, $ASY-H$), and the solar wind (SW) velocity and temperature. Note that $SYM-H$ is essentially the same as the Dst index with a different time resolution. From table 5.1, the highest correlation is achieved when employing the Dst index, being about 45 % for equatorial and southern regions, and 52 % for the northern region. The corresponding time-delays for these maxima are null for high latitudes and about 3 h for low latitudes. The K-derived planetary indices (Kp , Ap , Am) show better represent high-latitude than low-latitude density variations in about 10 %, and with about 3, 6 and 9 h delay for the southern, northern, and equatorial regions respectively.

5.4.2. The March 2015 geomagnetic storm

On March 17th, 2015, the strongest geomagnetic storm of this dejected solar cycle occurred with the consequent variations in our planetary system. The energetic solar wind plasma with the favorable disposition of the IMF delivered Joule heating and particle precipitation on Earth, through the collisions between the ionospheric plasma and the thermospheric neutrals. Then, anomalous variations in the global thermospheric neutral density were consequently originated as a result of the released energy. The G4-level (severe) geomagnetic storm of March 2015 occurred at equinox period and under moderated solar-flux circumstances (F10.7 ~120 s.f.u.).

Plotted from right to left, Figure 5.18 shows the interpolated grid time-series of thermospheric neutral densities inferred from GRACE accelerometer measurements for the period 16 to 18 March 2015. In that moment, the GRACE satellites were located at 6:25 h LST and the corresponding +12 h for the complementary orbital leg. In this case-study, the removal of annual and LST variations has not been required because at equinox period and for the corresponding LST location of GRACE on that day both ascending and descending orbital legs provide relatively small differences.

In Figure 5.18, first anomalies on neutral density estimates are detected at 12 h (UT) 17th March 2015 on the southern cusp, followed by an equatorward traveling disturbance. The northern cusp shows to react few hours later. To peaks of density can be recognized at both high latitudes. At the bottom panels of Figure 5.18, the merging electric field (E_m) [Liu et al.,

2010] and the geomagnetic Am and Equatorial Dst indices are plotted for the same timeline. All three indices show to be clear precursors of density enhancements during this storm, being E_m and Am indices more analogous to cusp enhancements (two recognized peaks), and Dst index to equatorial variations.

Figure 5.19 and 5.20 show the daily-maxima and the daily-averaged deviations per latitude with respect to the monthly median (in %), for the G4-level (severe) geomagnetic storm of March 2015. When comparing to the quiet-time surrounding period, density enhancements reach maxima deviations of 500 % (Figure 5.19), and daily-averaged deviations arise up to 180 % (Figure 5.20).

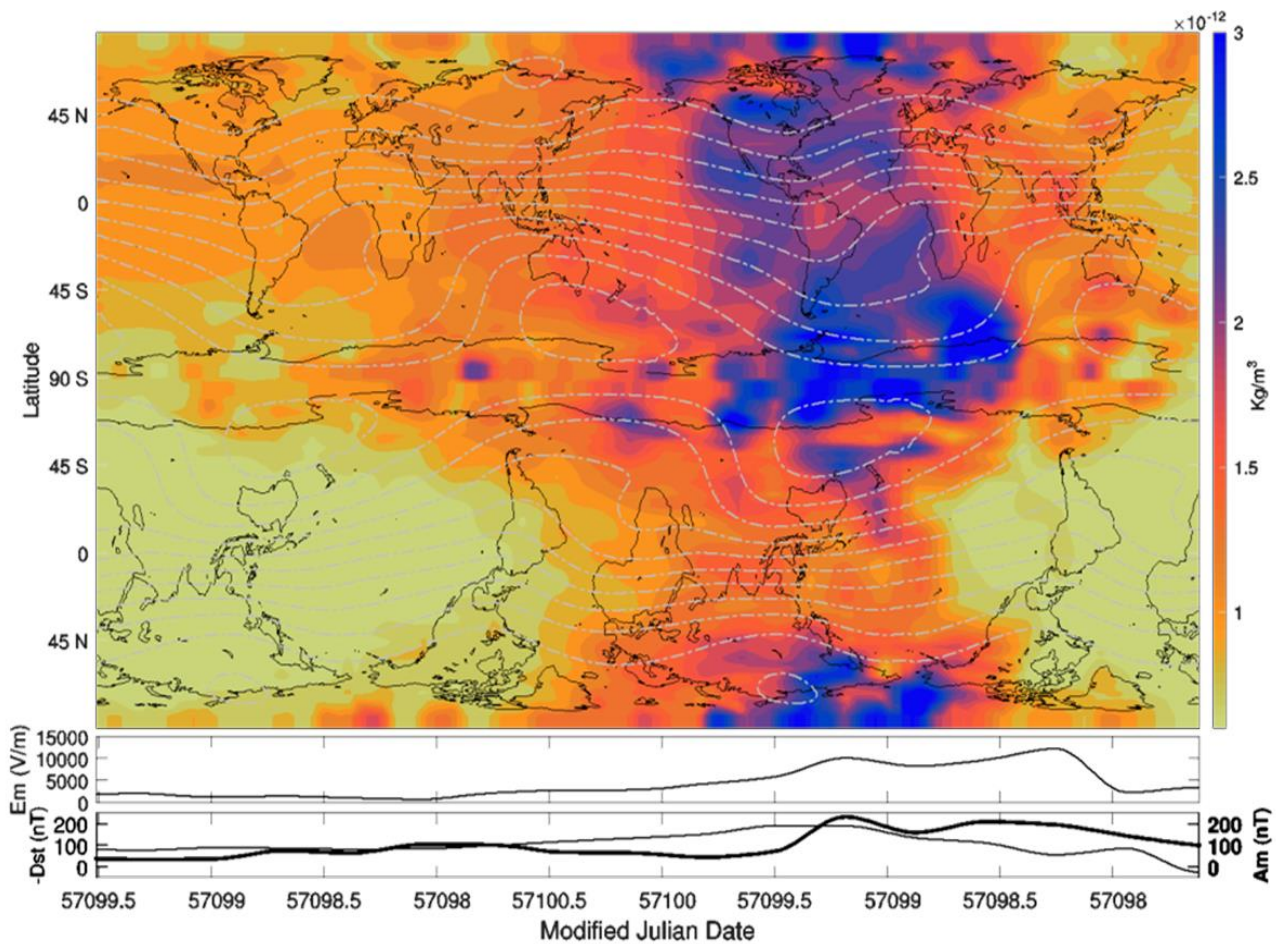


Figure 5.18 Densities inferred from GRACE for the G4-level (severe) geomagnetic storm of March 2015 (Top panel). Note that annual and LST variations have not been removed from density estimates. Dip isoclinic lines are plotted in dash-dot gray format to show the alignments. Bottom panels show the merging electric field (E_m), and geomagnetic Am (thick line) and Dst (thin line) indices. [Calabia and Jin, 2016d, Fig. 2].

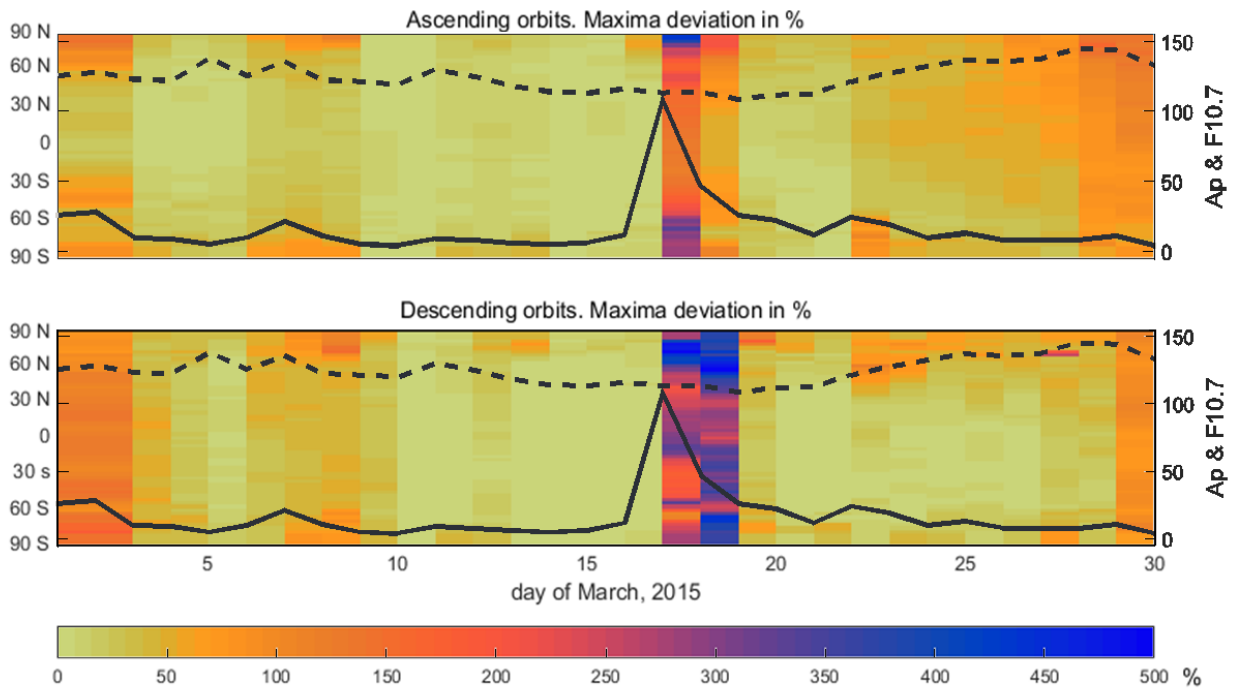


Figure 5.19 Daily maxima deviation per latitude with respect to the monthly median (in %), for the G4-level (severe) geomagnetic storm of March 2015. The dashed line denotes the solar F10.7 index and the solid line the geomagnetic Ap index, both scaled on the right.

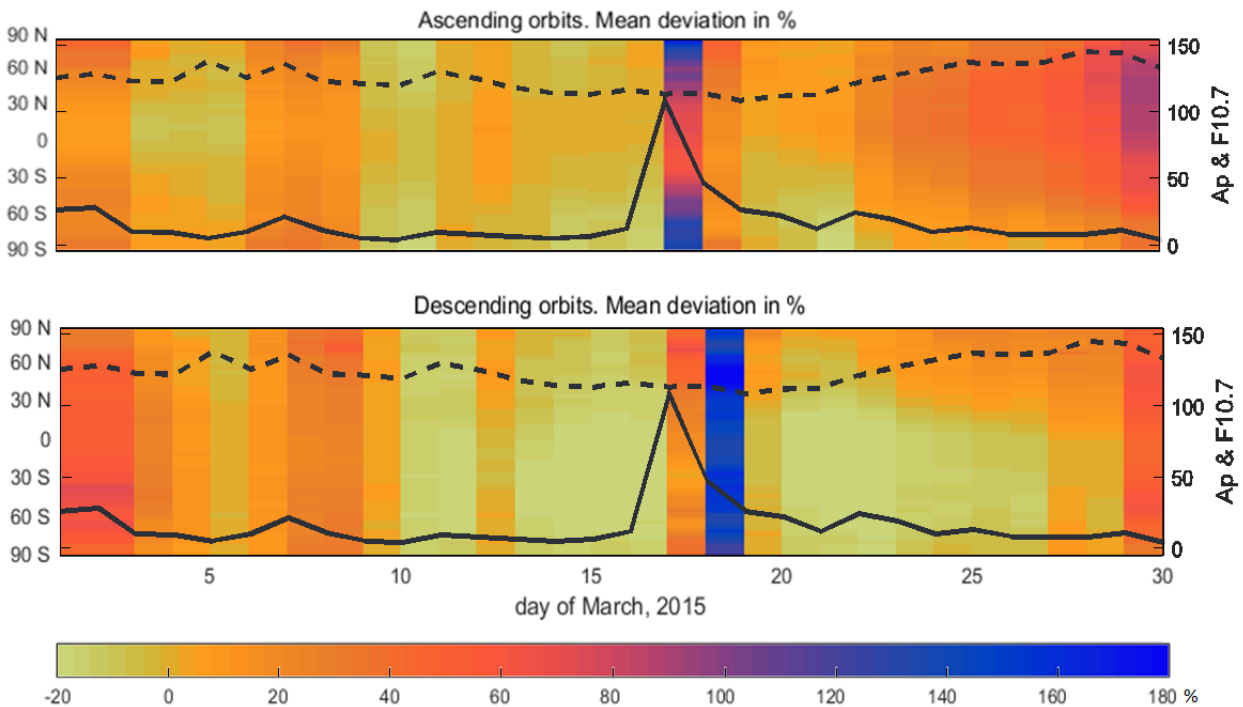


Figure 5.20 Daily mean deviation per latitude with respect to the monthly median (in %), for the G4-level (severe) geomagnetic storm of March 2015. The dashed line denotes the solar F10.7 index and the solid line the geomagnetic Ap index, both scaled on the right.

Figure 5.21 pictures the thermospheric neutral densities inferred from GRACE accelerometers and from the NRLMSISE-00 empirical model for the G4-level (severe) geomagnetic storm on 17-18 March, 2015, both normalized at 475 km altitude. Note that densities from the NRLMSISE-00 empirical models have been calculated along the satellite orbit at the same times as the accelerometer measurements. From this figure, it can be seen that the NRLMSISE-00 model is unable to reproduce most of the observed features, with smaller amplitudes and mean deviated values. First anomalies can be seen at 12 h UT on 17th March, 2015, reaching values at the end of the day up to $4 \cdot 10^{-12}$ kg/m³, while the NRLMSISE-00 model only up to $2 \cdot 10^{-12}$ kg/m³.

Figure 5.21 and 5.22 show that the NRLMSISE-00 model underestimates up to about the 70 % of the mean magnitude, and about the 50 % in amplitude at the peak of maximum density anomaly. After the storm, the NRLMSISE-00 model seems to overestimate the mean value of accelerometer measurements in about 170 % for a period of 48 hours. Since GRACE satellites were located at 6:25 h LT and the corresponding +12 h for the complementary orbital leg, higher values of density correspond to the sunlight side of Earth, and cusp enhancements are clearly located in between day-to-night transitions.

Finally, the mean-per-orbit neutral density estimates have been parameterized for this storm in terms of solar flux (F10.7), solar wind merging electric field (E_m), and geomagnetic A_p index. The optimal delay for best fitting is achieved at 6 h. Modeled neutral densities are plotted in Figure 5.22, showing a better representation of storm-time variations than those given by the NRLMSISE-00 empirical model.

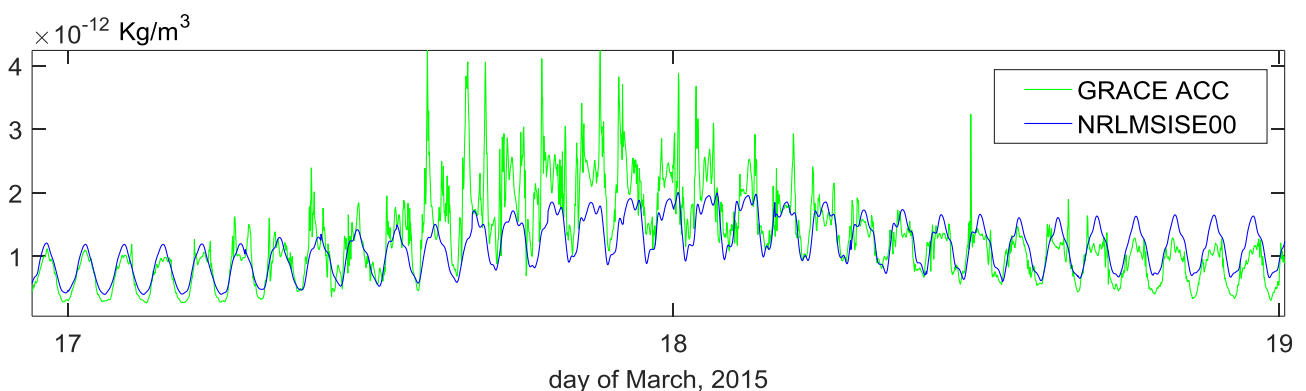


Figure 5.21 In green color neutral densities inferred from GRACE accelerometers normalized to 475 km on 17-18 March, 2015. Note that annual and LST variations have not been removed from density estimates. In blue color the NRLMSISE-00 neutral densities calculated along the satellite orbit at the same times as the accelerometer measurements. [Calabia and Jin, 2016d, Fig. 3].

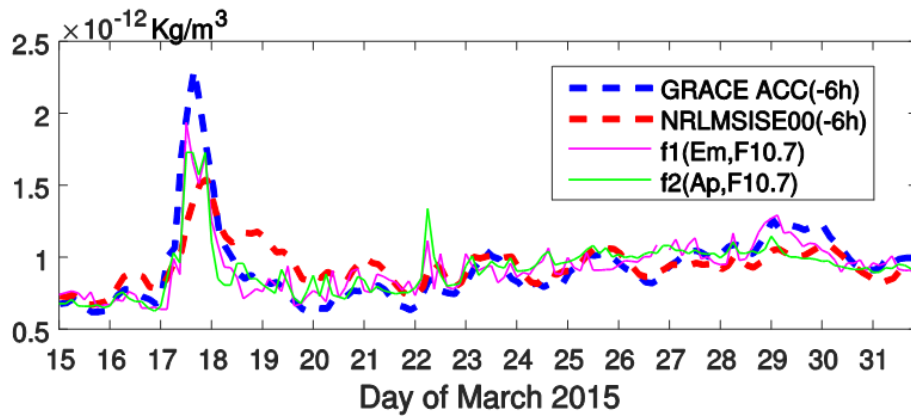


Figure 5.22 Mean values per orbit of neutral densities for GRACE normalized to 475 km on March, 2015. In blue color accelerometer measurements, in red color the NRLMSISE-00 neutral densities calculated along the satellite orbit at the same times as the accelerometer measurements. Parameterized densities $f1(Em, F10.7)$ and $f2(Ap, F10.7)$ are plotted in magenta and green colors, respectively. [Calabia and Jin, 2016d, Fig. 4].

5.4.3. *The March 2013 geomagnetic storm*

On March 15th, 2013, the Sun erupted with an Earth-directed CME during a period of low solar-flux circumstances ($F10.7 \approx 120$ s.f.u.). Consequently, the solar wind increased up to 700 Km/s, along with a southwards B_z component of the IMF. After two days, the halo CME arrived to Earth and produced a moderate G2-level geomagnetic storm. As a result, the energetic solar wind plasma with the favorable disposition of the IMF produced thermospheric Joule heating and particle precipitation along the Earth's magnetic field lines. Since neutral density in the upper atmosphere is too low for molecular interactions, the dynamics then acted through the collisions between the ionospheric plasma and the neutrals, creating consequently anomalous variations in the global distribution of neutral mass density.

Unfortunately, accelerometer measurements during this storm were unavailable for both for GRACE A and B satellites (due to instrument power-off). However, POE-based thermospheric mass densities (Section 4.2) can be employed to characterize the anomalous behavior of density distribution at this time. This section investigates thermospheric neutral density variations due to the moderate G2-level geomagnetic storm of March 2013 by only using GRACE's POE-based estimates.

On March 2013, the GRACE satellites were approximately located at 24 h LST and the corresponding +12 h for the complementary descending orbital leg. In order to study short-term variations in a proper manner, parameterized LST and annual variations (Section

5.2.2) have been extracted from the time-series of grids. Figure 5.23 compares thermospheric density variations inferred from GRACE POE during the moderate G2-level geomagnetic storm of 16-17 March 2013 (free from LST and annual variations) with the available space weather and geomagnetic indices (see Section 5.4.1 for description of each index).

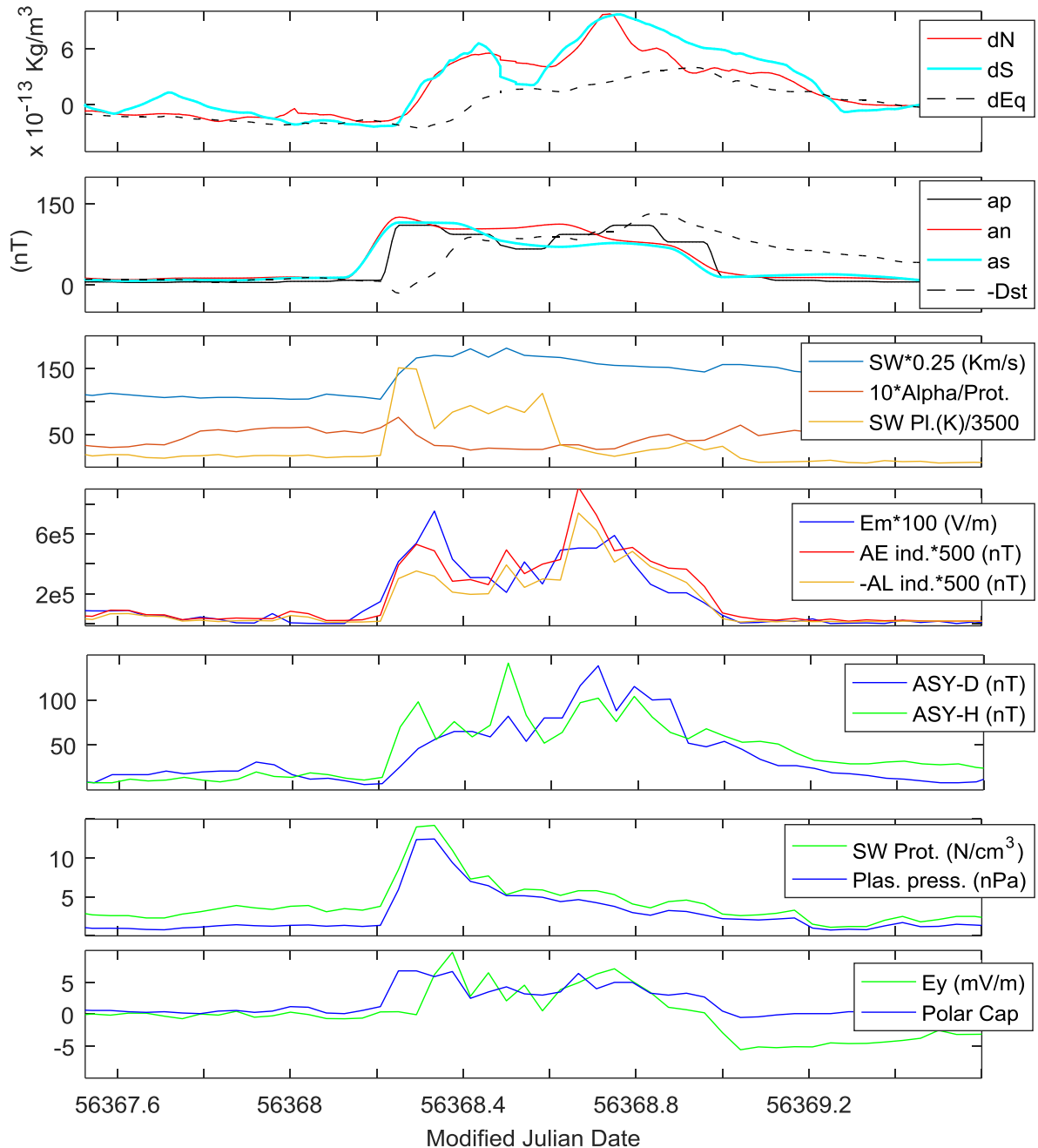


Figure 5.23 Top panel shows profiles at equator (dEq) and poles (dN , dS) of thermospheric neutral density inferred from GRACE POE (free from LST and annual variations). Space weather and geomagnetic indices are plotted in the below panels (see Section 5.4.1 for description of each index). Magnitudes have been re-scaled as indicated in the legends.

Density profiles in Figure 5.23 correspond to averaged values of a band of 30° width in latitude, located at equator (dEq) and each pole (dN , dS). Note that LST and annual variations have been removed, so the negative values indicate that neutral density decreases previous to the storm. This intriguing feature should be investigated in future research. As expected from Section 5.4.1, the most representative indices for this storm are the Ap , An , As , Dst , AE , AL , $ASY-D$, $ASY-H$ and PC indices, as well as the E_m and the SW velocity and temperature. In addition, first panel shows that high latitude variations follow a different pattern than the equatorial profile of density. The equatorial profile of density is better represented by the Dst index (dEq and Dst are plotted in dashed black line).

Figure 5.24 shows the interpolated grid time-series of thermospheric neutral densities for the same period (free from LST and annual variations). In this figure, time evolution is defined as the satellite measurements were taken, that is to say, from right to left as the Earth rotates with respect to GRACE's orbital plane, and from bottom to top following the along track direction. Bottom panels of Figure 5.24 show the corresponding dN , dS and dEq profiles of density, and the AE , E_m , Dst , Ap , As , and An indices (same as Figure 5.23). Note that geomagnetic An (North) and As (South) indices are the hemispheric indices employed to obtain the geomagnetic Am index ($Am = (An + As) / 2$).

Although Figure 5.17 and Table 5.1 show that density variations better correlate with Dst and k-derived geomagnetic indices, Figure 5.24 shows that high-latitude density (dN and dS) have better agreement with AE and E_m . For instance, the two peaks of density seen in dN and dS at 56368.4 MJD and 56368.7 MJD have better agreement with AE and E_m (3 h delay). On the other hand, An , As , and Ap in Figure 5.24 show deficiently correlate with these two peaks. As for the low latitude variations, the Dst index shows better agreement with the dEq profile (3 h delay). Low-latitude variations are well represented with the equatorial Dst index (3 h delay).

On March 26th 2013, a new sunspot was detected into the eastern solar limb, and a minor G1-level geomagnetic storm on Earth was noticed on March 29th 2013. Figure 5.25 shows the neutral density variations due to this minor geomagnetic storm. Similar results are found for this and the previous cases. A better agreement is depicted for AE and E_m indices when comparing with high-latitude variations (dN and dS), and the geomagnetic Dst index shows to better correlate with low-latitude variations (dEq).

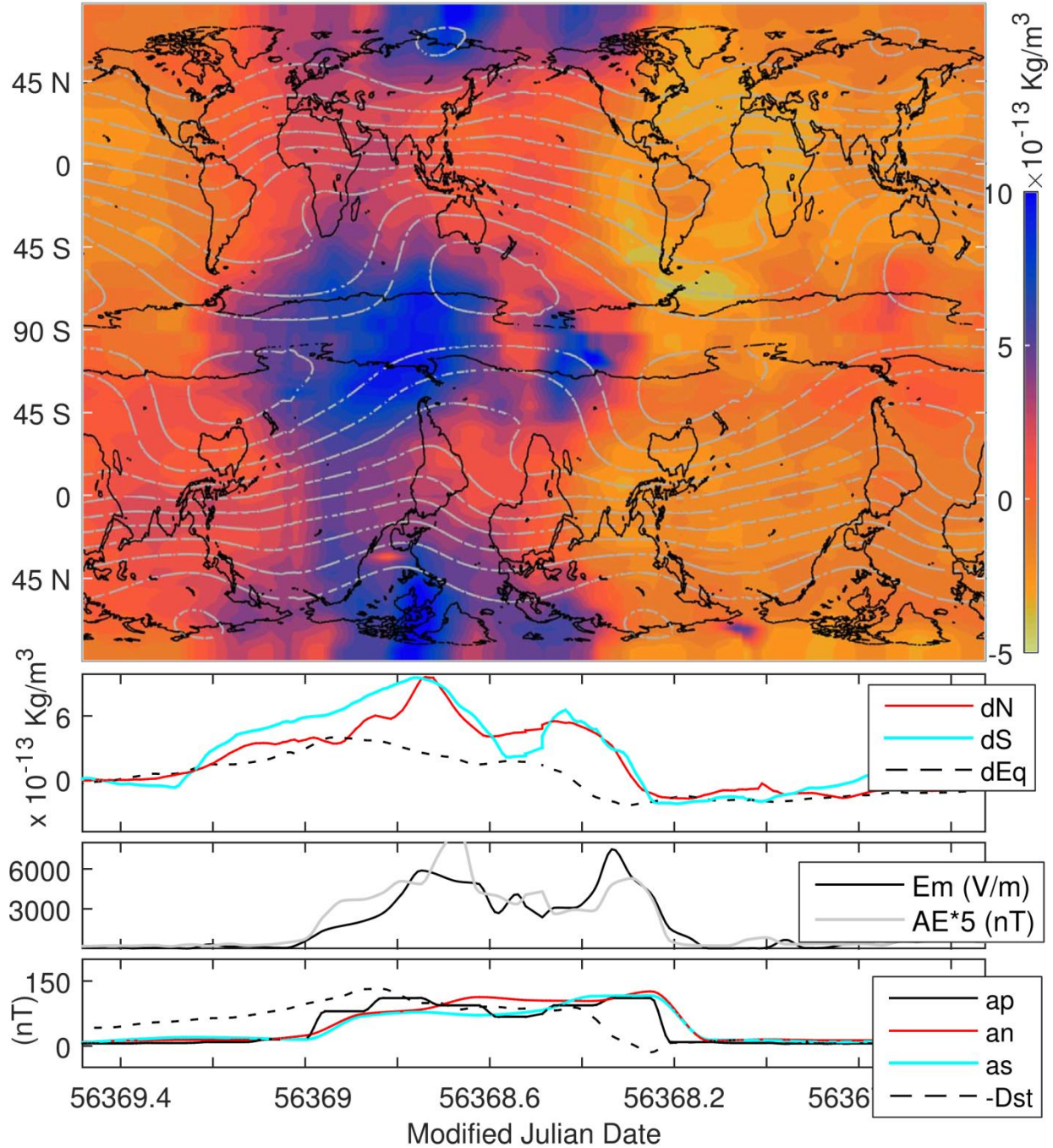


Figure 5.24 Thermospheric neutral density variations inferred from GRACE POE (free from LST and annual variations) and its profiles at equator (dEq) and poles (dN , dS), plotted together with E_m , AE , A_p , A_n , and, A_s indices, for the moderate G2-level geomagnetic storm of 16-17 March 2013 (from right to left and from bottom to top: 12^h 36^m 16/March/2013 to 11^h 35^m 18/March/2013). GRACE's angle β' during this period is 173° (Sun to ascending leg). Accelerometer-based densities are not available due to instrument power-off during this month. Dip isoclinic lines are plotted in dash-dot gray format. [Calabia and Jin, 2017, Fig. 11].

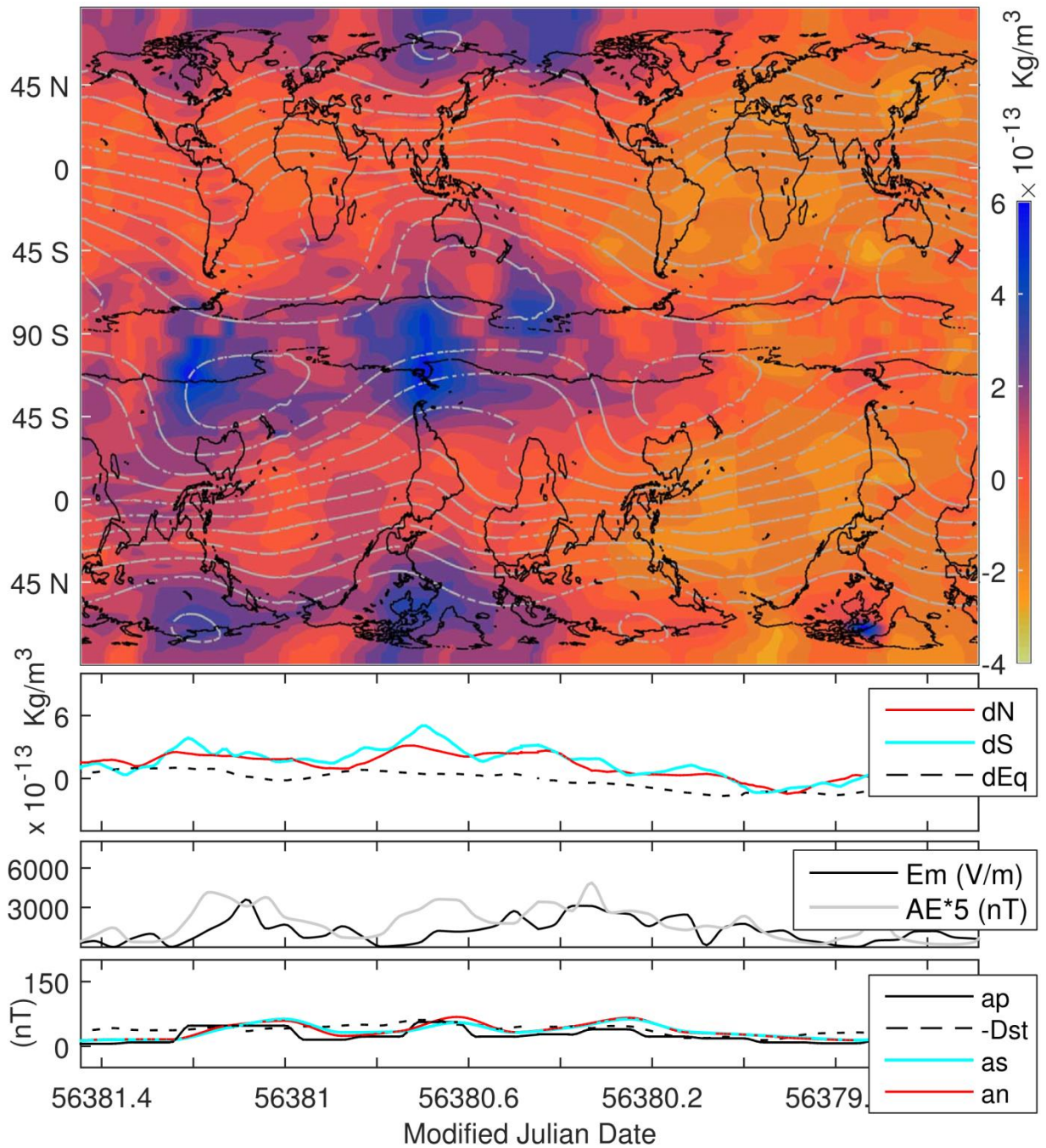


Figure 5.25 Thermospheric neutral density variations inferred from GRACE POE (free from LST and annual variations) and its profiles at equator (dEq) and poles (dN , dS), plotted together with E_m , AE , Ap , An , and As indices, for the minor G1-level geomagnetic storm of 28-29 March 2013 (from right to left and from bottom to top: 11^h 42^m 28/March/2013 to 10^h 41^m 30/March/2013). GRACE's angle β' during this period is 186° (Sun to ascending leg). Accelerometer-based densities are not available due to instrument power-off during this month. Dip isoclinic lines are plotted in dash-dot gray format. [Calabia and Jin, 2017, Fig. 12].

5.5. Summary

In this chapter, an extensive study on thermospheric neutral density distribution and variations is given from 13 years of GRACE measurements, including two geomagnetic storms. The main results are summarized as follows:

- Thermospheric neutral density variations from GRACE measurements for the period 2003-2016 have been successfully investigated using a new technique based in the PCA. The resulting modes have shown to be strongly controlled by solar flux and geomagnetic activity, and modulated by radiation-waves and annual fluctuations. At first, the selected PCA time-expansion coefficients have been parameterized in terms of LST, doy, and solar P10.7 flux and geomagnetic Am indices. The modeling of all periodic variations is the modulation in amplitude of sinusoidal functions, which have been previously fitted into a common-flux normalized data. The parameterization of the sub-solar-point annual-variation shows two maxima around June (one at early May, and a reduced at the end of July), and only one in December. The LST parameterization shows a new fluctuation controlling a middle-latitude 4-wave pattern, with two maxima at 12 h and 21 h LST and two minima at 1 h and 17 h LST. The model based in the PCA parameterization is suitable to represent small scale variations including, e.g., EMA and MDM, and can be used to improve the current thermosphere modeling. The results are in agreement with that given by previous studies, and show a better characterization of the global thermospheric air mass density distribution and variations, than that represented by the NRLMSISE00 empirical model. Overall, the differences between the analyzed densities and the MSIS model are significant in both structure and magnitude.
- Furthermore, the residuals from the PCA parameterization have been analyzed in the spectral domain, and additional periodic contributions have been found at the frequencies of the radiational tides (P1, K, T2, and R2). In addition, periodic contributions are found at the periods of 83, 93, 152 and 431 days. The 93-day period could be caused by the satellite's drift of perigee, and the 83 and 152 day periods might be attributed to solar activity. Variations at the free-core nutation frequency (431 day) suggest a possible core-MIT coupling.

- As for the long term variations, the average distribution shows a clear alignment with the geomagnetic field, with higher values in the southern hemisphere than in the northern hemisphere. Two asymmetric cells are located in the polar caps: a southern-enhancement, and a northern-attenuation, both located in their eastern polar sides. In addition, each polar-cell has a corresponding attenuation (enhancement) in the western polar side. The latitudinal variation shows higher values of density in the southern hemisphere during all time-span, and strongly controlled by the solar radiation. A considerable magnetospheric forcing on the long-term global thermospheric mass density is recognized, with a noticeable contribution in 2003.
- Space weather and geomagnetic indices have been correlated with neutral density variations during geomagnetic storm circumstances, and best results are found when employing the indices of Kp , Ap , Am , B_T , PC , E_m , AE , AL , Dst , $SYM-H$, $ASY-D$, $ASY-H$, and SW velocity and temperature. The highest correlation is achieved when employing the Dst index, with a time-delays null for high latitudes, and about 3 h for low latitudes. The K-derived planetary indices (Kp , Ap , Am) show better represent high-latitude than low-latitude density variations in about 10 %, and with about 3, 6 and 9 h delay for the southern, northern, and equatorial regions, respectively.
- The severe G4-level storm of March 2015 has been investigated from accelerometer measurements of GRACE, and compared to the NRLMSISE-00 empirical model. First anomalies are detected on the southern cusp, followed by several equatorward traveling atmospheric disturbances. When comparing to the quiet-time surrounding period, the corresponding density enhancements peaked at the cusp regions with absolute maxima deviation and maximum of mean latitudinal deviation above 500 % and 180 %, respectively. Mean values per orbit of neutral mass densities have been parameterized in terms of solar flux (F10.7), E_m , and Ap index. Both E_m and Ap parameterizations from GRACE seem to better represent storm-time neutral density variations than the NRLMSISE-00 empirical model. NRLMSISE-00 has shown to be incapable to reproduce most of the observed features, and with estimations clearly deviated in amplitude and mean value.

- The moderate G2-level geomagnetic storm of March 2013 has been investigated from GRACE's POE-based neutral density estimates. Accelerometer measurements were unavailable (due to instrument power-off) for both for GRACE A and B satellites during this storm, but the POE-based estimates have successfully characterized the anomalous behavior of density distribution. In order to study short-term variations in a proper manner, LST and annual variations have been extracted from the time-series of grids using the PCA parameterizations. The auroral electrojet activity index AE as well as the merging electric field E_m have shown good agreement with high latitude variations, and the low-latitude variations are better represented with the Dst index.

6. CONCLUSIONS AND PERSPECTIVE

6.1. Conclusions

In this dissertation at first, a new methodology is proposed to derive non-gravitational accelerations from the GRACE and GOCE first derivatives of precise-orbit velocities, by computing through an a-priori arc-to-chord threshold plus the subtraction of the time-varying gravity model. The new GPS POE-estimates for the GRACE mission show a very good agreement with accelerometer measurements, but the results for GOCE allocate little information to retrieve non-gravitational accelerations. After subtracting the modelled time-varying gravity forces from the POE-based accelerations, cross-track axes of both GRACE satellites have shown to be affected by a periodic error of unknown source. For the GOCE mission, the periodic error is pictured in all three axes, and with similar amplitudes and frequencies. Therefore, it is to assume these systematic errors are inherent to the generalized POD scheme, and not caused by errors related to a specific mission. This new method to derive non-gravitational accelerations does not require a POD scheme, and serves as a reliable reference with unbiased solution for accelerometer calibration. Then, calibration parameters for GRACE accelerometers have been modelled with lineal functions through a least squares robust fitting.

In addition, a new method based on the PCA technique to investigate spatial patterns of variability, their time variation and the measure of their importance from sparsely distributed measurements along orbits is proposed and successfully applied in three case-studies thoroughly this dissertation:

- In the first case, the conservative-force anomalies derived from analytical TVG models, accurate orbit solutions, and accelerometer measurements have been analyzed in space and time through this new method based on the PCA technique. The results have revealed intriguing structures at the sub-daily frequencies, and the use of an atmospheric tide model (e.g., *Biancale and Bode [2006]*) is strongly recommended for future research. Long-term anomalies show latitudinal variations related to the eclipse times, and residuals linked to geodynamical and hydrological processes.
- In the second case-study, both accelerometer and POE -based thermospheric neutral densities have been estimated using the drag-force formula, and the differences between accelerometer-based densities and the NRLMSISE00 estimates are investigated with the

new PCA-based technique for the period 2003-2015. Marked patterns of variability have shown the incapability of NRLMSISE00 to accurately represent the regular variations and the characteristic global distribution of thermospheric neutral density given by the measurements. GRACE's POE-based density estimates have shown good agreement with accelerometer-based densities and can be used for thermospheric modeling.

- In the last and most important case, an extensive study on thermospheric mass density distribution and variations is presented from 13 years of GRACE measurements using the new PCA-based technique. The resulting modes have been parameterized in terms of LST, *doy*, and solar P10.7 flux and geomagnetic *Am* indices. The parameterization of the sub-solar-point annual-variation shows two maxima around June, and only one in December. The LST parameterization shows an interesting fluctuation controlling a middle-latitude 4-wave pattern. This model is suitable to represent small scale variations including, e.g., EMA and MDM, and can be used to improve the current thermosphere modeling. The results are in agreement with that given by previous studies, and show a better characterization of the global thermospheric air mass density distribution and variations, than that represented by the NRLMSISE00 empirical model. The residuals from the PCA parameterization have been analyzed in the spectral domain, and additional periodic contributions have been found at the frequencies of the radiational tides (P1, K, T2, and R2). In addition, periodic contributions are found at the periods of 83, 93, 152 and 431 days. The 93-day period could be caused by the satellite's drift of perigee, and the 83 and 152 day periods might be attributed to solar activity. Variations at the free-core nutation frequency (431 day) suggest a possible Core-MIT coupling.

Moreover, a study on long-term variations has been performed by removing the main parameterized LST and annual variations. The average distribution shows a clear alignment with the geomagnetic field, with higher values in the southern hemisphere than in the northern hemisphere. Two asymmetric cells are located in the polar caps: a southern-enhancement, and a northern-attenuation, both located in their eastern polar sides. In addition, each polar-cell has a corresponding attenuation and enhancement in the western polar side. The latitudinal variation shows higher values of density in the southern hemisphere during all time-span, and strongly controlled by the solar radiation.

Finally, two geomagnetic storms have been investigated, one from accelerometer measurements (the severe G4-level storm of March 2015), and the other from POE-based estimates (the moderate G2-level storm of March 2013). For the severe G4-level storm of March 2015, first anomalies are detected on the southern cusp, followed by several equatorward traveling atmospheric disturbances. When comparing to the quiet-time surrounding period, the corresponding density enhancements peaked at the cusp regions with absolute maxima deviation and maximum of mean latitudinal deviation above 500 % and 180 %, respectively. Space weather and geomagnetic indices have been investigated in relation to neutral density variations during geomagnetic storm circumstances, and the highest correlation is achieved when employing the Dst index, with a time-delays null for high latitudes and about 3 h for low latitudes. The K-derived planetary indices (Kp , Ap , Am) show better represent high-latitude than low-latitude density variations, with about 3, 6 and 9 h delay for the southern, northern, and equatorial regions, respectively. Mean values per orbit of neutral mass densities have been parameterized in terms of solar flux (F10.7), E_m , and Ap index. Both E_m and Ap parameterizations from GRACE seem to better represent storm-time neutral density variations than the NRLMSISE-00 empirical model. The NRLMSISE-00 empirical model is incapable to reproduce most of the observed features, and with estimations clearly deviated in amplitude and mean value. During the moderate G2-level geomagnetic storm of March 2013, accelerometer measurements were unavailable (due to instrument power-off) for both for GRACE A and B satellites, but the new POE-based estimates have successfully characterized the anomalous behavior of density distribution. For this storm, AE as well as E_m have shown good agreement with high latitude variations, and the low-latitude variations are better represented with the Dst index.

6.2. Problems and perspective

The main source of ions for the ionosphere is originated by the photoabsorption, photoionization, and photodissociation of molecules through EUV solar radiation in the thermosphere, and energy-transfer varies with LST, annual, and solar-rotational cycles. Variations in energy exchange from ions to neutrals produce the expansion/contraction of the thermosphere, and the consequent changes of neutral density distribution. Existing plasma is also transported vertically with the neutral medium, and the energy-transfer along the magnetic field lines produce currents, joule heating, and electric fields. The present MIT models are unable to predict this complex variability as accurately and efficiently required,

and the resulting processes from geomagnetic storms, solar flares and solar wind (coronal mass ejections, shocks, high speed streams, and high intensity long duration aurora activity) are still not well understood.

During this current era of LEO and space/planetary exploration, geodetic small satellites are continuously evolving, and many scientific missions are providing abundant kinds of valuable measurements. For instance, besides on-board GNSS receivers, accelerometers and SLR reflectors, several instruments can be employed to improve the accuracy of the POD and related products (e.g., *Hwang et al. [2008]*; *Canuto et al. [2010]*). Since the accurate prediction of POE is the result of an integrated knowledge of the neutral mass density variation driven both by space weather and climate over the course of a LEO mission lifetime, the measured non-gravitational accelerations can be used to derive and investigate neutral mass density variations. With the increasing number of LEO satellites being equipped with a high-precision GNSS receivers and more enhanced data processing and orbit determination strategies, the recent advances in retrieving non-gravitational accelerations through POD estimators have shown very satisfactory results in neutral density estimation. However, these POD-based estimators require high technical knowledge and dedicated POD software (e.g., GEODYN, ODTK), and the feasible technique presented in this dissertation to determine non-gravitational accelerations and derived neutral density estimates through numerical differentiation of POE promises potentially good applications. For instance, although the current Swarm and planned GRACE FOLLOW-ON missions will provide accelerometer measurements throughout the next decade, non-gravitational accelerations can be also estimated through GNSS-based POD of LEO, in case of accelerometer failure, data corruption, or instrument power off.

Atmospheric drag from neutral density is the largest uncertainty in LEO prediction, because short-term variations produced by geomagnetic storms and solar flares, for example, are still not well modeled (e.g., *Marcos et al. [2010]*). In fact, seasonal, annual, and other long-term variations are not necessarily well represented in models (e.g., *Qian et al. [2009]*), presenting an additional challenge to neutral mass density modeling. The achievable scientific advance on thermospheric mass density sensing and modeling does not only concern to accelerometer-carried satellites, but also to all other non-scientific satellites and inactive debris, through the use of more accurate atmospheric mass density, winds, and time-varying gravity models, for a more precise orbit prediction. Is therefore that the

scientific contribution of accelerometers and GNSS receivers on small LEO satellites is a valuable source of information for the thermosphere research community. In order to improve our understanding and modeling of thermospheric mass density variations, this study has characterized, through an innovative use of satellite observations, the response of the upper atmosphere to different driver types.

With the continuous technologic advance and the increasing knowledge on thermospheric processes, LEO satellites are constantly decreasing in altitude, size and budget, and more experiments and new miniaturized instruments can be tested, e.g., the Broglia Drag Balance Instrument [*Santoni et al., 2010*], or the miniaturized pressure gauge devices [*Clemmons et al., 2008*]. Several other techniques could be involved and integrated in thermosphere research and modelling, including ultraviolet remote sensing [*Meier and Picone, 1994*], incoherent scatter radar [*Nicolls et al., 2014*], and atmospheric occultation [*Determan et al., 2007; Aikin et al., 1993*]. In addition, it has been demonstrated that the use of accurate solar radiation pressure and density and wind models can be employed to help attitude control and real-time maneuvers (e.g., *Singh and Yim [2005]*). These valuable contributions will increase the lifetime of the future LEO missions and make satellite tracking easier. In addition, the exponential increase of space objects (including the recent collision of the commercial Iridium satellite) has recently highlighted the importance of debris tracking, and the prediction of potential collisions with orbiting satellites has become an essential task. Finally, from the point of view of early control maneuvers and mission lifetime predictions, the combination of sudden commencements of geomagnetic storms with the real-time orbit determination of LEO (e.g., *Yang et al. [2016]*) will definitely improve the future LEO strategies. Geomagnetic storms are considered a key in the MIT system, and the automatic detection of sudden commencements is a relevant topic to investigate (e.g., *Hafez and Ghamry [2013]*).

An important topic to develop in future research is the modeling of simultaneous satellite measurements in a combined solution of wind and density estimates. A clear example is given in figure 6.1, where two simultaneous time-series of density and cross-winds of CHAMP and GOCE missions on April 5th 2010 have been plotted together. The intersection of different planes could reconstruct a 2-dymensional horizontal wind vector from various crosswind measurements. Therefore, monitoring wind and density estimates in multiple orbital planes will make possible the realization of more complete studies on density and

wind variability as a function of LST and altitude. In the future, the global nature of the observations will increase the understanding of the MIT system, and combining empirical with physical models, the complete understanding of all involved parameters and processes in the thermosphere will be achieved.

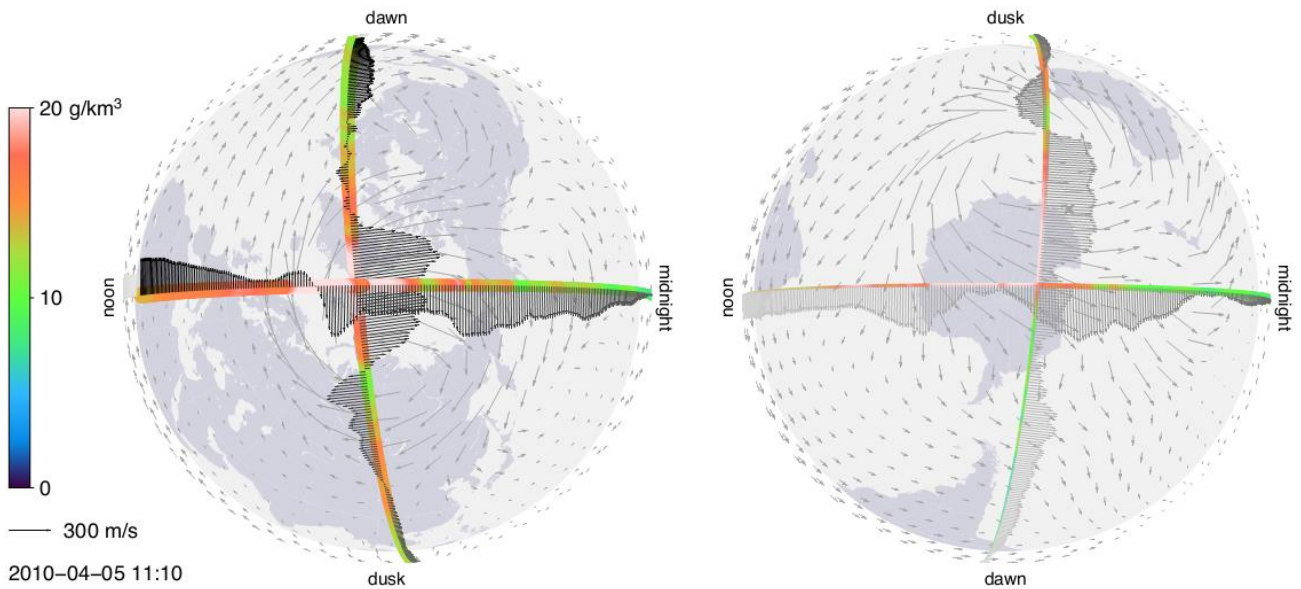


Figure 6.1 Density (color scale) and wind (arrows) data from both GOCE and CHAMP accelerometers, on April 5th, 2010. Densities normalized to 300 km altitude. The background wind field is from the HWM07 model. From [Doornbos et al. \[2014a, Fig. 5.1\]](#).

APPENDICES

Appendix A

Numerical differentiation to obtain acceleration from velocity using the arc-to-chord interpolation threshold (Section 2.2.1):

```

1. %%%%%%%%%%%%%%%%%%%%%%%%%%%%%%%%%%%%%%%%%%%%%%%%%%%%%%%%%%%%%%%%%%%%%%%%%
2. %Acceleration from velocity:
3. for i=1:3
4.     yyp1(1,:) = Vc(:,i);
5.     xx=[1:200:3456000];xia=[200:200:3455800];xib=[202:200:3455802];dt=0.05;%Using 0.05 sec
6.     %xx=[1:100:1728000];xia=[100:100:1727900];xib=[102:100:1727902];dt=0.1;%Using 0.1 sec
7.     %xx=[1:50:864000];xia=[50:50:863950];xib=[52:50:863952];dt=0.2;%Using 0.2 sec
8.     Ac(2:17280,i) = (lagint(xx,yyp1,xib,8)-lagint(xx,yyp1,xia,8))./dt;
9. end
10. Ac(1,:) = Ac(2,:)-Ac(3,:)+Ac(2,:);
11. %%%%%%%%%%%%%%%%%%%%%%%%%%%%%%%%%%%%%%%%%%%%%%%%%%%%%%%%%%%%%%%%%%%%%%%%%

```

In this algorithm, V_c is a 17280x3 vector of satellite velocities in the ICRS at a 5 s interval. The computation is ready for $\Delta t=0.05$ s, and the code to test $\Delta t=0.1$ s and $\Delta t=0.2$ s are included as a comments in the 6 and 7 lines. Here, $lagint()$ is the 1-D piecewise Lagrange interpolation [Henning, 2014]. The acceleration in the ICRS is given in Ac at a 5 s interval.

Appendix B

This function computes the gravity in ITRS from the EGM2008 and includes the frequency-independent and dependent solid tide, the rates for C low-degree, the C_{20} permanent tide, the oceanic tide, the pole solid tide and the pole ocean tide. In this code, St , Lt and Pt are the vectors of Moon, Sun and satellite coordinates in ITRS, $jdUT1day$ is the UT1 time in JD, and xp and yp are the sub-daily polar motion values (sub-daily polar motion computation is available in Appendix D).

```

1. function [gtid]=tides(Lt,St,Pt,jdUT1day, xp, xp)
2. load('tabDepend.mat');% T65a, T65b, T65c and despole tables
3. load('desaipolecoef.mat');% Ar, Br, Ai and Bi tables
4. [a,b,c,d,e,f] = invjday (jdUT1day(:));%year and days of the year (Vallado, 2013)
5. yr=decyear(a,b,c,d,e,f);%MATLAB functionCalculate decimal year
6. %love numbers
7. love(3,1)=0.30190;love(3,2)=0.29830;love(3,3)=0.30102;love(4,1:3)=0.093;love(4,4)=0.094;
8. loveIm=zeros(4,4);loveIm(3,2)=-0.00144;loveIm(3,3)=-0.00130;
9. love2(3,1)=-0.00089;love2(3,2)=-0.00080;love2(3,3)=-0.00057;
10. %frequency-independent solid tide:
11. [maxdeg,Ctid,Stid]=solid_ind(Lt,St,love,love2,loveIm);%function defined later
12. %wobble variables for pole tides:
13. if yr(1)<2010,
14.     mxp=(((yr-2000).^0).*55.974)+(((yr-2000)).*1.8243)+(((yr-2000).^2).*0.18413)+(((yr-2000).^3).*0.007024))./1000;
15.     myp=(((yr-2000).^0).*346.346)+(((yr-2000)).*1.7896)+(((yr-2000).^2).*(-0.10729))+(((yr-2000).^3).*(-0.000908))./1000;
16. else
17.     mxp=(((yr-2000).^0).*23.513)+(((yr-2000)).*7.6141))./1000;
18.     myp=(((yr-2000).^0).*358.891)+(((yr-2000)).*(-0.6287))./1000;
19. end
20. m1=xp-mxp;
21. m2=-yp-myp;
22. %solid pole tide:
23. Ctid(:,3,2)=Ctid(:,3,2)-1.333e-9.*(m1+0.0115.*m2);
24. Stid(:,3,2)=Stid(:,3,2)-1.333e-9.*(m2-0.0115.*m1);
25. %ocean pole tide:
26. degpoletide=120;cont=1;
27. for k=41:80:17241,
28.     [dCpt(cont, :, :), dSpt(cont, :, :)] = ocpoletide(m1(k), m2(k), Ar, Ai, Br, Bi, degpoletide);
29.     %function defined later
30.     cont=cont+1;
31. end
32. %load parameters:
33. load('EOT11a.mat');%cnmCos, snmCos, cnmSin, snmSin, doodsonMatrix and admittance tables
34. load('aeroegm2008.mat');% gravity model from MATLAB
35. Re=6378136.3;GM=3.986004415e+14;
36. degree=120;degtide=120;
37. %resize gravity model:
38. C=C(1:degree+1,1:degree+1);S=S(1:degree+1,1:degree+1);
39. %compute C low degree tide free correction for C20:
40. dCperm=4.4228e-8*(-0.31460)*love(3,1);%IERS2010 (6.14) permanent tide
41. Czero=-0.48416948E-3-dCperm; % IERS2010 (6.14) and table 6.2.
42. %save initial parameters:
43. C0=C(1:degree+1,1:degree+1);S0=S(1:degree+1,1:degree+1);
44. cont=1;% ocean pole tide counter
45. %compute gravity:
46. for i=1:80:17280%every 400s is small enough to desensitize from variations
47.     %load initial parameters:
48.     C=C0;S=S0;mjdut1=jdUT1day((i+40))-2400000.5;
49.     %apply low degree rates:
50.     C(3,1)=Czero+(yr(i+40)-2000)*11.6E-12;
51.     C(4,1)=0.9571612E-6+(yr(i+40)-2000)*4.9E-12;
52.     C(5,1)=0.5399659E-6+(yr(i+40)-2000)*4.7E-12;
53.     mxpr=mxp(i+40)*pi/(180*3600);mypr=mysp(i+40)*pi/(180*3600);
54.     C(3,2)=sqrt(3)*mxpr*(-0.48416948e-3)-mxpr*2.4393836e-6+mypr*(-1.4002737e-6);

```

Appendices

```

54. S(3,2)=-sqrt(3)*mypr*(-0.48416948e-3)-mypr*2.4393836e-6-mxpr*(-1.4002737e-6);
55. %apply ocean tide:
56. [dCtd,dStd]=paramANDY(mjdut1,cnmCos,snmCos,cnmSin,snmSin,doodsonMatrix,admittance,degtid
e); %function defined later
57. C(1:degtide+1,1:degtide+1)=C(1:degtide+1,1:degtide+1)+dCtd;
58. S(1:degtide+1,1:degtide+1)=S(1:degtide+1,1:degtide+1)+dStd;
59. %apply solid tide:
60. dC(:,:)=Ctid(i+40,,:);dS(:,:)=Stid(i+40,,:);
61. C(1:maxdeg+1,1:maxdeg+1)=C(1:maxdeg+1,1:maxdeg+1)+dC;
62. S(1:maxdeg+1,1:maxdeg+1)=S(1:maxdeg+1,1:maxdeg+1)+dS;
63. %apply solid tide frequency dependent correction:
64. [dCc,dSc]=solid_dep(mjdut1,T65a,T65b,T65c); %function defined later
65. C(1:3,1:3)=C(1:3,1:3)+dCc; S(1:3,1:3)=S(1:3,1:3)+dSc;
66. %apply ocean pole tide:
67. dC2(:,:)=dCpt(cont,,:);dS2(:,:)=dSpt(cont,,:);
68. cont=cont+1;
69. C(1:degpoletide+1,1:degpoletide+1)=C(1:degpoletide+1,1:degpoletide+1)+dC2;
70. S(1:degpoletide+1,1:degpoletide+1)=S(1:degpoletide+1,1:degpoletide+1)+dS2;
71. save('Stide.mat','degree','GM','C','S','Re');
72. [gtid(i:79+i,1), gtid(i:79+i,2), gtid(i:79+i,3)] = gravitysphericalharmonic(Pt(i:79+i,:),
'Custom',degree, {'Stide.mat' @load}, 'None');
73. end

```

```

1. function [maxdeg,Ctid,Stid]=solid_ind(Lt,St,love,love2,loveIm)
2. maxdeg=4;
3. Cti=zeros(17280,maxdeg+1,maxdeg+1);Sti=zeros(17280,maxdeg+1,maxdeg+1);
4. Ctid=Cti;Stid=Sti;
5. GMoon=4.902794E12;GS=1.32712442099E20;GM=3.9860044180E14;Re=6378136.6;
6. p=Lt;GMplanet=GMoon;
7. for planet=1:2
8. % Geocentric coord:
9. r = sqrt( sum( p.^2, 2 ));phic = asin( p(:,3)./ r );lambda = atan2( p(:,2), p(:,1) );
10. %Compute coeff:
11. smlambda = zeros( size(p,1),maxdeg);cmlambda = zeros( size(p,1),maxdeg);
12. slambda = sin(-lambda);%changed sing of lambda to follow tides formula
13. clambda = cos(-lambda);%changed sing of lambda to follow tides formula
14. smlambda(:,1)=0;cmlambda(:,1)=1;
15. smlambda(:,2)=slambda;cmlambda(:,2)=clambda;
16. for m=3:maxdeg+1
17. smlambda(:,m)=2.*clambda.*smlambda(:,m-1)-smlambda(:,m-2);
18. cmlambda(:,m)=2.*clambda.*cmlambda(:,m-1)-cmlambda(:,m-2);
19. end
20. % Compute normalized associated legendre polynomials:
21. [P ~]=loc_gravLegendre(phic,maxdeg);% internal function in gravitysphericalharmonic()
22. %compute coefficients up to degree 3:
23. for n = 2:3
24. k = n+1;
25. for m = 0:n
26. j = m+1;
27. Pleg=reshape(P(k,j,:),size(r));
28. Cti(:,k,j)=(love(k,j)/(2*n+1))*(GMplanet/GM).*((Re./r).^(n+1)).*Pleg.*cmlambda(:,j);
29. Cti(:,k,j)=Cti(:,k,j)-((loveIm(k,j)/(2*n+1))*(GMplanet/GM).*((Re./r).^(n+1)).*Pleg.*
smlambda(:,j));%anelastic part
30. Sti(:,k,j)=-(love(k,j)/(2*n+1))*(GMplanet/GM).*((Re./r).^(n+1)).*Pleg.*smlambda(:,j)
;
31. Sti(:,k,j)=Sti(:,k,j)-((loveIm(k,j)/(2*n+1))*(GMplanet/GM).*((Re./r).^(n+1)).*Pleg.*
cmlambda(:,j));%anelastic part
32. end
33. end
34. %compute coefficients degree 4:
35. n=2;k = n+1;
36. for m = 0:n
37. j = m+1;
38. Pleg=reshape(P(k,j,:),size(r));
39. Cti(:,k+2,j)=(love2(k,j)/(2*n+1))*(GMplanet/GM).*((Re./r).^(n+1)).*Pleg.*cmlambda(:,j)
;
40. Sti(:,k+2,j)=-(love2(k,j)/(2*n+1))*(GMplanet/GM).*((Re./r).^(n+1)).*Pleg.*smlambda(:,j)
);
41. end
42. %initialize second planet parameters:
43. GMplanet=GS;p=St;
44. Ctid=Ctid+Cti;Stid=Stid+Sti;
45. end

```

Appendices

```
1. function [dCc,dSc]=solid_dep(mjdut1,T65a,T65b,T65c)
2. dood=doodsonArguments(mjdut1);
3. dCc=zeros(3,3);dSc=zeros(3,3);
4. n=2;m=0;
5. ARG=T65b(:,2:7)*dood;Ar=T65b(:,14)*1e-12;Ai=T65b(:,16)*1e-12;
6. dCc(n+1,m+1)=sum(Ar.*cos(ARG)-Ai.*sin(ARG));
7. n=2;m=1;
8. ARG=T65a(:,2:7)*dood;Ar=T65a(:,15)*1e-12;Ai=T65a(:,16)*1e-12;
9. dCc(n+1,m+1)=sum(Ar.*sin(ARG)+Ai.*cos(ARG));
10. dSc(n+1,m+1)=sum(Ar.*cos(ARG)-Ai.*sin(ARG));
11. n=2;m=2;
12. ARG=T65c(:,2:7)*dood;Ar=T65c(:,14)*1e-12;
13. dCc(n+1,m+1)=sum(Ar.*cos(ARG));
14. dSc(n+1,m+1)=sum(-Ar.*sin(ARG));

1. function [dCpt,dSpt]=ocpoletide(m1,m2,Ar,Ai,Br,Bi,degmax)
2. m1=m1*pi/180/60/60;
3. m2=m2*pi/180/60/60;
4. kpr=zeros(degmax,1);
5. kpr(2:6)=[-0.3075 -0.195 -0.132 -0.1032 -0.0892];
6. for n=1:degmax,
7.   Rn=((7.292115e-5)^2)*((6378137)^4)*4*pi*1025*(6.67428e-11)*(1+kpr(n))/((2*n+1)*(3.986005e
8.   14)*9.7803278);
9.   dCpt(n+1,m+1)=Rn*(Ar(n+1,m+1)*(m1*0.6870+m2*0.0036)+Ai(n+1,m+1)*(m2*0.6870-m1*0.0036));
10.  dSpt(n+1,m+1)=Rn*(Br(n+1,m+1)*(m1*0.6870+m2*0.0036)+Bi(n+1,m+1)*(m2*0.6870-m1*0.0036));
11. end
12. end

1. function[cnm,snm]=paramANDY(mjdut1, cnmCos, snmCos, cnmSin, snmSin, doodsonMatrix, admittance, ma
xDegree)% modification of Rieser et al. (2012)
2. darwin={'OM1', 'OM2', 'SA', 'SSA', 'MM', 'MF', 'MTM', 'MSQ', 'Q1', 'O1', 'P1', 'K1', '2N2', 'N2', 'M2', '
S2', 'K2', 'M4'};
3. thetaf = doodsonMatrix * doodsonArguments(mjdut1); % 256 arguments for all tides
4. factorCos = admittance * cos(thetaf); % interpolation coeff for 18 major tides
5. factorSin = admittance * sin(thetaf);
6. % sum up all major tides:
7. cnm = zeros(maxDegree+1, maxDegree+1);
8. snm = zeros(maxDegree+1, maxDegree+1);
9. for i=1:size(darwin,2)
10.  cnm = cnm + factorCos(i) * cnmCos{i}(1:maxDegree+1,1:maxDegree+1) + factorSin(i) *
    cnmSin{i}(1:maxDegree+1,1:maxDegree+1);
11.  snm = snm + factorCos(i) * snmCos{i}(1:maxDegree+1,1:maxDegree+1) + factorSin(i) *
    snmSin{i}(1:maxDegree+1,1:maxDegree+1);
12. end
```

Appendix C

In this algorithm (Section 2.2.2), the gravity $gtidt$ computed in Appendix A, and rotated to the ICRS to obtain $gtidc$ (Section 2.2.3), is removed from the accelerations Ac (Section 2.2.1). Here, $gtidc$ is rotated to the SBS, to finally be removed from the Luni-solar tides and the relativistic effects:

```

1. %%%%%%%%%%%%%%%%%%%%%%%%%%%%%%%%%%%%%%%%%%%%%%%%%%%%%%%%%%%%%%%%%%%%%%%%%
2. %Difference of accelerations in ICRS:
3. AnonG0 =Ac(:, :)-gtidc(:, :);
4. %rotation to SBF:
5. AnonG1 =quatrotate(SCA, AnonG0);
6. %Relativity effect:
7. GM=3.986004418e14;c2=299792458^2;
8. rel= repmat((GM./(c2.*(sqrt(sum(Pc.^2,2)).^3))),1,3).*(( repmat((4*GM./sqrt(sum(Pc.^2,2))-
   dot(Vc',Vc')'),1,3).*Pc)+4* repmat(dot(Pc',Vc')',1,3).*Vc);
9. %Luni-solar tide:
10. GMoon=4.902800238000000e+12; GSun=1.32712442099E20;
11. acMi=GMoon*((Lc-Pc)./ repmat((sqrt(sum((Lc-Pc).^2,2)).^3),1,3))-(Lc./ repmat((sqrt(sum(Lc.^
   2,2)).^3),1,3));
12. acSi=GSun*((Sc-Pc)./ repmat((sqrt(sum((Sc-Pc).^2,2)).^3),1,3))-(Sc./ repmat((sqrt(sum(Sc.^2
   ,2)).^3),1,3));
13. atc=rel+acMi+acSi;
14. %%rotation to SBF:
15. atb=quatrotate(SCA,atc);
16. %apply:
17. AnonG= AnonG1-atb;
18. %%%%%%%%%%%%%%%%%%%%%%%%%%%%%%%%%%%%%%%%%%%%%%%%%%%%%%%%%%%%%%%%%%%%%%%%%

```

where SCA is a vector with the star camera quaternion, Sc and Lc are the coordinates of Sun and Moon in the ICRS, and $AnonG$ is the vector containing the POD-based non-gravitational accelerations.

Appendix D

The sub-daily EOP parameters (Section 2.2.3) can be computed as follows:

```

1. function [xp, yp, DUT1, lod, ddpsi, ddeps, LEAPi]=subparam(jdUTCday, LEAP);
2. s=size(jdUTCday,1);
3. [mm]=readIERS2( jdUTCday(s/2)-2400000.5); %function defined later
4. JD_TT=jdUTCday+(LEAP+32.184)/86400;
5. ttt=(JD_TT-2451545)./36525;
6. load data;%ocean and Luni-solar parameters from T8.3a and T8.3b of (Petit and Luzum, 2010)
7. for i=1:s
8.     m(1)=(jdUTCday(i)-2400000.5);
9.     for j=2:7
10.        yyp(1,:)=mm(:,j);
11.        xx=[mm(1),mm(2),mm(3),mm(4),mm(5)];
12.        xi=[m(1)];
13.        m(j)=lagint(xx,yyp,xi); %(Henning, 2014)
14.    end
15.    %add corrections:
16.    [CxyUT1lod]=subday(ttt(i),oc,luni);%function defined later
17.    xp(i)=m(2)+CxyUT1lod(1);
18.    yp(i)=m(3)+CxyUT1lod(2);
19.    DUT1(i)=m(4)+CxyUT1lod(3);
20.    lod(i)=m(5)+CxyUT1lod(4);
21.    ddpsi(i)=m(6);
22.    ddeps(i)=m(7);
23.    LEAPi(i)=LEAP;
24. end
25. xp=xp'*pi/(180*3600);yp=yp'*pi/(180*3600);
26. ddpsi=ddpsi'*pi/(180*3600);ddeps=ddeps'*pi/(180*3600);
27. DUT1=DUT1';lod=lod';

1. function [mm]=readIERS(MJD)
2. %gives EOP matrix with 10 day centered on requested date
3. file='eopc90-now.txt';%from IERS
4. fid = fopen(file);
5. while 1
6.     lin = fgetl(fid);
7.     resp = strfind(lin,'1990');
8.     if ~isempty(resp), break; end;
9. end;
10. while 1
11.     lin = fgetl(fid);
12.     if str2double(lin(14:19))==floor(MJD-2),
13.         for i=1:5
14.             mm(i,1)=str2double(lin(14:19));%MJD
15.             mm(i,2)=str2double(lin(21:30));%xp
16.             mm(i,3)=str2double(lin(32:41));%yp
17.             mm(i,4)=str2double(lin(43:53));%DUT1
18.             mm(i,5)=str2double(lin(55:65));%lod
19.             mm(i,6)=str2double(lin(67:76));%ddpsi
20.             mm(i,7)=str2double(lin(78:87));%ddeps
21.             lin = fgetl(fid);
22.         end
23.         break
24.     end
25. end
26. fclose(fid);

1. function [CxyUT1lod]=subday(ttt,oc,luni)
2. ttt2 = ttt*ttt;
3. ttt3 = ttt2*ttt;
4. ttt4 = ttt2*ttt2;
5. %Arguments in the following order: chi=GMST+pi,l,lp,F,D,Omega, and temporal derivatives:
6. ARG(1) = (67310.54841+(876600*3600+ 8640184.812866)*ttt +0.093104*ttt2 -6.2e-6*ttt3)*15.0 +
648000.0;
7. DARG(1) = (876600*3600 + 8640184.812866 + 2 * 0.093104 * ttt - 3 * 6.2e-6*ttt2)*15;
8. ARG(2) = -0.00024470*ttt4 + 0.051635*ttt3 + 31.8792*ttt2 + 1717915923.2178*ttt + 485868.249036;
9. DARG(2) = -4.*0.00024470*ttt3 + 3.*0.051635*ttt2 + 2.*31.8792*ttt + 1717915923.2178 ;

```

Appendices

```
10. ARG(3) = -0.00001149*ttt4 - 0.000136*ttt3 - 0.5532*ttt2 + 129596581.0481*ttt + 1287104.79305;
11. DARG(3) = -4.*0.00001149*ttt3 - 3.*0.000136*ttt2 - 2.*0.5532*ttt + 129596581.0481;
12. ARG(4) = 0.00000417*ttt4 - 0.001037*ttt3 - 12.7512*ttt2 + 1739527262.8478*ttt + 335779.526232;
13. DARG(4) = 4.*0.00000417*ttt3 - 3.*0.001037*ttt2 - 2. * 12.7512*ttt + 1739527262.8478 ;
14. ARG(5) = -0.00003169*ttt4 + 0.006593*ttt3 - 6.3706*ttt2 + 1602961601.2090*ttt + 1072260.70369;
15. DARG(5) = -4.*0.00003169*ttt3 + 3.*0.006593*ttt2 - 2. * 6.3706*ttt + 1602961601.2090;
16. ARG(6) = -0.00005939*ttt4 + 0.007702*ttt3 + 7.4722*ttt2 - 6962890.2665*ttt + 450160.398036;
17. DARG(6) = -4.*0.00005939*ttt3 + 3. * 0.007702*ttt2 + 2. * 7.4722*ttt - 6962890.2665;
18. secrad=pi/60/60/180;
19. ARG=rem(ARG,1296000).*secrad;
20. DARG= DARG.*secrad./36525.0;%rad/day
21. ARGm=repmat(ARG,71,1);
22. DARGm=repmat(DARG,71,1);
23. ag=sum(oc(:,1:6).*ARGm,2);
24. dag=sum(oc(:,1:6).*DARGm,2);
25. ag=rem(ag,2*pi);
26. dag=rem(dag,2*pi);
27. CxyUT1lod(1)= sum(oc(:,8).*cos(ag) +oc(:,7).*sin(ag))/1000000;%
28. CxyUT1lod(2)= sum(oc(:,10).*cos(ag)+oc(:,9).*sin(ag))/1000000;%
29. CxyUT1lod(3)= sum(oc(:,12).*cos(ag)+oc(:,11).*sin(ag))/1000000;%s
30. CxyUT1lod(4)= sum((oc(:,12).*sin(ag)-oc(:,11).*cos(ag)).*dag)/1000000;%(s)%formula from
    http://hpiers.obspm.fr/iers/models/interp.f
31. agluni= sum(luni(:,1:6).*ARGm(1:10,:),2);
32. agluni=rem(agluni,2*pi);
33. CxyUT1lod(1)= CxyUT1lod(1)+sum(luni(:,8).*cos(agluni)+luni(:,7).*sin(agluni))/1000000;%
34. CxyUT1lod(2)= CxyUT1lod(2)+sum(luni(:,10).*cos(agluni)+luni(:,9).*sin(agluni))/1000000;%
```


Appendix E

A feasible computation for the planetary eclipse ratio sh (Section 2.3.2), where Pc and Sc are the Satellite and Sun Cartesian coordinates in ICRS, is presented as follows:

```

1. %%%%%%%%%%%%%%%%%%%%%%%%%%%%%%%%%%%%%%%%%%%%%%%%%%%%%%%%%%%%%%%%%%%%%%%%%
2. Srad=696342000; Erad=6371000; %Sun and Earth radius
3. %Distance Earth to fundamental plane:
4. S0=-(Pc(:,1).*Sc(:,1)+ Pc(:,2).*Sc(:,2)+ Pc(:,3).*Sc(:,3))./sqrt(sum(Sc.^2,2));
5. %Angles 1 penumbra and 2 umbra:
6. sinf1=(Srad+Erad)./sqrt(sum(P(:,2:4).^2,2));
7. sinf2=(Srad-Erad)./sqrt(sum(P(:,2:4).^2,2));
8. %Cone vertex distances:
9. c1=S0+(Erad./sinf1);
10. c2=S0-(Erad./sinf2);
11. %Radius of (1)penumbra, (2)umbra on fundamental plane and (3)Satellite to Shadow axis:
12. l(:,2)=abs(c2.*tan(asin(sinf2)));
13. l(:,1)=abs(c1.*tan(asin(sinf1)));
14. l(:,3)=sqrt(sum(GNVA(:,2:4).^2,2)-S0.^2);
15. %Shadow disc function:
16. VSsat=Pc-Sc;
17. USSat=VSsat./repmat(sqrt(sum(VSsat.^2,2)),1,3);
18. Vps=repmat(USSat(:,1).*Pc(:,1)+USSat(:,2).*Pc(:,2)+USSat(:,3).*Pc(:,3),1,3).*USSat;
19. hg=sqrt(sum((Pc-Vps).^2,2))-Erad;
20. Rp=sqrt(sum(Vps.^2,2)).*Srad./sqrt(sum(VSsat.^2,2));
21. nnu=hg./Rp;
22. nnu=nnu.*(nnu>-1&nnu<1);
23. fg=1-(1/pi).*acos(nnu)+(nnu./pi).*sqrt(1-(nnu).^2);
24. fg(fg==0.5)=NaN;
25. %Shadow position:
26. for i=1:86400,%full day in seconds
27.     if S0(i)>-Erad*sinf1(i)&&l(i,3)>l(i,2)&&l(i,3)<l(i,1),sh(i)=fg(i);%Penumbra
28.     elseif S0(i)>Erad*sinf2(i)&&l(i,3)<l(i,2),sh(i)=0;%Umbra
29.     end%sunlight
30. end
31. %%%%%%%%%%%%%%%%%%%%%%%%%%%%%%%%%%%%%%%%%%%%%%%%%%%%%%%%%%%%%%%%%%%%%%%%%

```

Appendix F

Computation for the solar radiation (Section 2.3.2), where $VSSnB$ is the vector Satellite to Sun in the SBS, $MASS$ the satellite mass and sh are the shadow values (Appendix E):

```

1. function [accRad]=accelRad(VSSnB,MASS,sh)
2. AU=149597870660;
3. RR=1366; %W/m2
4. c=299792458; %m/s2
5. load('Plates.mat');
6. accRad=NaN(2,size(VSSnB,1),3);
7. Rsp=(Plates(:,5).*0.43+Plates(:,7).*0.53)./(0.43+0.53);
8. Rdi=(Plates(:,6).*0.43+Plates(:,8).*0.53)./(0.43+0.53);
9. for i=1:size(VSSnB,1)
10.  massc=MASS(floor((i-1)/86400)+1)*c;
11.  VSSnBi=VSSnB(i,:);
12.  USSnBi= repmat(VSSnBi'./norm(VSSnBi),size(Rsp,1),1);
13.  g=dot(Plates(:,2:4)',USSnBi)';
14.  A1=repmat(RR.*Plates(:,1).*g./massc,1,3);
15.  A2=2.*repmat(((Rdi./3)+Rsp.*g),1,3).*Plates(:,2:4);
16.  A3=(1-repmat(Rsp,1,3)).*(USSnBi);
17.  AA=-A1.*(A2+A3);
18.  accRad(i,:)=sum(reshape(AA(repmat(g>0,1,3)),[],3),1);
19. end
20. for co=1:3
21.  X=accRad(:,co);
22.  accRad(:,co)=X.*sh.*(AU./sqrt(sum(VSSnB.^2,3))).^2;
23. end

```

Appendix G

The Earth albedo given by the short-wave *accIRb* and the long-wave *accALb* radiation can be computed as follows (Section 2.3.2):

```

1. function [accIRb,accALb]=accelAlbIR(Pt,St,jdUTCDAY,SCA,MASS)
2. % Pt and St are satellite and Sun position in Cartesian ITRS
3. % jdUTCDAY is UTC time in Julian Date
4. % SCA and MASS are star camera quaternion and satellite mass
5. load('Plates.mat'); c=299792458;%m/s2
6. Rsp=(Plates(:,5).*0.43+Plates(:,7).*0.53)./(0.43+0.53);
7. Rdi=(Plates(:,6).*0.43+Plates(:,8).*0.53)./(0.43+0.53);
8. [~,month,~,~,~]=invjday(jdUTCDAY(size(St,1)/2));
9. load('refl_data\refleMonth.mat');%reflection data file
10. data(:,:)=refleMonth(month,,:);
11. data=resize(data,[90 180],'bicubic');
12. dy=1;lat=[-90+dy/2:dy:90-dy/2]';
13. accIRb=NaN(2,size(St,1),3);accALb=accIRb;
14. for j=1:size(St,1)
15.     sss(1,:)=Pt(j,:);
16.     [IRijD,ALijE,VGridSatIR,VGridSatAL] = albedo_andy(sss',St(j,:),data);
17.     %IRradiation:
18.     IR1E=lat(IRijD(:,1));
19.     dataforIR=IRijD(:,3);
20.     %Emissivity formula:
21.     tep=jdUTCDAY(j)-juliandate(1981,12,22);
22.     e1=-0.07*cos(2*pi*tep/365.25);
23.     e1w=0.68+e1.*sin(IR1E.*pi./180)-0.18.*(3*sin(IR1E.*pi./180).^2-1)./2;
24.     IR3E=e1w.*dataforIR;
25.     UPIRt=(-VGridSatIR)./(repmat(sqrt(sum(VGridSatIR.^2,2)),1,3));%unitary vector for pressure
        IR
26.     massc=MASS(floor((j-1)/86400)+1)*c;
27.     %Albedo radiation:
28.     if sum(ALijE(:,3))>0
29.         AL3E=ALijE(:,3);
30.         UPALt=(-VGridSatAL)./(repmat(sqrt(sum(VGridSatAL.^2,2)),1,3));%unitary vector for pressure
            AL
31.     end
32.     %Rotation plates from SBS to ICRS:
33.     SCAsat(1,:)=SCA(j,2:5);PLATc=quatrotate(quatconj(SCAsat),Plates(:,2:4));
34.     clear accALt accIRt
35.     for k=1:size(PLATc,1)
36.         [PLATt,~,~]=ICRStoITRS(PLATc(k,:)); %Rotation plates to ITRS
37.         %IR accelerations:
38.         g=dot(repmat(PLATt,1,size(UPIRt,1)),UPIRt)';
39.         A1=repmat(IR3E.*repmat(Plates(k,1),size(IR3E,1),1).*g./massc,1,3);
40.         A2=2.*repmat(((Rdi(k)/3)+Rsp(k)*g),1,3).*repmat(Plates(k,2:4),size(IR3E,1),1);
41.         A3=(1-repmat(Rsp(k),size(IR3E,1),3)).*UPIRt;
42.         AA=-A1.*(A2+A3);
43.         accIRt(k,:)=sum(reshape(AA(repmat(g>0,1,3)),[],3),1);
44.         %AL accelerations:
45.         if sum(ALijE(:,3))>0
46.             g=dot(repmat(PLATt,1,size(UPALt,1)),UPALt)';
47.             A1=repmat(AL3E.*repmat(Plates(k,1),size(AL3E,1),1).*g./massc,1,3);
48.             A2=2.*repmat(((Rdi(k)/3)+Rsp(k)*g),1,3).*repmat(Plates(k,2:4),size(AL3E,1),1);
49.             A3=(1-repmat(Rsp(k),size(AL3E,1),3)).*UPALt;
50.             AA=-A1.*(A2+A3);
51.             accALt(k,:)=sum(reshape(AA(repmat(g>0,1,3)),[],3),1);
52.         end
53.     end
54.     accIRt=sum(accIRt,1);
55.     if sum(ALijE(:,3))>0;accALt=sum(accALt,1);end
56.     [accIRc]=ITRStoICRS(accIRt); %Rotation IR to ICRS:
57.     accIRb(j,:)=quatrotate(SCAsat,accIRc)'; %rotation to SBF
58.     if sum(ALijE(:,3))>0
59.         [accALc,~,~]=ITRStoICRS(accALt); %Rotation AL to ICRS
60.         accALb(j,:)=quatrotate(SCAsat,accALc)'; %rotation AL to SBF
61.     else;accALb(j,:)=0 0 0];
62.     end
63. end

```

```

1. function [IRijD,ALijP,VGridSatIR,VGridSatAL] = albedo_andy(sat,sun,data);
2. % ALBEDO Calculation for a given satellite and Sun constellation and specified reflectivity
   data.
3. % Row vectors:
4. % sat and sun are the satellite and Sun vectors in Cartesian ITRS
5. % refl is the reflectivity data to use
6. % Andy's modification of Bhanderi (2009)
7. CONST.EMR = 6371.01e3;CONST.d2r = pi/180;
8. AU=149597870660; % Solar irradiance
9. [sy,sx] = size(data); % Data size
10. % Spherical coordinates:
11. [satsph(1),satsph(2),satsph(3)] = cart2sph(sat(1),sat(2),sat(3));
12. [sunsph(1),sunsph(2),sunsph(3)] = cart2sph(sun(1),sun(2),sun(3));
13. % Convert phi to polar angle:
14. satsph(2) = pi/2 - satsph(2);
15. sunsph(2) = pi/2 - sunsph(2);
16. % REFL indices:
17. [sun_i,sun_j] = rad2idx(sunsph(1),sunsph(2),sy,sx);
18. [sat_i,sat_j] = rad2idx(satsph(1),satsph(2),sy,sx);
19. fov = earthfov(satsph,[sy sx]); % Visible elements
20. vis = earthfov(sunsph,[sy sx]); % Sunlit elements
21. union = fov & vis; % Union
22. %index:
23. ies0= repmat([1:sy]',1,sx);
24. jas0= repmat([1:sx],sy,1);
25. %IR data:
26. IRijD(:,1)=ies0(fov~=0);
27. IRijD(:,2)=jas0(fov~=0);
28. % Distance to sat from grid:
29. [grid_theta grid_phi] = idx2rad(IRijD(:,1),IRijD(:,2),sy,sx);
30. griIR(:,1) griIR(:,2) griIR(:,3)] = sph2cart(grid_theta,pi./2-grid_phi,CONST.EMR);
31. VGridSnIR=repmat(sun',size(griIR,1),1)-griIR;%%
32. VGridSatIR=repmat(sat',size(griIR,1),1)-griIR;
33. satdist = sqrt(sum(VGridSatIR.^2,2));
34. % Angle to sat from grid:
35. phi_out=acos(dot((VGridSatIR./repmat(satdist,1,3))',(griIR./repmat(CONST.EMR,size(griIR,1)
   ,3))'))');
36. %IR data:
37. iradIR=239.*(AU./sqrt(sum(VGridSnIR.^2,2))).^2;
38. IRijD(:,3)=iradIR.*cellarea(IRijD(:,1),IRijD(:,2),sy,sx).*cos(phi_out)./(pi*satdist.^2);
39. %AL:
40. if sum(sum(union))>0
41. ALijP(:,1)=ies0(union~=0);
42. ALijP(:,2)=jas0(union~=0);
43. % Angle of incident solar irradiance:
44. phi_in = gridangleAndy(ALijP(:,1),ALijP(:,2),sun_i,sun_j,sy,sx);
45. % Account for numerical inaccuracies:
46. phi_in(phi_in >pi/2)=pi/2;
47. % Distance to sat from grid:
48. [grid_theta grid_phi] = idx2rad(ALijP(:,1),ALijP(:,2),sy,sx);
49. [griAL(:,1) griAL(:,2) griAL(:,3)] = sph2cart(grid_theta,pi./2-grid_phi,CONST.EMR);
50. VGridSnAL=repmat(sun',size(griAL,1),1)-griAL;%%
51. VGridSatAL=repmat(sat',size(griAL,1),1)-griAL;
52. satdist = sqrt(sum(VGridSatAL.^2,2));
53. % Angle to sat from grid:
54. phi_out=acos(dot((VGridSatAL./repmat(satdist,1,3))',(griAL./repmat(CONST.EMR,size(griAL,1)
   ,3))'))');
55. iradAL = 1366.9.*(AU./sqrt(sum(VGridSnAL.^2,2))).^2;
56. E_in = iradAL.*cellarea(ALijP(:,1),ALijP(:,2),sy,sx).*cos(phi_in);
57. ALijP(:,3) = E_in.*data(union~=0).*cos(phi_out)./(pi*satdist.^2);
58. else
59. ALijP=zeros(1,3);
60. VGridSatAL=zeros(1,3);
61. end

```

Appendix H

Computation for pressure and shear drag-coefficients (Section 2.3.3), where ρ is the NRLMSISE-00 output, T is the NRLMSISE-00 temperature ($^{\circ}\text{K}$) and pitchSide is a matrix containing the angles of pitch Φ and sideslip β :

```

1. function [CDs,CDp]=DragCoef(rho,T,pitchSide)
2. % rho : (1) HE number density in meters^-3,
3. %      (2) O number density in meters^-3,
4. %      (3) N2 number density in meters^-3,
5. %      (4) O2 number density in meters^-3,
6. %      (5) AR number density in meters^-3,
7. %      (6) total mass density in kilogram per meters cubed,
8. %      (7) H number density in meters^-3,
9. %      (8) N number density in meters^-3, and
10. %     (9) Anomalous oxygen number density in meters^-3.
11. CpsMehta=NaN(2,size(pitchSide,1));
12. load('MehtaTables.mat');
13. Po=rho(:,2).*T(1,:);
14. KPo=Po.*7.5e-17;
15. %partial densities(g/mol/m3):
16. He=4.002.*rho(:,1);%He
17. O=15.999.*rho(:,2);%O
18. N2=28.134.*rho(:,3);%N2
19. O2=31.998.*rho(:,4);%O2
20. Ar=39.948.*rho(:,5);%Ar
21. H=1.007.*rho(:,7);%H
22. N=14.0067.*rho(:,8);%N
23. Oa=16.999.*rho(1,9);%O[17]
24. %total n density (1/m3):
25. t=sum(rho(:,1:5),3)+sum(rho(:,7:9),3);
26. %mean molecular density(g/mol):
27. gm=(He+O+N2+O2+Ar+H+N)./t;
28. mu=gm./382;%molecular mass ratio
29. alpS=3.6.*mu./((1+mu).^2);
30. alp=(alpS+KPo)./(1+KPo);
31. ab(:,:)=floor(1000.*pitchSide(1:60:end,:).*180/pi)/1000;
32. [Adeg,Bdeg] = meshgrid(0:1:4,0:1:5);
33. pai=interp2(Adeg,Bdeg,pa,abs(ab(:,1)),abs(ab(:,2)),'cubic');
34. pbi=interp2(Adeg,Bdeg,pb,abs(ab(:,1)),abs(ab(:,2)),'cubic');
35. pci=interp2(Adeg,Bdeg,pc,abs(ab(:,1)),abs(ab(:,2)),'cubic');
36. sai=interp2(Adeg,Bdeg,sa,abs(ab(:,1)),abs(ab(:,2)),'cubic');
37. sbi=interp2(Adeg,Bdeg,sb,abs(ab(:,1)),abs(ab(:,2)),'cubic');
38. sci=interp2(Adeg,Bdeg,sc,abs(ab(:,1)),abs(ab(:,2)),'cubic');
39. sdi=interp2(Adeg,Bdeg,sd,abs(ab(:,1)),abs(ab(:,2)),'cubic');
40. CDp=pai.*(alp'.^pbi)+pci;
41. XHeT=rho(:,1).*T(:)./t;
42. CDs=sai.*exp(sbi.*XHeT')+sci.*exp(sdi.*XHeT');

```

Appendix I

In this code, ascending and descending orbits are separated in function of decreasing or increasing spacecraft's latitude (Section 2.4). For the development in longitude, the values must be biased 360° after a grid is completed. The variable $D(:,1:3)$ contains latitudes, longitudes (0° to 360°) and measurements to interpolate.

```

1. %%%%%%%%%%%%%%%%%%%%%%%%%%%%%%%%%%%%%%%%%%%%%%%%%%%%%%%%%%%%%%%%%%%%%%%%%%
2. %Extract descending orbits:
3. D(end+1,:)=D(:,end,:);D0(:,:)=D(1:end-1,:); D02(:,:)=D(2:end,:);
4. DDOWN=reshape(D0(repmat((D0(:,1)-D02(:,1))>0)',1,3)), [],3);
5. %Cut data from first optimal position:
6. for j=1:43200;if abs(DDOWN(j,1))<80&&DDOWN(j,2)>335;t0=j;break; end;end
7. LDOWN(:,2)=DDOWN(t0:end,2);LDOWN(:,1)=DDOWN(t0:end,1);LDOWN(:,3)=DDOWN(t0:end,3);
8. siz= size(LDOWN,1);
9. %Vectors to remove Eastern and Western non-desirable data:
10. cle1=LDOWN(:,2)>50;cle1=single(cle1);cle1(cle1==0)=nan;
11. cle2=LDOWN(:,2)<310;cle2=single(cle2);cle2(cle2==0)=nan;
12. LDOWN(abs(LDOWN(:,1))>87,2)=nan;LDOWNb=LDOWN; %Remove high latitudes:
13. %Remove Eastern non-desirable data:
14. LDOWNb(1:20000,2)= LDOWN(1:20000,2).*cle1(1:20000);
15. t0=0; limm=20000; %Initialize and constrain limit
16. while 1
17.   if size(TDOWN,1)-t0-limm<0;limm=size(TDOWN,1)-t0;end%Limit checking
18.   %Find next optimal position:
19.   for i=t0+limm:siz
20.     if abs(LDOWN(i,1))<80&&LDOWN(i,2)>335;t1=i;break; end;
21.   end
22.   if t1==t0;break;end
23.   t0=t1; %Refresh optimal position
24.   %Remove Western non-desirable data:
25.   LDOWNb(t0-limm:t0,2)= LDOWN(t0-limm:t0,2).*cle2(t0-limm:t0);
26.   %Add 360 to the previous grid:
27.   LDOWNb(t0:end,2)= LDOWN(t0:end,2)-360;LDOWNb(:,2)=LDOWNb(:,2)+360;
28.   %Limit checking and Remove Eastern non-desirable data:
29.   if t0+limm<size(cle1,1),
30.     LDOWNb(t0:t0+limm,2)= LDOWN(t0:t0+limm,2).*cle1(t0:t0+limm);
31.   else
32.     LDOWNb(t0:end,2)= LDOWNb(t0:end,2).*cle1(t0:end);
33.   end
34. end
35. LDOWN=LDOWNb(~isnan(LDOWNb(:,2)),:); %Remove NaN values
36. %%%%%%%%%%%%%%%%%%%%%%%%%%%%%%%%%%%%%%%%%%%%%%%%%%%%%%%%%%%%%%%%%%%%%%%%%%

```

Appendix J

Computation to obtain the grids from Stokes' coefficients given in Table K.3 (Appendix K):

```

1. function [DATA] = Stokes2grid(Alm,Blm)
2. degree=8;
3. phi=90:-1:-90;
4. phi=phi'*pi./180;
5. [plm ~] = legnorm(phi,degree);
6. rho = 180/pi;
7. for lon=0:359
8.   DATA(:,lon+1)=zeros(181,1);
9.   for n = 0:degree
10.    for m = 0:n
11.     Pl(:,:)=plm(n+1,m+1,:);
12.     aux=Pl.*cos(m*lon/rho)*Alm(n+1,m+1)+Pl.*sin(m*lon/rho)*Blm(n+1,m+1);
13.     DATA(:,lon+1)=DATA(:,lon+1)+aux;
14.    end
15.   end
16. end

```


Appendix K

Tables with coefficients for the parameterizations given in Section 5.2

Table K.1 Coefficients for solar and magnetospheric variations used in Section 5.2.1.

	PCA 1
	P10.7 & Am
p00	-1.98E-14
p10	-5.55E-16
p01	1.62E-17
p20	-6.09E-18
p11	1.45E-17
p02	7.10E-18

Table K.2 Coefficients for periodic variations used in Section 5.2, including % correlation coefficients for each parameterization (93-day period might not be used for modelling).

		S1	Annual	K1	P1	R2	T2	93-day
PCA 1 (96 %)	a	8.224	8.166	-	10.2	-	-	-
	b	3.341	3.383	-	2.37	-	-	-
	a0	1.64E-15	1.76E-15	-	1.10E-16	-	-	-
	a1	-2.25E-14	1.08E-14	-	1.01E-15	-	-	-
	b1	2.01E-14	2.60E-15	-	-3.18E-15	-	-	-
	a2	-9.48E-16	-9.41E-15	-	-	-	-	-
	b2	-6.35E-15	-4.75E-15	-	-	-	-	-
	a3	-2.17E-16	-1.51E-15	-	-	-	-	-
	b3	1.04E-15	-2.14E-15	-	-	-	-	-
PCA 2 (92 %)	a	8.2	8.209	8.166	7.958	-	8.142	9.886
	b	3.36	3.35	3.362	3.476	-	3.391	2.487
	a0	3.40E-14	-1.06E-13	4.99E-15	2.98E-14	-	6.97E-17	-3.40E-15
	a1	-5.69E-14	-1.10E-13	2.69E-15	-6.23E-15	-	1.65E-16	-1.73E-14
	b1	5.53E-14	2.23E-14	-2.24E-14	8.52E-15	-	9.04E-15	-7.35E-16
	a2	-1.90E-15	-2.35E-14	3.44E-15	-	-	-	-
	b2	-3.19E-14	7.88E-15	1.80E-15	-	-	-	-
	a3	-2.25E-15	1.18E-14	-	-	-	-	-
	b3	4.08E-15	7.96E-15	-	-	-	-	-
	a4	-1.60E-15	-2.42E-15	-	-	-	-	-
	b4	-1.77E-15	1.38E-14	-	-	-	-	-
	a5	-	-2.44E-17	-	-	-	-	-
b5	-	-3.49E-16	-	-	-	-	-	
PCA 3 (91 %)	a	8.192	8.167	7.264	8.29	-	-	13.73
	b	3.356	3.358	3.757	3.26	-	-	0.5774
	a0	6.67E-14	-7.89E-15	-2.20E-14	1.09E-14	-	-	4.27E-14
	a1	5.55E-14	-7.14E-14	1.01E-14	-8.71E-15	-	-	-1.53E-14
	b1	-3.70E-14	2.44E-14	-1.89E-14	2.32E-14	-	-	-1.93E-15
	a2	-1.18E-14	-1.22E-14	-1.59E-15	-	-	-	-
	b2	2.83E-14	-4.07E-15	-6.50E-15	-	-	-	-
	a3	6.58E-15	4.86E-15	-	-	-	-	-
	b3	-5.40E-15	-1.04E-15	-	-	-	-	-
	a4	-2.60E-16	-6.09E-15	-	-	-	-	-
	b4	1.06E-15	4.14E-15	-	-	-	-	-
	a5	7.82E-16	9.08E-16	-	-	-	-	-
b5	1.55E-15	-2.91E-16	-	-	-	-	-	
PCA 4 (75 %)	a	10.85	-	8.151	8.175	8.185	8.174	-
	b	2.062	-	3.331	3.366	3.373	3.362	-
	a0	-2.03E-14	-	1.18E-14	-3.40E-16	-2.26E-15	-2.22E-15	-
	a1	3.02E-15	-	9.33E-15	-8.84E-15	5.76E-15	6.02E-15	-
	b1	8.71E-15	-	-1.26E-14	1.25E-14	4.17E-15	8.75E-15	-
	a2	-7.80E-15	-	-1.28E-15	-	-	-	-
	b2	5.26E-15	-	-4.38E-15	-	-	-	-
	a3	1.45E-15	-	-	-	-	-	-
	b3	-2.08E-15	-	-	-	-	-	-
a4	4.90E-16	-	-	-	-	-	-	
b4	-4.50E-16	-	-	-	-	-	-	
PCA 5 (75 %)	a	9.571	-	-	-	-	-	-
	b	2.658	-	-	-	-	-	-
	a0	-3.69E-15	-	-	-	-	-	-
	a1	1.31E-15	-	-	-	-	-	-
	b1	7.28E-15	-	-	-	-	-	-
	a2	-1.27E-14	-	-	-	-	-	-
	b2	1.86E-14	-	-	-	-	-	-
	a3	1.43E-14	-	-	-	-	-	-
	b3	-1.14E-14	-	-	-	-	-	-
a4	-4.71E-15	-	-	-	-	-	-	
b4	3.26E-16	-	-	-	-	-	-	

Table K.3 Spherical harmonics parameterization of PCA spatial patterns, including % contribution to the total variance (Section 5.1, figure 5.1).

l	m	PCA 1 (90.3 %)		PCA 2 (3.5 %)		PCA 3 (2.9 %)		PCA 4 (0.1 %)		PCA 5 (0.1 %)	
		A	B	A	B	A	B	A	B	A	B
0	0	5.68	0	1.76E-01	0	-1.82E-01	0	1.02E-02	0	-7.58E-03	0
1	0	2.68E-01	0	-3.47E-01	0	-2.69E-01	0	-2.14E-01	0	-3.36E-03	0
2	0	-2.48E-01	0	-2.29E-01	0	3.25E-01	0	-1.20E-02	0	2.79E-01	0
3	0	5.57E-02	0	-5.39E-02	0	-1.91E-02	0	2.79E-01	0	4.37E-02	0
4	0	-7.36E-02	0	-5.31E-02	0	8.07E-02	0	2.00E-02	0	-3.05E-01	0
5	0	-1.91E-02	0	1.98E-02	0	1.87E-02	0	3.00E-02	0	-2.38E-02	0
6	0	1.83E-02	0	-1.04E-02	0	6.09E-03	0	-2.70E-02	0	-2.46E-02	0
7	0	-8.19E-03	0	-3.31E-03	0	-3.55E-03	0	9.31E-03	0	-3.57E-02	0
8	0	-3.99E-02	0	-1.11E-02	0	1.74E-02	0	7.64E-03	0	-2.28E-02	0
1	1	2.67E-02	2.22E-02	-4.93E-04	-6.79E-02	-3.03E-02	-2.99E-02	-1.86E-02	8.52E-03	9.57E-02	-3.46E-02
2	1	1.72E-02	-7.52E-02	-2.13E-03	1.86E-03	2.13E-02	-1.76E-02	4.02E-02	3.93E-02	1.82E-02	-4.10E-02
3	1	9.91E-03	-1.51E-02	3.03E-03	-2.07E-02	1.61E-02	5.74E-03	-3.37E-02	3.72E-02	-4.55E-02	1.44E-03
4	1	2.47E-02	-1.39E-02	-4.23E-03	-4.34E-03	1.18E-02	-1.52E-03	1.96E-03	3.24E-02	2.00E-02	-2.17E-02
5	1	3.63E-03	-1.76E-03	-1.26E-03	-1.53E-02	5.22E-03	-2.58E-03	-3.12E-02	4.98E-03	-7.03E-03	-1.24E-02
6	1	-2.01E-04	-4.11E-02	-4.53E-04	-1.01E-02	4.65E-03	1.16E-02	1.14E-02	3.07E-02	2.42E-02	-1.81E-02
7	1	-3.41E-03	-3.83E-04	7.42E-04	-2.35E-03	2.82E-03	4.13E-03	-5.43E-03	1.57E-02	-2.50E-03	-5.94E-03
8	1	-7.58E-03	2.64E-02	-2.59E-03	4.38E-03	3.22E-03	-5.61E-03	4.65E-03	1.36E-02	1.03E-02	7.77E-03
2	2	-2.68E-02	1.02E-02	4.34E-03	-1.77E-02	3.77E-03	-7.94E-03	-2.83E-02	-4.85E-02	2.19E-02	4.10E-02
3	2	3.12E-02	-1.59E-03	-1.37E-03	1.63E-03	-7.36E-03	-5.52E-03	8.88E-04	1.60E-03	-1.84E-03	-3.05E-02
4	2	-1.89E-03	-8.16E-03	-2.01E-03	-1.20E-03	-7.18E-03	-3.80E-03	6.79E-04	-3.32E-02	-1.38E-02	-2.19E-02
5	2	-6.89E-03	4.96E-04	-4.76E-03	-5.93E-04	9.97E-04	1.59E-04	4.87E-03	4.87E-04	-5.78E-03	-5.03E-03
6	2	-8.78E-03	-3.53E-03	1.15E-03	-2.32E-03	2.21E-03	-2.97E-03	8.53E-03	-2.42E-02	-4.30E-03	-1.43E-02
7	2	7.77E-03	-2.82E-03	-7.57E-04	-9.87E-04	-3.81E-04	-5.21E-04	-6.61E-04	6.20E-04	1.06E-02	-2.68E-03
8	2	7.59E-03	1.18E-02	-9.27E-04	9.40E-04	-3.08E-03	-3.07E-03	6.17E-03	-1.19E-02	-3.01E-03	-5.59E-03
3	3	-1.05E-02	-1.11E-02	1.56E-04	-4.93E-03	-2.50E-03	1.27E-02	-1.43E-02	-3.06E-02	-8.76E-03	-2.48E-02
4	3	-7.02E-03	3.60E-03	-1.47E-04	4.46E-04	7.79E-04	1.03E-03	5.79E-05	-8.00E-03	-7.97E-03	8.26E-03
5	3	-3.15E-03	2.78E-03	-1.45E-03	-2.78E-03	2.15E-03	-1.03E-03	-3.08E-03	-1.05E-02	8.32E-03	2.10E-02
6	3	6.91E-03	-3.98E-03	2.73E-04	-7.09E-04	-4.26E-03	-7.07E-04	-1.08E-02	1.93E-03	-1.12E-02	5.67E-04
7	3	3.27E-03	-4.91E-03	-4.20E-04	-1.71E-03	-1.59E-03	1.83E-03	2.43E-03	-1.72E-03	9.50E-03	1.34E-02
8	3	-1.63E-03	2.52E-03	1.53E-04	1.80E-03	-2.45E-04	-1.15E-03	1.20E-03	-3.74E-03	-4.86E-03	-5.02E-03
1	4	4.09E-03	-3.25E-03	-2.64E-03	-8.95E-03	-3.10E-04	1.99E-03	1.30E-03	-1.42E-02	1.25E-02	1.18E-02
2	4	9.54E-04	-4.70E-03	-2.29E-03	3.48E-03	2.80E-03	-4.57E-03	1.74E-02	1.20E-03	3.06E-02	-2.46E-02
3	4	1.24E-03	1.28E-03	9.02E-04	-1.81E-03	-1.16E-03	9.63E-04	-3.85E-03	-1.54E-02	-2.50E-03	-7.70E-03
4	4	-3.48E-03	-8.19E-04	-3.21E-04	1.65E-03	7.48E-04	-2.86E-03	1.12E-02	-9.43E-03	1.04E-02	-1.42E-02
5	4	4.42E-04	-7.71E-04	7.41E-04	-2.17E-03	-1.14E-03	1.51E-03	-5.28E-03	-9.98E-03	-4.76E-03	3.11E-03
6	5	1.12E-03	-3.64E-04	9.01E-04	-3.87E-03	-5.91E-04	3.04E-03	-4.54E-03	-1.19E-02	-1.22E-02	2.81E-03
7	5	-6.51E-04	3.22E-04	-3.04E-04	9.44E-04	-2.31E-05	-2.45E-03	-1.75E-04	1.82E-03	6.31E-03	-1.20E-02
8	5	2.75E-03	-1.62E-03	-1.22E-04	-1.08E-03	-2.18E-04	4.78E-04	1.78E-03	-5.53E-03	-6.09E-03	3.30E-03
2	5	1.38E-03	1.25E-03	-4.32E-04	9.71E-04	-2.58E-04	-2.45E-04	1.51E-03	-1.36E-03	6.23E-04	-4.96E-03
3	6	3.97E-03	9.13E-05	2.66E-04	-1.71E-03	-1.45E-03	6.11E-04	-1.23E-03	-8.06E-03	-3.23E-04	-4.58E-03
4	6	-1.75E-04	3.30E-04	-5.72E-04	1.47E-04	2.45E-04	-5.15E-04	3.07E-03	-1.39E-03	4.09E-03	8.14E-04
5	6	4.38E-04	7.94E-04	-1.68E-04	-1.49E-03	-1.41E-04	8.05E-04	1.96E-03	-6.70E-03	-4.53E-03	-3.57E-04
6	7	3.15E-03	1.60E-03	-3.30E-04	-1.56E-03	-2.34E-04	2.21E-04	7.34E-04	-8.58E-03	2.95E-03	-1.60E-03
7	7	2.60E-04	3.42E-05	8.19E-05	-5.40E-05	-4.51E-04	-6.72E-05	9.96E-04	-1.06E-03	-3.18E-03	-1.60E-03
8	8	2.53E-03	2.56E-04	-8.65E-05	-1.41E-03	4.21E-05	6.95E-04	-6.36E-04	-5.73E-03	1.29E-03	-1.27E-04

REFERENCES

- Aikin, A.C., A.E. Hedin, D.J. Kendig, and S. Drake (1993), Thermospheric molecular oxygen measurements using the ultraviolet spectrometer on the solar maximum mission spacecraft, *J. Geophys. Res.*, 98 (A10), 17607–17613, doi: 10.1029/93JA01468.
- Akmaev, R.A., F. Wu, T.J. Fuller-Rowell, H. Wang, and M.D. Iredell (2010), Midnight density and temperature maxima, and thermospheric dynamics in Whole Atmosphere Model simulations, *J. Geophys. Res.*, 115, A08326, doi: 10.1029/2010JA015651.
- Bates, D.R., (1959), Some problems concerning the terrestrial atmosphere above about the 100 km level, *Proc. R. Soc. London Ser., A* 253, 451-462.
- Barlier, F., C. Berger, J.L. Falin, G. Kockarts, and G. Thuillier (1978), A thermospheric model based on satellite drag data, *Annales de Geophysique*, 34(1), 9–24.
- Bettadpur, S., (2007), Product Specification Document, Technical Report CSR-GR-03-02, Center for Space Research, The University of Texas at Austin.
- Bettadpur, S., (2009), Recommendation for a-priori Bias & Scale Parameters for Level-1B ACC Data GRACE technical note no. 2, V.2. [Online].
Available: ftp://podaac.jpl.nasa.gov/allData/grace/docs/TN-02_ACC_CalInfo.pdf
- Bettadpur, S., (2012), UTCSR Level-2 processing standards document (For Level-2 Product Release 0005), GRACE(CSR-GR-12-xx), University of Texas at Austin, Austin, pp 327-742.
- Bezděk, A., (2010), Calibration of accelerometers aboard GRACE satellites by comparison with POD-based nongravitational accelerations, *Journal of Geodyn.*, vol. 50, no.5, pp. 410-423.
- Bhanderi, D., (2005), *Spacecraft Attitude Determination with Earth Albedo Corrected Sun Sensor Measurements*, Ph.D. dissertation, Aalborg University, Denmark.
- Biancale, R., and A. Bode (2006), Mean annual and seasonal atmospheric tide models based on 3-hourly and 6-hourly ECMWF surface pressure data, Scientific Technical Report STR06/01, Deutsches GeoForschungsZentrum, Potsdam, Germany.
- Bjornsson, H., and S.A. Venegas (1997), *A Manual for EOF and SVD Analyses of Climatic Data*, McGill University, CCGCR Report No. 97-1 Montréal, Québec, 52pp.

- Bowman, B.R., W.K. Tobiska, and M.J. Kendra (2008a), The thermospheric semiannual density response to solar EUV heating, *J. Atmos. Sol. Terr. Phys.*, 70(11–12), 1482–1496, doi:10.1016/j.jastp.2008.04.020.
- Bowman, B.R., W.K. Tobiska, F.A. Marcos, and C. Valladares (2008b), The JB2006 empirical thermospheric density model, *J. Atmos. Sol. Terr. Phys.*, 70(5), 774–793, doi:10.1016/j.jastp.2007.10.002.
- Bowman, B.R., W.K. Tobiska, F.A. Marcos, C.Y. Huang, C.S. Lin, and W.J. Burke (2008c), A new empirical thermospheric density model JB2008 using new solar and geomagnetic indices, in *AIAA/AAS Astrodynamics Specialist Conference and Exhibit*, 18–21 August 2008, Honolulu, Hawaii, number AIAA 2008–6438.
- Bruinsma, S.L., (2015), The DTM-2013 thermosphere model, *J. Space Weather Space Clim.* 5, A1, doi: 10.1051/swsc/2015001.
- Bruinsma, S., D. Tamagnan, and R. Biancale (2004), Atmospheric densities from CHAMP/STAR accelerometer observations, *Planet Space Sci.*, 52, 297–312, doi:10.1016/j.pss.2003.11.004.
- Bruinsma S., J.M. Forbes, R.S. Nerem, and X. Zhang (2006), Thermosphere density response to the 20–21 November 2003 solar and geomagnetic storm from CHAMP and GRACE accelerometer data, *J. Geophys. Res.*, 111, A06303.
- Bruinsma, S., R. Biancale, and F. Perosanz (2007), Calibration parameters of the CHAMP and GRACE accelerometers CNES. Poster Communication.
- Bruinsma, S.L., J.M. Lemoine, R. Biancale et al., (2010), CNES/GRGS 10-day gravity field models (release 2) and their evaluation, *Adv. Space Res.*, 45, 587–601.
- Burns, J.A., (1976), Elementary derivation of the perturbation equations of celestial mechanics, *American Journal of Physics*, 44(10), 944–949, doi:10.1119/1.10237.
- Calabia, A., and S.G. Jin (2015), GPS-based non-gravitational accelerations and accelerometer calibration, in *Satellite Positioning: Methods, Models and Applications*, S. Jin (Ed.), InTech-Publisher, Rijeka, Croatia, ISBN: 978-953-51-1738-4, pp.47-72.
- Calabia A., and S.G. Jin (2016a), Assessment of conservative force models from GRACE accelerometers and precise orbit determination, *Aerosp. Sci. Technol.*, 49, 80–87, doi: 10.1016/j.ast.2015.11.034.

-
- Calabia, A., and S.G. Jin (2016b), New modes and mechanisms of thermospheric mass density variations from GRACE accelerometers, *J. Geophys. Res. Space Physics*, 121(11), 11191-11212, doi: 10.1002/2016JA022594.
- Calabia, A., and S.G. Jin (2016c), Long-term variations of thermospheric air mass density derived from GRACE accelerometers, *Proceeding of Progress In Electromagnetics Research Symposium (PIERS2016)*, August 8-11, 2016, Shanghai, China, pp. 4759-4763, doi: 10.1109/PIERS.2016.7735744.
- Calabia, A., and S.G. Jin (2016d), Thermospheric mass density variations during the March 2015 geomagnetic storm from GRACE accelerometers, *Proceeding of Progress In Electromagnetics Research Symposium (PIERS2016)*, August 8-11, 2016, Shanghai, China, pp. 4976-4980, doi: 10.1109/PIERS.2016.7735812.
- Calabia, A., and S.G. Jin, (2017), Thermospheric density estimation and responses to the March 2013 geomagnetic storm from GRACE GPS-determined precise orbits, *J. Atmos. Sol. Terr. Phys.*, 154:167–179, doi:10.1016/j.jastp.2016.12.011.
- Calabia, A., S.G. Jin, and R. Tenzer (2015), A new GPS-based calibration of GRACE accelerometers using the arc-to-chord threshold uncovered sinusoidal disturbing signal, *Aerospace Sci. Technol.*, doi: 10.1016/j.ast.2015.05.013.
- Cane, H.V., I.G. Richardson, and T.T. von Rosenvinge (1998), Interplanetary magnetic field periodicity of ~153 days, *Geophys. Res. Lett.*, 25(24), 4437-4440, doi: 10.1029/1998GL900208.
- Canuto, E., A. Molano, and L. Massotti (2010), Drag-Free Control of the GOCE Satellite: Noise and Observer Design, *IEEE Transactions on Control Systems Technology*, vol. 18, no. 2, pp. 501-509, doi: 10.1109/TCST.2009.2020169.
- Case, K., G. Kruizinga, and S. Wu (2002), GRACE Level 1B Data Product User Handbook (JPL Publication D-22027).
- Cerri, L., J.M. Lemoine, F. Mercier, N.P. Zelensky, and F.G. Lemoine (2013), DORIS-based point mascons for the long term stability of precise orbit solutions, *Adv. Space Res.*, 52, 466–476.

- Chakrabarti, S., B. Bush, D. Cotton, G.R. Gladstone, R. Link, and T.W. Barbee (1990), Remote sensing of the thermosphere, plasmasphere, and exosphere, *IEEE Transactions on Nuclear Science*, vol. 37, no. 3, pp. 1274-1279, doi: 10.1109/23.57377.
- Chen, G.-M., J. Xu, W. Wang, and A.G. Burns (2014), A comparison of the effects of CIR- and CME-induced geomagnetic activity on thermospheric densities and spacecraft orbits: Statistical studies, *J. Geophys. Res.*, 119, 7928–7939.
- Cheng, M., J.C. Ries, and B.D. Tapley (2011), Variations of the Earth's figure axis from satellite laser ranging and GRACE, *J. Geophys. Res.*, 116 B01409.
- Clemmons, J.H., J.H. Hecht, D.R. Salem, and D.J. Strickland, (2008), Thermospheric density in the Earth's magnetic cusp as observed by the streak mission, *Geophys. Res. Lett.*, 35, L24103, doi: 10.1029/2008GL035972.
- Cook, G.E., (1965), Satellite drag coefficients, *Planet. Space Sci.*, 13, 929–946, doi: 10.1016/0032-0633(65)90150-9.
- Couhert, A., L. Cerri, J.F. Legeais, M. Ablain, N.P. Zelensky, B.J. Haines, F.G. Lemoine, W.I. Bertiger, S.D. Desai, and M. Otten (2015), Towards the 1 mm/y stability of the radial orbit error at regional scales, *Adv. Space Res.*, 55 2–23.
- Dahle, C., F. Flechtner, C. Gruber, et al., (2013), GFZ GRACE Level-2 processing standards document for level-2 product release 0005. Scientific Technical Report STR12/02—data, revised edition, Potsdam.
- Determan, J.R., S.A. Budzien, M.P. Kowalski, M.N. Lovellette, P.S. Ray, M.T. Wolff, K.S. Wood, L. Titarchuk, and R. Bandyopadhyay (2007), Measuring atmospheric density with X-ray occultation sounding, *J. Geophys. Res.*, 112, A06323, doi: 10.1029/2006JA012014
- Desai, S.D., (2002), Observing the pole tide with satellite altimetry, *J. Geophys. Res.*, 107(C11) 3186, [online]: http://62.161.69.131/iers/conv2010/convupdt/convupdt_c6.html
- Doornbos, E., (2011), *Thermospheric density and wind determination from satellite dynamics*, Ph.D dissertation. TU Delft.
- Doornbos, E., S. Bruinsma, S. Fritsche, G. Koppenwallner, P. Visser, J. van den IJssel, and J. de Teixeira de Encarnacao (2014a), GOCE+ theme 3: Air density and wind retrieval using GOCE data, Final report, Tech. Rep. 4000102847/NL/EL, TU Delft, Netherlands.

- Doornbos, E., P. Visser, G. Koppenwallner, and S. Fritsche (2014b), GOCE+ theme 3: Air density and wind retrieval using GOCE data, Algorithm Theoretical Basis Document, Tech. Rep. ESA AO/1-6367/10/NL/AF, TU Delft, Netherlands.
- Doornbos, E., J. van den IJssel, H. Lühr, M. Förster, and G. Koppenwallner (2010), Neutral density and cross-wind determination from arbitrarily oriented multi-axis accelerometers on satellites, *J. Spacecraft Rockets*, 47 (4), 580–589, doi:10.2514/1.48114.
- Drob, D.P., J.T. Emmert, G. Crowley, J.M. Picone, G.G. Shepherd, W. Skinner, P. Hays, R.J. Niciejewski, M. Larsen, C.Y. She, J.W. Meriwether, G. Hernandez, M.J. Jarvis, D.P. Sipler, C.A. Tepley, M.S. O'Brien, J.R. Bowman, Q. Wu, Y. Murayama, S. Kawamura, I.M. Reid, and R.A. Vincent (2008), An empirical model of the earth's horizontal wind fields: HWM07, *J. Geophys. Res.*, 113(A12304), doi:10.1029/2008JA013668.
- Drob, D.P., J.T. Emmert, J.W. Meriwether, J.J. Makela, E. Doornbos, M. Conde, G. Hernandez, J. Noto, K.A. Zawdie, S.E. McDonald, J.D. Huba, J.H. Klenzing (2015), An update to the Horizontal Wind Model (HWM): The quiet time thermosphere, *Earth and Space Science*, 2, 301–319, doi:10.1002/2014EA000089.
- Emmert, J.T., (2015a), Thermospheric mass density: A review, *Adv. Space Res.*, 56(5), 773-824, doi: 10.1016/j.asr.2015.05.038.
- Emmert, J.T., (2015b), Altitude and solar activity dependence of 1967–2005 thermospheric density trends derived from orbital drag, *J. Geophys. Res. Space Phys.*, 120, doi: 10.1002/2015JA021047.
- Emmert, J.T., J.M. Picone, J.L. Lean, and S.H. Knowles (2004), Global change in the thermosphere: compelling evidence of a secular decrease in density, *J. Geophys. Res.*, 109, A02301, doi: 10.1029/2003JA010176.
- Emmert, J.T., and J.M. Picone (2010), Climatology of globally averaged thermospheric mass density, *J. Geophys. Res.*, 115, A09326, doi:10.1029/2010JA015298.
- Fletcher, F., (2007), AOD1B product description document, GRACE project documentation, JPL 327–750, Rev. 1.0. JPL, Pasadena, CA. 17 August 2011.
- Forbes, J.M., and R.G. Roble (1990), Thermosphere-ionosphere coupling: An experiment in interactive modeling, *J. Geophys. Res.*, 95(A1), 201–208, doi:10.1029/JA095iA01p00201.

- Forbes, J. M., X. Zhang, S. Bruinsma, and J. Oberheide (2013), Lunar semidiurnal tide in the thermosphere under solar minimum conditions, *J. Geophys. Res. Space Physics*, 118, 1788–1801, doi:10.1029/2012JA017962.
- Förste, C., S. Bruinsma, R. Shako, et al., (2011), EIGEN-6: a new combined global gravity field model including GOCE data from the collaboration of GFZ-Potsdam and GRGS-Toulouse, *Ocean Surface Topography Science Team Meeting*, San Diego, USA.
- Goiginger, H., D. Rieser, T. Mayer-Gürr, et al., (2011), The combined satellite-only global gravity field model GOCO02S, *Geophysical Research Abstracts*, 13, EGU2011-10, 571.
- Goodman, F.O., (1964), *Fourth International Symposium on Rarefied Gas Dynamics*, Academic press, New York.
- Gummow, R.A., (2002), GIC effects on pipeline corrosion and corrosion control systems, *J. Atmos. Sol.-Terr. Phys.*, 64 (16), 1755-1764.
- Guo, J., W. Wan, J.M. Forbes, E. Sutton, R.S. Nerem, T.N. Woods, S. Bruinsma, and L. Liu (2007), Effects of solar variability on thermosphere density from CHAMP accelerometer data, *J. Geophys. Res.*, 112, A10308, doi:10.1029/2007JA012409.
- Guo, J., W. Wan, J.M. Forbes, E. Sutton, R.S. Nerem, and S. Bruinsma (2008), Interannual and latitudinal variability of the thermosphere density annual harmonics, *J. Geophys. Res.*, 113, A 08301, doi:10.1029/2008JA013056.
- Hafez, A.G., and E. Ghamry (2013), Geomagnetic Sudden Commencement Automatic Detection via MODWT, *IEEE Transactions on Geoscience and Remote Sensing*, vol. 51, no. 3, pp. 1547-1554, doi: 10.1109/TGRS.2012.2207962
- Hagan M.E., R.G. Roble, J. Hackney (2001), Migrating thermospheric tides, *J. Geophys. Res. Atmospheres*, 106(106):12739-12752.
- Harris, I., and W. Priester (1962), Time-dependent structure of the upper atmosphere, *Journal of the Atmospheric Sciences*, 19(4), 286–301.
- Häusler, K., M.E. Hagan, A.J.G. Baumgaertner, A. Maute, G. Lu, E. Doornbos, S. Bruinsma, J.M. Forbes, and F. Gasperini (2014), Improved short-term variability in the thermosphere-ionospheremesosphere- electrodynamics general circulation model, *J. Geophys. Res. Space Physics*, 119, 6623–6630, doi: 10.1002/2014JA020006.

- Hedin, A.E. (1983), A revised thermospheric model based on mass spectrometer and incoherent scatter data: MSIS-83, *J. Geophys. Res.*, 88, 10170–10188.
- Hedin, A.E., E.L. Fleming, A.H. Manson, F.J. Schmidlin, S.K. Avery, R.R. Clark, S.J. Franke, G.J. Fraser, T. Tsuda, F. Vial, and R.A. Vincent (1996), Empirical wind model for the upper, middle and lower atmosphere, *J. Atmos. Sol. Terr. Phys.*, 58, 1421–1447, doi: 10.1016/0021-9169(95)00122-0.
- Hedin, A.E., C.A. Reber, G.P. Newton, N.W. Spencer, J.E. Salah, J.V. Evans, D.C. Kayser, D. Alcaide, P. Bauer, and L. Cogger (1977), A global thermospheric model based on mass spectrometer and incoherent scatter data MSIS. I - N₂ density and temperature, *J. Geophys. Res.*, 82, 2139–2147.
- Henning, J., (2014), LAGINT 1-D piecewise Lagrange interpolation [Online] Available: <http://www.mathworks.com/matlabcentral/fileexchange/36800-interpolation-utilities/content/lagint.m>
- Hwang, C., T.J. Lin, T.P. Tseng, and B.F. Chao (2008), Modeling Orbit Dynamics of FORMOSAT-3/COSMIC Satellites for Recovery of Temporal Gravity Variations, *IEEE Transactions on Geoscience and Remote Sensing*, vol. 46, no. 11, pp. 3412-3423, doi: 10.1109/TGRS.2008.2004789.
- Ijssel, J. van den (2014), *GPS-based precise orbit determination and accelerometry for low flying satellites*, Ph.D. dissertation, Technische Universiteit Delft.
- Ijssel, J. van den, P. Visser, R. Haagmans (2004), Determination of non-conservative accelerations from orbit analysis. in: Reigber, Ch., Luhr, H., Schwintzer, P., Wickert, J. (Eds.), *Earth Observation with CHAMP Results from Three Years in Orbit*, Springer, pp. 95-100.
- Ijssel, J. van den, P. Visser (2005), Determination of non-gravitational accelerations from GPS satellite-to-satellite tracking of CHAMP, *Adv. Space Res.*, 36 (3), 418–423.
- Jacchia, L.G., (1964), Static diffusion models of the upper atmosphere with empirical temperature profiles, *Smithsonian Astrophysical Observatory Special Report*, 170.
- Jin, S.G., J. Park, J. Wang, B. Choi, and P. Park (2006), Electron density profiles derived from ground-based GPS observations, *J. Navig.*, 59(3), 395–401, doi: 10.1017/S0373463306003821.

- Jin, S.G., and J. Park (2007), GPS ionospheric tomography: a comparison with the IRI-2001 model over South Korea, *Earth Planets Space*, 59 (4), 287–292.
- Jin, S.G., O. Luo, and P. Park (2008), GPS observations of the ionospheric F2-layer behavior during the 20th November 2003 geomagnetic storm over South Korea, *J. Geod.*, 82 (12), 883–892, doi: 10.1007/s00190-008-0217-x.
- Jin, S.G., T. van Dam, and S. Wdowinski (2013), Observing and understanding the Earth system variations from space geodesy, *J. Geodyn.*, 72:1-10, doi: 10.1016/j.jog.2013.08.001
- Jin, S.G., L.J. Zhang, and B.D. Tapley (2011), The understanding of length-of-day variations from satellite gravity and laser ranging measurements, *Geophys. J. Int.*, 184(2) 651-660.
- Joshi, B., and A. Joshi (2005), Intermediate-Term Periodicities in Soft X-ray Flare Index During Solar Cycles 21, 22 and 23, *Sol. Phys.*, 226:153. doi:10.1007/s11207-005-5716-9.
- Kappenman, J.G., (1996), Geomagnetic storms and their impact on power systems. *IEEE Engineering Review*, 7.
- King-Hele, D., (1987), *Satellite orbits in an atmosphere, theory and applications*, Blackie.
- Kim, J.S., J.V. Urbina, T.J. Kane, and D.B. Spencer (2012), Improvement of TIE-GCM thermospheric density predictions via incorporation of helium data from NRLMSISE-00, *J. Atmos. Sol.-Terr. Phys.*, 77, 19–25.
- Knocke, P., and J. Ries (1987), Earth Radiation Pressure Effects on Satellites, Center for Space Research, The University of Texas at Austin, Technical Memorandum, CSR-TM-87-01.
- Knudsen, P., and O. Andersen (2002), Correcting GRACE gravity fields for ocean tide effects, *Geophys. Res. Lett.*, 29(8), 1–4.
- Kuang, D., S. Desai, A. Sibthorpe, and X. Pi (2014), Measuring atmospheric density using GPS–LEO tracking data, *Adv. Space Res.*, 53(2):243-256, doi:10.1016/j.asr.2013.11.022
- Kwak, Y.S., K.H. Kim, Y. Deng, and J.M. Forbes (2011), Response of thermosphere density to changes in interplanetary magnetic field sector polarity, *J. Geophys. Res.*, 116, A11316.

- Kwak, Y.S., A.D. Richmond, Y. Deng, J.M. Forbes, and K.H. Kim (2009), Dependence of the high-latitude thermospheric densities on the interplanetary magnetic field, *J. Geophys. Res.*, 114, A05304.
- Lathuillère, C., M. Menvielle, A. Marchaudon, and S. Bruinsma (2008), A statistical study of the observed and modeled global thermosphere response to magnetic activity at middle and low latitudes, *J. Geophys. Res.*, 113, A07311, doi:10.1029/2007JA012991.
- Lechtenberg, T.F., C.A. McLaughlin, T. Locke, and D. Mysore Krishna (2013), Thermospheric density variations: Observability using precision satellite orbits and effects on orbit propagation, *Space Weather*, 11, 34–45, doi:10.1029/2012SW000848.1.
- Lei, J., T. Matsuo, X. Dou, E. Sutton, and X. Luan (2012a), Annual and semiannual variations of thermospheric density: EOF analysis of CHAMP and GRACE data, *J. Geophys. Res.*, 117, A01310, doi:10.1029/2011JA017324.
- Lei, J., J.P. Thayer, W. Wang, X. Luan, X. Dou, and R. Roble (2012b), Simulations of the equatorial thermosphere anomaly: Physical mechanisms for crest formation, *J. Geophys. Res.*, 117, A06318, doi:10.1029/2012JA017613.
- Lemoine, J.M., S. Bruinsma, S. Loyer et al., (2007), Temporal gravity field models inferred from GRACE data, *Adv. Space Res.*, 39 (10), 1620–1629.
- Lemoine, F.G., N.P. Zelensky, D.S. Chinn, D.E. Pavlis, D.D. Rowlands, B.D. Beckley, S.B. Luthcke, P. Willis, M. Ziebart, A. Sibthorpe, J.P. Boy, and V. Luceri (2010), Towards development of a consistent orbit series for TOPEX, Jason-1, and Jason-2, *Adv. Space Res.*, 46 1513–1540.
- Li, S.Y., and C.H. Liu (2004), Modeling the effects of ionospheric scintillations on LEO Satellite communications, *IEEE Communications Letters*, vol. 8, no. 3, pp. 147-149, doi: 10.1109/LCOMM.2004.823404
- Lieberman, R., R. Akmaev, T. Fuller-Rowell, and E. Doornbos (2013), Thermospheric zonal mean winds and tides revealed by CHAMP, *Geophys. Res. Lett.*, 40, 2439–2443, doi:10.1002/grl.50481.
- Liebmann, B., and C.A. Smith (1996), Description of a Complete (Interpolated) Outgoing Longwave Radiation Dataset. *Bulletin of the American Meteorological Society*, 77, 1275-1277.

- Liu, H., H. Lühr, V. Henize, and W. Köhler (2005), Global distribution of the thermospheric total mass density derived from CHAMP, *J. Geophys. Res.*, 110, A04301.
- Liu, H., and H. Lühr (2005), Strong disturbance of the upper thermospheric density due to magnetic storms: CHAMP observations, *J. Geophys. Res.*, 110, A09S29.
- Liu, H., H. Lühr, and S. Watanabe (2007), Climatology of the equatorial thermospheric mass density anomaly, *J. Geophys. Res.*, 112, A05305.
- Liu, H., M. Yamamoto, and H. Lühr (2009), Wave-4 pattern of the equatorial mass density anomaly: A thermospheric signature of tropical deep convection, *Geophys. Res. Lett.*, 36, L18104.
- Liu, H., T. Hirano, and S. Watanabe (2013), Empirical model of the thermospheric mass density based on CHAMP satellite observation, *J. Geophys. Res. Space Physics*, 118, 843–848.
- Liu, R., H. Lühr, E. Doornbos, and S.-Y. Ma (2010), Thermospheric mass density variations during geomagnetic storms and a prediction model based on the merging electric field *Ann. Geophys.*, 28, 1633-1645.
- Liu, R., S.-Y. Ma, and H. Lühr (2011), Predicting storm-time thermospheric mass density variations at CHAMP and GRACE altitudes, *Ann. Geophys.*, 29, 443-453.
- Luthcke, S.B., J.A. Marshall, S.C. Rowton, K.E. Rachlin, C.M. Cox and, R.G. Williamson (1997), Enhanced Radiative Force Modeling of the Tracking and Data Relay Satellites, *Journal of the Astronautical Sciences*, Vol. 45, No. 3, pp. 349–370.
- Luthcke, S.B., D.D. Rowlands, F.G. Lemoine et al., (2006), Monthly spherical harmonic gravity field solutions determined from GRACE inter-satellite range-rate data alone, *Geophys. Res. Lett.*, 33, L02402.
- Ma, R., J. Xu, W. Wang, J. Lei, H.-L. Liu, A. Maute, and M. Hagan (2010), Variations of the nighttime thermospheric mass density at low and middle latitudes, *J. Geophys. Res.*, 115, A12301.
- Marcos, F.A., D.F. Gillette, and E.C. Robinson (1983), Evaluation of selected global thermospheric density models during low solar flux conditions, *Adv. Space Res.*, 3, 85-89.
- Marcos, F.A., and J.M. Forbes (1985), Thermospheric winds from the satellite electrostatic triaxial accelerometer system, *J. Geophys. Res.*, 90, 6543-6552.

- Matsuo, T., and J.M. Forbes (2010), Principal modes of thermospheric density variability: Empirical orthogonal function analysis of CHAMP 2001-2008 data, *J. Geophys. Res.*, 115 A07309.
- Matsuo, T., A.D. Richmond, and D.W. Nychka (2002), Modes of high latitude electric field variability derived from DE-2 measurements: Empirical Orthogonal Function (EOF) analysis, *Geophys. Res. Lett.*, 29(7) 1107.
- McLaughlin, C.A., T. Lechtenberg, E. Fattig, and D. Mysore Krishna (2013), Estimating density using precision satellite orbits from multiple satellites, *Journal of the Astronautical Sciences*, 59(1-2):84-100, doi: 10.1007/s40295-013-0007-4.
- Mehta, P.M., A Walker, C.A. McLaughlin, and J. Koller (2014), Comparing Physical Drag Coefficients Computed Using Different Gas–Surface Interaction Models, *J. Spacecraft Rockets*, 51-3, 873-883.
- Mehta, P.M., C.A. McLaughlin, and E.K. Sutton (2013), Drag coefficient modeling for grace using Direct Simulation Monte Carlo, *Adv. Space Res.*, 52:2035-2051, doi:10.1016/j.asr.2013.08.033
- Meier, R.R., and J.M. Picone (1994), Retrieval of absolute thermospheric concentrations from the far UV dayglow: an application of discrete inverse theory, *J. Geophys. Res.*, 99, 6307–6320.
- Melachroinos, S., F. Lemoine, D. Chinn, N. Zelensky, J. Nicholas, and B. Beckley (2014), The effect of seasonal and long-period geopotential variations on the GPS orbits, *GPS Solut.*, 18 (4) 497-507.
- Molinski, T., (1996), Geomagnetically induced currents: causes, effect, and mitigation, *IEEE Canadian Review*, 13.
- Montenbruck O and Gill E (2013), *Satellite orbits: Models, methods and applications*, Berlin: Springer.
- Müller, S., H. Lühr, and S. Rentz (2009), Solar and geomagnetic forcing of the low latitude thermospheric mass density as observed by CHAMP, *Ann. Geophys.*, 27, 2087-2099.
- Munk, W.H., and D.E. Cartwright (1966), Tidal spectroscopy and prediction, *Phil. Trans. Roy. Soc.*, London, A259, 533–581.

- Nicolls, M.J., H. Bahcivan, I. Häggström, and M. Rietveld (2014), Direct measurement of lower thermospheric neutral density using multifre-quency incoherent scattering, *Geophys. Res. Lett.*, 41, doi: 10.1002/2014GL062204.
- Owens, J.K., W.W. Vaughan, K.O. Niehuss, and J. Minow (2000), Space weather, Earth's neutral upper atmosphere (thermosphere), and spacecraft orbital lifetime/dynamics, *IEEE Transactions on Plasma Science*, vol. 28, no. 6, pp. 1920-1930, doi: 10.1109/27.902220
- Petit, G., and B. Luzum (2010), IERS conventions (2010), IERS technical note 36, International Earth Rotation and Reference Systems Service (IERS), Frankfurt am Main: Verlag des Bundesamts für Kartographie und Geodäsie.
- Pavlis, N.K., S.A. Holmes, S.C. Kenyon, and J.K. Factor (2012), The development and evaluation of the Earth Gravitational Model 2008 (EGM2008), *J. Geophys. Res.*, 117, B04406.
- Picone, J.M., A.E. Hedin, D.P. Drob, and A.C. Aikin (2002), NRLMSISE-00 empirical model of the atmosphere: Statistical comparisons and scientific issues, *J. Geophys. Res.*, 107(A12), 1468, doi:10.1029/2002JA009430.
- Picone, J.M., J.T. Emmert, and J.L. Lean (2005), Thermospheric densities derived from spacecraft orbits: accurate processing of two-line element sets, *J. Geophys. Res.*, 110, A03301, doi: 10.1029/2004JA010585.
- Pilinski, M.D., (2011), *Dynamic Gas-Surface Interaction Modeling for Satellite Aerodynamic Computations*, Ph.D. Dissertation, University of Colorado, Boulder.
- Preisendorfer, R., (1988), *Principal component analysis in meteorology and oceanography*, Amsterdam: Elsevier.
- Priester, W., M. Roemer, and H. Volland (1967), The physical behavior of the upper atmosphere deduced from satellite drag data, *Space Sci. Rev.*, 6:707-780, doi: 10.1186/BF03351782.
- Qian, L., A.G. Burns, B.A. Emery, B. Foster, G. Lu, A. Maute, A.D. Richmond, R.G. Roble, S.C. Solomon, and W. Wang (2014), The NCAR TIE-GCM: a community model of the coupled thermosphere/ionosphere system, *Geophys. Monogr.*, Ser. 201, 73–83.
- Qian, L., S.C. Solomon, and T.J. Kane (2009), Seasonal variation of thermospheric density and composition, *J. Geophys. Res.*, 114, A01312, doi: 10.1029/2008JA013643.

- Ray, R.D., R.J. Eanes, G.D. Egbert, and N.K. Pavlis (2001), Error spectrum for the global M₂ ocean tide, *Geophys. Res. Lett.*, 28, 21–24.
- Rentz, S., and H. Lühr (2008), Climatology of the cusp-related thermospheric mass density anomaly, as derived from CHAMP observations, *Ann. Geophys.*, 26, 2807–2823.
- Reubelt, T., M. Götzelmann, and E.W. Grafarend (2006), Harmonic analysis of the Earth's gravitational field from kinematic CHAMP orbits based on numerically derived satellite accelerations, in *Observation of the Earth System from Space*, Berlin Heidelberg, Springer-Verlag, Part I, pp. 27-42.
- Rice, C.J., V.L. Carter, S.R. La Valle, W.T. Chater, D.A. Jones, C.G. King, and D.F. Nelson (1973), Atmosphere Explorer pressure measurements: Ion gauge and capacitance manometer, *Radio Sci.*, 8, 305-314
- Richmond, A.D., E.C. Ridley, and R.G. Roble (1992), A thermosphere/ionosphere general circulation model with coupled electrodynamics, *Geophys. Res. Lett.*, 19, 601–604.
- Rieser, D. et al., (2012), The ocean tide model EOT11a in spherical harmonics representation. [Online]. Available: <ftp://ftp.dgfi.badw.de/pub/EOT11a>
- Ruan, H., J. Lei, X. Dou, W. Wan, and Y.C.-M. Liu (2014), Midnight density maximum in the thermosphere from the CHAMP observations, *J. Geophys. Res. Space Physics*, 119, 3741-3746, doi:10.1002/2013JA019566.
- Ruan, H., J. Du, M. Cook, W. Wang, J. Yue, Q. Gan, X. Dou, and J. Lei (2015), A numerical study of the effects of migrating tides on thermosphere midnight density maximum, *J. Geophys. Res. Space Physics*, 120, 6766-6778, doi:10.1002/2015JA021190.
- Rudenko, S., D. Dettmering, S. Esselborn, T. Schöne, C. Förste, J.M. Lemoine, M. Ablain, D. Alexandre, and K.H. Neumayer (2014), Influence of time variable geopotential models on precise orbits of altimetry satellites, global and regional mean sea level trends, *Adv. Space Res.*, 54 92–118.
- Santoni, F., F. Piergentili, and F. Graziani (2010), Broglie drag balance for neutral thermosphere density measurement on UNICubeSAT, *Adv. Space Res.*, 45 (5), 651–660.
- Schamberg, R.A., (1959), *New Analytic Representation of Surface Interaction for Hyperthermal Free Molecular Flow*, Rand Corporation, TR RM-2313.

- Sentman, L.H., (1961), *Free Molecule Flow Theory and its Application to the Determination of Aerodynamic Forces*, Lockheed Missile and Space Co., Sunnyvale, CA, TR LMSC-448514, AD 265-409.
- SERCO/DATAMAT_Consortium, (2006), GOCE L1b Products User Handbook Technical Note GOCE-GSEG-EOPG-TN-06-0137.
- Siemes, C., J. de Teixeira da Encarnação, E. Doornbos et al., (2016), Swarm accelerometer data processing from raw accelerations to thermospheric neutral densities, *Earth Planet Sp.*, 68: 92. doi:10.1186/s40623-016-0474-5.
- Singh, S.N., and W. Yim (2005), Nonlinear adaptive spacecraft attitude control using solar radiation pressure, *IEEE Transactions on Aerospace and Electronic Systems*, vol. 41, no. 3, pp. 770-779, doi: 10.1109/TAES.2005.1541428.
- Sutton, E.K., (2011), Accelerometer-derived atmospheric densities from the CHAMP and GRACE accelerometers: Version 2.3, Tech. Memo, Air Force Res. Lab., Kirtland Air Force Base.
- Sutton, E.K., J.M. Forbes, and R.S. Nerem (2005), Global thermospheric neutral density and wind response to the severe 2003 geomagnetic storms from CHAMP accelerometer data, *J. Geophys. Res.*, 110, A09S40.
- Sutton, E.K., R.S. Nerem, and J.M. Forbes (2007), Density and winds in the thermosphere deduced from accelerometer data, *J. Spacecraft Rockets*, 44(6), 1210-1219, doi:10.2514/1.28641.
- Sutton, E.K., J.M. Forbes, and D.J. Knipp (2009), Rapid response of the thermosphere to variations in Joule heating, *J. Geophys. Res.*, 114, A04319.
- Tapley, B.D., B.E. Schutz, and G.H. Born (2004), *Statistical Orbit Determination*, Elsevier, Academic press, San Diego.
- Taylor, F.W., (2005), *Elementary Climate Physics*, Oxford U. Press.
- Vallado, D.A., (2013), *Fundamentals of Astrodynamics and Applications* (Fourth Edition), ISBN: 978-11881883180, Microcosm Press. Astrodynamics Software [Online]. Available: <http://celestrak.com/software/vallado-sw.asp>

- Visser, P., E. Doornbos, J. van den IJssel, and J. de Teixeira da Encarnação (2013), Thermospheric density and wind retrieval from Swarm observations, *Earth Planets Space*, 65, 1319–1331, doi: 10.5047/eps.2013.08.003.
- Watkins, M., and D.N. Yuan (2012), JPL Level-2 Processing Standards Document for Level-2 Product Release 05, GRACE Document, pp 327–744.
- Weigelt, M., and N. Sneeuw (2005), Numerical Velocity determination and Calibration Methods for CHAMP Using the Energy Balance Approach, *Int. Assoc. of Geodesy Symposia*, vol. 129, pp. 54-59.
- Wertz, J.R., (1991), *Spacecraft Attitude Determination and Control Kluwer*, Academic Publishers Dordrecht, Boston, London.
- Wilks, D.S., (1995), *Statistical Methods in the Atmospheric Sciences*, Academic Press, San Diego.
- Wright, J.R., (2003), Real-Time Estimation of Local Atmospheric Density, *Adv. Astronaut Sci.*, 114, 927-950, AAS 03-164.
- Wu, S.C., T.P. Yunck, and C.L. Thornton (1991), Reduced-dynamic technique for precise orbit determination of low earth satellites, *J. Guidance Control Dynam.*, 14(1): 24-30. doi:10.2514/3.20600.
- Xu, J., W. Wang, and H. Gao (2013), The longitudinal variation of the daily mean thermospheric mass density, *J. Geophys. Res. Space Physics*, 118, 515–523, doi:10.1029/2012JA017918.
- Yang, Y., X. Yue, and A.G. Dempster (2016), GPS-based onboard real-time orbit determination for LEO satellites using consider Kalman filter, *IEEE Transactions on Aerospace and Electronic Systems*, vol. 52, no. 2, pp. 769-777, doi: 10.1109/TAES.2015.140758.
- Zadunaisky, P.E., (2003), Small perturbations on artificial satellites as an inverse problem, *IEEE Transactions on Aerospace and Electronic Systems*, vol. 39, no. 4, pp. 1270-1276, doi: 10.1109/TAES.2003.1261127.
- Zelensky, N.P., F.G. Lemoine, B.D. Beckley et al., (2012), Improved modeling of time variable gravity for altimeter satellite POD. Poster presented at OSTST Venice, Italy.

Zelensky, N.P., F.G. Lemoine, D.S. Chinn, S. Melachroinos, B.D. Beckley, J.W. Beall, and O. Bordyugov (2014), Estimated SLR station position and network frame sensitivity to time-varying gravity, *J. Geod.*, 88 517–537.

ACKNOWLEDGMENTS

Personal thanks are given to my Ph.D. advisor, Professor Shuanggen Jin, for his countless hours of reflecting, encouraging, and most of all patience throughout the entire process. I would like to acknowledge and thank to University of Chinese Academy of Science and Shanghai Astronomical Observatory for allowing me to conduct my research and providing any assistance requested. Great appreciation is extended to the ISDC, NASA and ESA for providing the observational data access. I would like to thank all the reviewers involved in my publications along these years for their corrections and suggestions. This work has been supported by the Chinese Government Scholarship (China Scholarship Council), National Keystone Basic Research Program (MOST 973) (Grant No. 2012CB72000), Main Direction Project of Chinese Academy of Sciences (Grant No. KJCX2-EW-T03), National Natural Science Foundation of China (NSFC) Project (Grant No. 11173050 and 11373059), and Shanghai Science and Technology Commission Project (Grant No. 12DZ2273300).

CURRICULUM VITAE

Andres Calabia Aibar

✉ andres@calabia.com

[in https://www.linkedin.com/in/andr%C3%A9s-calabia-aibar-28b81225](https://www.linkedin.com/in/andr%C3%A9s-calabia-aibar-28b81225)



Profile

Andres Calabia is a recognized academic and accomplished professional geodetic engineer, with over 7 years' experience in industry, and about 5 years' experience in academic research. He is highly skilled in geodesy, navigation and remote sensing, and with a broad range of analytic techniques, including data analysis and algorithm development. His current research interests include the upper atmosphere environments and coupling between Earth and space weather; the repercussions of these environments on low Earth orbiters and radio propagation; the utilization of accelerometers, GNSS, and other geodetic techniques to interpret the planetary variability, and to test, validate, and develop geophysical models.

Professional experience

- | | |
|------------------------|---|
| Jan. 2014 - Jun. 2017 | Graduate Research Assistant, Space/Planetary Exploration & Dynamics, Shanghai Astronomical Observatory, CAS, Shanghai, China. |
| Jun. 2013 - Jan. 2014 | Geographical Engineer, InfoTech Enterprises Europe Ltd, Rural Payments Agency, Government administration, London, United Kingdom. |
| Sept. 2012 - Jun. 2013 | Graduate Research Assistant, Department of Geodesy and Cartography, Polytechnic University of Madrid, Spain. |
| Sept. 2010 - Jun. 2012 | Graduate Research Assistant, Department of Geography, University of Alcalá de Henares, Madrid, Spain. |
| Jan. 2007 - Dec. 2009 | Civil Site Engineer (Head of production), EMCOFA S.A., Carrer de Mossèn Cinto Verdaguer, 40, Igualada, 08700, Spain. |
| Jan. 2005 - Dec. 2006 | Topographical Land Surveyor, CISGA S.A., Carrer d'Àngel Guimerà, 21, Reus, 43202, Spain. |

Education

Ph.D. in Space Geodesy and Geodynamics, 2017, Chinese Academy of Sciences, Shanghai, China. Thesis: “*Thermospheric neutral density variations from LEO accelerometers and POD*” (Prof. Dr. SG Jin, advisor).

Coursework in Geographical Engineering, 2013, Polytechnic University of Madrid, Spain (Prof. Dr. A Bethencourt, advisor).

M.Sc. in Geodesy and Cartography, 2012, University of Alcalá de Henares, Madrid, Spain, Thesis: “*Methodology for the uncertainty analysis of a model based on Multi-Criteria Evaluation techniques and Geographic Information Systems*” (Prof. Dr. M Gomez, advisor).

B.Sc. in Land Surveying, 2005, Polytechnic University of Catalonia, Barcelona, Spain, Thesis: “*Study of Llobregat river with medium resolution remote Sensing*” (Prof. Dr. JJM Benjamin, advisor).

Awards & Honours

Honourable mention at NASA LWS Jack Eddy Postdoctoral Fellowship Program, 2017, UCAR CPAESS / Heliophysics. <https://cpaess.ucar.edu/heliophysics/jack-eddy/alumni>

Scholarship for Ph.D. in Space Geodesy and Geodynamics, 2014, Chinese Academy of Sciences, China.

Grant for Collaboration with University of Alcalá, 2010, Ministry of Education, Spain.

Honours in Mathematics, 2009, University of Alcalá, Madrid, Spain.

Scholarship for M.Sc. in Geodesy and Cartography, 2009, University of Alcalá, Madrid, Spain.

Professional Society Memberships

- Institute of Electrical and Electronics Engineers (IEEE).

Relevant Skills

- Atmospheric sensing from satellite measurements.
- Geodetic Reference Systems.
- Earth rotation and time-varying gravity.

- Satellite navigation/positioning: Precise Orbit Determination; GNSS data analysis; Static differential and Real Time Kinematic GNSS positioning.
- Surveying network adjustments with Robotic Total Station, Theodolites and Precision Level instruments (GeoLab, SKY Pro).
- Statistical and mathematical modelling (MATLAB, C++, JAVA).
- Differential geometry for cartographic projections.
- Remote-sensing and multispectral analysis, including InSAR and PolSAR data processing (ArcGIS, Geomedia, ENVI, PCI, IDRISI, PolSARpro, NEST, CAD).

Service to the Profession and Research Community

- 2014 - Present Associate Editor for Journal of Geodetic Science, De Gruyter.
- 8 - 11 Aug. 2016 Session Chair, Proceeding of Progress In Electromagnetics Research Symposium (PIERS2016), Shanghai, China.

Other Noteworthy Activities

Reviewer for Aerospace Science and Technology, Journal, Elsevier

Journal Articles

1. Jin, S.G., **A. Calabria**, and L. Yuan (2017), Thermospheric sensing from GNSS and accelerometer on small satellites, Proc. IEEE. (SCI)
2. **Calabria, A.**, and S.G. Jin (2017), Thermospheric density variations following the March 2013 geomagnetic storm from GRACE GPS-determined precise orbit, J. Atmos. Solar Terrest. Phys. 154, 167-179, doi: 10.1016/j.jastp.2016.12.011. (SCI)
3. **Calabria, A.**, and S.G. Jin (2016), New modes and mechanisms of thermospheric mass density variations from GRACE accelerometers, J. Geophys. Res. Space Physics, 121(11), 11191-11212, doi: 10.1002/2016JA022594. (SCI)
4. **Calabria, A.**, and S.G. Jin (2016), Assessment of conservative force models from GRACE accelerometers and precise orbit determination, Aerosp. Sci. Technol., 49, 80-87, doi: 10.1016/j.ast.2015.11.034. (SCI)
5. **Calabria, A.**, S.G. Jin, and R. Tenzer (2015), A new GPS-based calibration of GRACE accelerometers using the arc-to-chord threshold uncovered sinusoidal disturbing signal, Aerosp. Sci. Technol., 45, 265-271, doi: 10.1016/j.ast.2015.05.013. (SCI)

Papers Presented at Conferences and Workshops

1. **Calabria, A.**, and S.G. Jin, Thermospheric mass density variations during the March 2015 geomagnetic storm from GRACE accelerometers, Proceeding of Progress In Electromagnetics Research Symposium (PIERS2016), August 8-11, 2016, Shanghai, China, pp. 4976-4980, doi: 10.1109/PIERS.2016.7735812. (EI)

2. **Calabia, A.**, and S.G. Jin, Long-term variations of thermospheric air mass density derived from GRACE accelerometers, Proceeding of Progress In Electromagnetics Research Symposium (PIERS2016), August 8-11, 2016, Shanghai, China, pp. 4759-4763, doi: 10.1109/PIERS.2016.7735744. (EI)
3. Li, D., S.G. Jin, G. Zheng, and **A. Calabia**, Evaluation of 3-D ionospheric tomography from denser GNSS array observations in Japan, Proceeding of Progress In Electromagnetics Research Symposium (PIERS2016), August 8-11, 2016, Shanghai, China, pp. 4986-4990, doi: 10.1109/PIERS.2016.7735814. (EI)
4. **Calabia, A.**, and S.G. Jin, Variations of thermospheric air mass density derived from GRACE accelerations and GPS POD, The 1st International Conference on GNSS+ (ICG+2016), July 27-30, 2016, Shanghai, China.
5. **Calabia, A.**, M. Gomez, G. Benavides, Validación de un modelo basado en Técnicas de Evaluación Multicriterio y SIG a partir de análisis de incertidumbre. Una propuesta para mejorar la introducción de distorsión en las variables de partida, Proceeding of XV National Congress of Geographical Information Technologies, 20-21 September 2012, Madrid, Spain.

Book Chapters

1. **Calabia A.**, and S.G. Jin (2015), GPS-based non gravitational accelerations and accelerometer calibration, in S. Jin (Ed.), Satellite Positioning: Methods, Models and Applications, In Tech-Publisher, Rijeka, Croatia, ISBN: 978-953-51-1738-4, pp.47-72.
2. Gomez Delgado, M., R. Plata Rocha, J. Oran Caceres, and **A. Calabia** (2012), Urban dynamics analysis and simulation of future development scenarios with Geographic Information Technologies, in Ra-Ma (Ed.), Paracuellos de Jarama, Madrid, Spain, ISBN: 978-84-9964-125-6, Chapter nº 5, pp. 237-274